Analysis and Design of Antennas and Radiometers for Radio Astronomy Applications in Microwave, Mm-wave, and THz Bands

by

Kerlos Atia Abdalmalak Dawoud

A dissertation submitted by in partial fulfillment of the requirements for the degree of Doctor of Philosophy in

MULTIMEDIA AND COMMUNICATION

Universidad Carlos III de Madrid

Advisor:

Luis Enrique García Muñoz

February 2022

To my dear wife Shereen and lovely daughter Ereeny

ACKNOWLEDGEMENTS

It's my pleasure to write this acknowledgment of gratitude and appreciation to every person who helped me during the Ph.D. period by technical means, gaining practical experience, moral support, or any ways that assist to relieve work pressure.

First of all, I am extremely grateful to my supervisor Prof. Luis Enrique for his invaluable advice, offered guidance, continuous support, and patience during my Ph.D. study, also to give me such chance to start researching in the radio astronomy field which was completely new for me. I appreciate that he was always available not only for technical concerns but for personal matters too. Many thanks to the head of GREMA research group (Prof. Daniel Segovia) which I considered as my father in Spain and his knowledge and experience have encouraged me all the time of my research and daily life. Thanks also for his simplicity and removing all the borders between us, I still remember the great moments we spent together, playing football, climbing mountains, and riding zip lines.

For all the professors, colleagues, and Ph.D./master students that I met in the GREMA (UC3M, Spain), I would like to recognize the precious assistance that you all provided and the surprising kindness you showed during the Ph.D. period. Prof. Luis Emilio and Dr. Sergio Llorente for their consecutive help and support especially the ones related to HFSS and cluster problems. Dr. Alejandro Rivera, the lab master who gave me a hand for learning both EM and optical measurements and all tricks about the lab without wavering in his support. Dr. Gabriel Santamaría for his awesome assistance in theoretical models and calculations particularly for nonlinear optics, besides being a good friend. Dr. Mallika Irene for the valuable comments for the thesis and for the useful setups and experiments we performed in the optical lab. Dr. Adrián Amor for assisting me in base-station antenna measurements and the long enjoyable time we stayed over together in the office. Dr. Ana López for her unforgettable supersizes she prepared, all Palmeras she bought, and for her advice to keep my health. Ahmed El Yousfi, Abdenasser Lamkaddem, and Enderson Falcon for the profitable measurements we did together and all fun we had in playing football. Prof. Vicente Gonzalez, Sergio Martin, Paula Fernández, and Iván Bailón for their kind support in the base station and antenna array feed. Dr. Gabriel Galindo and Dr. José Juan for all their jokes and for the amazing trip to USA (I would never forget your words, what happens in USA, stays in USA). Dr. Alejandro García for entertaining walks in Madrid and useful information he consistently provides. Dr. Fernando for the good time we had in the office and his great hot gifts. Michal Wasiak for his beneficial life tips which I always consider as my human development coach. Monica Borgoños and Dr. Álvaro Pascual for the short but good periods we enjoyed and the interesting ping pong matches. Iván Fernández for his aid in manufacturing many PCB circuits.

Thanks should also go to Prof. Elliott R. Brown (Wright State University, USA) for all the work we did together especially the ones related to the metal losses in the THz antennas, and for the great insightful suggestions during our scientific visit to the astronomical observatory of the Institute of Astrophysics of the Canary Islands (IAC). Prof. Zoya Popovic (University of Colorado, USA) for her valuable feedback and comments about my work in UWB feed antennas. Prof. Choon lee, Dr. Ayman Althuwayb, and Khalid Alsirhani for the generous hospitality I had during my stay at Southern Methodist University, USA, and for the key studies we performed related to dielectric resonator antennas.

Special thanks to Jonas Flygare (Onsala Space Observatory, Chalmers University of Technology, Sweden) and Prof. Miroslav Pantaleev (RUAG Space, Switzerland) for their contributory discussions about state-of-the-art VLBI radio telescope feeds. José Manuel, Dr. José López-Fernández, Dr. Jose Antonio Lopez-Perez, all the team in Yebes astronomical observatory (Spain), and people in the National Institute for Aerospace Technology (INTA), Spain for their assistance in the measurements of the VLBI UWB feed.

I very much appreciate Juan Segador, Alejandro Murillo, Dr. Bruno Biscontini, and other team members from HUAWEI Technologies Duesseldorf GMBH, Germany for the productive meetings we had and the innovative ideas raised on them related to antenna design and fabrication methods. Dr. David Gonzalez-Ovejero, Prof. Olivier De Sagazan, and Xavier Morvan (Rennes University, France) for their valuable talks and help with the micro-machining of the satellite radiometer. Dr. Dominika Warmowska and Prof. Zbynek Raida (Brno University of Technology, Czech Republic) for their helpful discussions about THz antennas fabrication. Prof. Guillermo Carpintero, Jessica Cesar, Dr. Muhsin Ali, Dr. Robinson Guzman, and all people in the Optoelectronic and laser technology (GOTL) group (UC3M, Spain) for their kind support during nonlinear up-conversion measurements.

Finally, my sincere thankfulness to my wife which the completion of my Ph.D. thesis would be much harder without her motivation, unparalleled support, and endless patience. My father, sister, brother, mother-in-law, all family in Egypt, and all friends in Spain for their continuous encouragement. Fam for encouraging me to continue my postgraduate studies in Spain. Finally, Dr. Mohamed Abdel-Nasser for his constructive criticism and for being always beside me.

PUBLISHED AND SUBMITTED CONTENT

The content from the following publications has been partially or totally included in this thesis. The material from these sources included in this thesis is not singled out with typographic means and references

Journal papers:

1. **K. A. Abdalmalak** et al., "Ultrawideband Conical Log-Spiral Circularly Polarized Feed for Radio Astronomy," in IEEE Transactions on Antennas and Propagation, vol. 68, no. 3, pp. 1995-2007, Mar. 2020.
   URL: https://doi.org/10.1109/TAP.2019.2949700
   It is fully included in Chapters 1 and 2.

2. E. García-Muñoz, **K. A. Abdalmalak**, et al., "Photonic-based Integrated Sources and Antenna Arrays for Broadband Wireless Links in Terahertz Communications," in Semiconductor Science and Technology, vol. 34, no. 5, pp. 054001, Mar. 2019.
   URL: https://doi.org/10.1088/1361-6641/aaf8f2
   It is partially included in Chapter 3.

3. D. Warmowska, **K. A. Abdalmalak**, L. E. G. Muñoz, and Z. Raida, "High-gain, Circularly-polarized THz Antenna with Proper Modeling of Structures with Thin Metallic Wall," in IEEE Access, vol. 8, pp. 125223-125233, Jul. 2020.
   URL: https://doi.org/10.1109/ACCESS.2020.3007576
   It is partially included in Chapter 3.

4. A. Rivera-Lavado, L. García-Muñoz, A. Generalov, D. Lioubtchenko, **K. A. Abdalmalak** et al., "Design of a Dielectric Rod Waveguide Antenna Array for Millimeter Waves," in Journal of Infrared, Millimeter, and Terahertz Waves, vol. 38, pp. 33-46, 2017.
   URL: https://doi.org/10.1007/s10762-016-0310-9
   It is partially included in Chapter 3.

5. **K. A. Abdalmalak** et al., "An Integrated mm-wave Satellite Radiometer Working at Room-temperature with High Photonic Efficiency," To be submitted to Optics Express.
   It is fully included in Chapter 4.

6. G. Santamaría-Botello, Z. Popovic, **K. A. Abdalmalak** et al., "Sensitivity and noise in THz electro-optic upconversion radiometers," in Scientific Reports, vol. 10, pp. 9403, 2020.
   URL: https://doi.org/10.1038/s41598-020-65987-x
   It is partially included in Chapter 4.

7. A. A. Althuwayb, **K. A. Abdalmalak** et al., "3-D-Printed Dielectric Resonator Antenna Arrays Based on Standing-Wave Feeding Approach," in IEEE Antennas and Wireless Propagation Letters, vol. 18, no. 10, pp. 2180-2183, Oct. 2019.
   URL: https://doi.org/10.1109/LAWP.2019.2939734
   It is partially included in Chapter 4.

8. G. S. Botello, F. Sedlmeir, A. Rueda, **K. A. Abdalmalak** et al., "Sensitivity limits of millimeter-wave photonic radiometers based on efficient electro-optic upconverters," in Optica, vol. 5, no. 10, pp. 1210-1219, 2018.
   URL: https://doi.org/10.1364/OPTICA.5.001210
   It is partially included in Chapter 4.

9. **K. A. Abdalmalak** et al., "Standing-Wave Feeding for High-Gain Linear Dielectric Resonator Antenna (DRA) Array," Under review in IEEE Access.
   URL: https://martinlara3.webnode.es/_files/200000042-56b3756b3a/TAP.pdf
   It is partially included in Chapter 4.

10. A. Rivera-Lavado, L. García-Muñoz, D. Lioubtchenko, S. Preu, **K. A. Abdalmalak** et al., "Planar Lens–Based Ultra-Wideband Dielectric Rod Waveguide Antenna for Tunable THz and Sub-THz Photomixer Sources," in Journal of Infrared, Millimeter, and Terahertz Waves, vol. 40, pp. 838–855, 2019.
    URL: https://doi.org/10.1007/s10762-019-00612-1
    It is partially included in Chapter 4.

11. G. A. Santamaría-Botello, L. E. G. Muñoz, F. Sedlmeir, S. Preu, D. Segovia-Vargas, **K. A. Abdalmalak** et al., "Maximization of the optical intra-cavity power of whispering-gallery mode resonators via coupling prism," in Optic Express, vol. 24, no. 23, pp. 26503-26514, 2016.
    URL: https://doi.org/10.1364/OE.24.026503
    It is partially included in Chapter 4.

Conference contributions:

12. **K. A. Abdalmalak** et al., "Radio astronomy ultra wideband receiver covering the 2–14 GHz frequency band for VGOS applications," 2016 10th European Conference on Antennas and Propagation (EuCAP), 2016, pp. 1-5, Davos, Switzerland.
    URL: https://doi.org/10.1109/EuCAP.2016.7481889
    It is fully included in Chapters 1 and 2.

13. **K. A. Abdalmalak** et al., "An updated version of the Dyson Conical Quad-Spiral Array (DYQSA) feed system for VGOS applications," 2017 IEEE International Symposium on Antennas and Propagation & USNC/URSI National Radio Science Meeting, 2017, pp. 1539-1540, California, United States.

URL: https://doi.org/10.1109/APUSNCURSINRSM.2017.8072812
It is fully included in Chapter 2.

14. **K. A. Abdalmalak**, S. L. Romano, L. E. García Muñoz, and D. S. Vargas, "Dual polarized ultra wideband feed system for VLBI global observation system applications," 2016 Global Symposium on Millimeter Waves (GSMM) & ESA Workshop on Millimetre-Wave Technology and Applications, 2016, pp. 1-4, Espoo, Finland.
URL: https://doi.org/10.1109/GSMM.2016.7500321
It is fully included in Chapter 2.

15. A. Rivera-Lavado, **K. A. Abdalmalak** et al., "High-power terahertz emitter for a communication link: The chessboard array," 2017 11th European Conference on Antennas and Propagation (EuCAP), 2017, pp. 1377-1380, Paris, France.
URL: https://doi.org/10.23919/EuCAP.2017.7928543
It is partially included in Chapter 3.

16. A. Rivera-Lavado, **K. A. Abdalmalak** et al., "High-power terahertz emitter arrays," 2017 International Workshop on Antenna Technology: Small Antennas, Innovative Structures, and Applications (iWAT), 2017, pp. 142-145, Athens, Greece.
URL: https://doi.org/10.1109/IWAT.2017.7915341
It is partially included in Chapter 3.

17. **K. A. Abdalmalak** et al., "Microwave Radiation Coupling into a WGM Resonator for a High-Photonic-Efficiency Nonlinear Receiver," 2018 48th European Microwave Conference (EuMC), 2018, pp. 781-784, Madrid, Spain.
URL: https://doi.org/10.23919/EuMC.2018.854162
It is fully included in Chapter 4.

18. K. Alsirhani, **K. A. Abdalmalak** et al., "Dielectric Resonator Antenna Fed by Tapered Dielectric Rod Waveguide for 5G mm-Wave Applications," 2020 IEEE International Symposium on Antennas and Propagation and North American Radio Science Meeting, 2020, pp. 149-150, Montreal, Canada, California, United States.
URL: https://doi.org/10.1109/IEEECONF35879.2020.9329488
It is partially included in Chapter 4.

19. E. R. Brown, **K. A. Abdalmalak**, and W. Zhang, "Effect of Metal Resistive Losses on the Gain of a THz Planar Spiral Antenna," 2020 14th European Conference on Antennas and Propagation (EuCAP), 2020, pp. 1-4, Copenhagen, Denmark.
URL: https://doi.org/10.23919/EuCAP48036.2020.9135409
It is partially included in Chapter 4.

20. M. Wasiak, G. S. Botello, **K. A. Abdalmalak** et al., "Compact Millimeter and Submillimeter-Wave Photonic Radiometer for Cubesats," 2020 14th European Conference on Antennas and Propagation (EuCAP), 2020, pp. 1-5, Copenhagen, Denmark.

URL: https://doi.org/10.23919/EuCAP48036.2020.9135962
It is partially included in Chapter 4.

21. L. E. G. Muñoz, G. S. Botello, **K. A. Abdalmalak**, and M. Wasiak "Room temperature radiometer based on an up conversion process for CubeSats applications," Proc. SPIE 11348, Terahertz Photonics, 1134809, 2020, pp. 27-34, Online.
URL: https://doi.org/10.1117/12.2555654
It is partially included in Chapter 4.

22. G. S. Botello, **K. A. Abdalmalak**, D. Segovia-Vargas, and L. E. G. Muñoz, "Photonic upconversion for THz radiometry," 2019 44th International Conference on Infrared, Millimeter, and Terahertz Waves (IRMMW-THz), 2019, pp. 1-2, Paris, France.
URL: https://doi.org/10.1109/IRMMW-THz.2019.8874282
It is partially included in Chapter 4.

23. G. S. Botello, **K. A. Abdalmalak** et al., "On the Comparison Between Low Noise Amplifiers and Photonic Upconverters for Millimeter and Terahertz Radiometry," 2019 30th International Symposium on Space Terahertz Technology (ISSTT), 2019, Gothenburg, Sweden.
URL: https://www.nrao.edu/meetings/isstt/papers/2019/2019229232.pdf
It is partially included in Chapter 4.

24. G. S. Botello, **K. A. Abdalmalak** et al., "Dielectric tuning of millimeter-wave whispering-gallery modes for electro-optic phase matching," 2017 DPG Spring Meeting (DPG), 2019, Regensburg, Germany.
URL: https://www.dpg-verhandlungen.de/year/2019/conference/regensburg/part/kfm/session/4/contribution/5
It is partially included in Chapter 4.

25. D. Warmowska, **K. A. Abdalmalak**, L. E. G. Muñoz, and Z. Raida, "A Compact Circularly Polarized High-Gain Antenna Array for Ka-band CubeSats Applications," 2019 IEEE-APS Topical Conference on Antennas and Propagation in Wireless Communications (APWC), 2019, pp. 178-1804, Granada, Spain.
URL: https://doi.org/10.1109/APWC.2019.8870395
It is partially included in Chapter 4.

26. G. S. Botello, **K. A. Abdalmalak** et al., "Full-vector Analytical Coupling Model of Mm-wave Whispering-Gallery Resonances in Spheres," 2018 XXXIII national symposium of the International Scientific Radio Union (URSI), 2018, Granada, Spain.
It is partially included in Chapter 4.

27. G. S. Botello, **K. A. Abdalmalak** et al., "Microwave radiometers based on optical up-conversion," 2018 SPIE Astronomical Telescopes + Instrumentation, 2018, Texas, United States.
It is partially included in Chapter 4.

28. G. S. Botello, **K. A. Abdalmalak** et al., "Room-temperature photon-counting receiver for cosmic microwave background spectroscopy," 2017 38th ESA Antenna Workshop (ESA), 2017, Noordwijk, The Netherlands.
It is partially included in Chapter 4.

29. G. S. Botello, **K. A. Abdalmalak** et al., "Study of Free-space Coupling into Mm-wave Whispering-Gallery Mode Resonators for a Radioastronomy Receiver," 2017 IEEE International Symposium on Antennas and Propagation & USNC/URSI National Radio Science Meeting, 2017, pp. 1277-1278, California, United States.
URL: https://doi.org/10.1109/APUSNCURSINRSM.2017.8072681
It is partially included in Chapter 4.

30. G. S. Botello, **K. A. Abdalmalak** et al., "New Mm-wave Receiver Scheme With High Photonic Efficiency," 2017 XXXII national symposium of the International Scientific Radio Union (URSI), 2017, Cartagena, Spain.
It is partially included in Chapter 4.

31. **K. A. Abdalmalak** et al., "An Enhancement of the Electrical and Mechanical Properties of DYQSA Feed System," 2017 XXXII national symposium of the International Scientific Radio Union (URSI), 2017, Cartagena, Spain.
It is partially included in Chapter 2.

32. G. S. Botello, **K. A. Abdalmalak**, D. Segovia-Vargas and L. E. G. Muñoz, "Study of Near-field Coupling in Whispering Gallery Mode Resonators," 2017 IEEE MTT-S International Conference on Numerical Electromagnetic and Multiphysics Modeling and Optimization for RF, Microwave, and Terahertz Applications (NEMO), 2017, pp. 155-157, Sevilla, Spain.
URL: https://doi.org/10.1109/NEMO.2017.7964218
It is partially included in Chapter 4.

33. G. S. Botello, **K. A. Abdalmalak** et al., "Analytical Study of Free-Space Coupling of THz Radiation for a New Radioastronomy Receiver Concept," 2017 11th European Conference on Antennas and Propagation (EuCAP), 2017, pp. 836-840, Paris, France.
URL: https://doi.org/10.23919/EuCAP.2017.7928543
It is partially included in Chapter 4.

34. G. S. Botello, **K. A. Abdalmalak** et al., "Nonlinear up-conversion for room-temperature high-sensitivity microwave radiometers," 2017 3rd Australian New Zealand Conference on Optics and Photonics (ANZCOP), 2017, Queenstown, New Zealand.
It is partially included in Chapter 4.

OTHER RESEARCH MERITS

- Participated in 12 R&D projects financed by public funds and/or private companies
- Received the Young Scientists Award (2nd prize) by URSI/Spain in 2017.
- A three-months research-stay as a visiting scholar at Southern Methodist University, USA hosted by Prof. Choon lee.
- Served as a Reviewer/TPC Member for several JCR journals and international conferences
- Participated in several international and European events (Eg. conferences, workshops, seminars)
- Was selected as IEEE Ambassador for the IEEEXtreme 14.0 Competition in 2020.
- Was selected as the IEEE section lead for Spain for the IEEEXtreme 15.0 Competition in 2021.

Additionally, the development of this Ph.D. dissertation led to several journal and conference publications which are not directly related to the main topic of this Ph.D. dissertation. Below are some selected ones

Journal papers:

1. A. E. Yousfi, A. Lamkaddem, **K. A. Abdalmalak**, and D. S. Vargas, "A Miniaturized Triple-Band and Dual-Polarized Monopole Antenna based on a CSRR perturbed Ground Plane," in IEEE Access, accepted, 2021.
URL: https://doi.org/10.1109/ACCESS.2021.3134497

2. A. Lamkaddem, A. E. Yousfi, **K. A. Abdalmalak** et al., "Circularly polarized miniaturized implantable antenna for leadless pacemaker devices," Under review in IEEE Transactions on Antennas and Propagation.

3. **K. A. Abdalmalak** and A. Gallardo-Antolín, "Enhancement of a text-independent speaker verification system by using feature combination and parallel structure classifiers," in Neural Computing and Applications, vol. 29, no. 3, pp. 637-651, 2018.
URL: https://doi.org/10.1007/s00521-016-2470-x

Conference contributions:

4. A. Lamkaddem, A. El Yousfi, **K. A. Abdalmalak**, and D. Segovia-Vargas, "UWB Monopole Antenna Miniaturization and Gain Enhancement using FSS Reflector,"

2021 International Symposium on Antennas and Propagation (ISAP), 2021, pp. 1-3, Taipei, Taiwan.
URL: https://doi.org/10.23919/ISAP47258.2021.9614563

5. A. E. Yousfi, A. Lamkaddem, **K. A. Abdalmalak**, and D. S. Vargas, "Design of a Broadband Circularly-Polarized Single-Layer Metasurface Antenna Using CMA," 2021 15th European Conference on Antennas and Propagation (EuCAP), 2021, pp. 1-5, Virtual Conference.
URL: https://doi.org/10.23919/EuCAP51087.2021.9411443

6. A. Lamkaddem, A. El Yousfi, **K. A. Abdalmalak**, V. González Posadas, L. Enrique García Muñoz, and D. Segovia-Vargas, "A Compact Design for Dual-band Implantable Antenna Applications," 2021 15th European Conference on Antennas and Propagation (EuCAP), 2021, pp. 1-3, Virtual Conference.
URL: https://doi.org/10.23919/EuCAP51087.2021.9410941

7. A. E. Yousfi, A. Lamkaddem, **K. A. Abdalmalak** et al., "Miniaturized Circularly polarized Single-layer Metasurface antenna using Characteritic Modes," 2021 IEEE International Symposium on Antennas and Propagation & USNC-URSI Radio Science Meeting (AP-S/URSI), 2021, Marina Bay Sands, Singapore.

8. A. E. Yousfi, A. Lamkaddem, **K. A. Abdalmalak**, and D. S. Vargas, "Broadband Low Profile Circularly Polarized Metasurface Antenna Based on Characteristic Mode Analysis," XXXVI national symposium of the International Scientific Radio Union (URSI), 2021, Vigo, Spain.

9. A. Lamkaddem, A. E. Yousfi, **K. A. Abdalmalak**, L. E. G. Muñoz, and D. Segovia-Vargas, "Gain enhancement and miniaturization of UWB antenna using metamaterial-based FSS," 2020 International Symposium on Antennas and Propagation (ISAP), 2021, pp. 557-558, Osaka, Japan.
URL: https://doi.org/10.23919/ISAP47053.2021.9391294

10. A. Lamkaddem, A. Es-Salhi, A. E. Yousfi, **K. A. Abdalmalak** et al., "Miniaturization of a compact circularly polarized implantable antenna," XXXV national symposium of the International Scientific Radio Union (URSI), 2020, Málaga, Spain.

ABSTRACT

We are living in interesting times for astronomy science, since the birth of the radio astronomy field in the 20th century by Karl Jansky, the availability of new and better radio astronomy receivers is in increasing demand to push the human understanding of the universe. In this thesis, various components (antennas, baluns, antenna-arrays, and radiometers) are proposed for radio astronomy receivers. The proposed designs are belonging to three receiver topologies (direct detection, down-conversion, and up-conversion) that operate at different frequency bands from MHz up to a few of THz. Also, to demonstrate that the same proposed design is capable of working efficiently at different operating frequencies, multiple adjusted designs are presented for several practical radio astronomy and space applications.

Firstly, a receiver based on the direct detection of the Electromagnetic (EM) radiation through a radio telescope working on cryogenic cooling conditions. In this part, the focus is on designing conical log-spiral antennas and baluns (balanced to unbalanced transformers) to be used as feeds for VLBI Global Observing System (VGOS) ground-based radio telescopes. The feeds cover the Ultrawideband (UWB) from 2 GHz to 14 GHz with Circular Polarization (CP) radiation and stable radiation patterns. After integration of the feeds to the radio telescope, the whole system operates with high aperture efficiency and high System Equivalent Flux Density (SEFD) over the whole required wide range. The fabrication, assembly, and measurements for single-element and four-elements array are provided for achieving the requirements for single CP and dual CP operation. Also, in the same first part, the proposed single-element feed (antenna + balun) is readjusted for being used for CryoRad spaceborne Earth observations. This feed has a single CP over low-frequency UWB from 400 MHz to 2 GHz with low weight and physical size compared to standard horn feeds.

The second part of the thesis is dedicated to a THz source to be used as a local oscillator for heterodyne radio astronomy THz receivers in which the down-conversion of the THz radiation to a lower frequency occurs. The source is based on an array of self-complementary bow-tie antennas and photomixers that lies on a dielectric lens. The source can be scaled easily to cover different UWB ranges, three ranges are analyzed from 200 GHz to 2 THz, 100 GHz to 1 THz, and 50 GHz to 0.5 THz. Additionally, in this part, a complete study for the effects of metal losses on such THz planar antennas is performed which are not well-investigated in literature yet, the physical explanations behind such effects are also provided.

Although these proposed THz sources themselves can work at room temperature, the receiver probably still needs the cooling for the other receiver components (such as the mixer) to work efficiently at such high frequencies. This is the motivation for the third part of this thesis which presents a different type of radio astronomy receiver that is completely

able to work without cooling.

The third receiver is based on the nonlinear up-converting of the microwave radiation into the optical domain using Whispering Gallery Mode (WGM) resonators which can work at room temperature efficiently. For such advantage and since this concept is naturally narrow-band, it can be a proper candidate for Cosmic Microwave Background (CMB) spectroscopy and space applications. The system design and its performance are analyzed for Ku band at 12 GHz with proposing a novel microwave coupling scheme for enhancing the up-conversion photonic efficiency which is the main limitation for such up-conversion systems. Likewise, several high gain 3D-printed Dielectric Resonator Antenna (DRA)s are proposed in both isolated and array configurations to have a direct coupling of the microwave radiation to the proposed scheme. Another practical application for such receiver is presented for CubeSat missions at the mm-wave band (183 GHz) for climate change forecasting. It is clear here that removing the cryogenic cooling conditions decreases satellite weight and cost, which in turn significantly increases its lifetime.

Also, it is worth noting that besides the radio astronomy applications, the proposed receivers (and/or their antenna/components) can be used for many other applications. For example, the UWB antennas in the first part can be used as wideband scalable probes for EM compatibility testing or other wireless systems that require single or dual CP such as radar and military applications. This is because the solutions provide constant beam characteristics with good CP polarization purity and stable performance over the operating UWB. In the same way, the proposed THz source in the second part can be used in several THz applications such as very high-speed wireless communications, high-resolution imaging for medical and security purposes. This is because of its key benefits as decade bandwidth, compact size, low noise, low power demand, high tunability, and the ability to work at room temperature. For the up-conversion scheme proposed in the third part, due to its high photonic efficiency, low noise level which enables it to work at room temperature, and its scalability from a few GHz up to several THz, it is suitable for low-cost and high sensitivity applications. Specifically, the ones that need to get rid of the hard cryogenic cooling conditions, or at least, relax them and allow the system to work efficiently at higher temperatures. For instance, portable mm-wave and THz systems for quality control, security, and biochemistry. Finally, in this part, the proposed DRA elements and arrays, due to their low cost, high gain, and low losses, can be used for sensing applications and 5G base station antennas.

CONTENTS

LIST OF FIGURES

LIST OF TABLES

LIST OF ACRONYMS/ ABBREVIATIONS

AC Alternating Current. 55

AE Antenna-based Emitter. xxvii, 54–58, 64, 65, 71, 73, 74, 84, 87, 119

Au-Ge Gold-Germanium. 76

BW Bandwidth. 8, 9, 54, 55, 60, 61, 92, 121

BWO Backward Wave Oscillator. 7

CMB Cosmic Microwave Background. xix, 9, 92, 96

CNC Computer Numerical Control. 111, 112, 116

CP Circular Polarization. xviii, xix, 1, 2, 4, 14, 18, 29, 30, 41, 44, 47, 48, 51, 52, 118

CST Computer Simulation Technology. 18

CVD Chemical Vapor Deposition. 111, 112, 115

CW Continuous-Wave. 55, 58, 71, 85, 119

DC Alternating Current. 58, 71, 77, 85

DFG Difference-Frequency Generation. 10

DIG Dielectric Image Guide. 100, 101, 103

DORIS Doppler Orbitography and Radiopositioning Integrated by Satellite. 1

DRA Dielectric Resonator Antenna. xix, 87, 94, 96, 99–101, 103, 104, 115, 118, 119, 121

DRW Dielectric Rod Waveguide. 10, 90, 92, 94, 96, 101, 107

DYQSA DYson Quad-Spiral Array. 14, 29, 32, 35–40, 44, 51, 52, 118, 120

EHT Event Horizon Telescope. 2

EM Electromagnetic. xviii, xix, 48, 60, 80, 83

ESA European Space Agency. 4

EVI Earth Venture Instrument. 4

FoW Field of View. 4

GaAs Gallium Arsenide. 55, 74, 77, 81, 89

GaP Gallium Phosphide. 89

GNSS Global Navigation Satellite System. 1

GRASP General Reflector Antenna Software Package. 6, 27, 29, 32, 36

. xii

HEB Hot Electron Bolometer. 10

HFSS High Frequency Structure Simulator. 18, 29, 80, 91

HHI Heinrich Hertz Institute. 65

IF Intermediate Frequency. 8

InGaAs Indium Gallium Arsenide. 65

InP Indium Phosphide. 55, 58, 74

InP-HEMTs Indium Phosphide-High Electron Mobility Transistors. 41

INTA Instituto Nacional de Técnica Aeroespacial. 41

JPL Jet Propulsion Laboratory. 36

LHCP Left-Hand Circular Polarization. 22, 29, 41, 48, 51, 74, 78

$Li_2B_4O_7$ Lithium Tetraborate. 89

$LiNbO_3$ Lithium Niobate. 89, 91, 105, 107, 112

LLR Lunar Laser Ranging. 1

LNA Low Noise Amplifier. 6, 14, 16, 18, 20, 23, 35, 37–41, 51, 87, 89, 118, 122

MMIC Monolithic Microwave Integrated Circuit. 41

NASA National Aeronautics and Space Administration. 4, 36

NGST Northrop Grumman Space Technology. 41

OSO Onsala Space Observatory. 36

PCB Printed Circuit Board. 71, 85

PEC Perfect Electric Conductor. 105

PLA Polylactic Acid. 96

PO Physical Optics. 6, 60

PTD Physical Theory of Diffraction. 6

QCLs Quantum Cascade Lasers. 7, 8

QRFH Quadruple-Ridged Flared Horn. 2, 4, 29, 35–39, 44, 51

RHCP Right-Hand Circular Polarization. 22, 29, 41, 48, 51, 74

RMS Root Mean Square. 83

RTA Rapid-Thermal Anneal. 77

SEFD System Equivalent Flux Density. xviii, 2, 14, 37

SFG Sum-Frequency Generation. 10

SIW Substrate Integrated Waveguide. 100, 101, 103

SKA Square Kilometre Array. 7

SLR Satellite Laser Ranging. 1

SNR Signal to Noise Ratio. 2, 4

TEM Transverse Electromagnetic. 104

TES Transition Edge Sensor. 10

TIR Total Internal Reflection. 56

UC3M Carlos III University of Madrid. 4

UTC-PD Uni-Traveling Carrier Photodiode. 73

UWB Ultrawideband. xviii, xix, 1, 2, 4–8, 14–16, 20, 35, 40, 44, 48, 51, 52, 54, 56, 58, 60, 61, 64, 73, 74, 84, 85, 118

VGOS VLBI Global Observing System. xviii, 2, 4, 14–16, 22, 29, 35, 36, 39, 40, 44, 47, 51, 52, 120

VLBI Very Long Baseline Interferometry. 1, 2, 14, 30, 48, 118

WGM Whispering Gallery Mode. xix, 10–12, 87–89, 91, 92, 94, 96, 101, 105, 107, 109, 115, 118, 119

ZnSe Zinc Selenide. 89

1. INTRODUCTION AND MOTIVATIONS

The thesis is divided into three principal parts where each one is corresponding to one topology of radio astronomy receivers.

- UWB microwave CP radio telescope feed for Very Long Baseline Interferometry (VLBI) space geodesy and Earth observation spaceborne receivers (Sec. 1.1).
- UWB THz antenna arrays for heterodyne receiver and THz applications (Sec. 1.2).
- Mm-wave up-conversion satellite receiver working at room temperature for climate change forecasting (Sec. 1.3).

1.1. UWB feed for radio telescope systems

1.1.1. VGOS: VLBI Global Observing System

Space geodesy can be divided to four main techniques, 1- VLBI, 2- Satellite Laser Ranging (SLR) / Lunar Laser Ranging (LLR), 3- Global Navigation Satellite System (GNSS), and 4- Doppler Orbitography and Radiopositioning Integrated by Satellite (DORIS). VLBI has been successfully used over the last 40 years, it is based on the use of several radio telescopes (Fig. 1.1) located on Earth (or in space) for receiving the signals from astronomical radio sources such as quasar [1].

This system of radio telescopes acts as a large-size radio telescope with a size equal to the maximum space between the different telescopes which enables the system to provide accurate observations of the inertial reference frame of such astronomical sources. This is the technique used recently to capture the black hole image [2] by a network of radio telescopes called Event Horizon Telescope (EHT) consists of eight ground-based radio telescopes around Earth acting as a radio telescope with the size of the entire planet [3].

Also, from a different point of view, by measuring the time difference of arrival of such signals at these different telescopes, the distance between them can be estimated. Knowing that the locations of such receivers are fixed to the Earth, then they can monitor the variations in the Earth's rotation and orientation with high precision [4]. This enables accurate tracking of the Earth's motion due to external sources such as the gravitational forces of the Sun and Moon. The new observation system VGOS [5] aims to improve VLBI data. A broadband signal acquisition chain with fully digital electronics is needed for an expected position accuracy of about 1 mm [6].

For increasing sensitivity, VGOS requires a dual circularly polarized feed that covers the UWB frequency range from 2 GHz to 14 GHz without the need to adjust its focal position to account for the frequency-dependent phase center variations. The feed

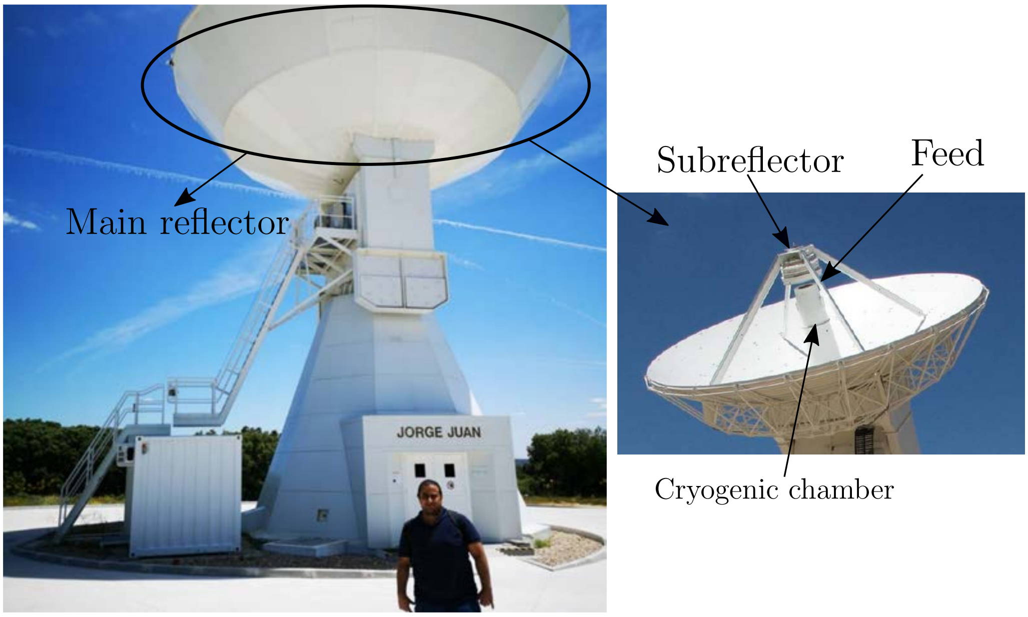

Figure 1.1: VGOS radio telescope in Yebes, Spain.

also needs to enable the reflector to have a SEFD below 2500 Jansky (Jy) [7], while $1\,\mathrm{Jy} = 10^{-26}\,\mathrm{W\,m^{-2}\,Hz^{-1}}$. This is for achieving acceptable Signal to Noise Ratio (SNR) values within reasonable integration times. This can be achieved by maximizing the total aperture efficiency and minimizing the noise contribution of the feed to the total system noise. The development of a novel feed that provides simultaneously all of these requirements are supported by DIFRAGEOS project [8] which stands of Development of Photonic and Radiofrequency Instrumentations and Application to Space Geodesy Experimental Techniques (Spanish original name: "Desarrollos instrumentales fotónicos y de radiofrecuencia y aplicación a técnicas experimentales de geodesia espacial") funded by Madrid Regional Ministry of Education.

Two main feed solutions are currently under consideration for the next generation of radio telescopes as shown in Fig. 1.2. Quadruple-Ridged Flared Horn (QRFH) [9] developed at California Institute of Technology and the Eleven feed [10], [11] developed at Chalmers University of Technology. These two feeds have some deficiencies to be overcome [12], [13] such as the stability of the beamwidth and beam symmetry [14] at higher frequencies as will be discussed later in Chapter 2. Also, both solutions provide linear polarization so more circuits are needed to get the CP required by most of radio astronomy applications which subsequently increases cost, losses, and size. This is in addition to the heavy weight of QRFH and complex manufacturing of Eleven.

VGOS radio telescope is a reflector antenna that consists of the main parabolic mirror and a ring-focus subreflector as shown in Fig. 1.3. The main parameters of the reflector are summarized in Table 1.1. As can be seen from Table 1.1, it has a diameter (D_m) of 13.2 m and $F_m/D_m \approx 0.28$ while most of the existing VLBI reflectors have significantly larger diameters like the Effelsberg radio telescope in Germany which has a diameter

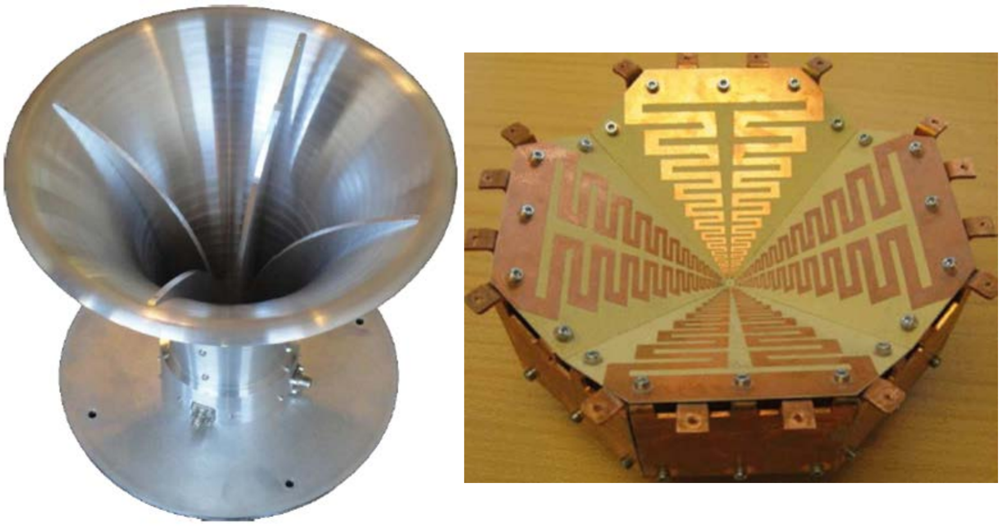

Figure 1.2: The state-of-the-art radio telescope feeds (QRFH and Eleven).

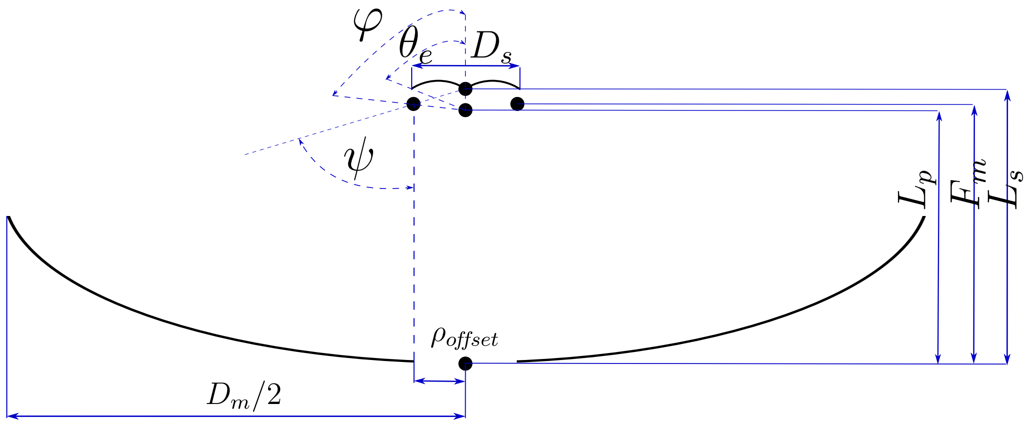

Figure 1.3: Geometry of VGOS reflector.

of 100 m. This compact size will significantly reduce the overall cost of the system. Moreover, such small reflectors can provide fast-slew speeds greater than 360 deg/min allowing a larger number of observations, which in turn, increases the system precision. The feed is placed in the focal point of the reflector geometry, where it is cooled down to 15 K inside the cryogenic receiver.

1.1.2. Cryorad low-frequency future Earth observation spaceborne system

Besides the use of radio telescopes on Earth (or even in space) for monitoring astronomical radio sources, spaceborne radio telescopes can be also used for monitoring Earth itself for different applications. One of these interesting applications is the remote sensing of the Earth's cold regions which despite its importance, is still not satisfactorily covered by state-of-the-art devices.

Table 1.1: Main parameters of VGOS reflector

Parameter	Symbol	Value
Main reflector diameter	D_m	13200 mm
Main reflector focal length	F_m	3700 mm
Subreflector diameter	D_s	1550 mm
Half subtended angle	θ_e	65°
Parabola hole radius	ρ_{offset}	740 mm
Subvertex position	L_s	3914.446 mm
Secondary focus position	L_p	3611.662 mm
Half flare main angle	Ψ	73.839°
Foci line tilt	φ	83.193°

A new spaceborne mission concept called CryoRad [15] is suggested in the framework of European Space Agency (ESA) Earth Explorer 10 and 11 call which also agrees well with National Aeronautics and Space Administration (NASA) PolarRad mission, known by Earth Venture Instrument (EVI)-6 [16]. These missions aim to a low-frequency microwave radiometer for the deep study of the Cryosphere at the range from 400 MHz to 2 GHz with continuous sampling of the band. This low-frequency band is most appropriate for these studies as the atmosphere is almost transparent so the main radiation is coming from the water vapor and the molecular oxygen.

These receivers would help in knowing different interesting parameters such as ice sheet, sea ice volume, shelf temperature profile of Antarctica and Greenland, and sea surface salinity [15]. Although these parameters are important for understanding the whole Earth system, improving the forecasting of global climate change, and seeing the projection of human activities on the environment, they were poorly measured or even never previously measured from space in the previous missions.

In contrast with VGOS radio telescope which is usually built in a ground station and directed around the Zenith, here this radio telescope would be installed on a polar-orbit satellite with altitude of 650 km and directed to the Nadir. CryoRad push-broom multi-beam radiometer is based on a large deployable offset parabolic reflector with maximum diameter (D_m) of 12.5 m and $F_m/D_m \approx 0.4$. The reflector is illuminated by multiple feeds to scan a ground swath width of 120 km with a resolution between 8 km and 45 km for high and low frequencies respectively. For developing such antenna feed, a project called "A Low-Frequency and Wide-Band Reflector Antenna Feed for Future Earth Observation Radiometers" is funded by ESA where Carlos III University of Madrid (UC3M) is subcontracted from the prime contractor (EOS INGENIERÍA).

The feed should cover the UWB frequency range with pure single CP (axial ratio ≤ 1.5 dB) to avoid the Faraday rotation. It should provide stable radiation patterns within a Field of View (FoW) of 50° with a gain above 10 dBi. Additionally, it has to be of low weight and compact size to be proper for satellite installation [17], especially that here we need multiple feeds. This is the motivation for avoiding QRFH as its weight and physical size at this low-frequency range will not be practical for such applications. Recalling that for QRFH, even though only single CP is required, still dual linear polarization antennas are needed for obtaining the CP performance. Finally, the return and isolation losses of the feed should be minimized to reduce its contribution to the system noise temperature.

1.1.3. Radio telescope performance estimation

The SNR of a radio telescope system based on continuous observations can be calculated using the following equation

$$\mathrm{SNR} = \frac{S\,\sqrt{tB}}{\mathrm{SEFD}} \tag{1.1}$$

where S is the flux density coming from the observed radio source in Jy, t is the integration time in seconds (s), B is the available bandwidth of the receiver system in hertz (Hz), SEFD includes the combined effect of reflector antenna and all other receiver noise sources into one parameter. Equation (1.1) shows that, firstly, for a fixed SNR, lower SEFD yields lower integration time. Secondly, for a fixed incoming flux density and integration time, the SNR will be proportional to the square root of the bandwidth. Therefore, the UWB coverage for the receiver system (and therefore its feed) is critical.

The SEFD can be calculated following [18] as

$$\mathrm{SEFD} = \frac{2kT_{\mathrm{sys}}}{A_{\mathrm{eff}}} \tag{1.2}$$

where k is the Boltzmann constant, T_{sys} is the equivalent system noise temperature, A_{eff} is the effective area of the reflector antenna and can be calculated from the total aperture efficiency of the reflector (η_{tot}) as $A_{\mathrm{eff}} = \eta_{\mathrm{tot}} A_{\mathrm{phy}}$ where $A_{\mathrm{phy}} = \pi\,(D_m/2)^2$ is the physical area of the reflector. A_{eff} can also be estimated from the gain of the reflector antenna (G_A) at specific wavelength (λ) as $A_{\mathrm{eff}} = \left(G_A \lambda^2\right)/(4\pi)$. The previous discussion shows that the total aperture efficiency of the reflector can be split to

$$\eta_{\mathrm{tot}} = G_A \left(\frac{\lambda}{\pi D_m}\right)^2 \tag{1.3}$$

Another method for estimating the total aperture efficiency using a specific feed is to factorize it into its main four subefficiencies which are spillover (η_{sp}), polarization (η_{pol}), illumination (η_{ill}), and phase (η_{ph}) subefficiencies. Then the total aperture efficiency of the reflector can be calculated as $\eta_{\mathrm{tot}} = \eta_{\mathrm{sp}}\eta_{\mathrm{pol}}\eta_{\mathrm{ill}}\eta_{\mathrm{ph}}$. These subefficiencies can be estimated by integration of the feed's radiation patterns following [19] using the closed-form equations from (1.4) to (1.7).

$$\eta_{\mathrm{sp}} = \frac{\int_0^{\theta_e} \left[|g_{\mathrm{Co}}(\theta,\phi,f)|^2 + \left|g_{\mathrm{Xp}}(\theta,\phi,f)\right|^2 \right] \sin\theta \,\mathrm{d}\theta}{\int_0^{\pi} \left[|g_{\mathrm{Co}}(\theta,\phi,f)|^2 + \left|g_{\mathrm{Xp}}(\theta,\phi,f)\right|^2 \right] \sin\theta \,\mathrm{d}\theta} \tag{1.4}$$

$$\eta_{\text{pol}} = \frac{\int_0^{\theta_e} \left[|g_{\text{Co}}(\theta, \phi, f)|^2 \right] \sin\theta \, \mathrm{d}\theta}{\int_0^{\theta_e} \left[|g_{\text{Co}}(\theta, \phi, f)|^2 + \left| g_{\text{Xp}}(\theta, \phi, f) \right|^2 \right] \sin\theta \, \mathrm{d}\theta} \tag{1.5}$$

$$\eta_{\text{ill}} = 2\cot^2\left(\frac{\theta_e}{2}\right) \frac{\left[\int_0^{\theta_e} |g_{\text{Co}}(\theta, \phi, f)| \tan(\theta/2) \, \mathrm{d}\theta \right]^2}{\int_0^{\theta_e} \left[|g_{\text{Co}}(\theta, \phi, f)|^2 \right] \sin\theta \, \mathrm{d}\theta} \tag{1.6}$$

$$\eta_{\text{ph}} = \frac{\left| \int_0^{\theta_e} g_{\text{Co}}(\theta, \phi, f) \tan(\theta/2) \, \mathrm{d}\theta \right|^2}{\left[\int_0^{\theta_e} |g_{\text{Co}}(\theta, \phi, f)| \tan(\theta/2) \, \mathrm{d}\theta \right]^2} \tag{1.7}$$

where $g_{\text{Co}}(\theta, \phi, f)$ and $g_{\text{Xp}}(\theta, \phi, f)$ are the co-polar and the cross-polar polarizations of the feed respectively. With this factorization, one may get an idea of the contribution of each subefficiency on the overall performance and investigate the source of any degradation related to beamwidth (η_{sp} and η_{ill}), high cross-polarization levels (η_{pol}) or phase center variations (η_{ph}).

Also from the previous equations, it can be seen that η_{ph} is critically based on the location of the feed as it depends on the phase of the radiation patterns. Therefore, excluding it from the total efficiency will result in another parameter that can be defined as $\eta_{\text{max}} = \eta_{\text{sp}}\eta_{\text{pol}}\eta_{\text{ill}}$ which is only depending on the amplitude of the radiation patterns of the feed. Then the best location of the feed can be defined as the one which will maximize η_{ph}, making η_{tot} close as possible to η_{max}. Although this can be easily adjusted at a single frequency, this issue is a tricky challenge in UWB systems as the feed needs to provide good performance over the whole frequency range with no need to compensate for the phase center changes via mechanical movement. Hence, the proper feed should provide a nearly constant phase center over the whole UWB band.

Returning to (1.2), the equivalent system noise temperature T_{sys} which takes into account all the noise sources in the system can be defined as

$$T_{\text{sys}} = \eta_{\text{rad}} T_A + (1 - \eta_{\text{rad}}) T_{\text{phy}} + T_{\text{rec}} \tag{1.8}$$

where the first term consists of the multiplication of the antenna radiation efficiency (η_{rad}) by the antenna noise temperature (T_A) including noise picked up from the sky and the spillover noise. The second term is the noise temperature contribution from the feed's ohmic losses where T_{phy} is the physical temperature of the antenna. At last, the third term is the noise temperature of the receiver chain (T_{rec}) including the receiver components such as the cryogenic Low Noise Amplifier (LNA), coaxial cables, and calibration couplers.

Using (1.8), the SEFD in (1.2) can be calculated as

$$\text{SEFD} = \frac{8k \left[\eta_{\text{rad}} T_A + (1 - \eta_{\text{rad}}) T_{\text{phy}} + T_{\text{rec}} \right]}{\pi D_m^2 \eta_{\text{tot}}} \tag{1.9}$$

The above equation demonstrates the dependence of the SEFD (and hence SNR) on the feed selection which strongly affects both aperture efficiency and noise temperature of the reflector antenna. The calculation of the antenna noise temperature can be performed following [20] as

$$T_A = \frac{\int_0^{2\pi} \int_0^{\pi} F(\theta, \phi, f) T_b(\theta, \phi, f) \sin\theta \, d\theta \, d\phi}{\int_0^{2\pi} \int_0^{\pi} F(\theta, \phi, f) \sin\theta \, d\theta \, d\phi} \tag{1.10}$$

where $F(\theta, \phi, f)$ is the total power pattern of the reflector antenna which can be calculated using a combination of Physical Optics (PO) and Physical Theory of Diffraction (PTD) with the simulation software TICRA General Reflector Antenna Software Package (GRASP) [21] after exciting it by the proper feed. Parameters θ, ϕ, and f are the angle from the zenith (= 90 - elevation angle), the azimuth angle, and the frequency respectively.

$T_b(\theta, \phi, f)$ is the surrounding brightness temperature seen by the radio telescope, which can be divided into two main components, above and below the horizon as

$$T_b(\theta, \phi, f) = \begin{cases} T_{\text{sky}}(\theta, \phi, f) & 0^\circ \le |\theta| < 90^\circ \\ T_{\text{gnd}}(\theta, \phi, f) & 90^\circ \le |\theta| \le 180^\circ \end{cases} \tag{1.11}$$

The brightness temperature model used in these calculations is the Square Kilometre Array (SKA) general brightness temperature model [22]. Once the noise temperature is calculated from (1.10), the spillover noise temperature T_{sp} can be drawn from $T_A = T_{\text{sky}} + T_{\text{sp}}$.

1.2. THz antenna-based source

Nowadays, mm-wave and THz ranges are getting more interest for different applications such as radio astronomy, wireless communications, medical imaging, security and several other ones [23]. Mm-wave range are widely defined for the band from 30 GHz to 300 GHz while THz range is sometimes defined from 300 GHz to 3 THz [24] and others it is extended to be from 100 GHz to 10 THz [23], [25].

The systems at these frequency ranges could provide unique characteristics compared to other ranges. For instance, for radio astronomy, 98% of all photons emitted since the Big Bang are in these frequency ranges [26] so they are essential for understanding the evolution of the universe. For wireless communications, mm-wave and THz systems can provide high-data rates above tens or hundreds of Gb/s [27], [28] while also opening the door to the future Tb/s data rates [29]. The same importance is in medical imaging for getting very high-resolution images which help in the early-stage detection of diseases [30], [31]. Likewise, for security applications to replace the current X-rays as THz systems can detect both metallic and non-metallic objects from a distance even underneath the clothing or other concealing barriers. This is in addition to minimal risk to human health [32].

Despite all advantages that THz systems can have, there are still some limitations that delay their real implementations in current practical applications. This is mainly be-

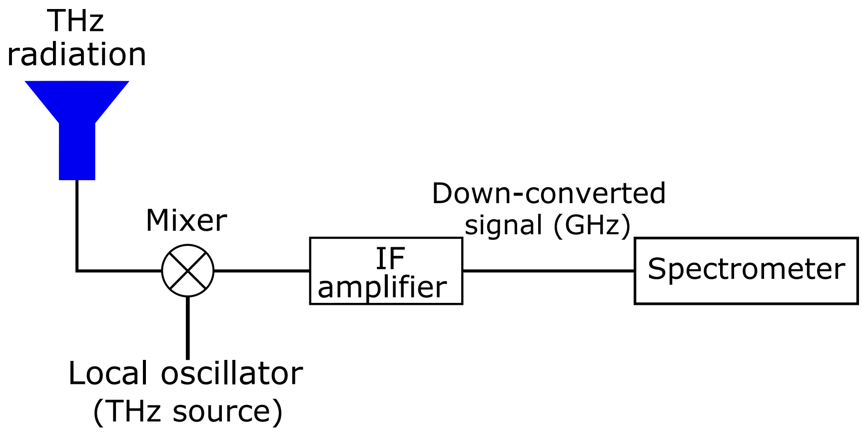

Figure 1.4: General THz radio astronomy heterodyne receiver based on THz source.

cause of the lack of suitable technologies and components for making efficient, tunable, cost-effective, UWB, and powerful THz sources/detectors that can operate at room temperature. Hence, the term called "THz gap" has been coined to define the range between microwave and infrared ranges [23], [33].

Mainly there are two type for THz radiation sources, firstly, the natural one which is released in the black-body radiation from objects with temperatures above 10 K [34]. Secondly, the artificial sources [35] [36] such as photomixer (up to 4 THz), Gyrotron (up to 0.5 THz), Backward Wave Oscillator (BWO) (up to 1.5 THz), and Quantum Cascade Lasers (QCLs) (up to 10 THz). Photomixers [37] are efficient solutions in terms of continuous tunability with high spectral resolutions of about a few MHz, compactness, cost-affordable as they work at room temperature without the need for cooling. Such mentioned advantages make it a good solution even though it suffers from the low emitted power on the order of a few μW. Especially that other high-power solutions such as QCLs (which are capable of delivering power in range of tens of mW [35]) will provide only hundreds of nW if they are used at room temperature [38].

Despite that THz source is a critical component for transmitters for different applications, it can be also used for THz receivers such as radio astronomy ones [39]. For these applications, it acts as a broadly tunable local oscillator for heterodyne receivers [40]. This is done by mixing the produced signal from the THz source with the received THz radiation and achieving the frequency down-conversion by generating the Intermediate Frequency (IF) signal as summarized in Fig. 1.4.

Another core component in the THz system is the antenna element, one of the most common THz antenna topologies are horn antennas. However, they have three drawbacks that limit their usage in several applications. Firstly, their relatively small Bandwidth (BW) as their operation band is limited by the single waveguide mode band. Secondly, it cannot be integrated directly with other electronic components which prevents its insertion in a fully integrated system. Ultimately, their limited directivity and therefore, excessive electrically-large lengths are needed in case higher directivity is required. Because of these limitations, currently, there is a trend towards the use of alternative planar THz antennas. There, high directive beams can be obtained by putting the antennas on a dielectric lens.

Hence, for increasing the generated THz power, an array of balanced planar antennas is used where a separated photomixer is introduced in the center of each array element. To demonstrate the scalability of the proposed THz antenna array, three versions have been tested covering different UWB ranges from 50 GHz to 500 THz, 100 GHz to 1 THz, and 200 GHz to 2 THz. All the photomixers are coherently excited by the same optical pump by a means of a microlens array that focuses the laser beams into its corresponding photomixer.

The antenna elements are electrically small and their distribution is adjusted to provide high-density of sources. This would ensure constructive interference and hence only one electrically large Si lens can be used without having problems of out-of-focus for the photomixers that are far away from the lens center. A study of each array configuration together with its proper lenses are presented. The proposed antennas outperform the standard THz horn antennas in several aspects such as much higher BW, very high directivity (of about 35 dBi) with much smaller sizes, fully integrated solution, and the possibility to extend to arrays with a larger number of elements for achieving higher power without an increase in designing or alignment complexities.

Furthermore, a complete study to demonstrate the effect of the metal resistive losses in THz planar spiral antennas is performed. As the THz antenna metalization implies annealing and alloying processes to promote good adhesion of the metal to the semiconductor substrate to make the metal-semiconductor contact as much ohmic as possible. This, in turn, prevents the creation of Schottky barriers that impede the flowing of generated THz current into the antenna arms. This study demonstrates a significant reduction (up to 30 dB) in the antenna gain in case the actually measured metal resistivity of the gold alloy is used. This is in comparison with the standard pure gold which is usually used in literature for designing THz antennas. This reduction has its maximum at the lower frequency range because, at such frequencies, the metal thickness is not much larger than the metal skin depth so the metal performance diverges from being a good conductor.

As these metal losses cause a reduction in the THz radiated power (the same amount as the gain reduction), such losses need to be relaxed for most of the THz practical applications. Hence, two solutions can be used, firstly, by increasing the metal thickness so it is higher or at least comparable to the skin depth for the most of frequency range. Or secondly, by reducing the metal density which can be achieved by using different antenna typologies such as log-spiral. Although both solutions provide a significant enhancement of 10 dB and 25 dB respectively, each of them has its drawbacks. For instance, the first method requires a larger amount of gold in the stack of metal films which increases the fabrication cost and complexity. Also, for the second solution, it is clear that larger areas affect the antenna compactness specifically in the case of array configurations. So the designers should choose the most suitable of this trade-off or a mixture of them based on their specific system requirements.

1.3. WGM up-conversion receiver working at room temperature

The cryogenic cooling requirement is one of the main limitations of radio astronomy receivers as it dramatically increases the receiver cost, size, and power consumption which are all critical parameters for most space applications. For example, accurate measurements of the CMB radiation would allow the improvement of the standard cosmological model. Specifically, by observing the polarization of the CMB through radio telescopes, a polarization map of the sky can be created to identify the so-called B-mode of the CMB, which is partially produced by primordial gravitational waves created in the Big Bang. However, this CMB signal is weak and photon-counting sub-THz receivers are required.

Currently, the high sensitivity, that photon-counting detectors provide, can be only achieved with instruments cooled at sub-Kelvin temperatures such as kinetic inductance detectors, Hot Electron Bolometer (HEB) or Transition Edge Sensor (TES) bolometer [41], [42]. This makes the available technology expensive and impractical for many applications. Room temperature receivers will overcome such limitation, one of the main candidates for these room temperature receivers is the photonic nonlinear up-conversion receiver [43] based on WGM waves inside a resonator [44], [45]. Here, the weak radiation signal is up-converted into the optical domain where it is easier to detect at room temperature with the currently available technologies.

WGM waves were first explained in the 19th century by Lord Rayleigh for sound waves heard in Whispering Gallery of St. Paul's Cathedral, London [46], [47]. The same phenomenon is observed with other signals such as microwave or optical which makes WGM interesting for several applications such as radio astronomy. The up-conversion can be done by exciting two input WGM signals, for the microwave (or even mm-wave or THz) with frequency ω_m together with an optical WGM with frequency ω_p coming from an optical pump laser. Then they are mixed via the second-order nonlinear response of a dielectric resonator [48], [49].

Several schemes can be used for achieving the nonlinear up-conversion, Fig. 1.5 shows a common example for it. In this, Dielectric Rod Waveguide (DRW) and prism are used for coupling the microwave and optical signal respectively. After coupling the two input signals and mixing them inside the resonator, two other resonant optical sidebands are produced at frequencies corresponding to Sum-Frequency Generation (SFG) and Difference-Frequency Generation (DFG) processes as presented in Fig. 1.6. Here, both SFG and DFG contain all the information from the input signal. $P(r)$ is the electric polarization which can be calculated in terms of the electric field and the electric susceptibilities of the resonator material (χ) as following $P(r) = \epsilon_0 \chi^{(1)} E_m(r) + \epsilon_0 \chi^{(2)} E_m^2(r)$.

So, in total, four WGMs are excited in the nonlinear resonator, two are corresponding

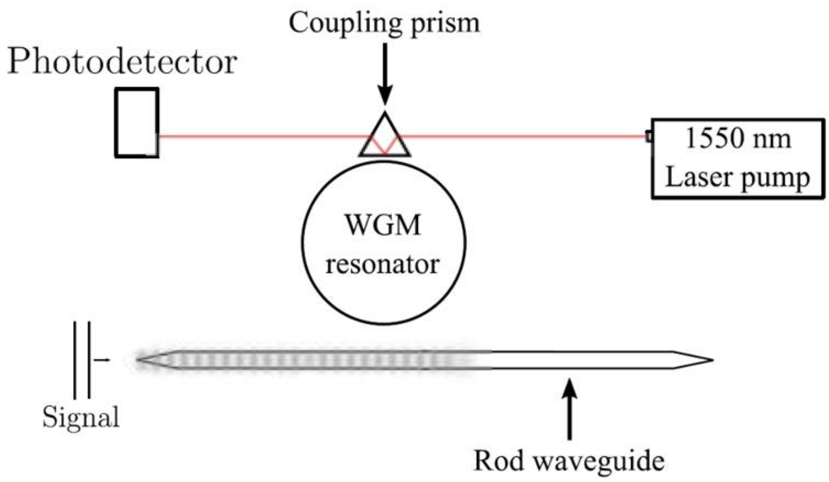

Figure 1.5: The common scheme for the nonlinear up-conversion system.

to the input signals, and the other two for the SFG and DFG ones. The up-converting of the input signals only occurs when the phase-matching and energy conservation conditions are fulfilled. This can be simplified following [50] to the condition that the angular velocities of the microwave and the optical signals are equal. Otherwise, the nonlinear polarization would not efficiently generate the output signals [51]. It is worth noting here that this promising technique has the advantage of up-converting any desired frequency so it can be used for several applications to receive radiation at different frequencies from a few GHz [52] up to several THz [53] range.

Mm-wave and THz radiation detection are critical for many applications such as satellite Earth observation, radio astronomy, planetary missions, and spectroscopy. For example, there is a focus on mm-wave radiation at 183 GHz and 60 GHz for water vapor profile measurements and weather forecasting [54]. Direct detection of such radiation at room temperature with high-sensitivity mm-wave receivers is tricky as the radiation is masked by the thermal noise of the receiver components itself. Hence most of these receivers need to operate under cryogenic conditions [55] which makes them bulky and high-cost [56].

On the other hand, up-converting this mm-wave radiation into the optical domain makes them less affected by thermal noise even without cooling. This is because, at such high-frequency of optical range (193 THz), the optical photons will have much higher energy compared to mm-waves [57]. This will allow the detection at room temperature with commercially available optical devices which will reduce the cost, weight, and volume of the satellite receiver. Additionally, removing such cryogenic components will significantly increase the satellite mission lifetime. However, this requires very high photonic efficiency which can be defined as the percentage of the up-converted photons with respect to the incoming input photons. Standard WGM up-conversion systems fail to provide such high efficiency specifically at mm-wave and THz range. This is the motivation for novel up-conversion schemes that can work with much higher photonic efficiency.

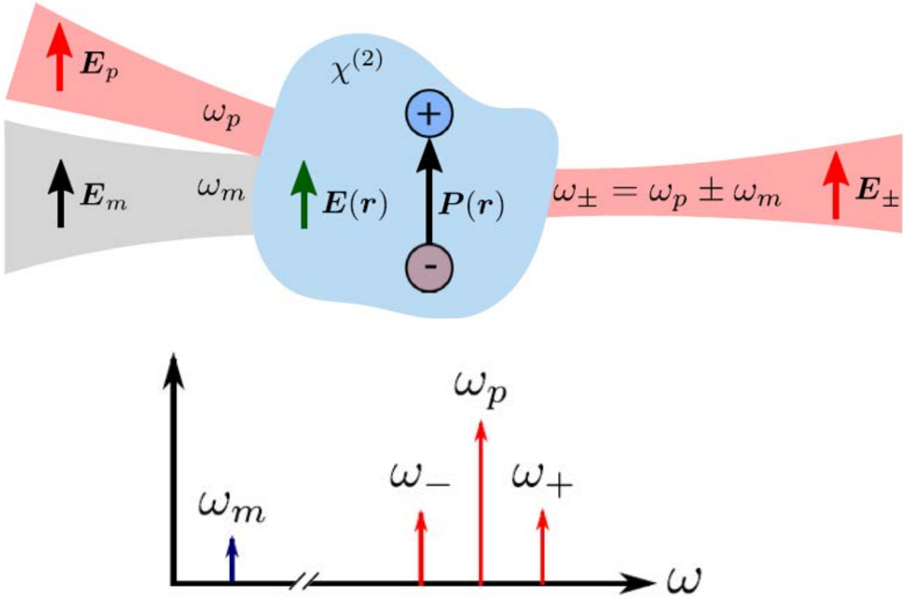

Figure 1.6: Photonic nonlinear up-conversion process.

Based on the previous discussion, an integrated mm-wave receiver working at room temperature for satellite applications is presented. This work is supported by MARTINLARA-CM project [58] (Millimeter wave Array at Room Temperature for Instruments in Leo Altitude Radio Astronomy) funded by Madrid Regional Ministry of Education and REFTA project (Photon counting receiver working at room temperature) funded by SENER company. The proposed receiver has high photonic efficiency due to the enhanced overlapping between the mm-wave and optical signals. Its photonic efficiency outperforms best-reported ones for mm-wave WGM up-conversion by around three orders of magnitudes. Fabrication tolerances of the main design parameters are studied with showing their effects on the performance. The system is able to perform a refined tuning on the order of tens of MHz covering a wide range of frequencies of 45 GHz around a center frequency of 183 GHz. This will compensate the fabrication and assembly tolerances in addition to relaxing the manufacturing complexity.

2. UWB SINGLE AND DUAL CIRCULAR POLARIZATION ANTENNAS

2.1. Introduction

As shown in the previous chapter, the first direct radio astronomy receiver which is related to radio telescope is illustrated in detail in this chapter. To completely achieve the requirements of the new generation of VLBI radio telescopes, a novel topology called DYson Quad-Spiral Array (DYQSA) [56] has been developed. A brief discussion of the conical log-spiral antenna is given along with its design procedure and how to overcome manufacturing limitations for such relatively high-frequency ranges.

The focus is on a practical project to use such proposed feeds for VGOS radio telescope in the range from 2 GHz to 14 GHz. The simulation results for the designed single antenna element and proper balun are shown in both isolated form and integrated with the radio telescope. To have an upper limit estimation of the total system efficiency, the analysis of the optimum performance of the radio telescope fed by an ideal Gaussian beam will be performed. Then the design for the DYQSA solution for providing dual CP, compared to dual linear polarization presented in the state-of-the-art feeds, is discussed with mentioning the advantages for having a direct CP feeds.

Also, to prove the suitability of the proposed solution as a feed for VGOS radio telescope, an analysis of the reflector fed by DYQSA is performed, including five main parameters: total radiation patterns, noise temperatures, directivity, aperture efficiency, and SEFD. Comparisons between the proposed feed and the state-of-the-art ones are given in terms of total aperture efficiencies, design adaptability to different reflectors, physical volume, cost, required number of LNAs per feed, and calibration signal injection. The fabrication descriptions along with the challenging issues and the measurement results of both the single element and the array feed are presented.

Finally, to prove the adaptability of the proposed feeds for different applications, another radio astronomy system is addressed which is CryoRad spaceborne for cold Earth regions. It requires a single CP operating at a low-frequency UWB from 400 MHz to 14 GHz. The simulation results for the designed single-element are shown and discussed.

2.2. Conical log-spiral antenna

The proposed solutions are based on the self-complementary log-periodic spiral antenna wrapped around a conical shape as depicted in Fig. 2.1. The log-spiral antenna has four main geometrical parameters to control its electromagnetic features: the smallest diameter (d), the largest one (D), the spiral angle (α), and the conical angle (θ).

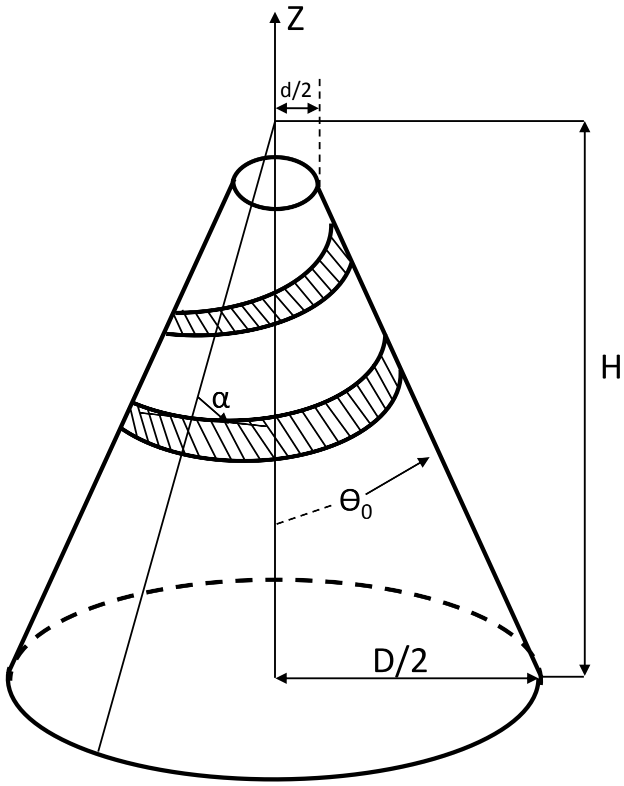

Figure 2.1: Geometry of the conical log-spiral antenna.

2.2.1. Why not just planar spiral!

The reasons behind using such topology are, firstly, the log-spiral is preferable in the case of UWB applications as it requires a much lower number of turns compared to the Archimedean spiral. Secondly, despite that the planar spiral antennas are indeed preferable for easy manufacturing (especially at such high frequencies which require small radii at the antenna center), they will provide bidirectional radiation patterns which are not acceptable if the antenna is to be used for high-gain applications [59]. Moreover, planar spirals are not applicable for radio telescope feeds because the bidirectional behavior will dramatically decrease the spillover efficiency (1.4) in addition to increasing the antenna noise temperature (1.10).

Despite the fact that planar spirals can provide unidirectional patterns with the use of either absorbing cavities [60] or dielectric lens, these two options are also not applicable for feeding radio telescopes. This is because the absorbing cavities will cause a 3-dB loss characteristic which will increase the system noise temperature. And the dielectric lens dimensions would need to be electrically huge (several wavelengths [61]) to cover the low-frequency band. For all of these, the suitable configuration for such applications is using the spiral in a conical log-periodic shape.

Recently, other solutions have included self-complementary structures printed in conical shapes for covering large bandwidths such as the inverted conical sinuous antenna

[62], [63] which is based on the projection of a sinuous pattern onto a cone placed above a ground plane. Although this solution exhibits stable radiation patterns and an almost fixed phase center, it has three main drawbacks for being a good candidate as a VGOS feed. Firstly, the addition of the ground plane affects its self-complementary nature and produces a frequency-dependent impedance. For example, in [62], the imaginary part of the impedance varies between 0 and -300Ω even, over a relatively small bandwidth from 1 GHz to 3 GHz. This significantly increases the complexity of the LNA design and integration, especially for the required UWB range. Secondly, it provides linear polarizations so additional circuits or digital post-processing techniques have to be added for linear-to-circular polarization conversion which has several disadvantages as will be discussed later in Sec. 2.4.2. Finally, the complexity of the manufacturing and assembly process for covering frequencies up to 14 GHz is higher. The situation gets worse as the sinuous antenna has to be over-designed at the higher frequency to have stable properties at the high-frequency end [64].

2.2.2. Design procedure

Even though the conical log-spiral antenna has been proposed in the 20th century by Prof. Dyson [65], to the best of the authors' knowledge, no prototypes have been shown at the high frequencies required for VGOS (up to 14 GHz). This is due to the high manufacturing complexity and the stringent tolerance levels at the apex part. Figure 2.2 presents a systematic procedure for overcoming these design challenges. The design procedure consists of two main stages: first, the conical and spiral angles are selected. It is worth noting that lower values of the conical angles (θ) are more reasonable as they imply larger space between the arms of the spiral, which will facilitate the fabrication process. However, it will be demonstrated that for our application (which requires high-frequency coverage), too small conical angles are not recommended as this will require a very small diameter at the top part of the cone (d) to cover up to 14 GHz.

Thus, the selection of the proper spiral angle (α) will be a trade-off between the separation distance between the turns and the smallest diameter of the cone. Both represent the most-critical fabrication challenges of this topology. The relation between beamwidths and approximate directivity vs spiral angle (α) can be found in [66]. These relations are estimated for different conical angles (θ). After several optimization rounds, considering the requirements of VGOS, we select a spiral angle $\alpha = 85°$ which corresponds to a conical angle $\theta = 10°$.

The second stage of the design process involves the selection of the smallest (d) and the largest diameters (D) of the cone. These two parameters control the maximum and the minimum working frequencies respectively. From the study of the relation between the smallest radius ($d/2$) vs the largest one ($D/2$) for different spiral (α) and conical (θ) angles [66], it can be observed that the smallest radius ($d/2$) is proportional to the conical angle (θ). This confirms the previous statement that a low conical angle will result in a small

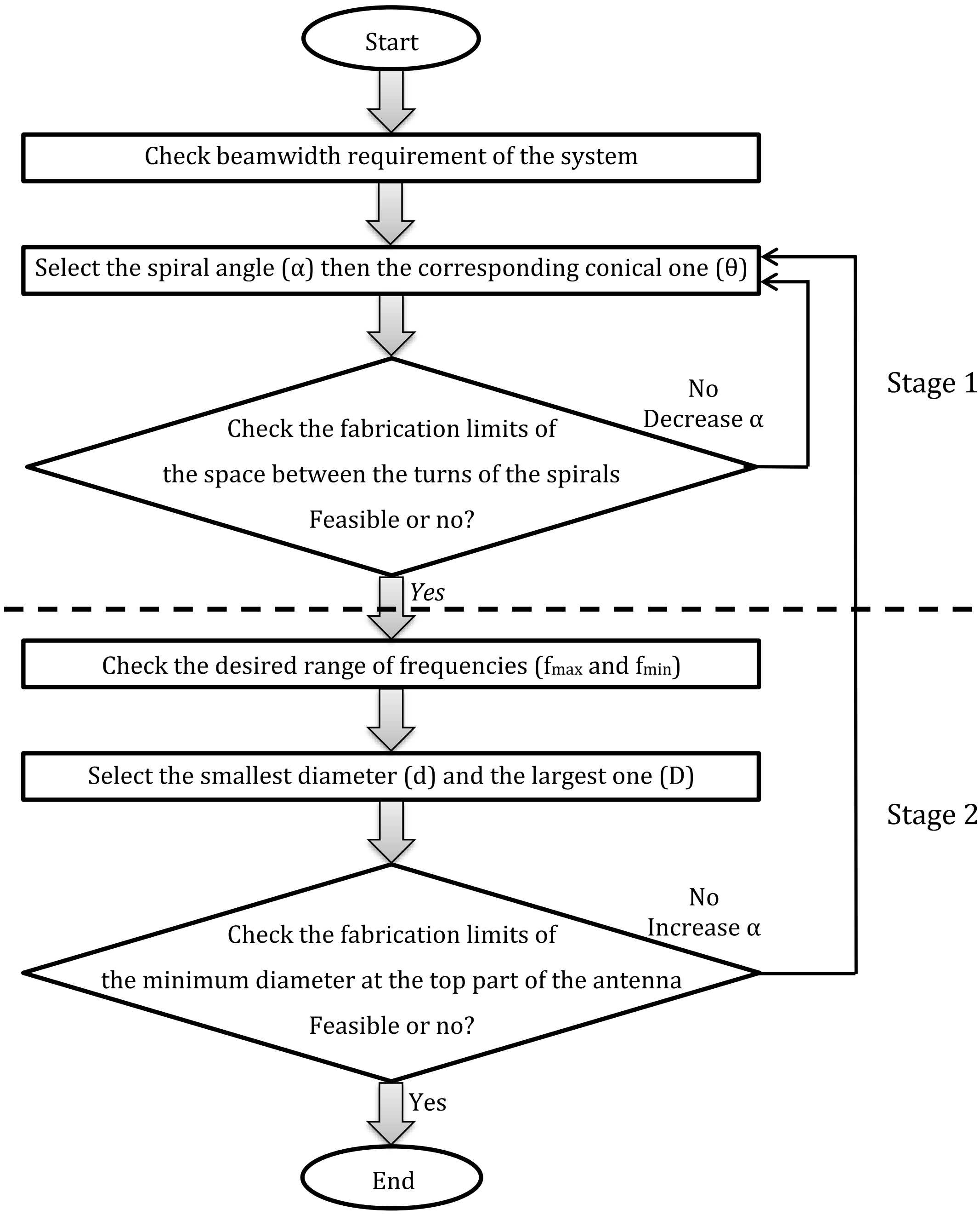

Figure 2.2: The flowchart of the design procedure of the conical log-spiral antenna.

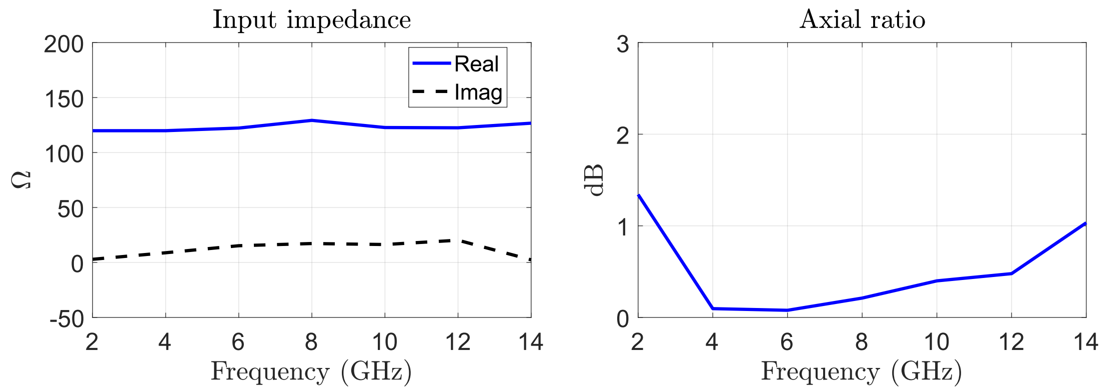

Figure 2.3: Input impedance and axial ratio of the single-element antenna.

radius at the vertex of the cone, which will require a more complex fabrication process to cover the desired higher band. Considering VGOS system that requires covering a bandwidth from 2 GHz up to 14 GHz, d = 3.2 mm and D = 60 mm are good candidates.

2.2.3. Simulation results

Figure 2.3 presents the real and imaginary parts of the input impedance of the proposed conical log-spiral antenna in solid-blue and dashed-green respectively. As expected for this self-complementary topology, the impedance is constant and almost real over the required frequency range. This is one of the main strengths of this solution as it will simplify the design of the LNA connected to the feed. Figure 2.3 also shows that the antenna radiates purely CP as the axial ratio is below 1.4 dB in the required band.

The simulated radiation patterns of this log-spiral antenna are shown in Fig. 2.4. The simulated results were obtained using High Frequency Structure Simulator (HFSS) [67] and Computer Simulation Technology (CST) [68], giving similar results for both simulators.

These radiation patterns are for frequencies from 2 GHz to 14 GHz in steps of 2 GHz and for different cut planes from $\phi = 0°$ up to $\phi = 180°$ in steps of 15°. The blue and the red lines represent the CP co-polar and cross-polar components respectively. The green lines describe the half subtended angle from the focus of the subreflector (θ_e) while the green circle indicates the Co/Xp-ratio to get the CP performance. Figure 2.4 evidences the rotational symmetry of the radiation patterns at all frequencies with a gain around 10 dBi and Co/Xp-ratio at broadside ($\theta = 0°$) greater than 20 dB.

The phase center frequency dependence along the three axes estimated following [69] is presented in Fig. 2.5. A_x, A_y, and A_z are the x, y, and z coordinates of the phase center position respectively. The origin of the coordinate system for the phase center estimation is placed at the virtual apex of the cone (as in Fig. 2.6). A_{z1} and A_{z2} are the phase center calculated using two orthogonal cuts $\phi = 0°$ and $\phi = 90°$ respectively. All the phase

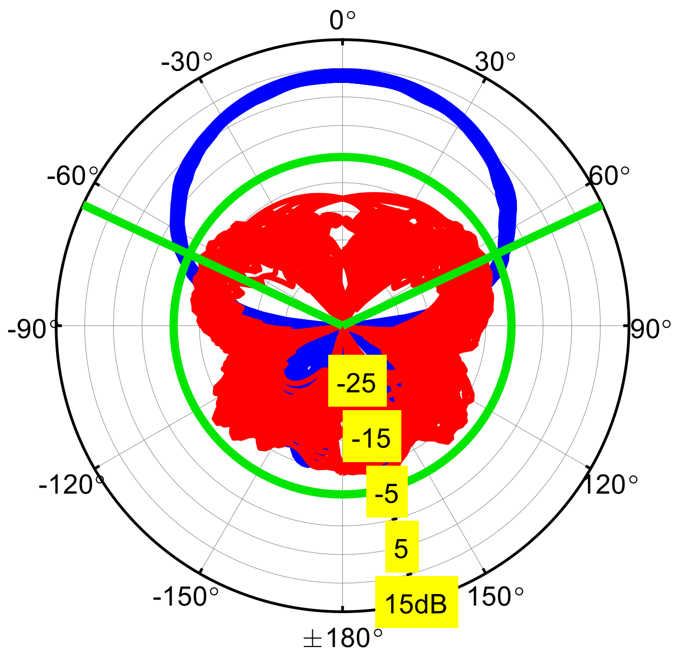

Figure 2.4: Radiation patterns of the single-element antenna.

centers have been calculated in the range $\pm\theta_e$. Although the phase center is strongly shifted at lower frequencies which in general affects the total feed efficiency [70], it is possible to find an optimum position of the feed to get reasonable efficiency values as will be demonstrated in Sec. 2.4. Additionally, in the complete solution (considering the two CPs), this issue is totally solved as will be presented later in Sec. 2.3.

2.2.4. Balun

As this spiral is a balanced antenna which has a differential port in the top part (the starting point for the two arms), there are three options for connecting it to the LNA. Firstly, connect a standard single-ended LNA to each arm which will result in two LNAs for each antenna. Secondly, using a differential LNA directly connected to the two arms or thirdly, use a balun between the antenna and the LNA.

It can be seen that although the first option is the simplest one from the point of view of designing complexity, the other two options are preferable from the point of view of cost as they decrease the number of the required LNAs to the half. To have the antenna prepared to be connected to either differential LNA or balun, two bow-ties metallic patches are added at the apex of the spiral cone as depicted in Fig. 2.6.

Although differential LNAs are available for such broadband frequency range [71], UWB balun that can efficiently excite such conical balanced spiral antenna is still needed for two reasons. First, in the case of different applications that the antenna needs to have a coaxial connector at its end to connect to the rest of the devices, or even in case of

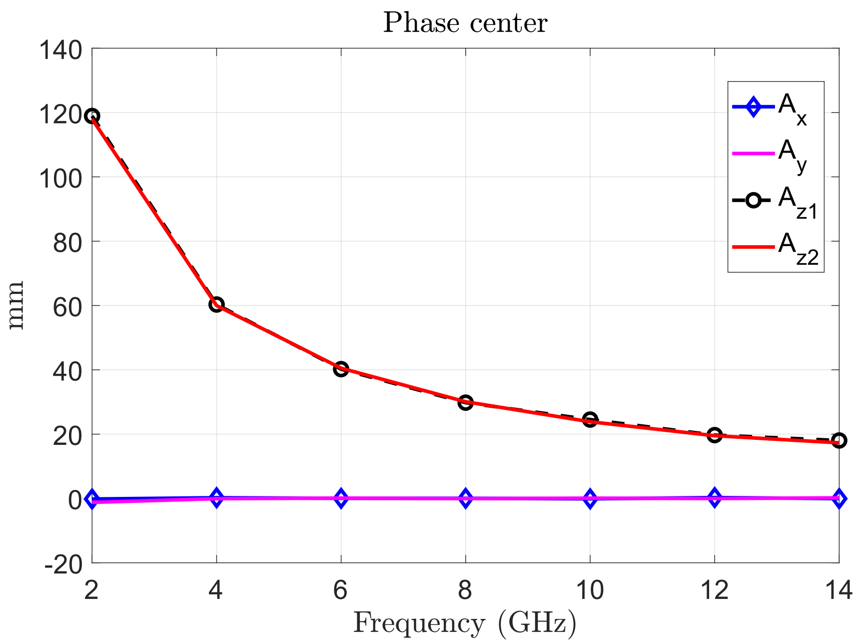

Figure 2.5: Phase center estimation of the single-element antenna.

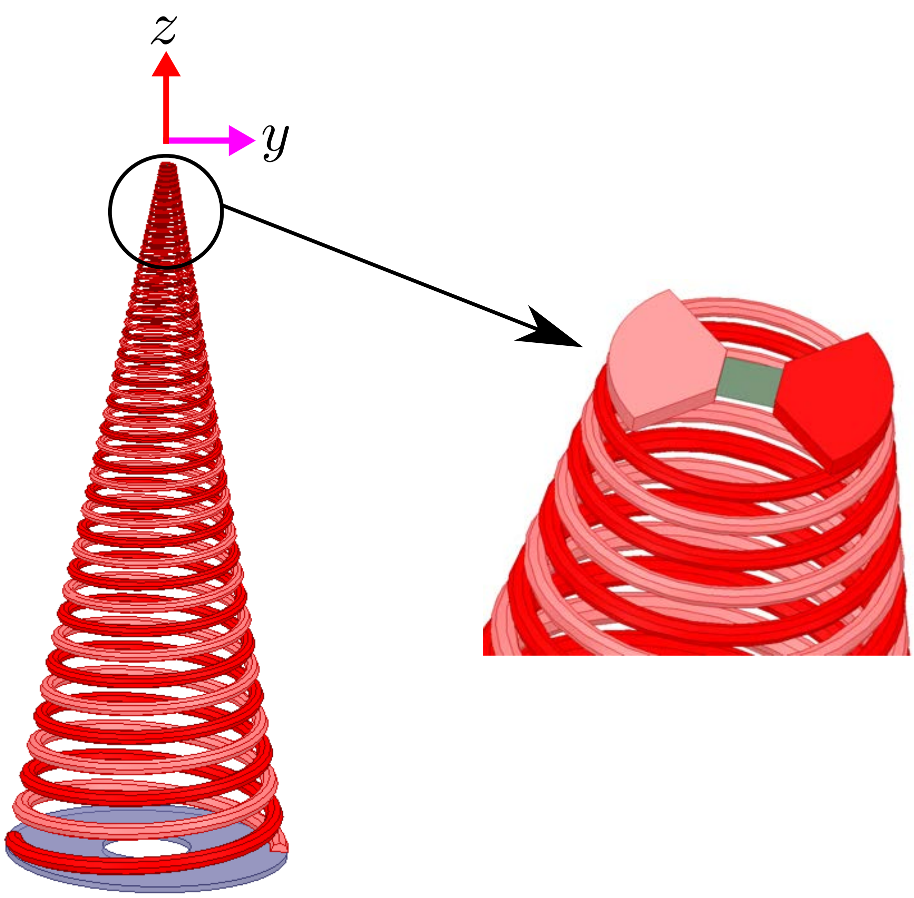

Figure 2.6: Conical log-spiral antenna with its top part.

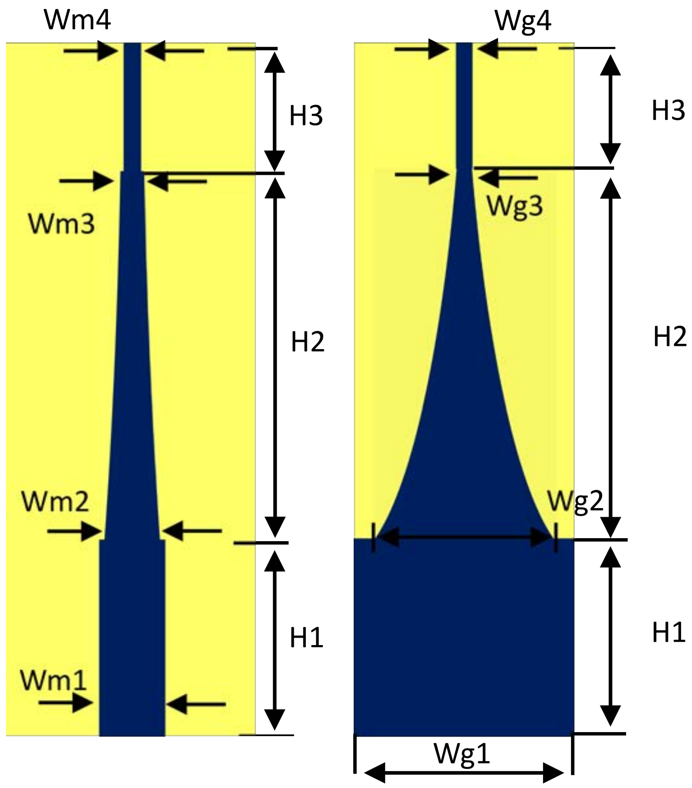

Figure 2.7: Proposed broadband balun with its main design parameters (figures not drawn to scale).

direct measurements of the isolated antenna and testing its characteristics without the need to connect it to the differential LNA. Then, in case standard single-ended LNAs are preferable. Hence, a UWB balun which covers the frequency range from 2 GHz to 14 GHz with a constant behavior is proposed.

The balun is based on tapered microstrip to parallel strip transformer [72] as shown in Fig. 2.7. To match the impedance of the proposed antenna (Fig. 2.3), it provides an output impedance around 120Ω with an input impedance of 50Ω to match the standard LNA or coaxial connectors. The standard linear-tapered 120Ω/50Ω transformer section is replaced by a fourth-order polynomial one for achieving better performance (flatter behavior over the UWB range).

The heights of the baluns are set to have a total height equals to the total height of the proposed conical antenna. However, they can be scaled down (to a quarter or even less) while having similar performance if a compact design (for example for lower-profile antennas or planar ones) or lower losses are required. The balun is printed on Duroid5880 ($\epsilon_r = 2.2$) with a thickness of 0.254 mm and its optimized dimensions are presented in Table 2.1.

The results of the proposed balun (Fig. 2.8) demonstrate the flat characteristics of the balun over the whole band with a good matching below −16 dB. As the output port (port 2) will be connected to the antenna, two modes inside it have been studied: differential mode (solid line) and common mode (dash line). From this perspective, Fig. 2.8 shows

Table 2.1: Optimized dimensions (in mm) of the balun

Parameter	**Value**	**Parameter**	**Value**	**Parameter**	**Value**
H_1	27.35	W_{m1}	0.80	W_{g1}	2.80
H_2	74.60	W_{m2}	0.65	W_{g2}	2.15
H_3	75.00	W_{m3}	0.25	W_{g3}	0.25
		W_{m4}	0.25	W_{g4}	0.25

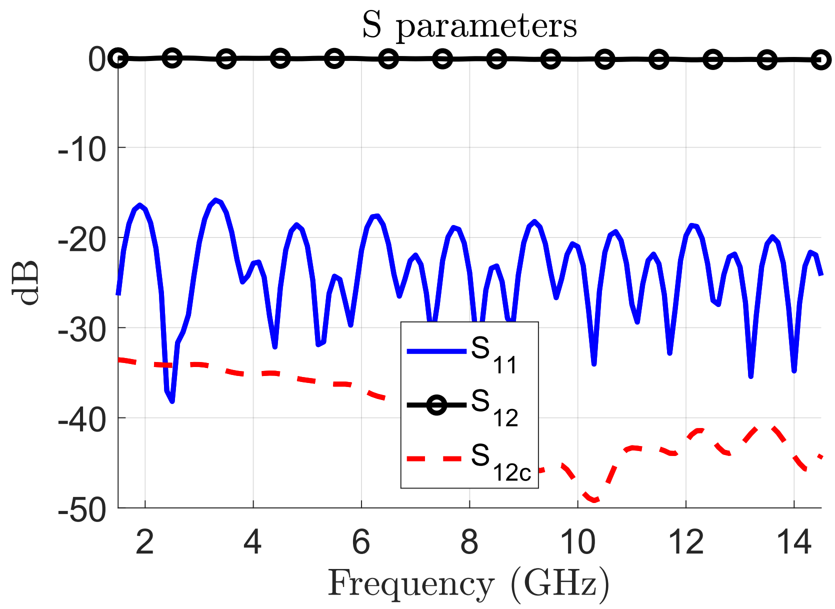

Figure 2.8: S parameters of the balun

that the balun excites purely the differential mode only (with low losses below 0.5 dB) and perfectly isolates the common one (ratio below −30 dB in all band).

2.3. DYson conical quad-spiral array

To achieve the dual-polarization requirement of VGOS, the implementation of an array with four elements of conical log-spiral antennas is used as sketched in Fig. 2.9. Each pair of antennas is devoted to a given polarization, one pair for the Right-Hand Circular Polarization (RHCP) and the other one for Left-Hand Circular Polarization (LHCP). The reason why four antennas are used instead of two (one per polarization) is that in the latter case, the total radiation patterns of the radio telescope will be squinted. One polarization will be squinted to the left from broadside and the opposite for the other polarization since the focus of the system is located close to the subreflector mirror. This effect is corrected by using two antennas per polarization. Impedance and axial ratio of the array are presented in Fig. 2.10. These results confirm the predictions from the results of the single element with small deviations at higher frequencies.

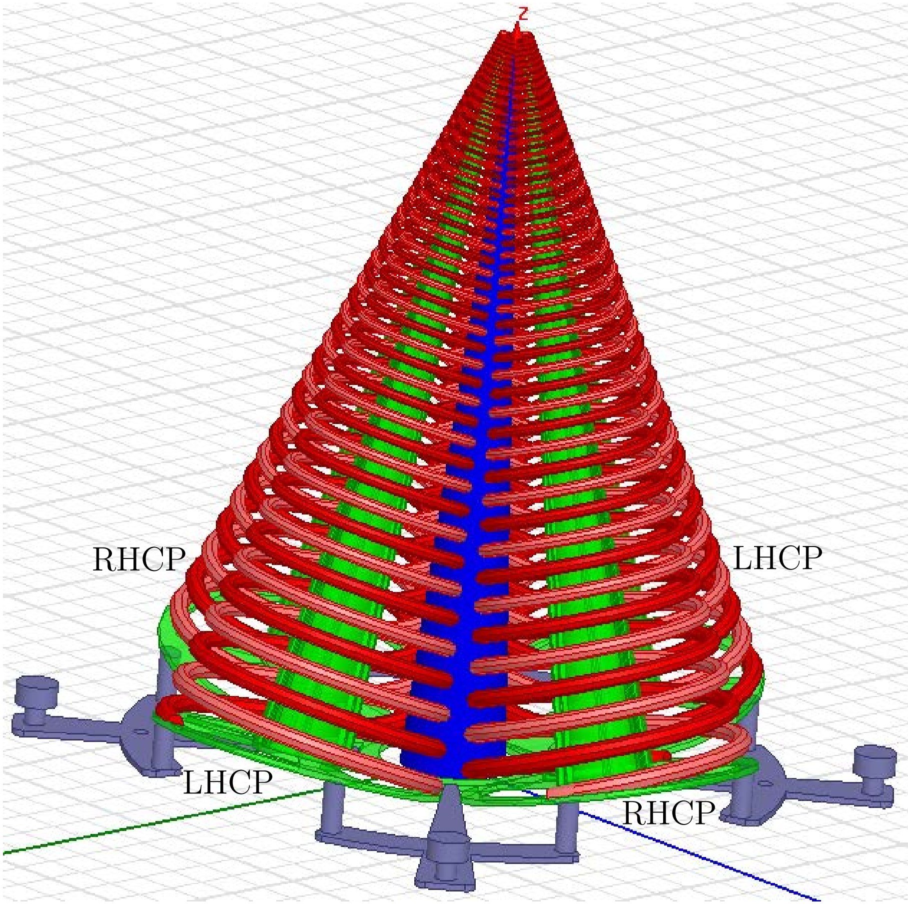

Figure 2.9: Four-elements array (DYQSA antenna) with possible balun configurations.

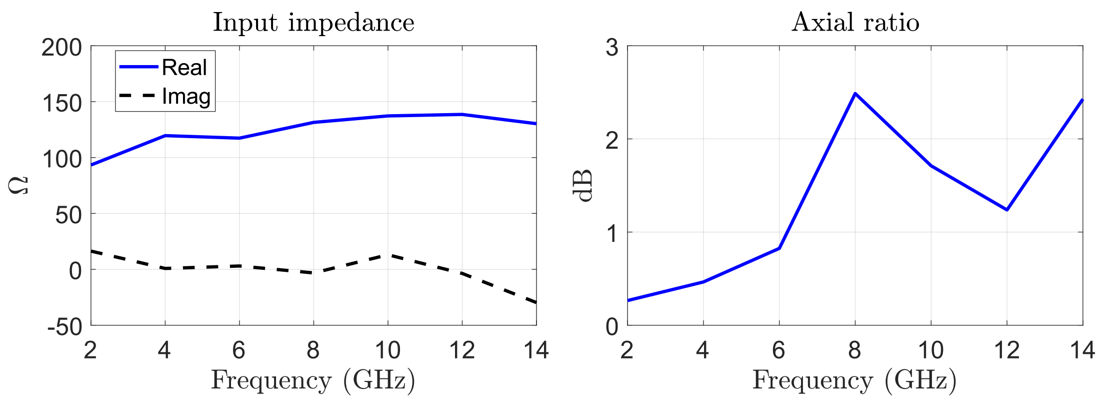

Figure 2.10: Input impedance and axial ratio of DYQSA feed.

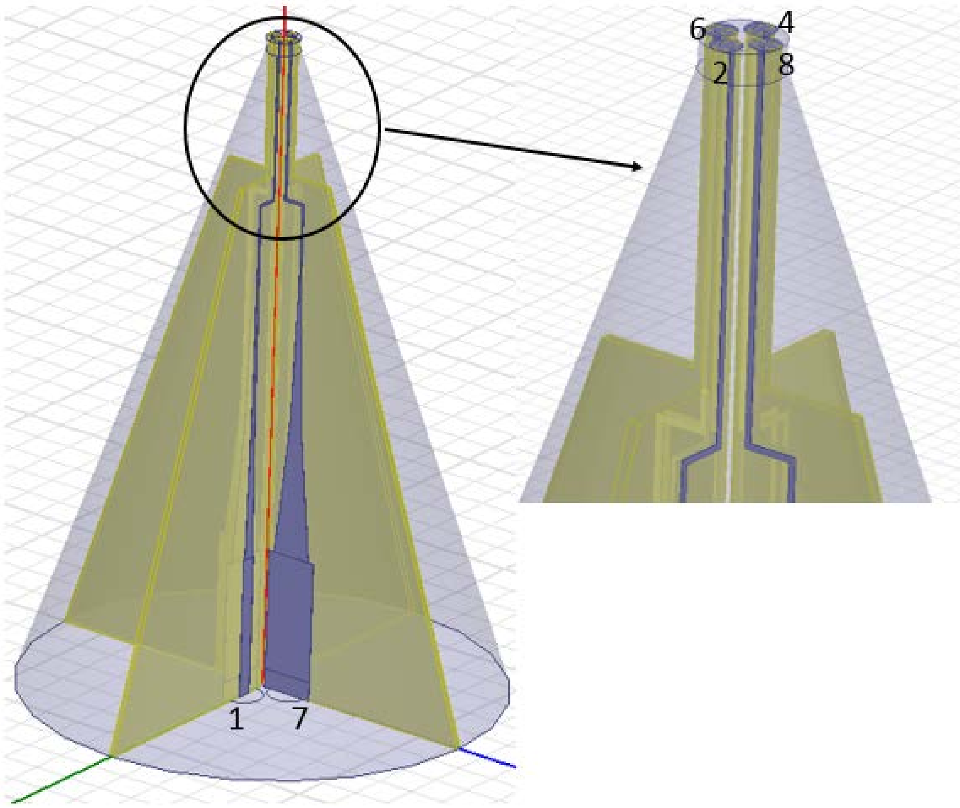

Figure 2.11: Baluns system structure and its different input-output ports.

An extensive study has been done to design the balun for this balanced array antenna and the proper position for it to fit into the geometry without disturbing the electromagnetic response of the antenna. The first method is following the same procedure presented in Sec. 2.2 and placing each balun inside its corresponding conical spiral antenna and shielding it with a metallic cone as the four green cones shown in Fig. 2.9. Although this excitation method is straightforward in its implementation, there is a high mutual coupling effect between the four metallic shields which significantly affects the radiation pattern stability over the required bandwidth. Thus, to enhance the electric properties of the system and reduce the effects of this metallic shielding, an updated version has been proposed. In this version, the four individual baluns have been replaced by one system of four baluns connected and introduced inside one metallic shielding through the center of the four spirals system [73] as presented in the blue cone in Fig. 2.9.

The geometry for the baluns system which can feed this proposed array is depicted in Fig. 2.11. The extra substrate is kept deliberately for giving robustness to the structure. Each balun is represented by 2 ports: one (labeled with an odd number) which will be connected to the unbalanced part (coaxial or LNA), the other (labeled with an even number) will be connected to the balanced part (spiral element).

Although this design provides better performance, it is, at the same time, a new design challenge (at such frequency band) due to the small cone dimensions which have a

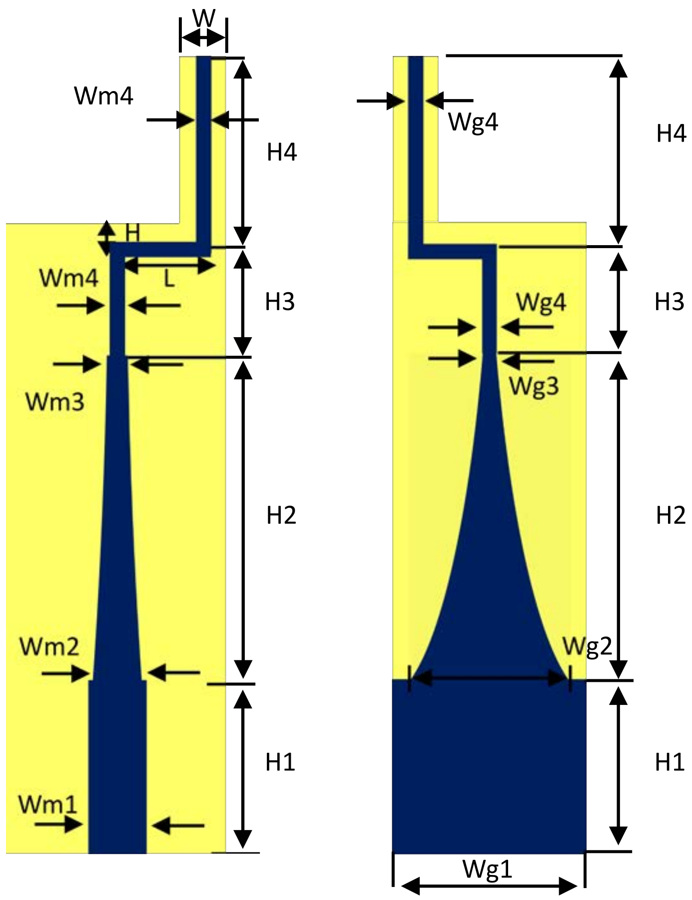

Figure 2.12: Single element of the proposed baluns system.

radius less than 1 mm at the top part of the antenna. Each element of this balun system is adjusted to provide an output impedance of about 150Ω to match the modified larger impedance of the spiral antenna in its array configuration (Fig. 2.10). The single element of the proposed balun system is presented in Fig. 2.12 with a summary of its optimized dimensions in Table 2.2.

Due to the symmetry of the structure and for simplicity, the results of port 1 and port 2 and their relations to all other ports are shown in Fig. 2.13. The S parameters between these two ports and other ports within the same polarization are given in Fig. 2.13 (a) while Fig. 2.13 (b) is dedicated for their relations to the other polarization. All output ports (which have even indices) are represented by two solid and dashed curves which stand for differential modes and common ones respectively.

It can be demonstrated from Fig. 2.13 that the proposed baluns system is feeding the antennas properly as it excites only the differential mode in the structure with small common-mode ratios below −10 dB. Figure 2.13 proves also the stable performance of the balun over the whole band with small losses around 0.5 dB and isolation between different ports greater than 15 dB in most of the band. The simulated radiation patterns of the antenna array are presented in Fig. 2.14 covering the required bandwidth for different

Table 2.2: Balun system dimensions (in mm)

Parameter	Value	Parameter	Value	Parameter	Value
H_1	37.35	W_{m1}	0.80	W_{g1}	2.80
H_2	74.55	W_{m2}	0.65	W_{g2}	2.10
H_3	22.00	W_{m3}	0.15	W_{g3}	0.15
H_4	43.00	W_{m4}	0.15	W_{g4}	0.15
H	5.23	W	0.60	L	1.10

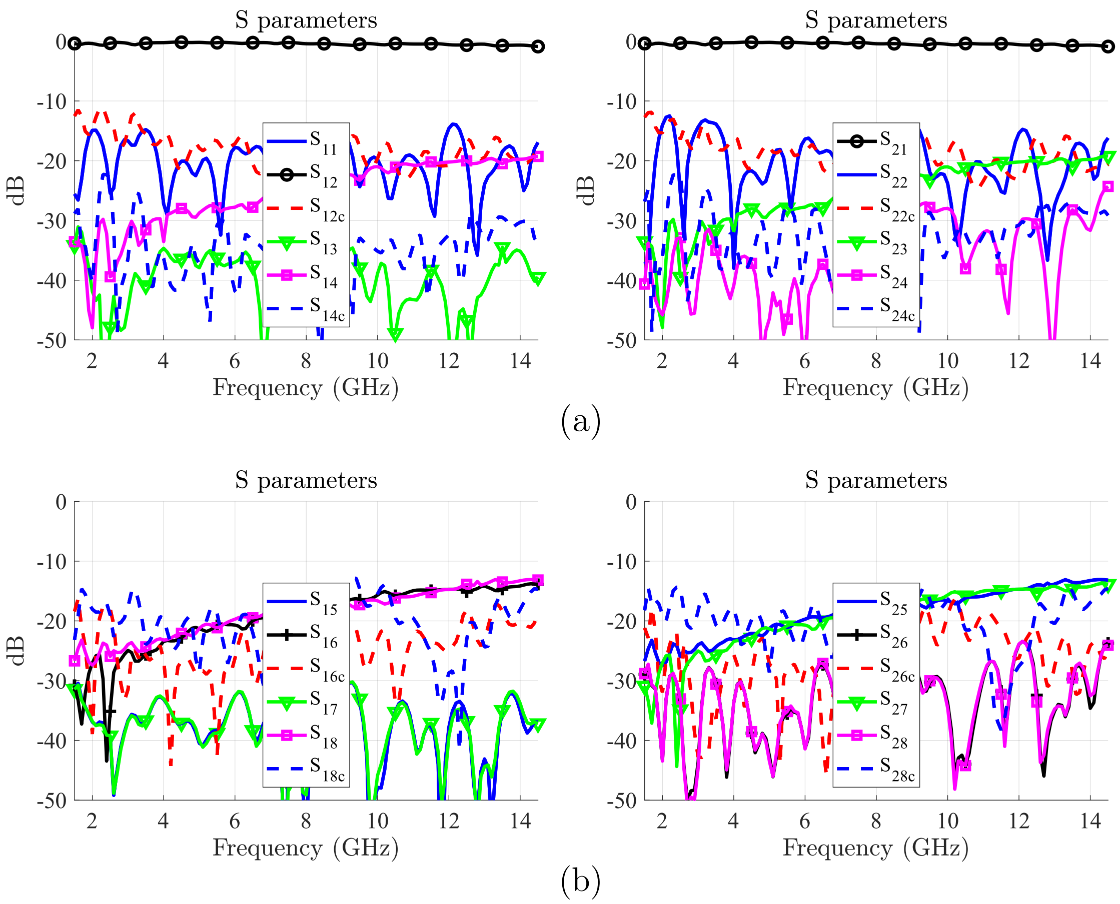

Figure 2.13: S parameters of the baluns system (a) for the same polarization, (b) between the two different polarizations.

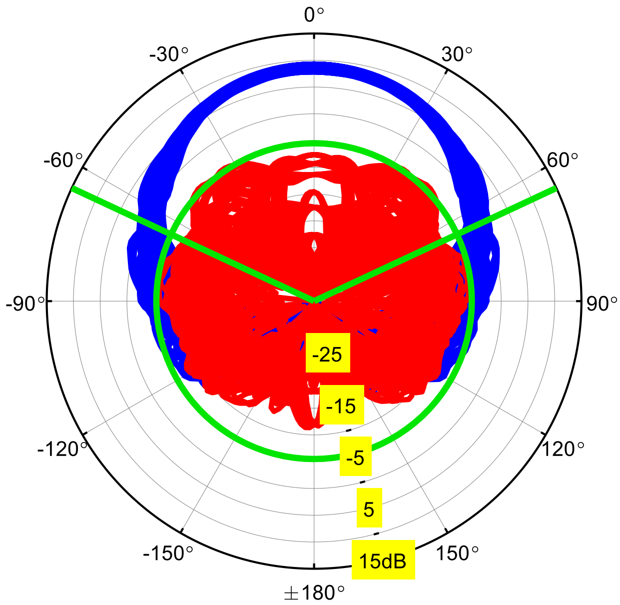

Figure 2.14: Radiation patterns of the four-elements array (DYQSA antenna).

ϕ planes from 0° to 180° in steps of 15°. Figure 2.14 confirms the high symmetry of the radiation patterns over the whole band. The maximum Co/Xp-ratio is above 15 dB with a constant gain of around 10 dBi.

Figure 2.15 shows the phase center estimation of the whole array when the origin of coordinates is placed in the virtual apex of the four cones. Although the phase center is not totally constant in the whole band, its variation in the 4 GHz - 14 GHz band is around two centimeters. The overall variation is significantly lower than the case of the single conical log-spiral element. In Sec. 2.4, it will be shown that such small phase center variations have negligible effects on the overall feed efficiency of the system.

2.4. Integration of the single-element and DYQSA feeds to the radio telescope

2.4.1. VGOS radio telescope fed by an ideal Gaussian feed

For comparison purposes through the thesis, it is convenient to analyze the radiation patterns obtained for the radio telescope using an ideal Gaussian feed system. With this analysis, it is possible to have an upper limit estimation of the total aperture efficiency and directivity of the reflector system which are key parameters for designing the proper feed [74].

To do this, a feed illuminating the reflector system with an ideal Gaussian beam pattern is placed in the focus of the subreflector. GRASP software has been used to analyze the whole reflector system at the desired range of frequencies from 2 GHz up to 14 GHz. The directivity and aperture efficiency vs frequency of the reflector using this ideal Gaussian feed are shown in Fig. 2.16.

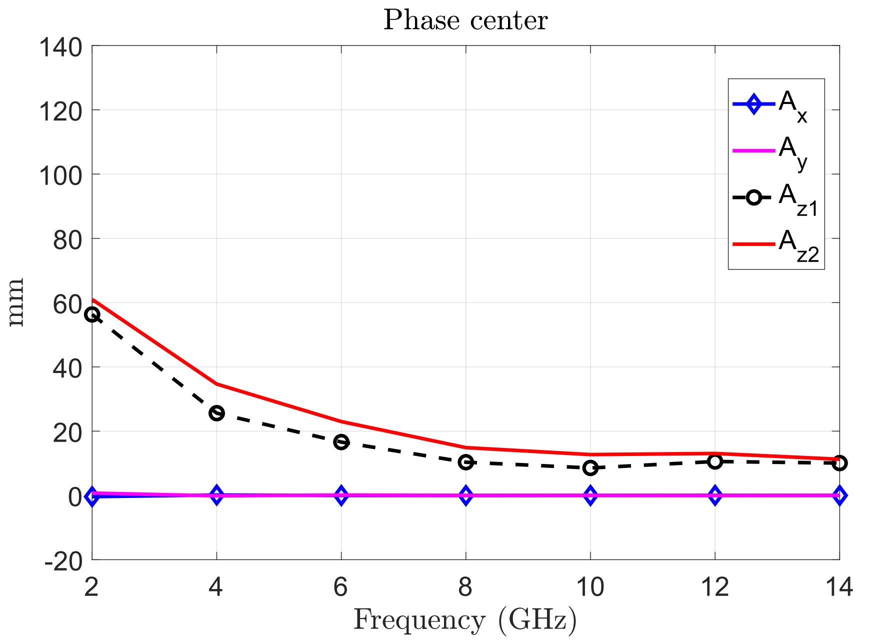

Figure 2.15: Phase center estimation (in mm) of DYQSA feed.

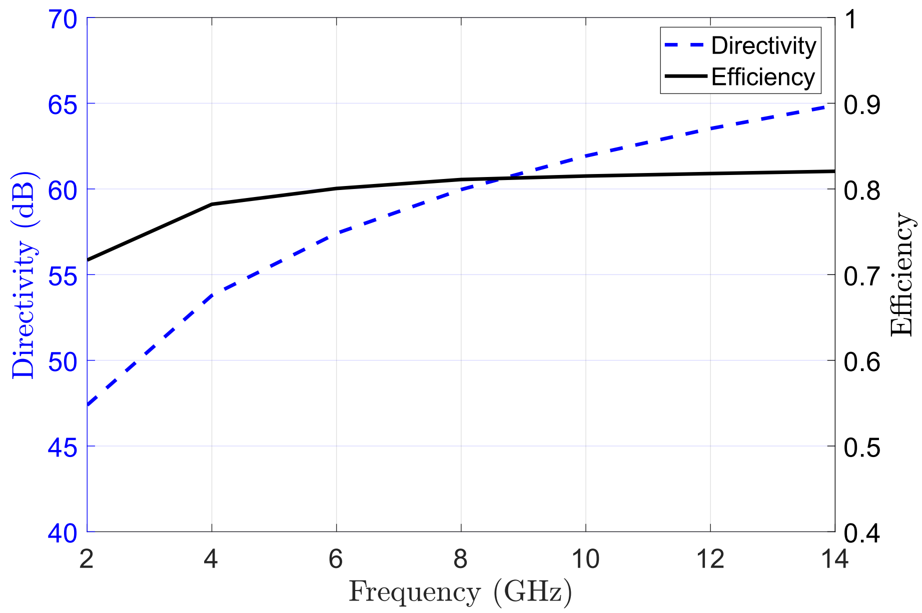

Figure 2.16: Directivity and aperture efficiency of the reflector fed by an ideal Gaussian feed.

Figure 2.16 proves that the radio telescope has an almost flat efficiency of about 80% with a reduction of about 10% at lower frequencies. It can be demonstrated from this study that the efficiency has an upper limit and cannot reach unity, the physical explanation for this behavior is coming from the trade-off between spillover and illumination which both depend on the beamwidth of the radiation patterns of the feed. Maximization of the aperture efficiency implies the maximization of this trade-off product [75].

At the broadside ($\theta = 0°$), the expected directivity of the radio telescope using this ideal feed is in almost linear proportion with the frequency and varies from 47 dB at 2 GHz to 65 dB at 14 GHz. The radiation patterns of the reflector are given in Fig. 2.17. It shows perfectly symmetric radiation patterns as expected from the excitation with this symmetric beam with an excellent Co/Xp-ratio level.

Following what has been done so far in this section, the proposed antennas can be tested by checking the performance of the VGOS radio telescope while using such feeds to excite it. In the next two subsections (Sec. 2.4.2 and Sec. 2.4.3), the results for the whole reflector will be presented in two cases. Firstly, feeding it using the conical log-spiral feed in case of single CP. Secondly, feeding it using DYQSA feed for achieving dual CP. As it is common when designing feeds for reflectors such as in the case of QRFH [9] or Eleven [11], losses due to blockage and support structures are not included in the calculations as they are issues of the reflector itself instead of the feed.

2.4.2. Analysis of VGOS radio telescope fed by the single-element antenna

Figure 2.18 presents the reflector subefficiencies calculated using (1.4) to (1.7). The dotted black line is the total efficiency excluding the phase efficiency which is critically dependent on the location of the feed. The frequency-averaged total efficiency has been maximized by studying its strong dependence on the displacement of the feed along the z-axis as shown in Fig. 2.19. The optimum performance is achieved when the virtual apex of the antenna is placed at 26 mm beyond the focus of the system.

Radiation patterns of the VGOS radio telescope have been analyzed using GRASP software by introducing the radiation patterns of the single-element from HFSS as the feed of the reflector. The radiation patterns for the reflector that covers the single-polarization are shown in Fig. 2.20. For simplicity, results of three cut planes only have been included ($\phi = 0°$, 45°, and 90°). Solid and dashed lines represent the CP co-polar and cross-polar field components respectively (RHCP and LHCP).

Figure 2.20 presents a high level of symmetry along the different cut planes with a Co/Xp-ratio at broadside greater than 23 dB for the whole 2 GHz – 14 GHz range. This performance is comparable to the ideal case performance obtained by the ideal Gaussian beam (Fig. 2.17) which is confirmed by the comparison of the reflector directivity for both cases as described in Fig. 2.21.

The previous results demonstrate that the proposed antenna can be used as a broad-

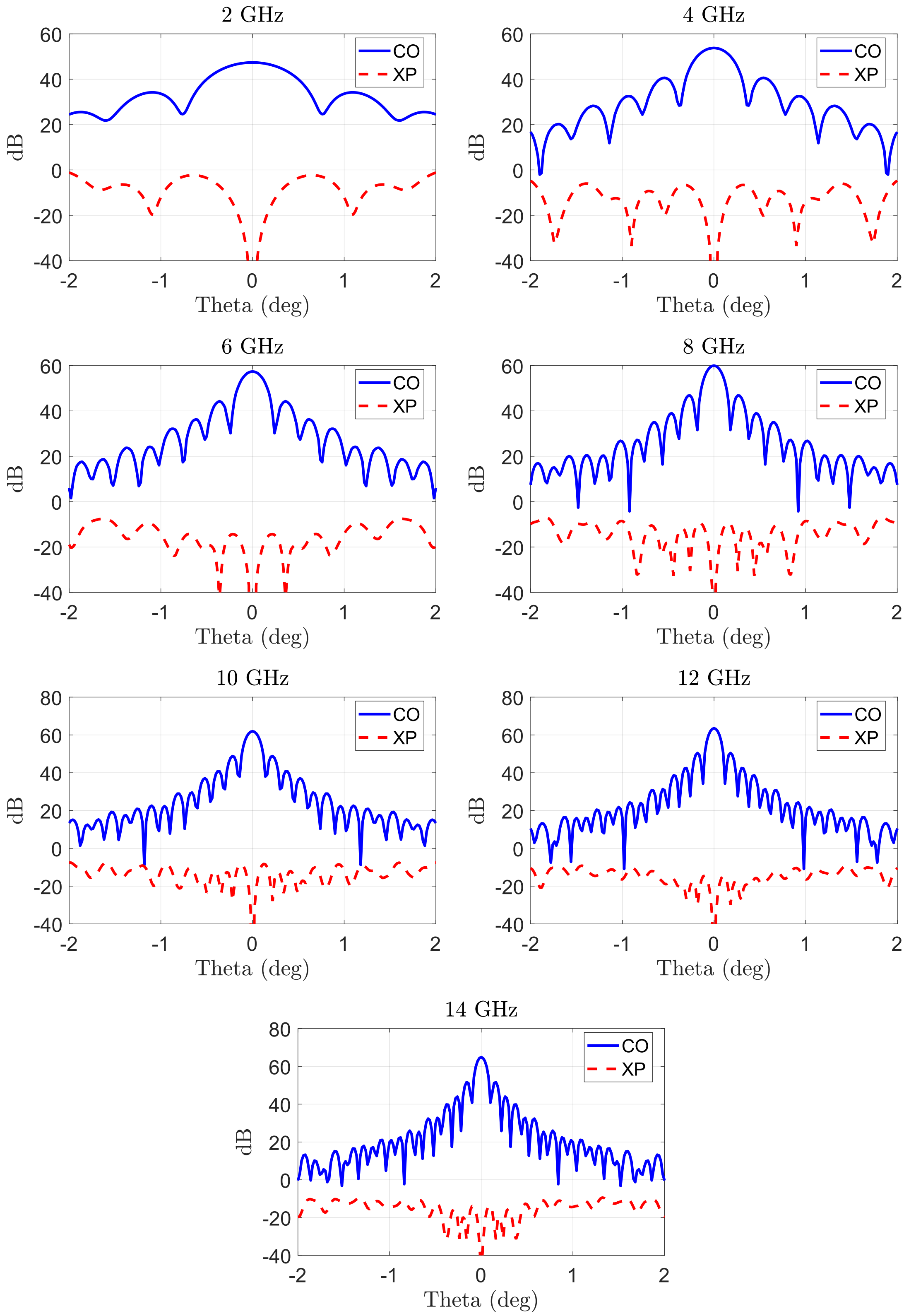

Figure 2.17: Radiation patterns of the reflector fed by an ideal Gaussian feed.

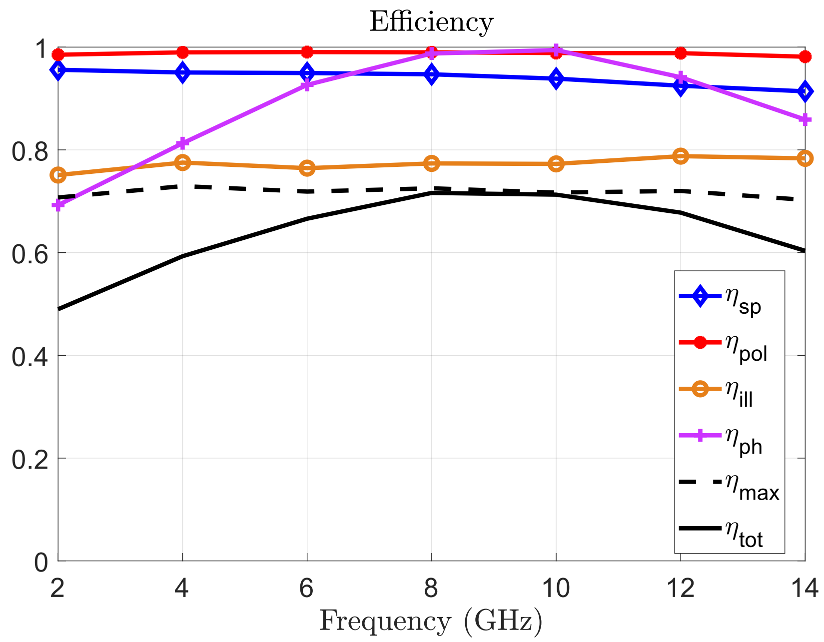

Figure 2.18: Feed efficiency of the radio telescope based on the simulated radiation patterns of the single-element antenna.

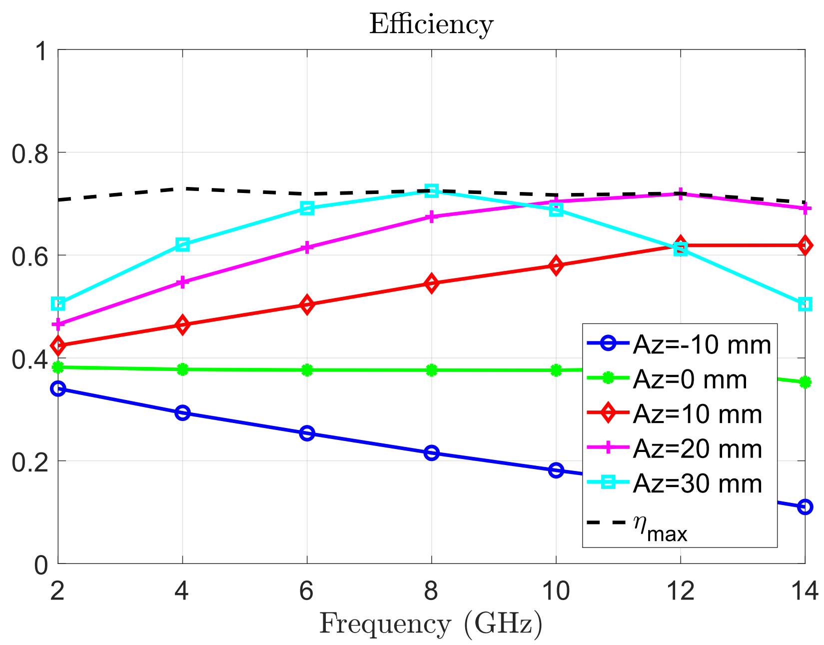

Figure 2.19: Effect of the feed position on the aperture efficiencies.

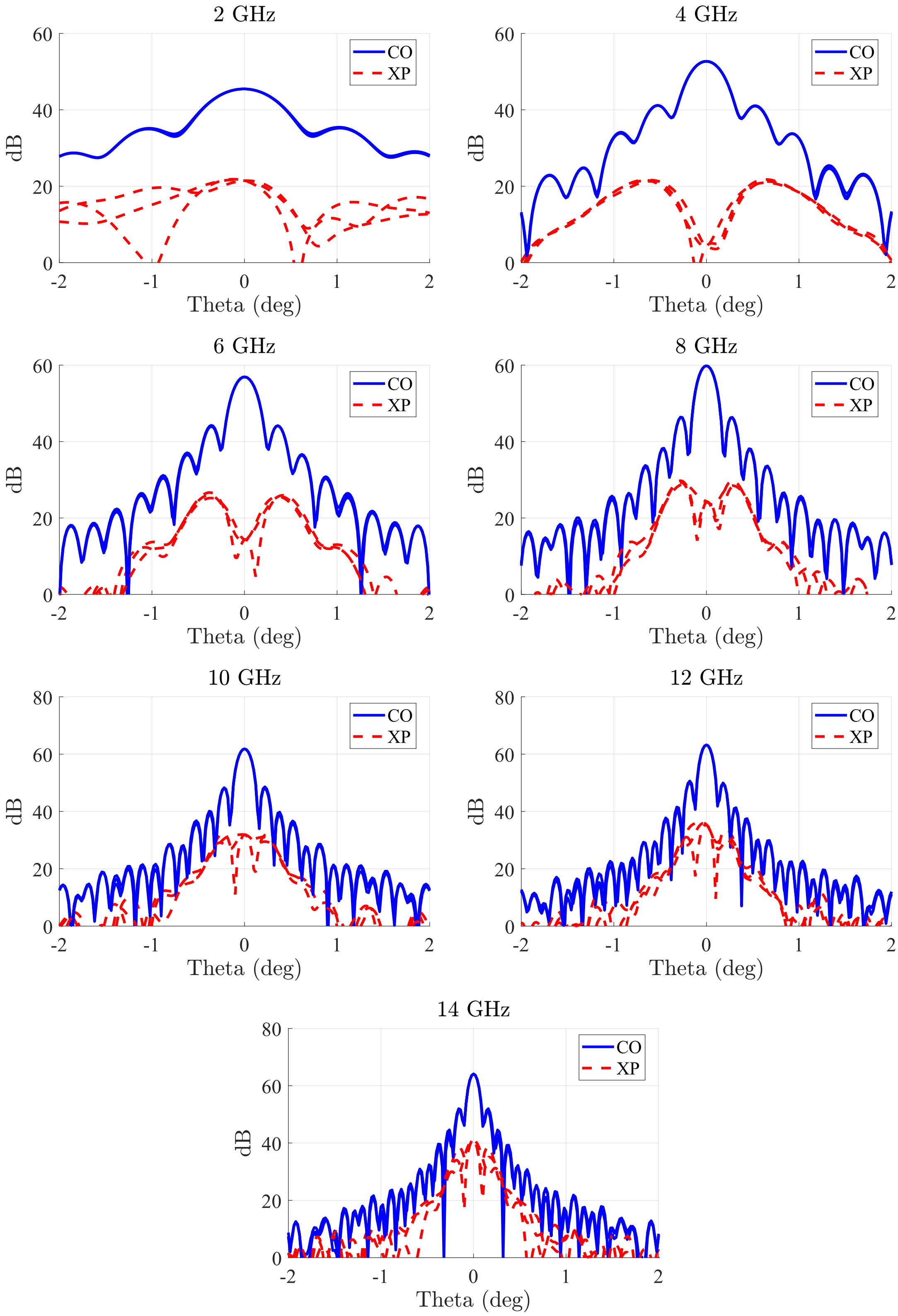

Figure 2.20: Radiation patterns of the reflector fed by the single-element antenna.

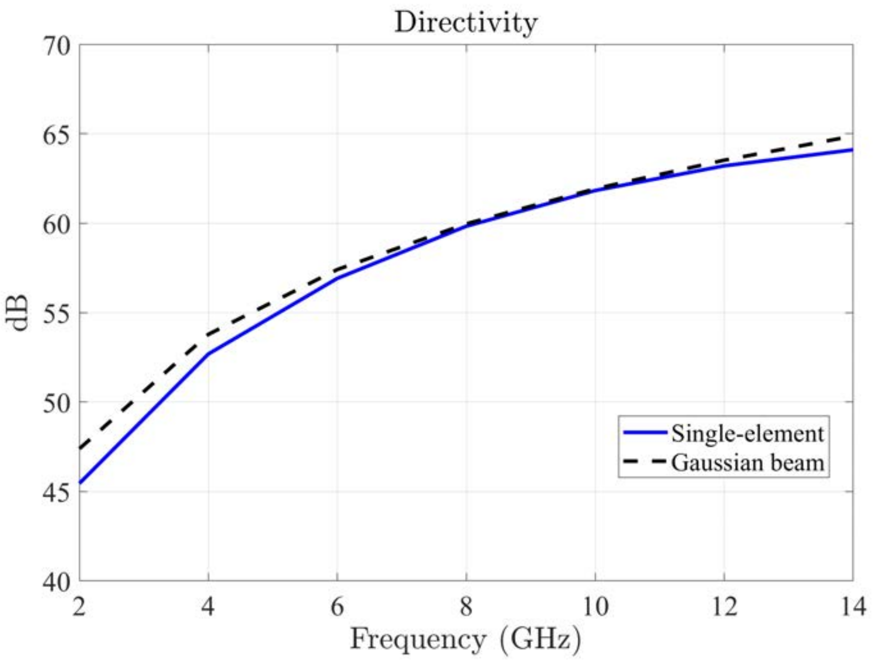

Figure 2.21: Directivity of the reflector fed by the single-element antenna.

band feed for radio astronomy reflectors. It exhibits CP in contrast to the linear polarization as the state-of-the-art antennas. This could be potentially very useful as CP (which is simpler to handle) is the required polarization for VLBI applications.

It is true that CP receivers can be built using linear-polarization feeds by the addition of linear-to-circular polarization conversion circuits like quarter-wave plates or other equivalent devices [76]. However, this yields some drawbacks such as lower polarization purity and narrower effective bandwidth [77]. These are particularly relevant in the case of broadband receivers as most of these devices can provide a perfect 90° phase shift at only one or some frequencies, yielding phase errors away from these frequencies [78].

Another approach for the conversion from the linear polarization to the circular one is to reconstruct the CP by recombining the signals after digitization. However, it still needs a good calibration system to compensate for phase and amplitude differences in the two paths which will increase the system complexity. On the other hand, the proposed solution is capable of directly providing CP without the need for either additional analog hardware or digital software. Moreover, the direct use of linear-polarization receivers will cause the loss of coherence between the different wide-separated stations in the network. This is because the linear dipoles will not remain parallel to each other, requiring tricky parallactic angle corrections compared to the simple phase correction for the CP case.

2.4.3. Analysis of VGOS radio telescope fed by the four-elements array

As presented in Sec. 2.4.2, there is an optimum position of the feed. For this array system, the maximum total efficiency averaged over the frequency band (the optimum performance) is achieved when the apex of the array is placed 14 mm beyond the focus of the system.

The radiation patterns of the reflector after introducing the array as a feed for it are shown in Fig. 2.22 for three cut planes. Figure 2.22 demonstrates that the radio telescope fed by DYQSA has a high level of symmetry in its radiation patterns over the required frequency range with a minimum Co/Xp-ratio level of 15 dB.

Using the previous radiation patterns (Fig. 2.22) in (1.10), the antenna noise temperature (T_A) along with the spillover noise temperature (T_{sp}) are estimated. The calculations have been done for two different cases. First, at zenith $\theta = 0°$ (corresponding to an elevation angle of 90°) when the reflector antenna is pointing vertically directly towards the sky and following by the case of 45° zenith angle. The average spillover noise and antenna noise temperatures over the whole band are 6 K and 14 K respectively at zenith as presented in Fig. 2.23. These average values increase by about 7 K at the lower elevation ($\theta = 45°$).

The directivity of the system versus the frequency is calculated using GRASP and is plotted in Fig. 2.24. For comparison purposes, the directivity of the reflector fed by an ideal Gaussian beam is included. Figure 2.24 shows that DYQSA can provide a comparable directivity to the optimum case (i.e. the difference in the directivity is below 1.2 dB). Considering all the previous results and the results presented in Sec. 2.4.1, it can be concluded that the performance of both proposed antennas has a high level of matching compared with the optimum performance obtained using the ideal Gaussian feed.

The aperture efficiencies for the radio telescope are shown in Fig. 2.25. It presents an almost constant total efficiency of around 65%. As expected from the phase center estimation of the array in Fig. 2.15, its small variations have negligible effects on the total feed efficiency (the average phase efficiency over the required bandwidth is 97%).

The receiver noise temperature T_{rec} can be calculated by combining the noise temperatures for each source. First, the cryogenic LNA proposed by Yebes Observatory for VGOS reflectors has an almost flat measured noise temperature of 7.5 K in the operation band from 2 GHz to 14 GHz [73]. Then, following the estimations that have been done for QRFH, the other noise sources (calibration coupler and coaxial cables) will have a sum of noise temperatures of about 13 K [9], thus, the expected T_{rec} will be around 20 K.

The noise contribution due to ohmic losses is 7 K per 0.1 dB loss at room temperature but as the feed will be cooled down to 15 K, this noise temperature will be smaller by a factor of 20 to be around 0.3 K per 0.1 dB loss. For DYQSA feed, the simulated radiation efficiency is around 0.9 (losses are less than 0.5 dB) which corresponds to 1.5 K of ohmic losses noise contribution. Hence, under the cryogenic cooling ($T_{\mathrm{phy}} \approx T_A$) and for this

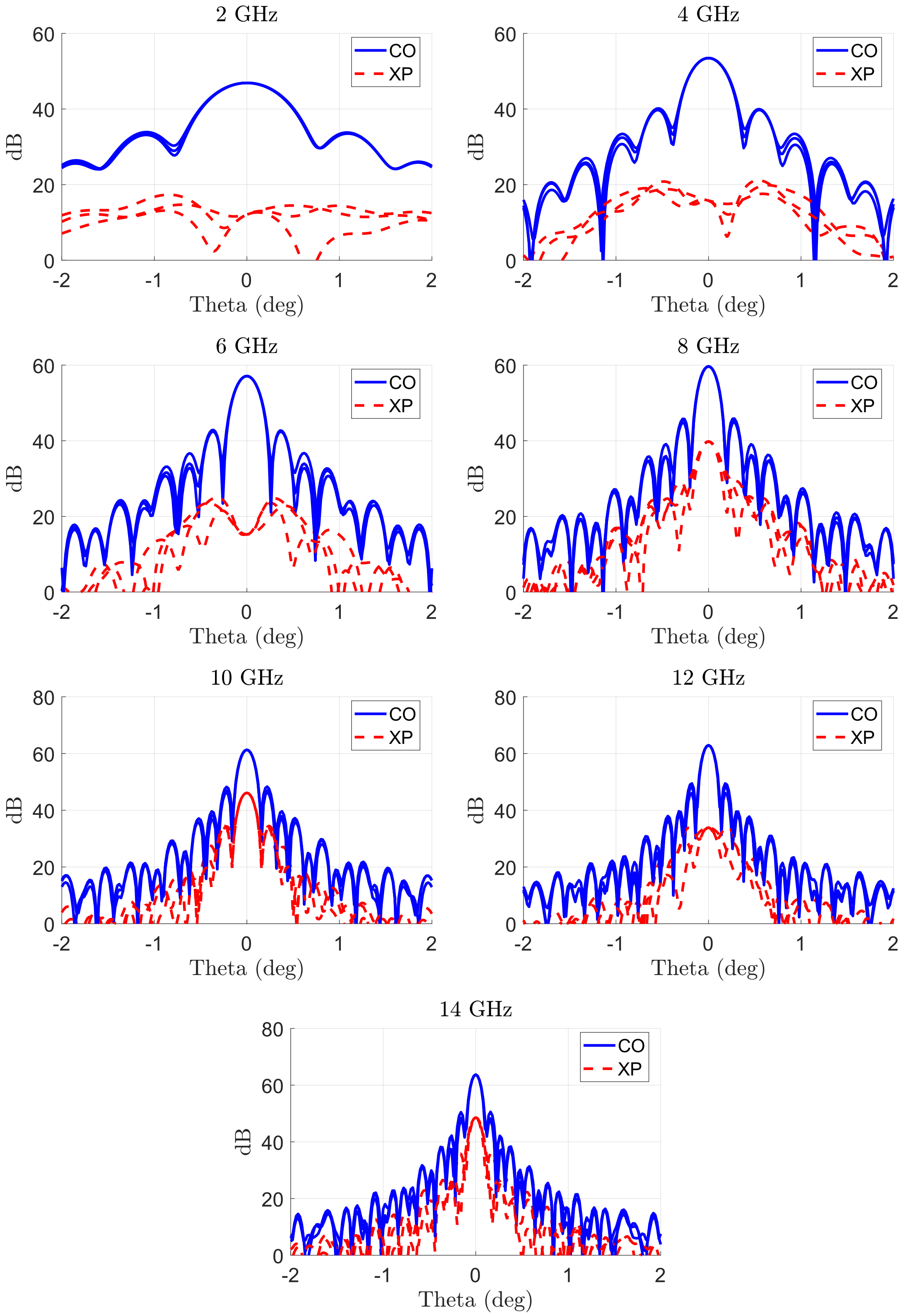

Figure 2.22: Radiation patterns of the reflector fed by DYQSA.

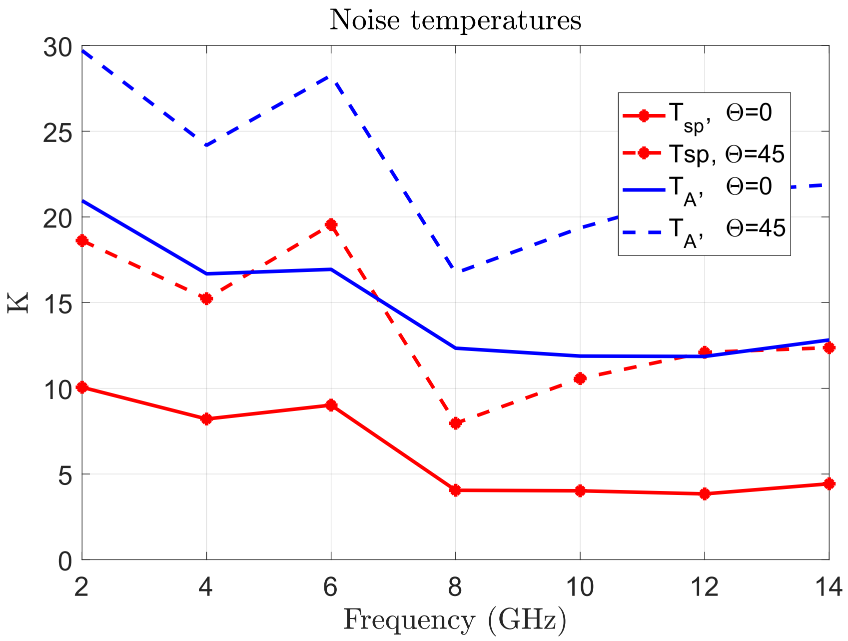

Figure 2.23: Spillover and antenna noise temperatures of the reflector fed by DYQSA.

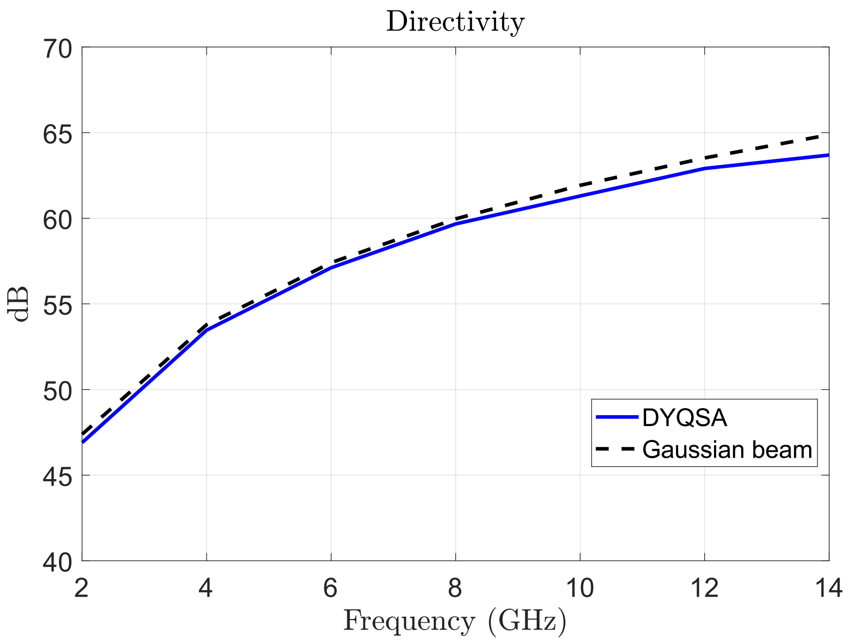

Figure 2.24: Directivity of the reflector fed by DYQSA antenna

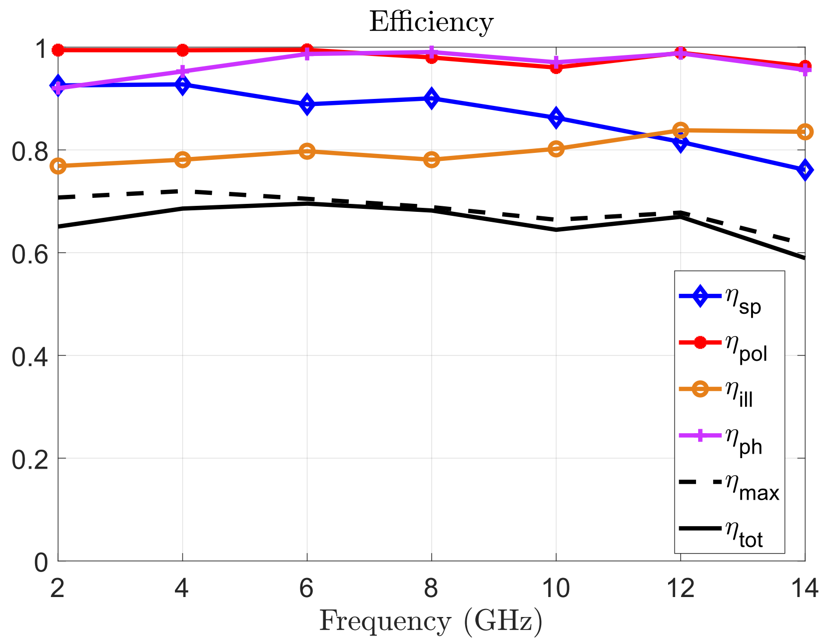

Figure 2.25: Feed efficiency of the reflector based on the simulated radiation patterns of DYQSA.

radiation efficiency, the system noise temperature in (1.8) can be approximated as $T_{sys} \approx T_A + T_{rec}$.

The estimated SEFD of VGOS radio telescope based on DYQSA feed is presented in Fig. 2.26. A SEFD below 1800 Jy with an average of about 1300 Jy over the required UWB range at zenith is obtained. At a zenith angle of 45°, the average SEFD value is 1600 Jy. This confirms that DYQSA efficiently fulfills the requirements of VGOS system. All these results demonstrate that the proposed DYQSA solution is a potential feed candidate for future radio telescopes.

2.5. Comparisons and measurements

This section presents comparisons between DYQSA feed and the two-main state-of-the-art feeds (QRFH and Eleven). These comparisons include six critical terms which are total aperture efficiencies, design adaptability to different reflectors, physical volume, the required number of LNAs per feed, cost, and calibration signal injection. Additionally, it shows the measurements of both the single-element antenna and the four-elements array.

2.5.1. Feed aperture efficiency

A comparison between the three feeds from the aperture efficiency point of view is plotted in Fig. 2.27. For DYQSA feed, the efficiencies have been calculated using two different approaches. First, following [19] by integrating the radiation patterns using the closed-form equations (1.4) to (1.7). This is represented by the dotted-black line in Fig. 2.27.

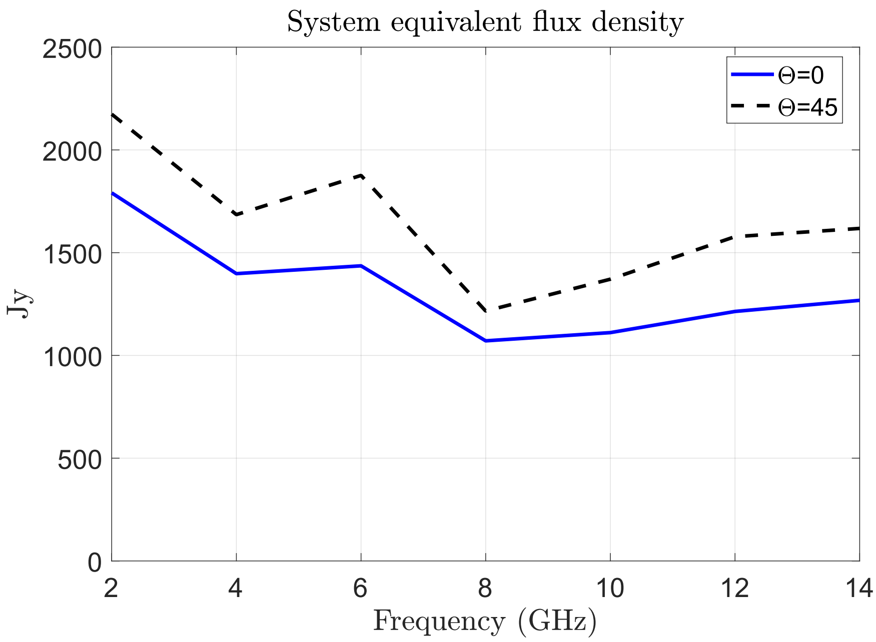

Figure 2.26: Estimated SEFD of the reflector fed by DYQSA.

Second, using GRASP software where the measured radiation patterns are used as the feed for the reflector, this is given by the solid-blue line in Fig. 2.27.

For comparison purposes, the aperture efficiencies of both Eleven and QRFH feeds as they would perform in the VGOS reflector system [12],[79] are also shown in Fig. 2.27. The feed efficiency of the Eleven solution has been calculated using GRASP software at Onsala Space Observatory (OSO) while the QRFH efficiency calculation has been done using physical optics software at NASA Jet Propulsion Laboratory (JPL). The version of QRFH used in this comparison was designed for the frequency range from 2 GHz to 12 GHz so there is no available data for the comparison up to 14 GHz.

Figure 2.27 proves that DYQSA exhibits better performance than the other two solutions at higher frequencies, which face a linear degradation. Some recent work has been done for other different versions of QRFH feed for enhancing its properties and getting a flat performance over a wide bandwidth, for example by adding a dielectric spear [80]. However, it still has not been tested for the high frequencies required by VGOS. On the other hand, DYQSA has a flat behavior which demonstrates that the phase center shifting is compensated.

It can be seen from the estimation of the phase center (Sec. 2.3) as well as in the efficiency calculated in this section, that DYQSA shows an improvement in the global efficiency of the system due to the stability of the phase center. Furthermore, from a general system perspective, and after connecting a feed to the LNAs, usually, the SEFD suffers from an increase in the receiver noise temperatures at the high frequencies. From that perspective, the constant efficiency of the proposed solution at high frequencies is an attractive characteristic.

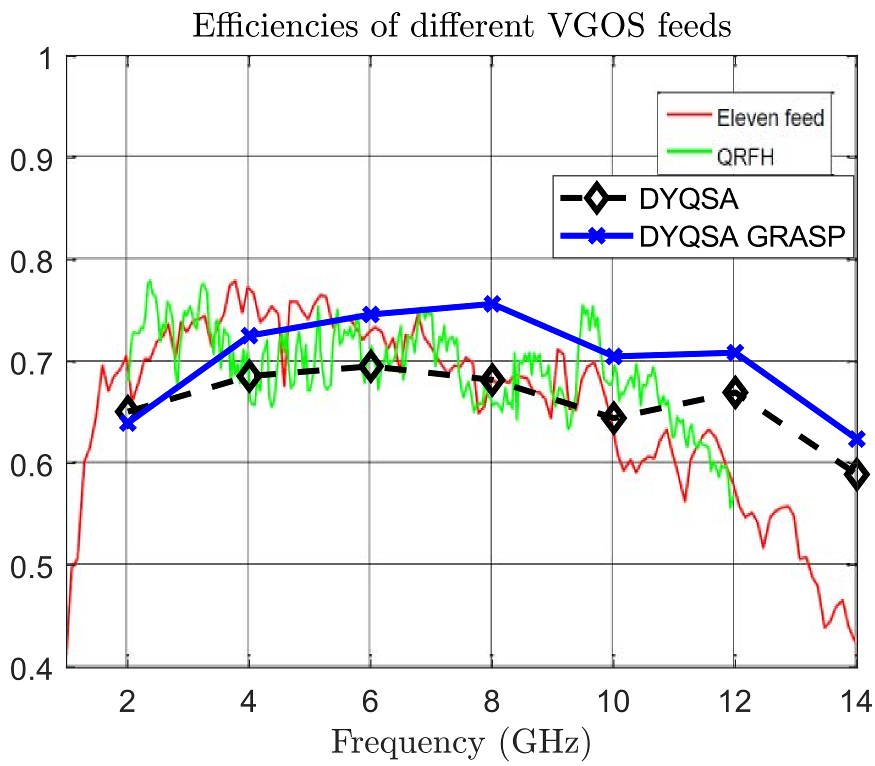

Figure 2.27: Comparison of the aperture efficiency of DYQSA, Eleven and QRFH feeds.

2.5.2. Design adaptability of the feed (different applications)

Another key parameter for the comparison purposes is the adaptation ease of the design, which ensures that the antenna can be reoptimized to be used for several radio astronomy reflectors or even for different applications. While QRFH antenna can be optimized for different antenna optics, Eleven antenna has an almost fixed edge taper level of $-10\,\text{dB}$ at around 65° from broadside. The performance of Eleven indeed will not dramatically change with small changes of the antenna optics, however, for reflectors that require significant changes in the angles of the edge taper, the QRFH design-adaptability will result in better performance.

From this perspective, both the single-element and DYQSA feeds have the full ability to be reconfigurable for a wide range of F_m/D_m ratios even larger than QRFH. This is as has been shown in the design procedure of Sec. 2.2.2 that the beamwidth (and therefore the gain) and the frequency can be easily adjusted according to the requirements of the application without affecting the feed performance. Also, this would be confirmed in Sec. 2.7 when the feed would be adjusted to work for satellite earth observations in a lower-frequency band starting from $400 MHz$ with higher gain above $10\,\text{dB}$.

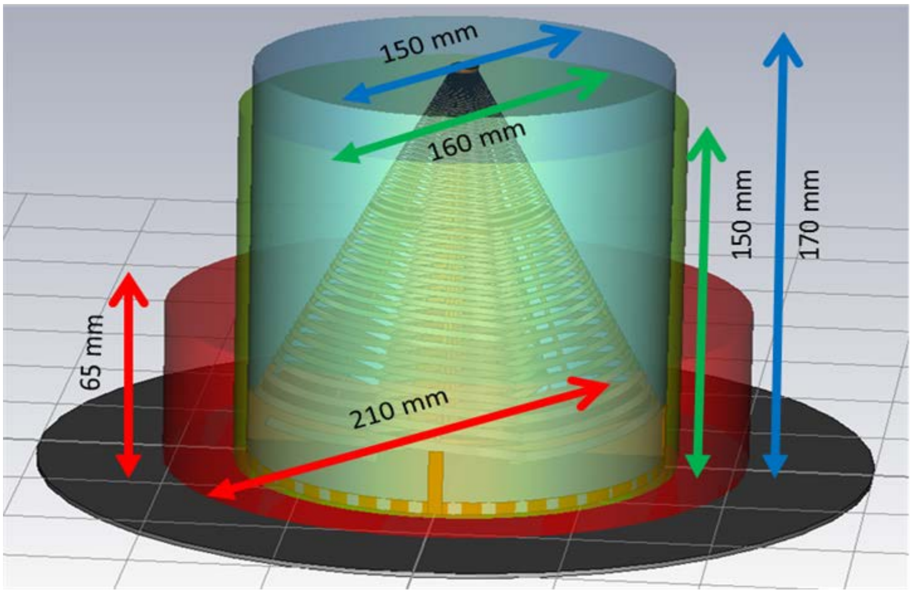

Figure 2.28: Volumetric comparison of DYQSA (blue), Eleven (red), and QRFH (green) feeds.

2.5.3. Feed volume

A volumetric comparison between DYQSA (in blue), Eleven (in red), and QRFH (in green) is sketched in Fig. 2.28. This comparison depicts that the size of DYQSA is similar to that of QRFH, and both have narrower-longer dimensions compared to Eleven feed.

2.5.4. LNAs needed for the feed & feed cost

To avoid noise degradation from the combining network, the LNAs can be directly connected to the balun. This will result in a total number of two LNAs per polarization or four LNAs per DYQSA feed which is half of the number of LNAs required by Eleven feed. Also, the LNAs need to be matched within specified limits, otherwise, the performance of the feed will be affected. Even though QRFH does not require any combining network (it has only one LNA per polarization), it still has degradation in the performance caused by the non-constant radiation patterns.

Regarding the cost of the feeds, DYQSA has the lowest cost (€8k) compared to the $33k and $15k of Eleven and QRFH antennas respectively [79]. However, from the point of view of the whole system, the low number of LNAs needed for QRFH (two per feed) makes it the lowest cost solution. The overall cost of a system based on DYQSA, including the LNAs, will be around 15% higher than QRFH (the cost of one LNA is around $5k) and less than half the cost of Eleven feed which has the highest number of LNAs per feed.

Table 2.3: Comparison between DYQSA and state-of-the-art UWB feeds

Parameter	**QRFH**	**Eleven**	**DYQSA**
Structure		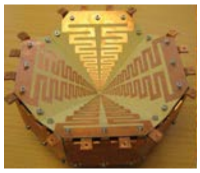	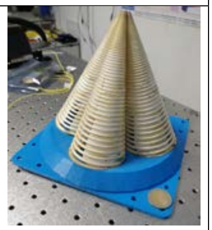
Polarization	Dual linear	Dual linear	**Dual circular**
Frequency range (GHz)	2.2-14	1.2-14	2-14
Aperture efficiency Details in Fig. 2.27	$> 40\%$	$> 40\%$	65%
Adaptability 10-dB half-beamwidth	Adaptable 15°-70°	No 65°	Adaptable 35°-180°
Size (D/H) in mm	160/150	210/65	150/170
Cost	\$15k	\$33k	€8k
LNA per polarization	1	4	2
Calibration signal injection: A)Radiated B)Post-LNA C)Pre-LNA	A/B/C	A/B	A/B

2.5.5. Calibration signal injection

Generally, there are three main methods of calibration signal injection for VGOS feeds: radiating the signal directly into the feed via a small transmitting probe, coupling it into the signal chain after the LNA, or injecting it before the LNA (between the feed and LNA). Although QRFH supports the three methods, the third method is not applicable for DYQSA and Eleven feeds due to the multiple required LNAs. The comparisons summary between the proposed antenna and QRFH/Eleven antennas is shown in Table 2.3 based on data from [12].

2.6. Fabrication and measurements results

The antennas have been manufactured in titanium following a 3D printing growing technique [81] which becomes a promising technique especially for antennas at such frequency ranges where the sensitivity of the fabrication is critical. Then, the feeds are silver plated at the end of the process. As discussed in Sec. 2.3, the first prototype has been manufactured in dielectric-free structure as shown in Fig. 2.29. This design faces some mechanical issues arising from the low vibration tolerances of the system especially at the top of the antenna. This affects the stability of the system and could cause short-circuit problems between the spiral arms at the element apices.

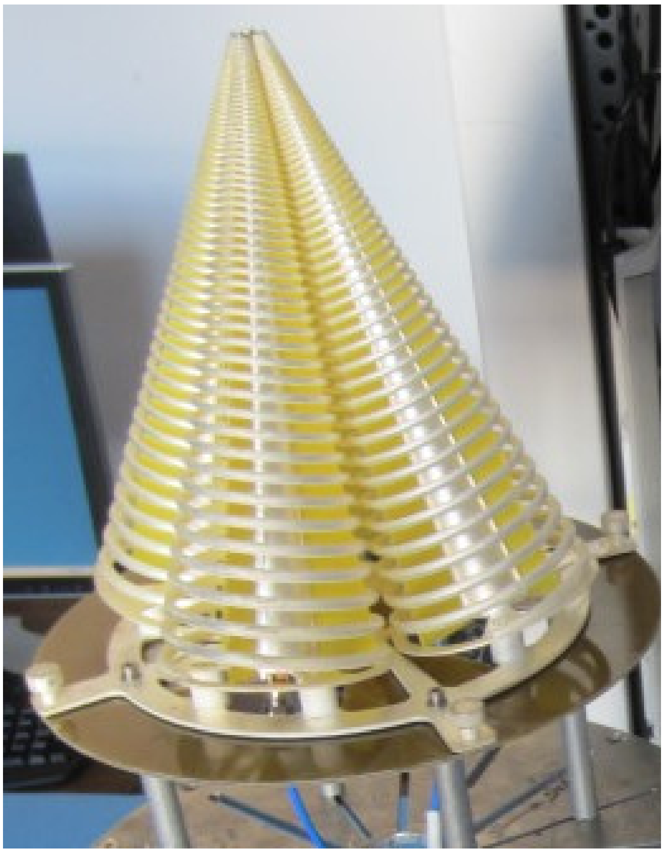

Figure 2.29: Manufactured dielectric-free DYQSA version.

To overcome these mechanical issues, new dielectric-filled prototypes have been proposed [82] where four thin supporting dielectric cones have been used for supporting the structure as shown in Fig. 2.30. This addition significantly enhances the robustness of the system against vibrations and increases the design stability. Also, to keep the same performance of the antennas and avoid any interference in the electric properties, the cones are thin with thickness of 1 mm and are made of a low permittivity durable polyamide (Nylon) material.

It can be seen from Fig. 2.30, the baluns and the metallic cones inside each spiral have been converted to a single baluns system inside the center of DYQSA solution. This new configuration enhances the electric properties of the feed as it reduces the coupling between the metallic shielding and the antennas [83].

Regarding the LNA, to cover the UWB frequency range required by VGOS, several LNAs have been devolved in Yebes Observatory following two main techniques: Monolithic Microwave Integrated Circuit (MMIC) and hybrid amplifiers. Multiple tests have been performed using different transistors in the first stage of hybrid amplifiers. Northrop Grumman Space Technology (NGST) Indium Phosphide-High Electron Mobility Transistors (InP-HEMTs) provide best results in terms of lower noise temperature at such cryogenic temperatures and significantly lower power consumption [84]. Figure 2.31 presents the photograph of the designed hybrid LNA [85].

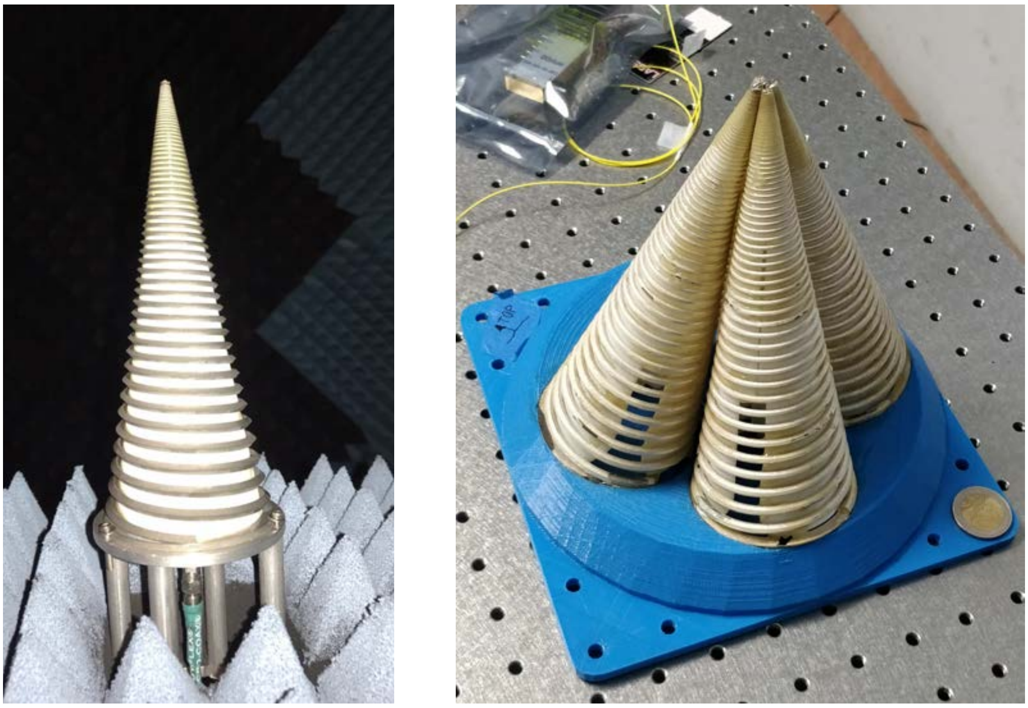

Figure 2.30: Manufactured dielectric-filled prototypes for single-element and DYQSA antennas.

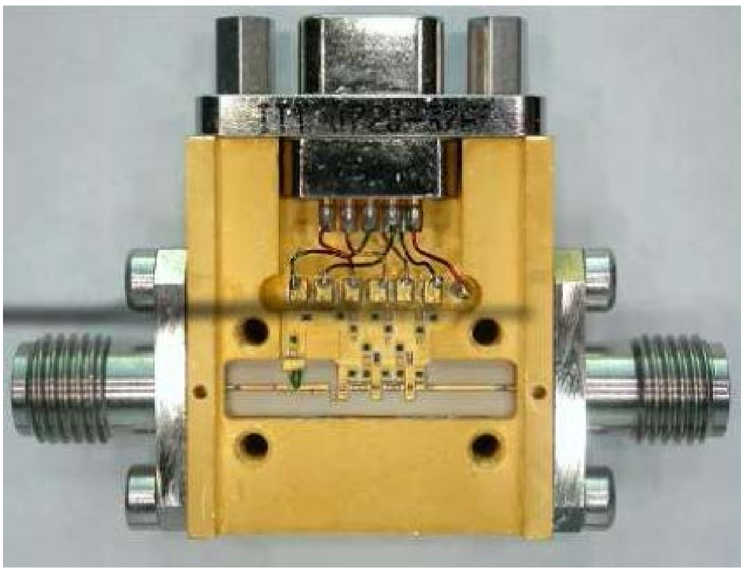

Figure 2.31: Manufactured LNA for VGOS radio telescope.

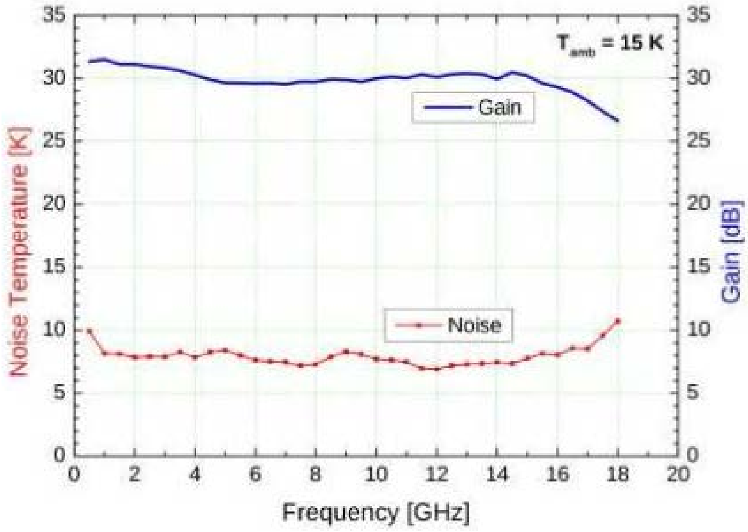

Figure 2.32: Measured cryogenic gain and noise temperature of the manufactured LNA.

Measured results for the LNA under a cryogenic temperature of 15 K present an almost flat gain of about 30 dB over the frequency range from 2 GHz to 14 GHz with an average noise temperature of 7.5 K as shown in Fig. 2.32.

Single-element and array version antennas have been measured at Yebes Observatory and Instituto Nacional de Técnica Aeroespacial (INTA). Figure 2.33 and Fig. 2.34 present the measured radiation patterns of the single-element and the DYQSA antennas respectively for four different ϕ cuts. Both CP components are plotted: RHCP (co-pol) in solid lines and LHCP (cross-polar) in dashed-ones.

The measurements for the single element have been done from 7 GHz to 14 GHz only as proof of the concept. Although the single element provides high level of symmetry between the cuts in its measured radiation patterns with Co/Xp-ratio levels in broadside greater than 15 dB, there is a reduction in the performance for the array version. The rest of this section is dedicated to analyzing the effect of this reduction on the whole reflector system and the possible causes of it.

Figure 2.35 presents the radiation patterns of VGOS radio telescope when the DYQSA is used as the feed for cut planes $\phi = 0°$, $45°$, and $90°$. They indicate the rotational symmetry of the radiation patterns with the Co/Xp-ratio level above 15 dB for the lower band and above 30 dB for the higher one which demonstrates that the small degradation of DYQSA radiation patterns does not significantly affect the overall radiation patterns of the reflector system.

The feed efficiency estimation based on the measured radiation patterns is presented in Fig. 2.36, showing an almost flat performance. The total aperture efficiency is about 70% for the single conical spiral from 7 GHz to 14 GHz, which is in excellent agreement with the simulated results. However, for DYQSA array, the average drops to about 50% over the required bandwidth contrary to the 65% obtained from the simulations.

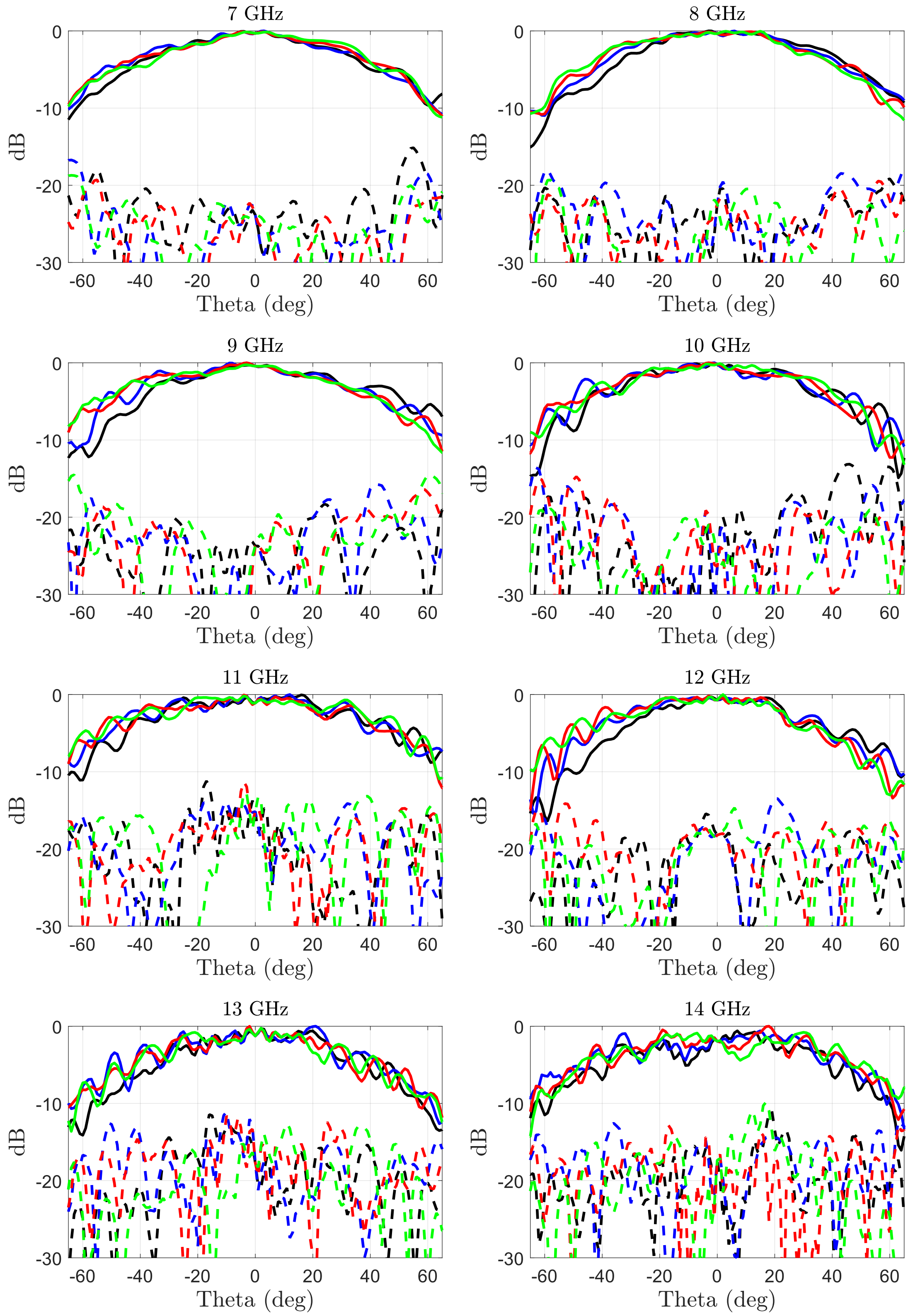

Figure 2.33: Measured radiation patterns of the single-element feed.

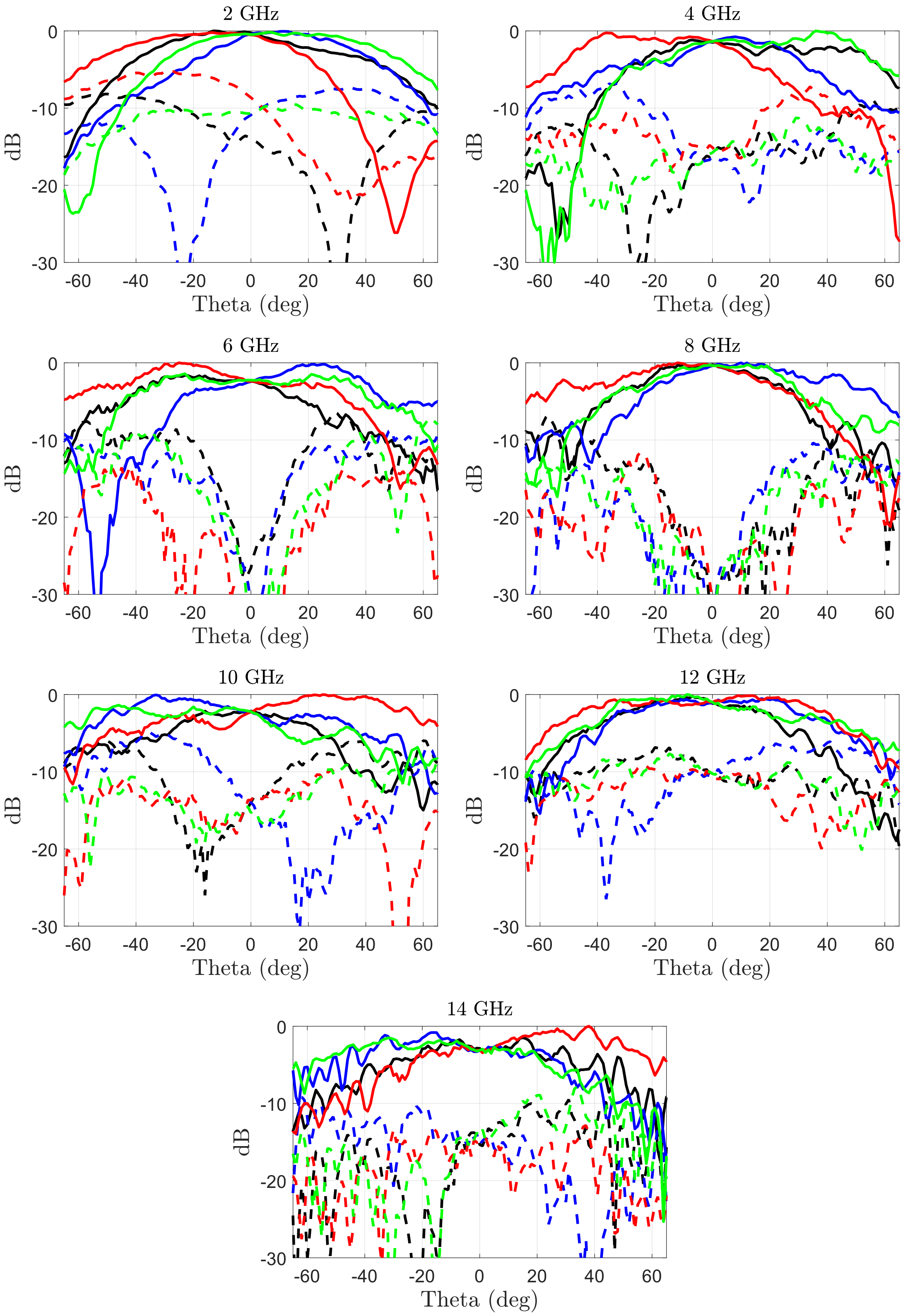

Figure 2.34: Measured radiation patterns of DYQSA feed.

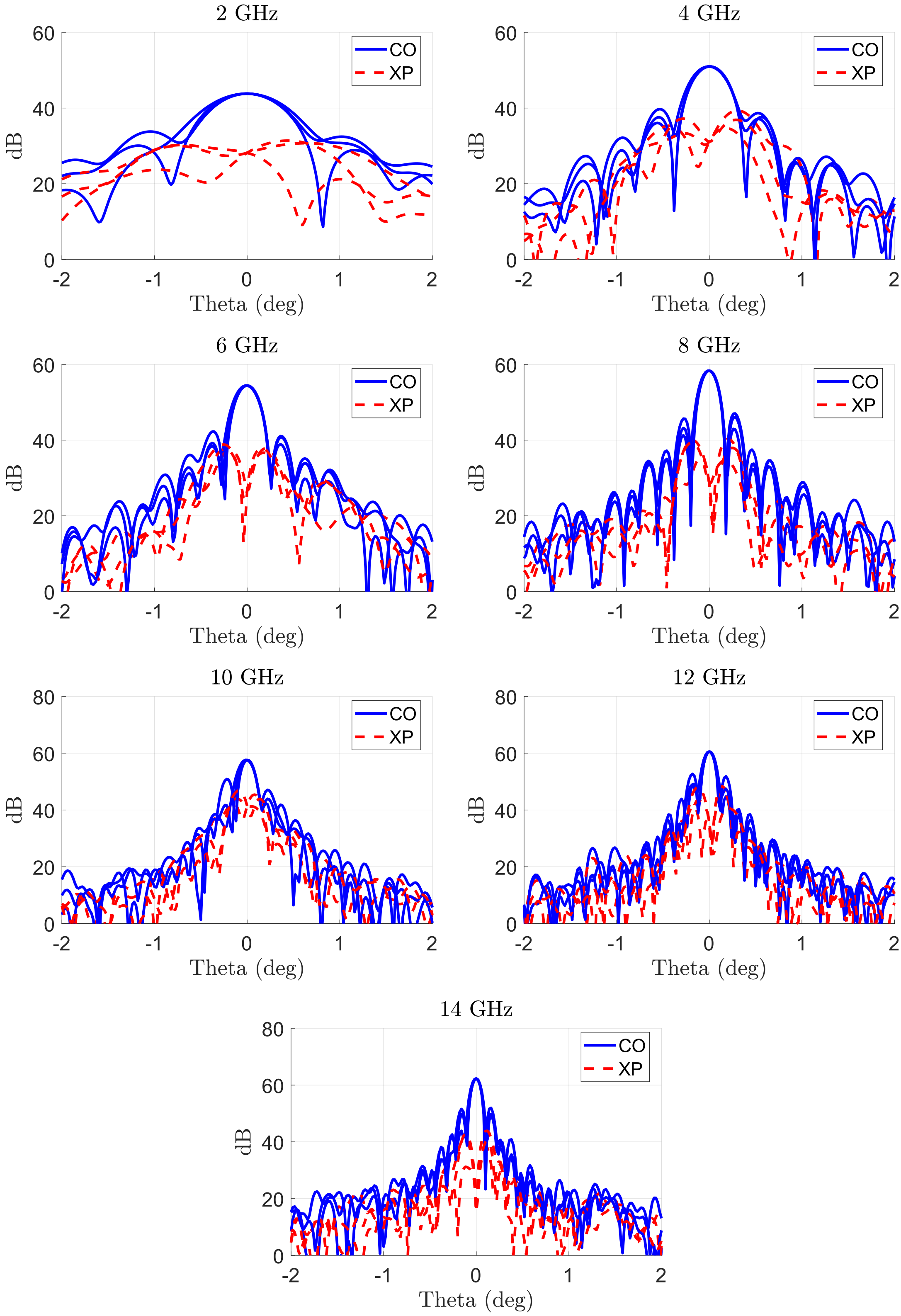

Figure 2.35: Radiation patterns of the reflector based on the measured results of DYQSA feed (the ones in Fig. 2.34).

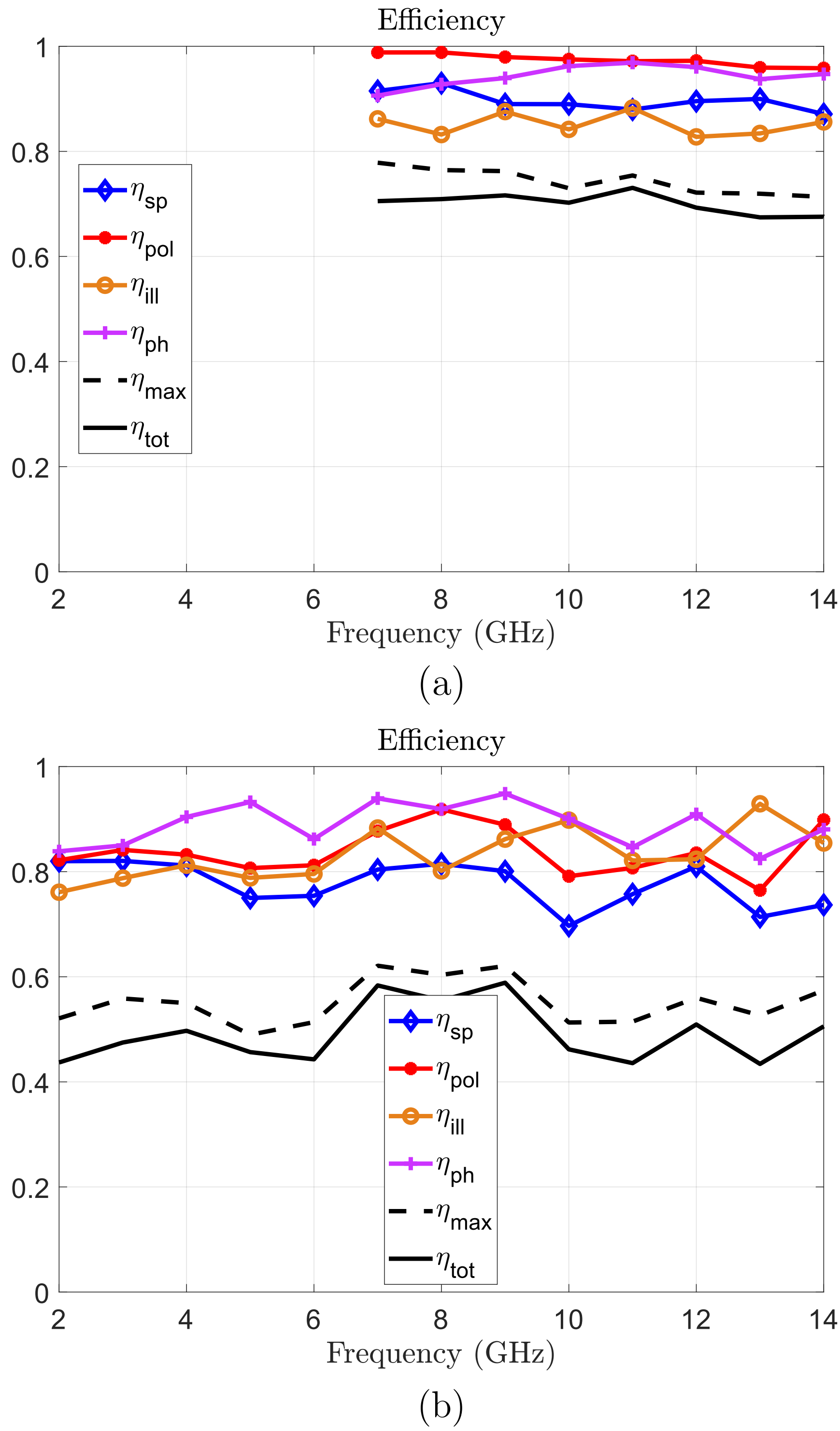

Figure 2.36: Feed efficiency of the radio telescope based on the measured radiation patterns of (a) single-element and (b) DYQSA.

Nevertheless, it is worth noting that these current results outperform the reported measurement results of the state-of-the-art feeds, especially at higher frequencies. For example, in Eleven feed, the estimated efficiency based on the measured radiation patterns drops to about 30% at the higher frequencies [11], [86]. The same for QRFH feed which despite providing an average feed efficiency of 40% over the band from 2 GHz up to 14 GHz, the efficiency at the higher frequencies drops to be around 30% and 15% based on the simulated and measured radiation patterns respectively [75].

2.7. Feed for CryoRad low-frequency Earth observation

As it was mentioned in Sec. 2.5.2, the proposed feeds are easily adapted to different applications. In this section, the results of the single-element feed along with its balun are presented for Earth observation spaceborne missions for the remote sensing of the Earth's cold regions. Recalling the feed requirements shown in Sec. 1.1.2, the feed should cover the low-frequency UWB from 400 MHz to 2 GHz with a pure single CP keeping low weight and physical size. In addition to the comparison to state-of-the-art feeds (Sec. 2.5), conical log-spiral antenna presents the best candidate for these applications too.

The proposed conical spiral antenna proposed in 2.2 is readjusted for this application. Because of the lower frequency her and following the design procedure that was described in Fig. 2.2, the spiral angle can be even further increased without facing problems for the spacing between the spiral arms. So a larger spiral angle $\alpha = 86.5°$ is chosen, then following the required gain above 10 dBi, a corresponding conical angle $\theta = 6.5°$ is selected. Finally with the same design procedure and using these angles, the smallest and largest diameter ($d = 28$ mm) and ($D = 290$ mm) are estimated which are corresponding to a max frequency of 2 GHz of and minimum frequency of 400 MHz respectively. It can be seen that this antenna is of about 4.8 times bigger than the VGOS one which approximately equals to the minimum frequency factor between both applications.

The impedance and axial ratio of the readjusted spiral antenna are presented in Fig. 2.37. As expected from the antenna performance at higher band, it is a flat and almost pure real impedance with excellent pure CP that has axial ratio below 0.75 dB.

The proposed balun for VGOS application is rescaled to be used here, however, at such low frequency range, the physical dimensions of the balun would be large. This in turns would increase the weight of the complete system. To avoid that the balun is optimized to work with shorter length and simultaneously keep the good performance. The optimized balun dimensions (following the nomenclature in Fig. 2.7) are given in Table 2.4. The widths of the input microstrip (W_{m1}) and output parallel strip (W_{m4}) are calculated to provide input and output impedance of 50Ω and 188Ω respectively.

The balun is printed on Duroid5880 ($\epsilon_r = 2.2$) with a relatively larger thickness of 1.575 mm because for the lower thicknesses, smaller strip widths are needed to match the high spiral impedance which require higher accuracy for connecting the balun to the an-

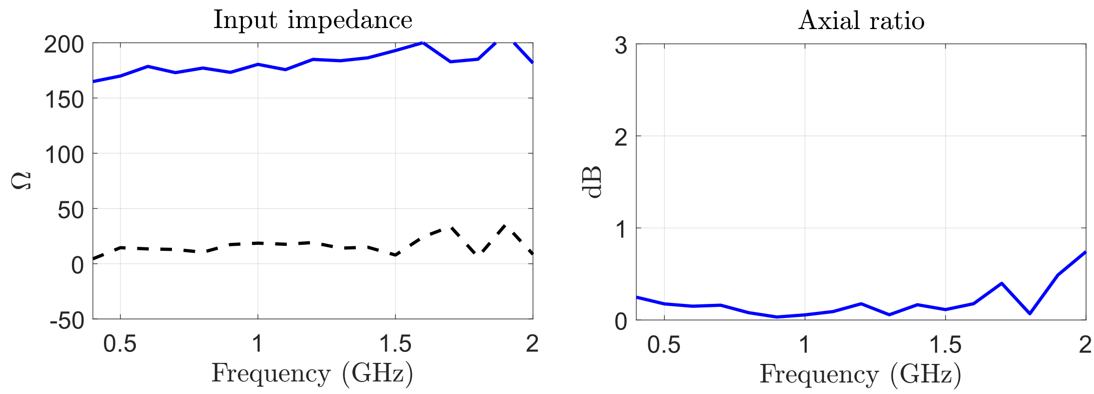

Figure 2.37: Input impedance and axial ratio of the low-frequency spiral.

Table 2.4: Dimensions (in mm) of the low-frequency balun

Parameter	Value	Parameter	Value	Parameter	Value
H_1	5	W_{m1}	4.8	W_{g1}	25
H_2	590	W_{m2}	3.8	W_{g2}	18.8
H_3	15	W_{m3}	0.8	W_{g3}	0.7
		W_{m4}	0.8	W_{g4}	0.8

tenna. Also this relatively larger thickness would provide reasonable performance as there is a trade off between the insertion loss and the amplitude/phase balances of the balun. So lower thickness would provide better balances but higher losses, and the opposite for the much higher thicknesses that would give lower losses but with the cost of higher balances. Figure 2.38a demonstrates the good performance of the balun over the whole frequency range with matching and common mode rejection below 17 dB and 23 dB respectively. The insertion losses are below 0.4 dB which can be even improved more by using thinner substrate.

To keep the pure CP of the antenna, the axial ratio of the balun itself should be decreased too, this can be adjusted by enhancing the amplitude and phase balances as demonstrated in Fig. 2.38b. The balun provides amplitude and phase balances below ±0.37 dB and ±5.5° respectively which is following the approximate estimation in [87] would produces axial ratio below 0.9 dB.

The balun is inserted inside a metallic cone which its dimensions are carefully optimized for keeping the spiral isolated from the balun and achieving better axial ratio values. The proposed complete feed antenna (conical spiral antenna + balun + metallic cone) is sketched in Fig. 2.39. The thin dielectric cone (in green) is included for mechanical supporting for the spiral arms and also can be used in form of flexible substrate so the spiral arms would be printed directly on it to be folded at the end of manufacturing process to form the conical shape. This is because, at such low frequency, tolerances are

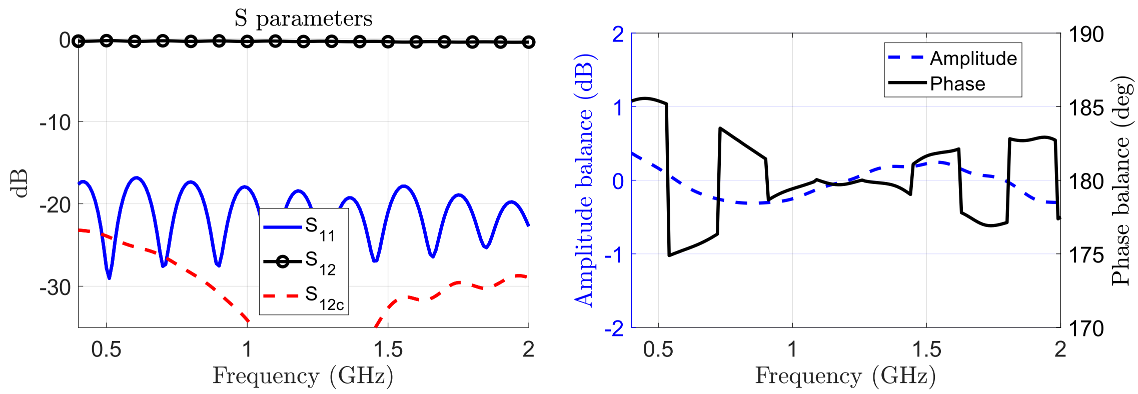

Figure 2.38: Balun performance (a) S parameters, (b) amplitude and phase balance.

not critical, so cheaper planar manufacturing techniques should be used especially that it would provide smaller weight and cost with high scalability.

The performance of the complete feed antenna is presented in Fig. 2.40 and Fig. 2.41 which demonstrate the powerful of such solution with providing stable behavior along the required UWB. For example, matching below 15.5 dB and pure CP with axial ratio below 1 dB are achieved in the while band. Also, regarding the gain, the whole feed provides a flat gain (in solid line) of 10.5 dB and a negligible cross-polar (in dashed line) level with Co/Xp-ratio at broadside ($\theta = 0°$) greater than 25 dB.

Figure 2.42 plots both CP components LHCP (co-pol) in solid lines and RHCP (cross-polar) in dashed-ones for $\phi = 0°, 45°, 45°$ and 135°. It shows how this solution provides stable radiation patterns and a rotational symmetry over the different phi cut planes. This is achieved for all frequencies from 400 MHz to 2 GHz.

2.8. Conclusions and principal remarks

Two UWB circularly-polarized antennas are presented which can be used as feeds for the radio telescope direct VLBI receiver. The proper baluns for exciting these antennas without disturbing the EM performance are discussed. The performance for the receiver including the different components (antenna feed, reflector, and LNA) is analyzed. The two antennas are single-element conical log spiral antenna for achieving single CP, while the other is an array version of four conical spirals (called DYQSA) for having dual CPs (RHCP and LHCP). The design and manufacturing procedures are explained in detail showing how to overcome manufacturing restrictions at such high frequencies which was one of the main limitations for practical implementation of the conical spiral at higher frequencies.

The proposed antennas present pretty similar radiation patterns for all the required frequencies from 2 GHz to 14 GHz with a gain of about 10 dBi. This is in addition to their relatively lower cost and constant with almost real impedance which facilitate the design

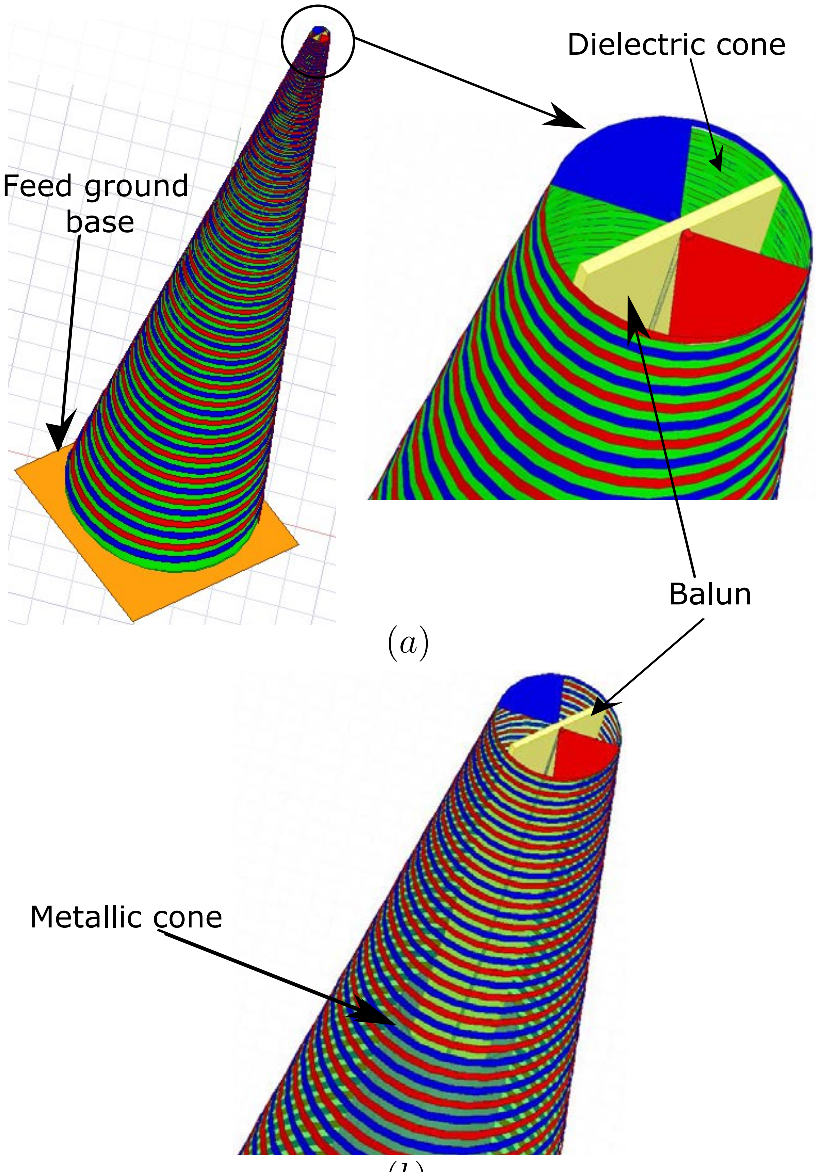

Figure 2.39: Low-frequency complete feed antenna (a) overall and zooming views, (b) internal components.

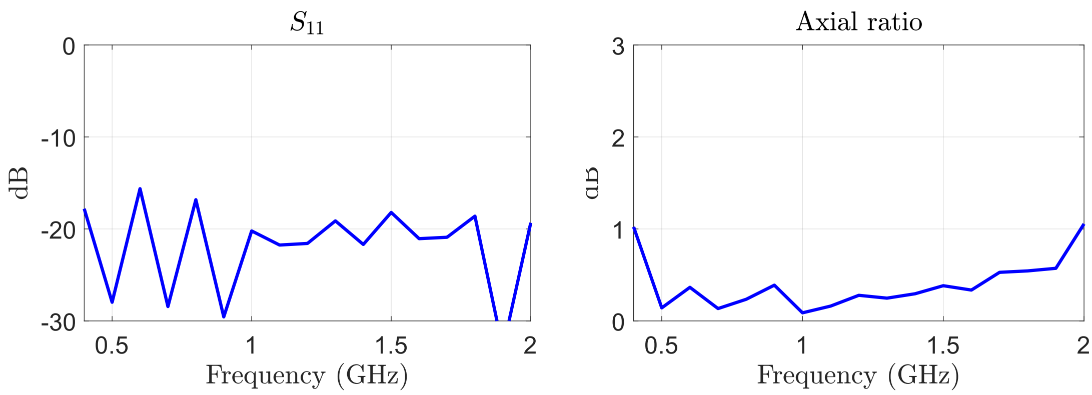

Figure 2.40: S_{11} and axial ratio of the low-frequency complete feed.

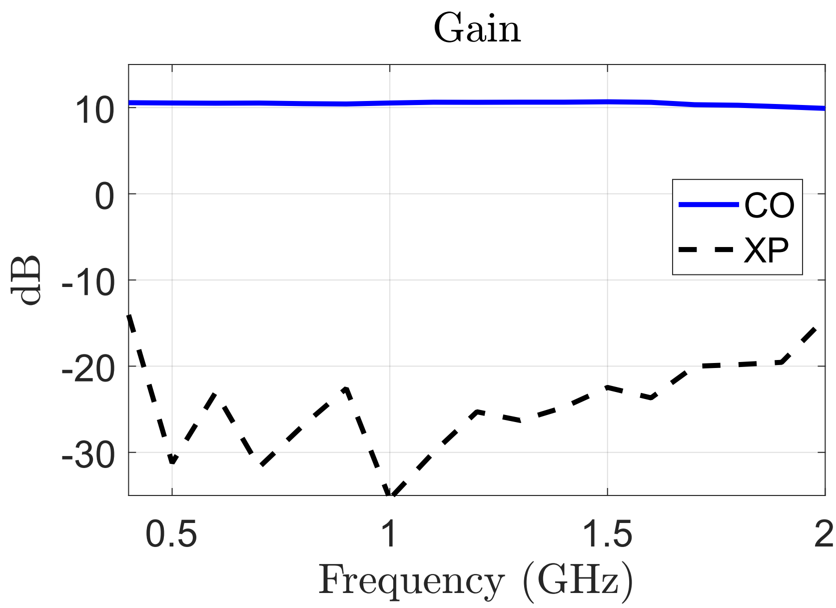

Figure 2.41: Gain vs frequency of the low-frequency complete feed.

of the other receiver components. For each conical spiral, two metallic bow-ties patches are included at the apex to have them ready for connecting to the balun, they can be also used for the direct connection to differential LNAs. A thin dielectric cone is inserted inside the antennas to enhance the mechanical stability specifically at the small top part where the spacing between antenna arms is small. Lastly, a balun (or baluns system) is inserted inside the center of the element (or the center of the array), it is covered by a metallic shielding cone to enhance the electric properties and prevent it from disturbing the antenna performance.

Regarding the single-element conical spiral solution, it has an excellent axial ratio below 1.4 dB. Its designed balun shows excellent results too with low losses below 0.5 dB, common-mode isolation below −30 dB, and good matching below −16 dB. When it is integrated with the VGOS radio telescope, it provides stable CP radiation patterns over the whole band with Co/Xp-ratio larger than 23 dB at the broadside. It enables the reflector to have a high directivity above 45 dB which is comparable to the reflector performance once it is fed by an ideal Gaussian beam.

Regarding the DYQSA solution, its axial ratio is below 2.5 dB with small phase center variations. Its balun array excitation system has low losses below 0.5 dB with good matching, common-mode rejection, and isolation between the ports of 15 dB in most of the band. Besides, when it is used to feed VGOS radio telescope, the proposed DYQSA solution enables the reflector to have high directivity as in the case of the single spiral antenna with a very small difference below 1.2 dB with comparison to the ideal Gaussian beam. The radio telescope fed by DYQSA provides an average spillover and antenna noise temperature of about 6 K and 14 K respectively when it points near the zenith. The noise temperatures face a small degradation of about 7 K when the radio telescope points

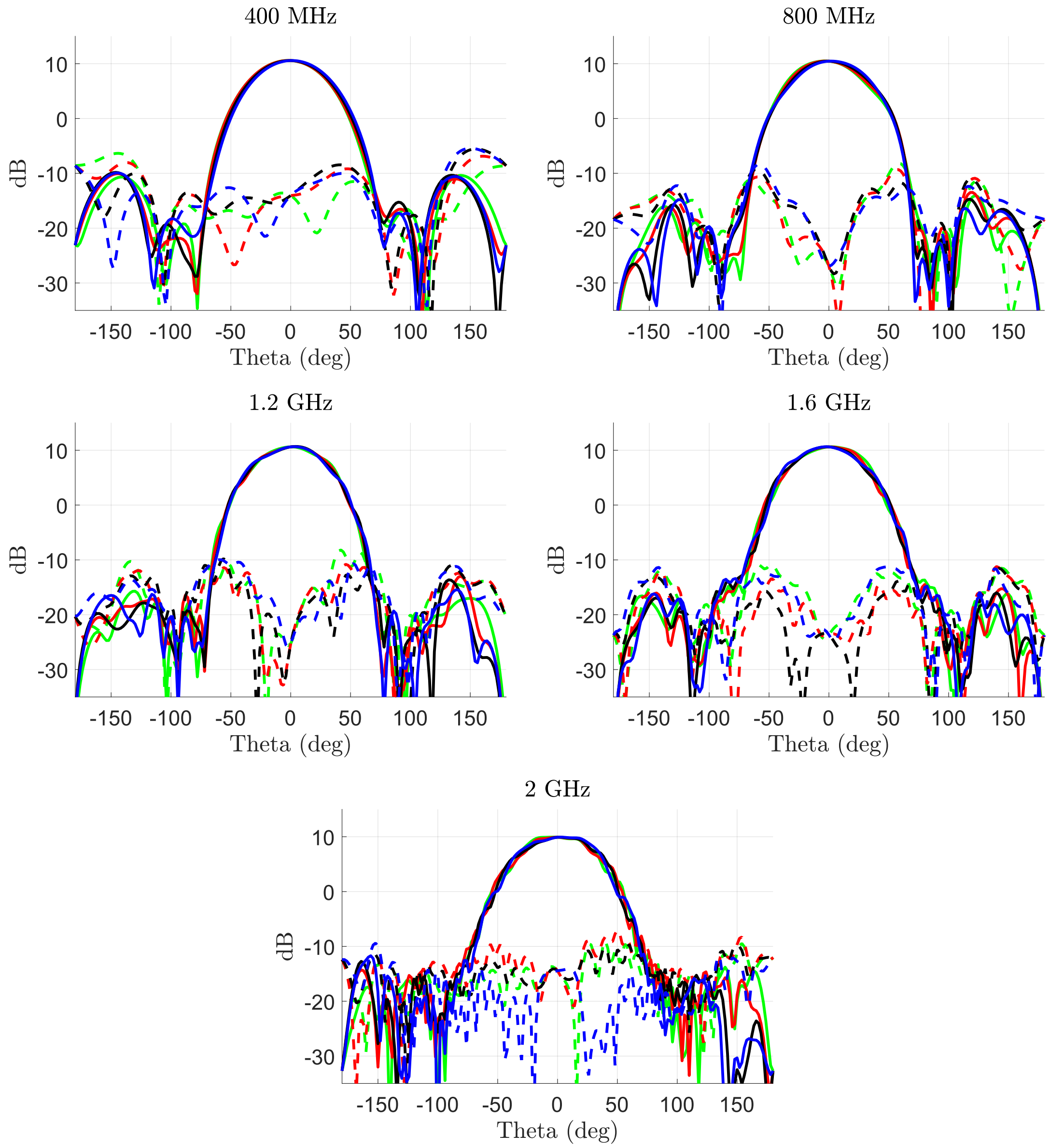

Figure 2.42: Radiation patterns of the low-frequency complete feed.

at further angles (for example, at a zenith angle of 45°). Including the noise temperature from the LNA designed by Yebes Observatory for VGOS radio telescope and other noise sources (calibration coupler, ohmic losses, and cables), the proposed DYQSA enables the receiver to have a SEFD of about 1300 Jy and 1600 Jy at zenith angles of 0° and 45° respectively.

The proposed design and the two main state-of-the-art UWB feed solutions (QRFH and Eleven) have been compared from different points of view. It can be concluded that DYQSA provides a direct CP without the need for either additional analog hardware or digital software that are used for linear-to-circular polarization converting. Also, it has the lowest cost with comparable size. From the critical total feed efficiencies point of view, this comparison demonstrates the frequency-independent behavior of DYQSA with an efficiency of $65 \pm 5\%$, contrary to the linear reduction for the other two solutions at high frequencies. Additionally, it is adaptable for a wide range of beamwidths which enables it to be used for different applications. These results show the potential of the proposed antennas as new candidates for future radio telescope feeds and many other CP UWB applications.

The two antennas are 3D manufactured in titanium with a thin Nylon supporter cone inside each conical element. The measurement results have a good level of agreement with the simulated ones. Based on the measured radiation patterns of the isolated antennas, VGOS radio telescope has good CP radiation patterns over the whole frequency range with a Co/Xp-ratio above 15 dB. The average aperture efficiencies are 70% for the frequencies range from 7 GHz to 14 GHz for the single-element with a small reduction in the DYQSA efficiency results to be 50% averaged over the entire band from 2 GHz to 14 GHz.

Regarding the second application in this chapter, a complete feed solution consisting of conical log-spiral antenna, balun, and metallic cone is provided for covering the requirements of the CryoRad Earth observation missions. The simulation results present stable radiation patterns over all the required UWB from 400 MHz to 2 GHz with pure CP which has an axial ratio below 1 dB over the whole band and flat high-gain of 10.5 dB. Moreover, the design provides low return and isolation losses keeping the compact size and low weight which all make it suitable for satellite installation.

3. UWB INTEGRATED THZ ANTENNA ARRAY

3.1. Introduction

In this chapter, an alternative to the previous proposed 3D UWB antennas for direct radio astronomy receivers, here, planar UWB THz sources are presented for both transmitter and heterodyne receivers. This THz source consists of a combination between antenna and photomixer which is widely defined by Antenna-based Emitter (AE). As a solution for the demand request to increase the radiated power of THz sources, UWB planar array consists of self-complementary bow-tie antennas with photomixers is presented. The array is called the Chessboard array following the resulting metal shape of joining the elements together in an optimized element- distribution with small element spacing [88] To demonstrate the easy extension of the solution for different frequency ranges in both THz and mm-wave bands, three arrays which cover UWB ranges from 200 GHz to 2 THz, from 100 GHz to 1 THz and from 50 GHz to 0.5 THz [61] are shown. These planar antennas can be integrated into a dielectric lens to significantly increase its directivity (and in terns the its radiated power), in case the proper lens dimensions are chosen, which is an alternative for reflector structures that is presented in Chapter 2.

Compared to the standard THz horn antennas working at a similar range, it can be seen how these solutions outperform horn antennas from different point of views. For instance, compared to the first array, the horn needs to be fed by WR3 which makes it cover a dramatically smaller BW from 220 GHz to 330 GHz. Furthermore, the proposed antenna is capable of providing very high directivity above 35 dBi with antenna dimensions of $6\lambda_{min} \times 9.3\lambda_{min}$, where λ_{min} corresponds to the minimum frequency of the UWB. This is along with the possibility for extending it to a larger number of elements without a corresponding increase in the fabrication/alignment complexity in case higher directivity is needed. From this perspective, horn antennas need a much larger dimensions for achieving such a high directivity, for example, horn antenna with a length of 75λ and a diameter of 15λ is needed for having a directivity of 30 dBi [89].

Additionally, an investigation of the metal resistive losses in THz planar antennas is performed over a frequency range from 100 GHz to 800 GHz. This is critical because it is one of the main reasons for the reduction in the radiated THz power for such kinds of THz sources which has rarely been analyzed in THz devices. This study compares two cases, one case considering the antenna metal as a pure gold which is the common assumption by most THz antenna designers and the other by measuring the actual metal resistivity and considering it in the losses estimations. To better interpret the observations, different metal thicknesses are considered with showing their relations to the skin depth of both metals. Also, the study is extended to include two common THz antenna types which are square spiral and log-spiral antennas.

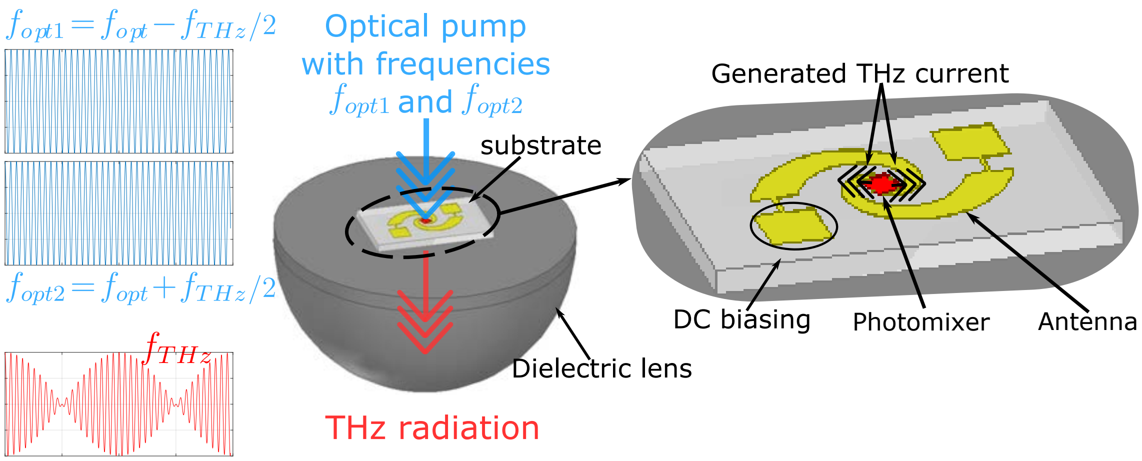

Figure 3.1: The working principle of THz source based on photomixer.

3.2. UWB Chessboard antenna array

3.2.1. Working principle for antenna-based emitter THz source

Continuous-Wave (CW) THz generation using photomixers and planar antennas excited by two optical laser sources has been reported in the early 1990s by Prof. Elliott R. Brown and his group at MIT [90], [91], [92]. The working principle is based on mixing two CW frequency-offset pump lasers which are spatially overlapped (or dual-mode laser [93]) then focusing them into an ultra-fast semiconductor material such as Indium Phosphide (InP) or Gallium Arsenide (GaAs). Once the Gaussian optical beam hits the semiconductor, the material conductivity would be altered due to the photonic absorption and short charge lifetime [90]. Then an Alternating Current (AC) based on the conductivity modulation is generated when a large electric field is applied (utilizing electrodes), this current has a frequency that equals to the two lasers' frequency difference. The photomixer is connected to a planar antenna which will radiate a CW THz signal proportionately to the generated current.

Figure 3.1 summarizes the working principle of the AE showing the electric field for the two input optical signals and the output THz signal. By default, the BW of the photomixer itself is so wide due to the ultra-fast nature of its impulse response function [94]. This is the reason that usually, the antenna of the AE is a self-complementary one to be able to cover a wide frequency range which is required for most of the THz applications [95].

The main limitation of the photomixers is the low generated power (P^{gen}_{THz}) which is proportional to the square of the generated THz current. Also, increasing the optical pump power is not practical as they have a fixed tolerable dissipated power level. Moreover, not all of this power is radiated into free-space, as a consequence, the efficiency of an AE can be defined as the ratio of the radiated THz power (P^{rad}_{THz}) per the generated power

($\eta_{AE} = P^{rad}_{THz}/P^{gen}_{THz}$). As the permittivity of photomixer material (which is the antenna substrate too) is relatively high of about 12, the efficiency of the plain AE is estimated to be smaller than 30% [96]. The exact value depends on several parameters such as substrate thickness, antenna type, and frequency.

The physical reason behind such low efficiency is that most of the power is trapped in the high permittivity substrate in the form of surface waves due to Total Internal Reflection (TIR) as can be seen in Fig. 3.2a [97]. This happens when the waves have an incident angle (θ) greater than the critical angle (θ_c) between the lens medium and free-space. For example, assuming that the lens has a permittivity of 12, therefore, only a fraction of the waves which have incident angles below $\pm 16.8°$ would be transmitted to the air. As the angle range is small, this fraction would be small too and the majority of the power will be trapped in the substrate. Because of this, the AE is placed on a relatively-large dielectric lens with closer permittivity values to the substrate (such as Si) and has a shape that enables it to avoid the substrate modes. This will focus the beam towards the dielectric side as depicted in Fig. 3.2b and produce unidirectional radiation with high directivity.

Although such hemispherical shapes would prevent the lens from having TIR, still the antenna needs to have a higher directivity to increase the radiated power, so different lens shapes are needed to be used. One of the common shapes of these dielectric lenses is the extended-hemispherical (Fig. 3.2c) which collimate the rays [98]. This subsequently will significantly increase the antenna's directivity depending on the lens dimensions (diameter D and length T). Hence, a higher AE efficiency of about 85% can be achieved. The extended-hemispherical is commercially known as bullet lens (or collimating lens) if the edges of the extension part are flat or as hyper-hemispherical lens if they have a curvature with the same diameter (D).

3.2.2. AE array structure

Although the extended-hemispherical dielectric lens can provide high directivity as will be shown later in this Chapter, the AE radiated power is still limited by the power that the photomixer can generate (hundreds of nW up to a few μW [99]). To solve such limitation, a novel integrated AE array has been developed by combining several photomixers which, as described in Fig. 3.3, each photomixer (the red circle) is connected to a balanced bow-tie antenna. Such self-complementary antennas with UWB performance with stable radiation patterns over the band and high symmetric between E- and H-planes.

This array will enhance the antenna directivity in addition to increasing the generated THz power [100]. The unit element of the AE array is shown at the right of Fig. 3.3 which has pitch sizes of P_x and P_y. These pitch sizes can be easily readjusted to have the antenna working on different operation bands with similar performance [88]. The distance between the elements is set to be electrically small (less than $0.05\lambda_{min}$) as in this case, the mutual coupling is purposefully increased which causes a constructive interference that helps the antenna performance especially in terms of side lobe levels. Also, such high-

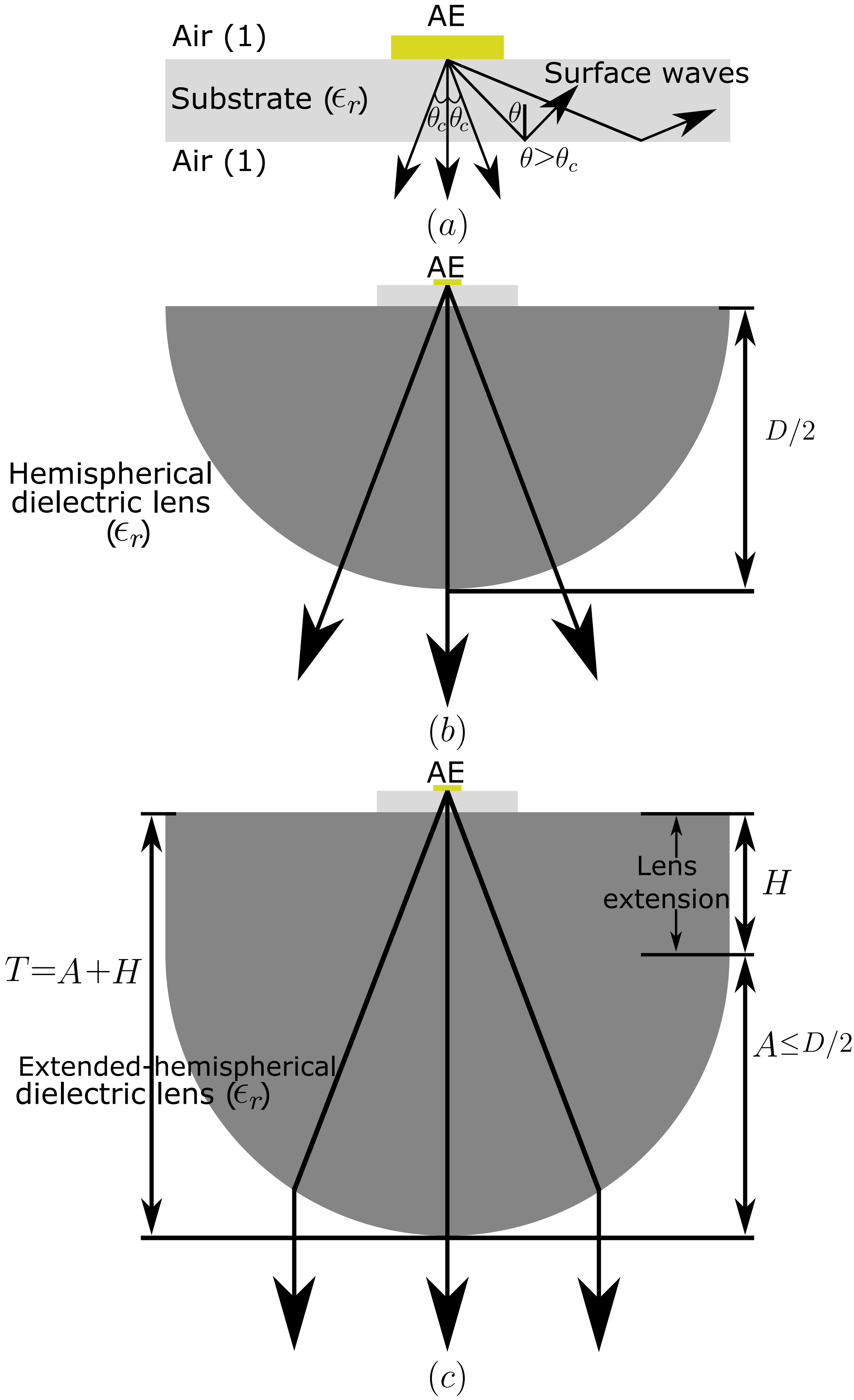

Figure 3.2: Ray tracing for THz AE, (a) without lens, (b) with hemispherical lens, and (c) with extended-hemispherical lens.

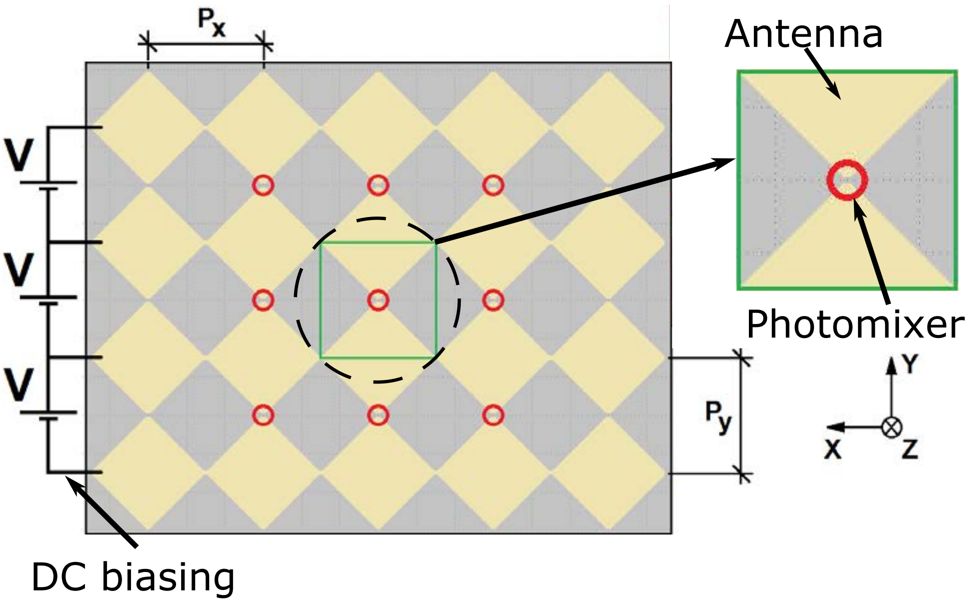

Figure 3.3: Chessboard array of 3×3 AE elements.

density and compact distribution of elements avoid the out-of-focus problem [101] for the edge photomixers in case only one electrically-large Si lens is used.

The array consists of 3×3 AE made of InP substrate, the two extra columns of passive bow-tie antennas have been added for avoiding truncation effects in the array and to act as biasing pads too. A proper biasing is granted by exciting each row of the array with the same voltage gap (V). The value of this voltage is set to have the row-to-row voltages equal to the required bias voltage for the photomixer. In this way, all devices will have the same Alternating Current (DC) biasing with a simple biasing setup.

To ensure mutual coherent properties for all of the photomixers [102], all of them should be excited by the same laser pump. This is performed by using a microlens array in which each small lens focuses the beam towards its corresponding element as shown in Fig. 3.4. So the optical signal (in blue) is coming from the laser pump passing through a microlens array which is responsible for focusing the optical beams on the 2D photomixer rectangular array. This enhances the illumination efficiency as it focuses the beam to the needed places only and avoids the illumination of non-active areas. Then it is the rule of the bow-tie antennas (the ones in yellow) to radiate the THz signals into the free space through the Si lens.

Standard C-band CW 1550 nm optical pump laser is used here for three reasons. Firstly, it enables the photomixer to provide a four-time higher THz power compared to 780 nm (under using the same pump power) as it has a doubled relative photon flux. Secondly, it has the lowest loss in the Telecom optical band. Finally, for the lower cost and easy availability.

At such high THz frequencies, especially at the end of the frequency range, available

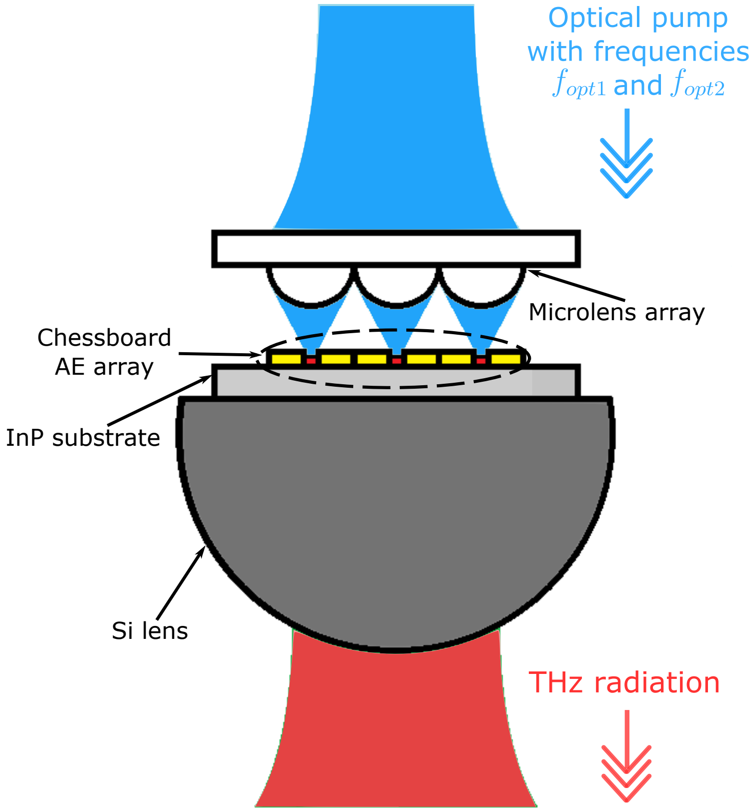

Figure 3.4: Sketch of the chessboard array with its assembly.

dielectric lenses are too thick in terms of the wavelength as the diameter can arrive to tens or 100 of λ_{max}, where λ_{max} corresponds to the maximum frequency of the UWB. Knowing that the planar antennas are typically smaller than 1 or 2 λ_{max}, the simulation of the whole AE (AE plus lens) is much heavier and requires greater computational sources and time consumption in case accurate results are needed. All these would reluctance the designing process of the lens despite that it has significant effects on the antenna's performance as will be shown later in Sec. 3.3. Therefore, following [103], an alternative method can be used to speed up the simulation process with keeping accurate results.

This hybrid method implies two steps, firstly, designing the planar antennas lying over semi-infinite substrate via a full-wave EM simulator to operate in the required band. Secondly, using their radiated fields as input to a ray tracing and PO custom program developed in [103]. This program is working under the assumption that the lens surface is in the far-field region of the planar antenna which is usually true due to the electrical-large size of the lens.

In Sec. 3.3, the simulated results of three arrays for operating at different mm-wave and THz ranges would be provided. Each of them covers a UWB of 10:1 (a percentage BW of about 165%). Tens of commercial extended-hemispherical Si lenses with different dimensions have been tested for achieving better antenna performance in terms of directivity, front-to-back ratio, and side lobe levels. For simplicity, the best cases are only

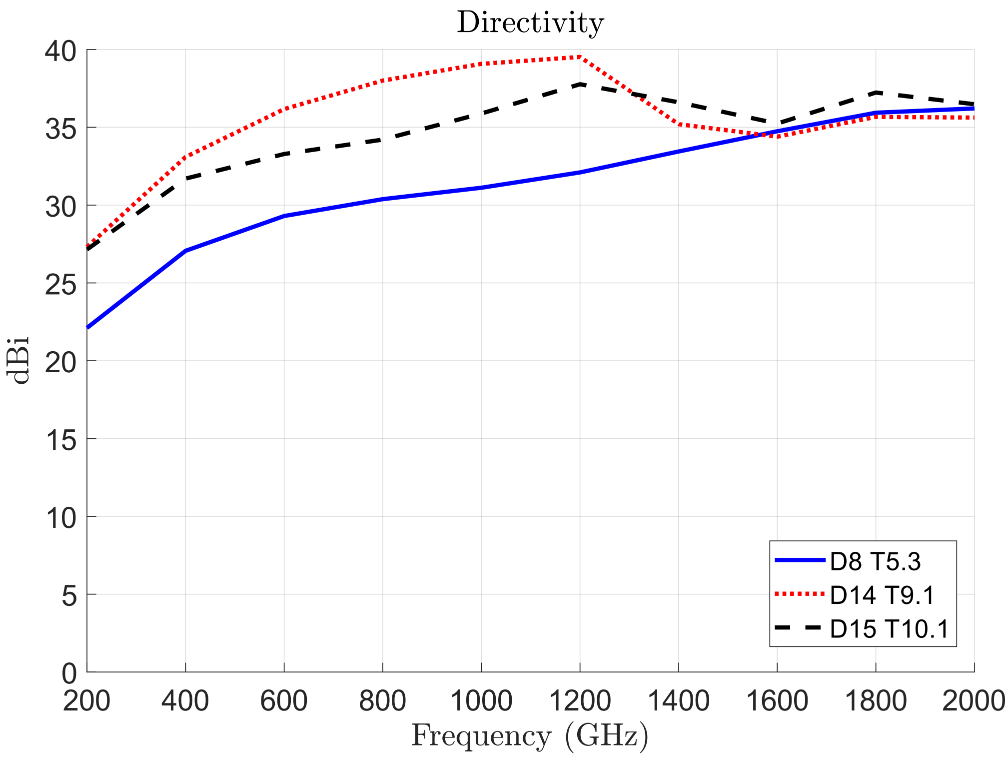

Figure 3.5: Directivity for the first Chessboard array.

reported with highlighting the lens diameter (D) and thickness (T) (both in mm) for each case.

3.3. Simulation and measurement for different Chessboard arrays

For the first Chessboard array, the pitch sizes are adjusted to be $P_x = P_y = 57\,\mu$m (corresponding to $0.038\lambda_{min} \times 0.038\lambda_{min}$) which enable the antenna array to cover a UWB from 200 GHz to 2 THz. Figure 3.5 presents the directivity of the array using the best commercial extended-hemispherical lenses.

It can be seen that the second and third lenses (dotted-red and dashed-black lines) provide comparable results with an average directivity of about 35 dBi. This is around 5 dB better compared to the results obtained using the first lens (solid-blue) which its smaller size affects the antenna performance at the lower frequency range. This is because at such frequencies, the lens extension thickness is comparable to the electrical length (H is less than a λ_{max}) so the lens acts more as a hemispherical lens instead of an extended-hemispherical one. This makes the antenna radiates wider beams as was presented in Fig. 3.2b instead of the focused ones (Fig. 3.2c). As a consequence, there is a linear increment in directivity vs frequency so better results can be obtained at higher frequencies where the lens extension thickness is much larger than the electrical lens and hence, all three lenses have similar directivity at this range.

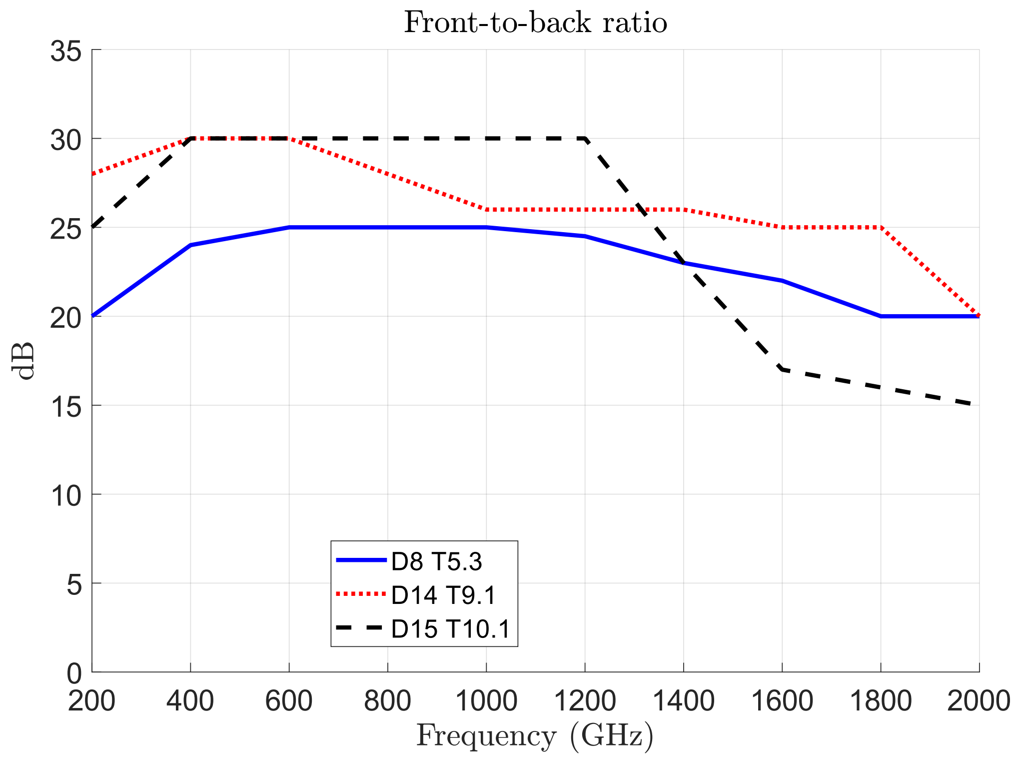

Figure 3.6: Front-to-back ratio for the first Chessboard array.

Although second and third lenses provide comparable directivity over the whole band, Fig. 3.6 shows that increasing the lens size (as in the third lens) has a negative effect on the front-to-back ratio in the range from 1.4 THz to 2 THz. This makes the medium-size lens (the second one) the preferable option of the three lenses (and of the other tested ones) for this array.

The radiation patterns of the array in case the second lens is used ($D = 14$ mm and $T = 9.1$ mm) are presented in Fig. 3.7 and Fig. 3.8. The cross-polar radiation patterns are omitted here for simplicity as they are negligible, which is expected for this antenna topology as it is belonging to the dipole family which has orthogonal E-plane and H-plane polarizations. The antenna provides stable radiation patterns along the whole UWB range from 200 GHz to 2 THz for both phi=0 and phi=90 corresponding to E- and H-planes respectively with low side lobe levels below -20 dB in most of the band. The narrow single lobe observed along all the frequencies confirms the constructive interference for such compact and high-density solution and that it does not suffer from the out-of-focus problem.

For the second array, the pitch size is doubled ($P_x = P_y = 114\,\mu$m) to shift the lowest cut-off frequency towards lower frequencies (100 GHz instead of 200 GHz) with keeping the same UWB 10:1 BW. Figure 3.9 shows the antenna array directivity considering the best two commercial extended-hemispherical Si lenses.

The first lens has diameter of 10 mm and thickness of 7.5 mm while the other has

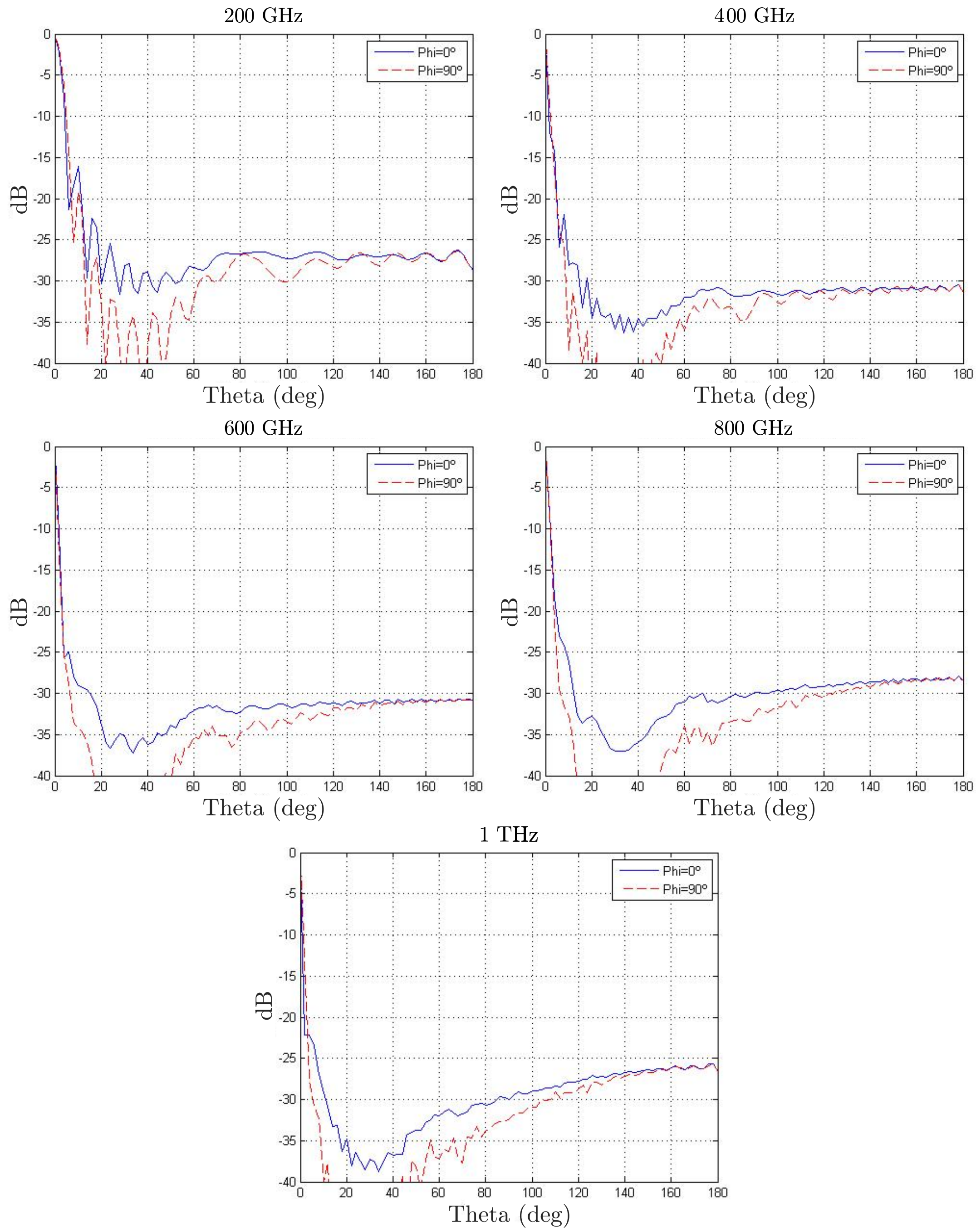

Figure 3.7: Radiation patterns for the first Chessboard array from 200 GHz to 1 THz.

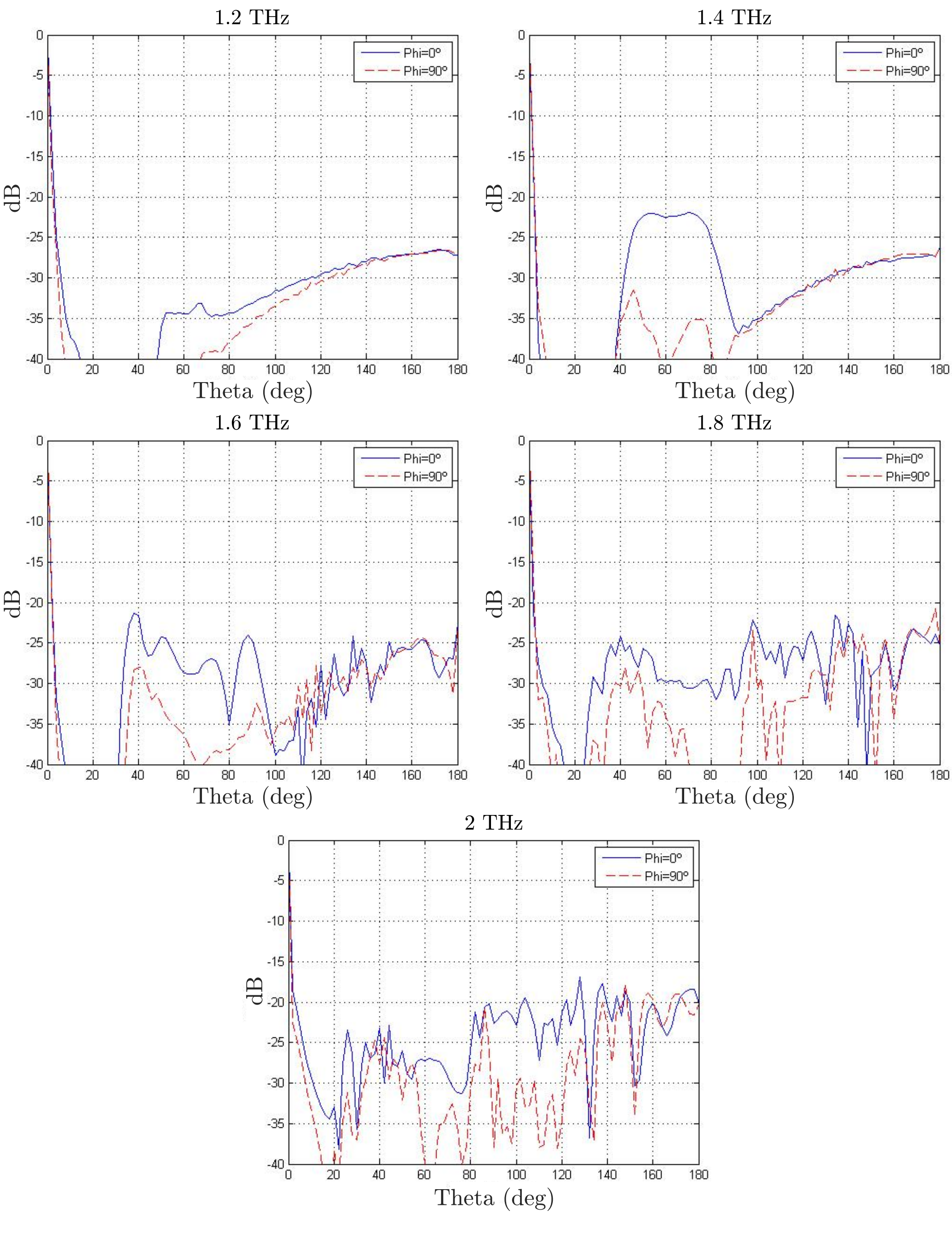

Figure 3.8: Radiation patterns for the first Chessboard array 1.2 THz to 2 THz.

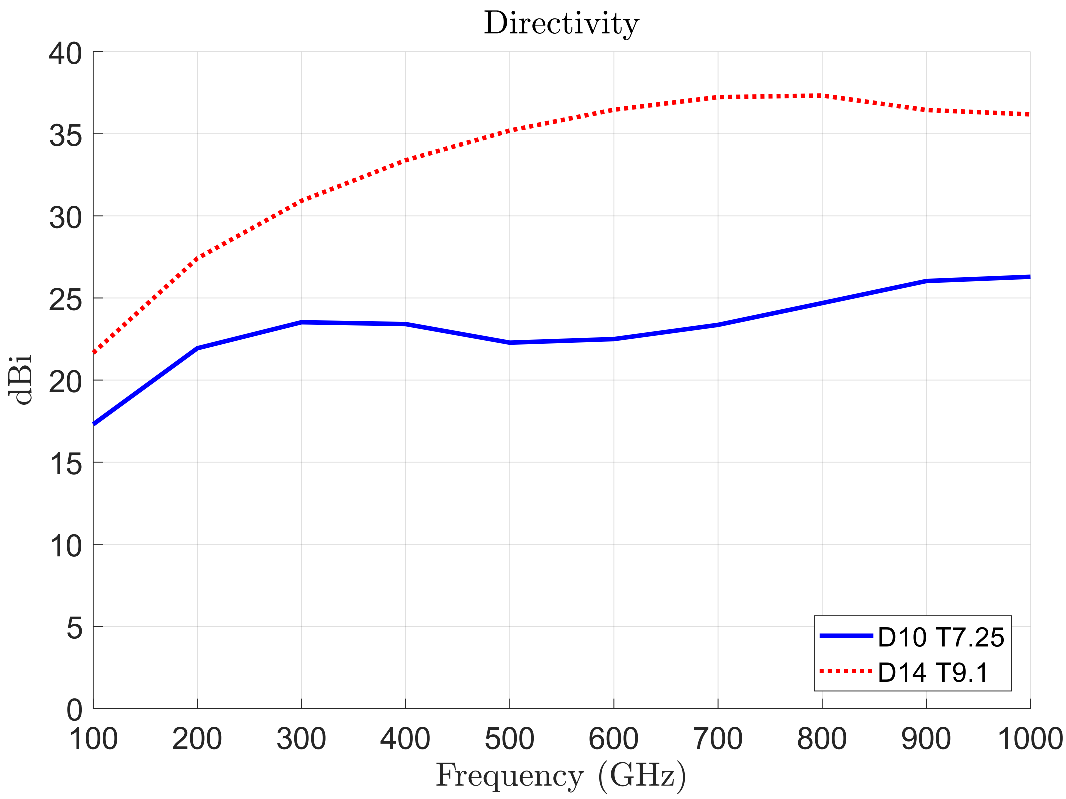

Figure 3.9: Directivity for the second Chessboard array.

larger dimensions of 14 mm and 9.1 mm respectively. This study clearly illustrates how the selection of the dielectric lens is so critical for THz AE. As for the same antenna, while the inclusion of the first lens makes the antenna produce an average directivity of 23 dBi, the obtained averaged directivity using the second lens is significantly higher (of about 33 dBi).

So the increase in the lens size by a factor of 30% enhances the directivity ten times, but this in the cost of losing the flatness front-to-back ratio as presented in Fig. 3.10. Nevertheless, the significantly higher directivity for the second lens makes it more suitable especially that its front-to-back ratio is still acceptable (above 15 dB) in most of the band.

Figures 3.11 and 3.12 describes the antenna radiation patterns using the second lens (D = 14 mm and T = 9.1 mm). Similar to what was shown for the first array, this one provides also symmetric and stable radiation patterns for the whole UWB frequency range. However, the side lobe level is slightly degraded to an acceptable level that is below −15 dB for both E- and H- planes along with the whole band.

The third array has a larger pitch size of $P_x = P_y = 227\,\mu$m to be able to cover a frequency range from 50 GHz to 0.5 THz. For this study, two commercial extended-hemispherical Si lenses are used which have diameters of 24 mm and 25 mm with thicknesses of 15.3 mm and 15.8 mm. The directivity for the third array is shown in Fig. 3.13. The smaller lens (the first one) has a slightly better directivity of about 27 dBi compared

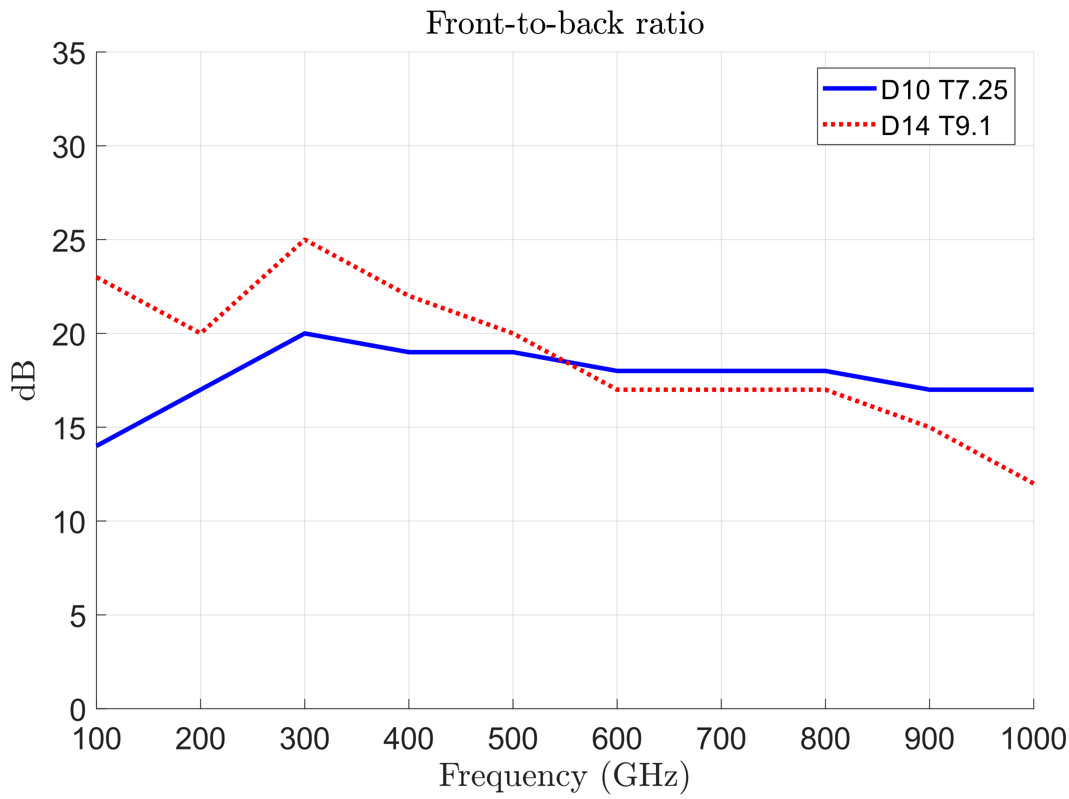

Figure 3.10: Front-to-back ratio for the second Chessboard array.

to 25.5 dBi in the case of using the second lens.

Regarding the front-to-back ratio, both lenses provide comparable results with a level higher than 20 dB and 17 dB for the first and second halves of the frequency band as shown in Fig. 3.14. Generally, this array has lower directivity compared to the previous two arrays (with frequencies up to 1 THz and 2 THz) because of the limitation of the maximum lens size forced in these studies. So better results can be achieved in case such limit is relaxed and larger lenses are allowed to be used.

For obtaining the antenna radiation patterns, the smaller extended-hemispherical lens (D = 24 mm and T = 15.3 mm) is used. As expected from the previous results, the array provides stable radiation patterns for both planes over the whole band as shown in Fig. 3.15 and Fig. 3.16. It is also slightly better side lobe level below −25 dB in most of the band.

The fabrication of a prototype of the proposed THz source along with detailed explanations for the complete assembly and measured THz radiated power would be shown in Sec. 3.4.

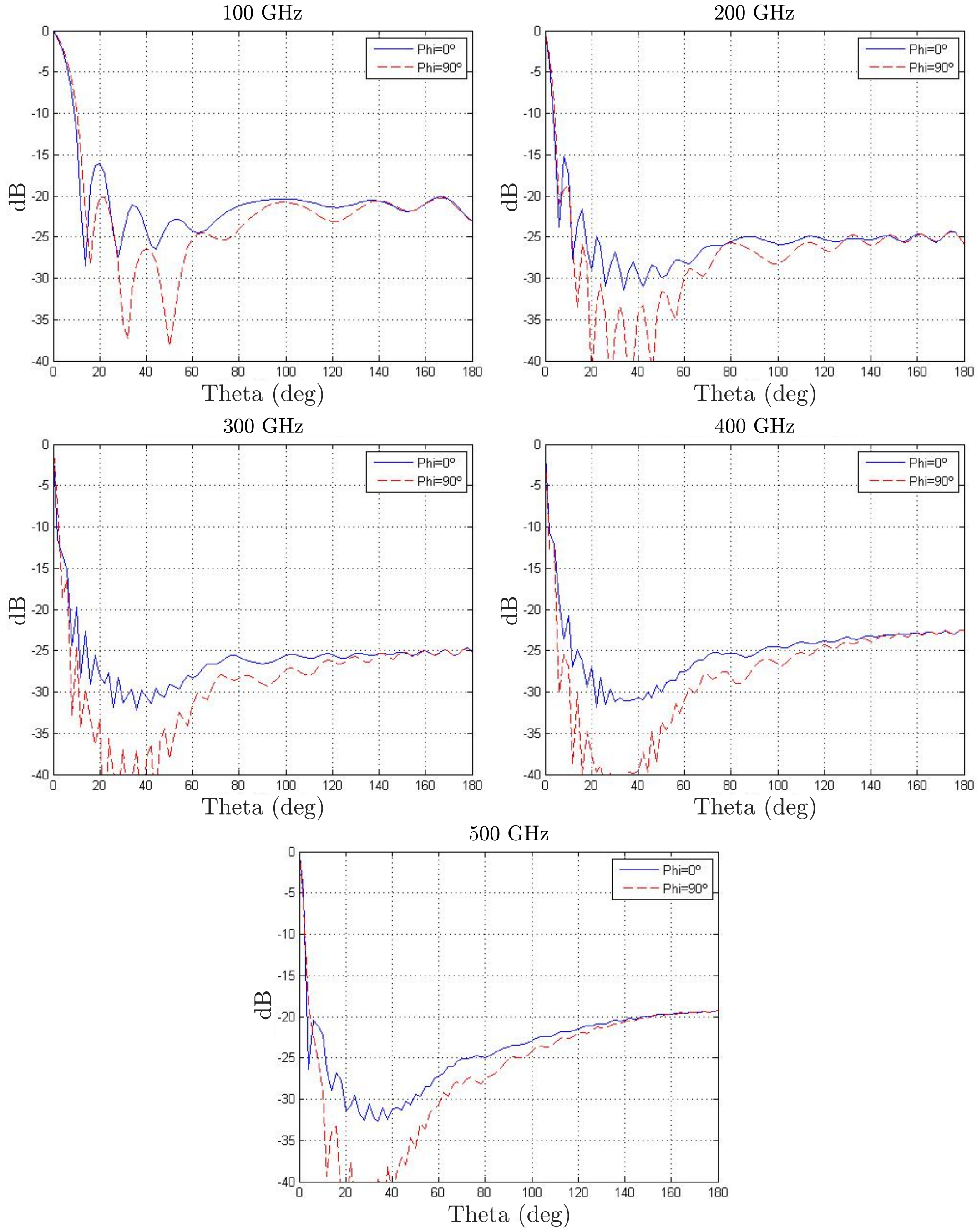

Figure 3.11: Radiation patterns for the second Chessboard array from 100 GHz to 0.5 THz.

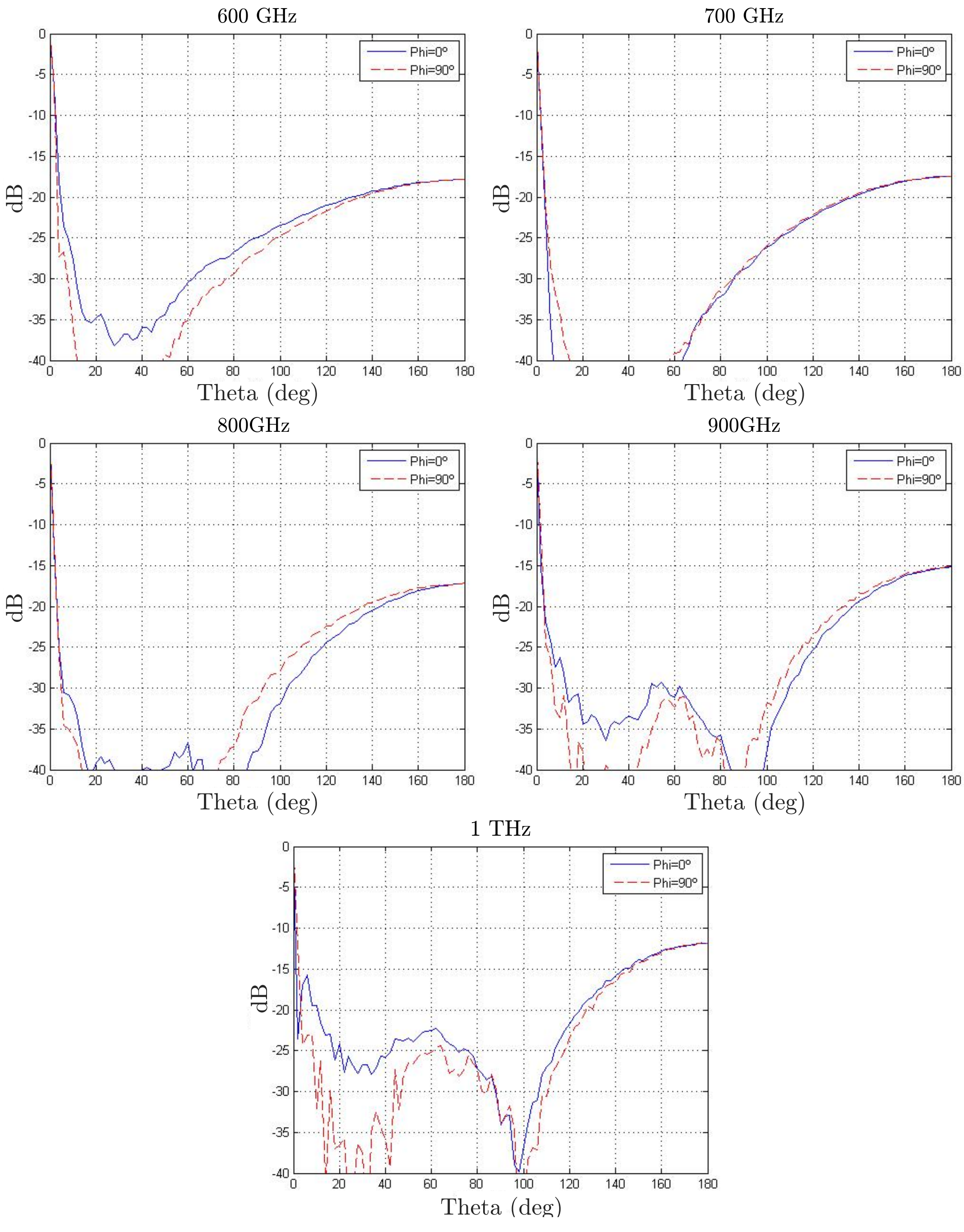

Figure 3.12: Radiation patterns for the second Chessboard array 0.5 THz to 1 THz.

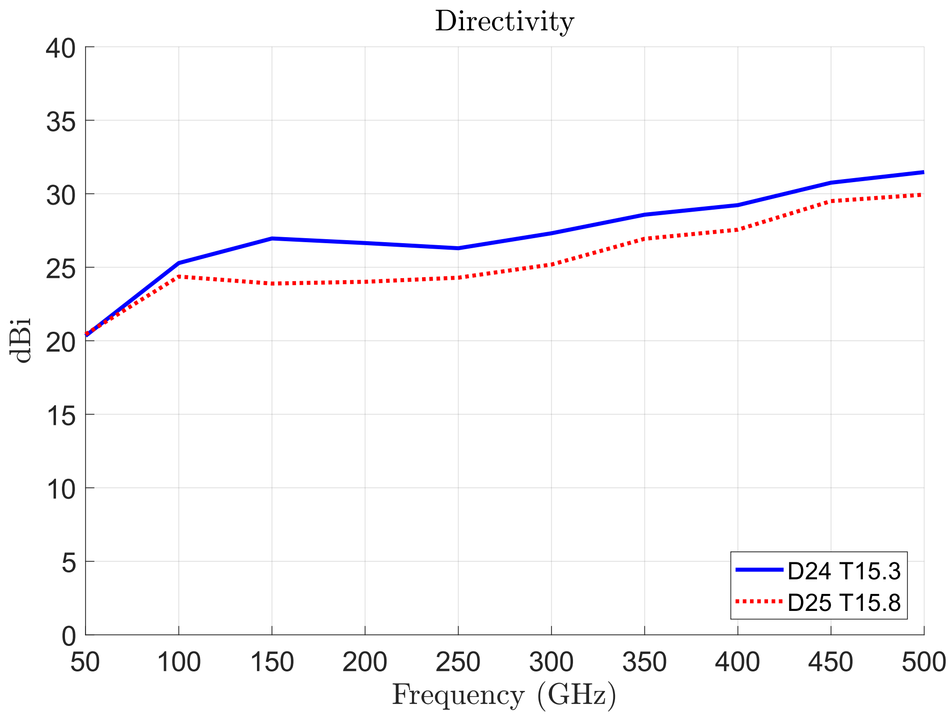

Figure 3.13: Directivity for the third Chessboard array.

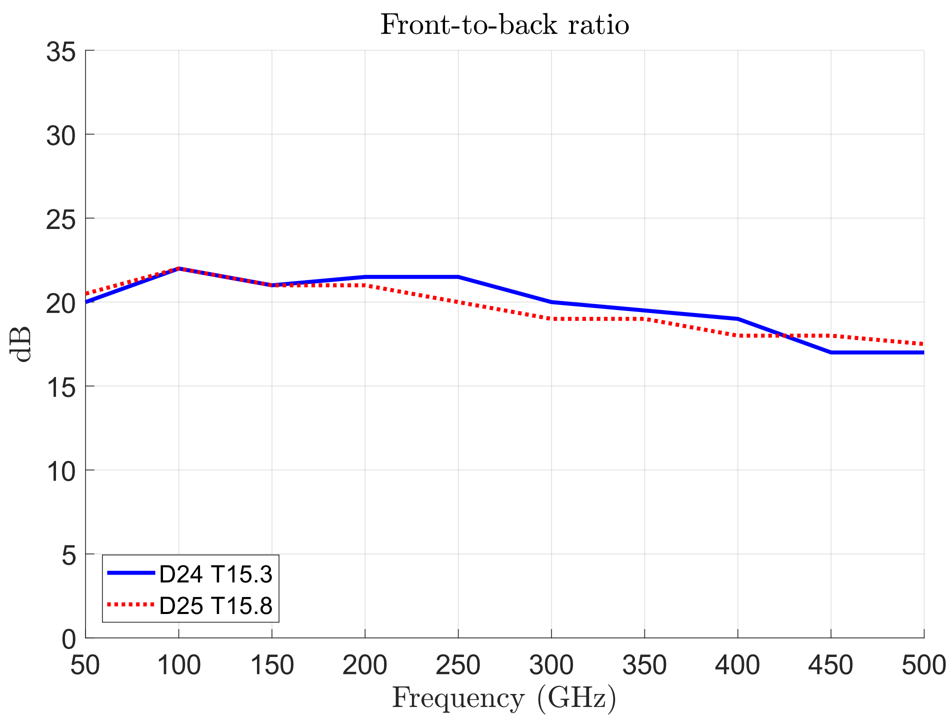

Figure 3.14: Front-to-back ratio for the third Chessboard array.

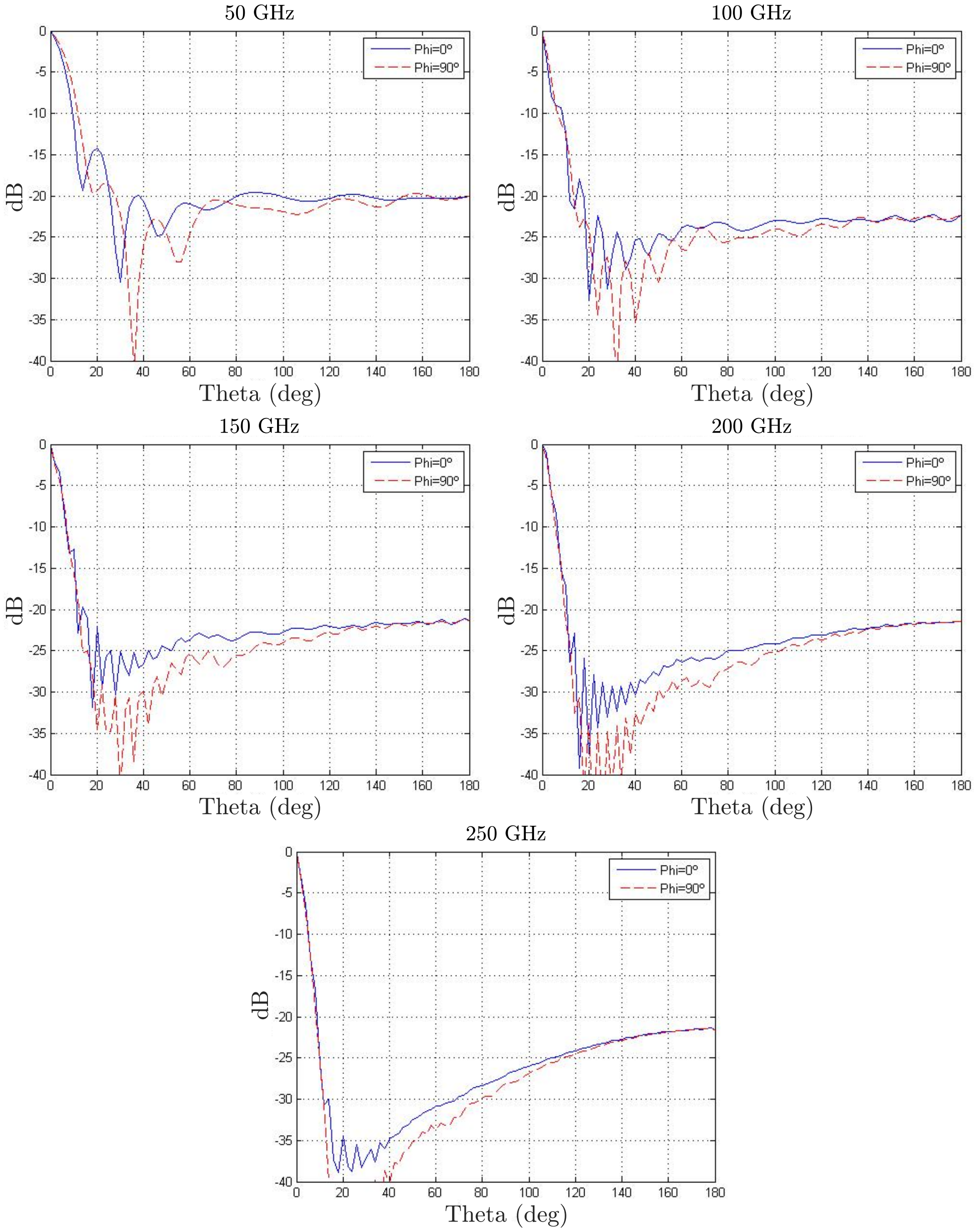

Figure 3.15: Radiation patterns for the third Chessboard array from 50 GHz to 250 GHz.

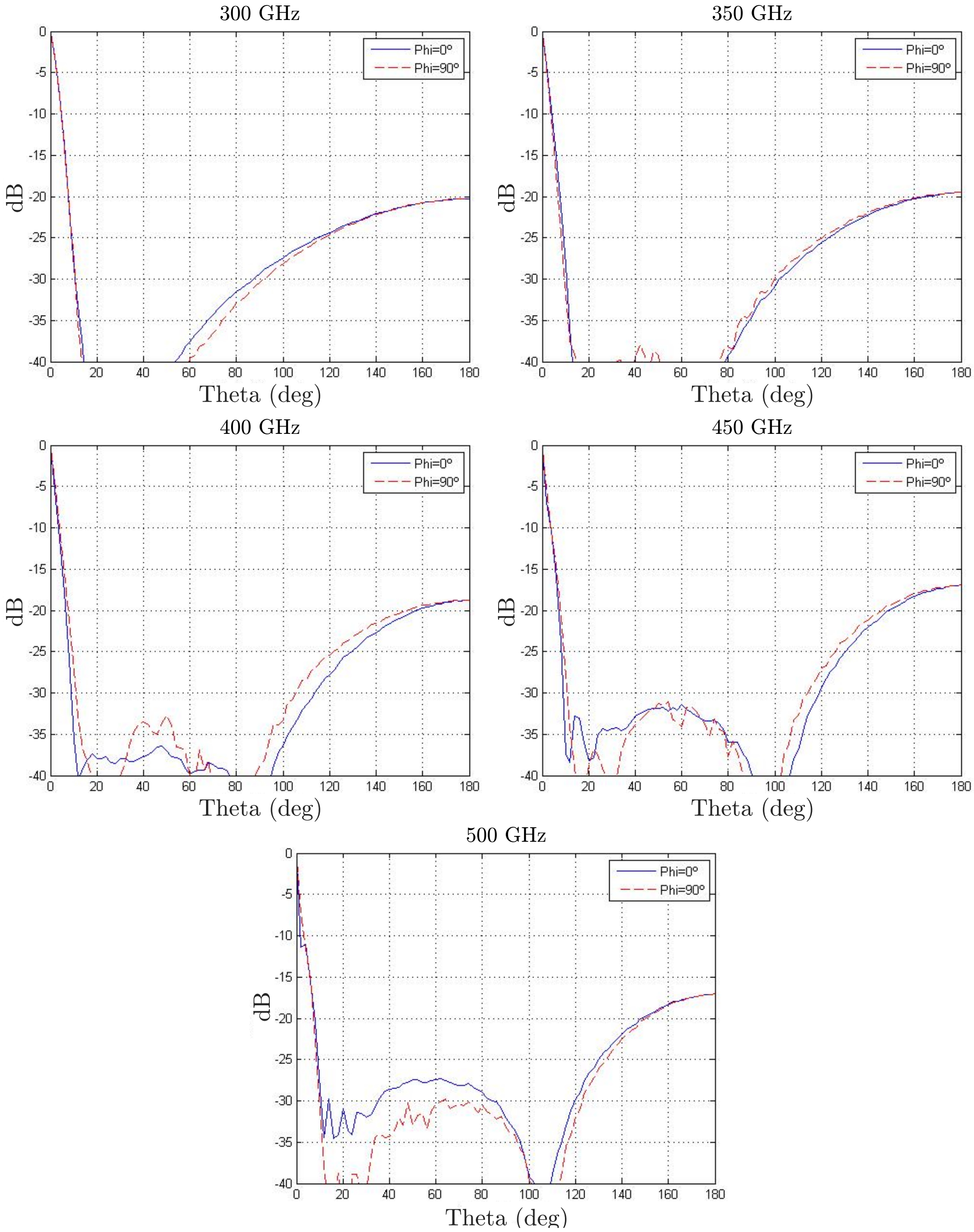

Figure 3.16: Radiation patterns for the third Chessboard array 300 GHz to 0.5 THz.

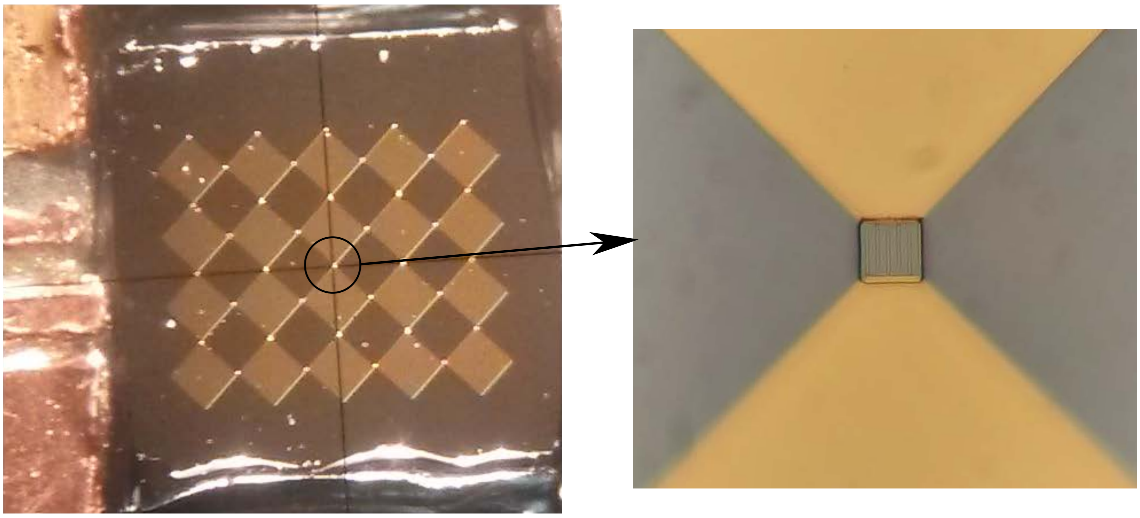

Figure 3.17: Micrograph of the manufactured Chessboard.

3.4. Assembly and measurement

The AE array is fabricated by Fraunhofer Heinrich Hertz Institute (HHI) using ultra-fast Indium Gallium Arsenide (InGaAs) photoconductive photomixers with an interdigitated-electrode structure. As this version is for a proof-of-concept and to facilitate the assembly and measurement processes, the pitch size is slightly increased to be $P_x = P_y = 300\,\mu$m which is corresponding to standard commercial-available microlens (MLA300-14AR) [104].

A micrograph for the manufactured array before adding the bias connections is shown Fig. 3.17) where each photomixer occupies an area of $10\,\mu$m $\times$ $10\,\mu$m. Then the center element of the array is centered to the Si-lens with an acceptable accuracy of $\pm 10\,\mu$m. This is done using a microscope with a reticle and a 2D micro-positioner. Figure 3.18 presents the array after assembly, a Printed Circuit Board (PCB) is introduced which is connected from one side to the array through silver ink and from the other side through cables going to the DC biasing source. A low-pass filter is implemented in the PCB too to protect the photomixers from the electric shocks. The whole THz source (AE array, PCB, and lens) is attached to foam disc which is held by a standard 30 mm cage plate. The foam has a low permittivity close to one to not affect the electric properties of the array.

To focus the beams to the photomixer array, the MLA300-14AR fused silica microlens array connected to a 5-axis mechanically-controlled micro-positioner is utilized as shown in Fig. 3.19. This is the most critical step in the experiment as high alignment accuracy is needed to ensure the correct alignment of the microlens array to be able to illuminate all photomixers. As the movement of the microlens in Z direction can control the spot size of the optical beams at the photomixers level, this alignment accuracy can be relaxed a little bit by moving the microlens in the outwards the Z direction to have a larger spot size but

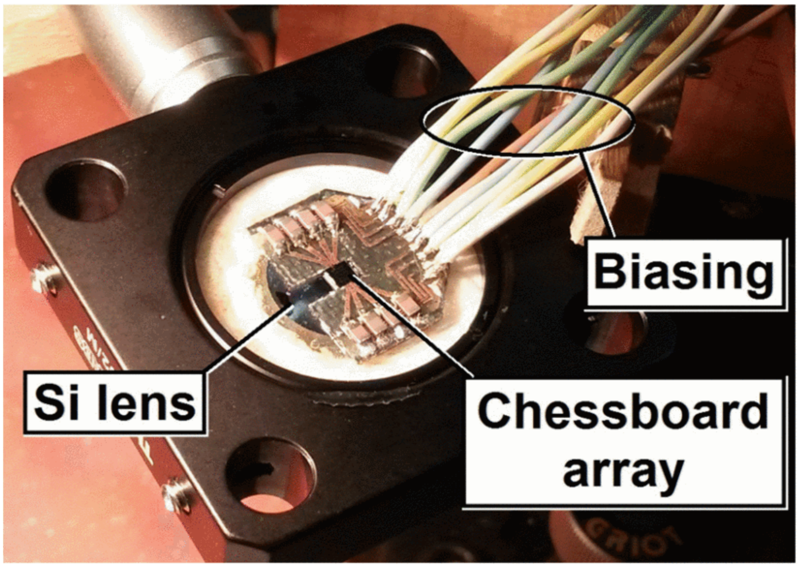

Figure 3.18: The assembly of the AE and Si lens.

this would be under the cost of lower illumination efficiency.

The radiated THz power from the AE is measured up to 500 GHz as shown in Fig. 3.20 using Golay cell. A maximum CW THz power of about 60 μW is obtained at 150 GHz, power levels of 10 μW and 1 μW are obtained at frequencies around 250 GHz and 500 GHz respectively. Such power outperforms the other obtained room temperature THz sources. For example, the THz source based on Uni-Traveling Carrier Photodiode (UTC-PD) and horn antenna we presented in [61] and which provides a very high data rate of about 10 Gb/s for THz wireless communications, is only delivering a THz power of 1.1 μW at a narrower band around 97 GHz.

These measured power levels also outperform the other integrated THz sources working at the same range which are based on photomixers and self-complementary antennas. For example, using bow-tie antennas [98], measured THz power levels are 1 μW, 0.8 μW, and 0.3 μW at 150 GHz, 250 GHz, and 500 GHz respectively. Moreover, at the same three frequencies, using log periodic antenna [105], the power values are around 1.5 μW, 0.9 μW, and 0.5 μW. While they are 4 μW, 2 μW, and 1 μW using square spiral antenna [106].

All the previous results confirm the possibility for the proposed AE to be a proper solution that overcomes the limitations for standard THz sources as it covers a UWB with very high directivity and high THz generated power, all in integrated compact form. This AE can be used as a local oscillator for heterodyne radio astronomy receivers with providing a broadly tunable generator working at room temperature. Also, it can be used as a transmitter for several THz applications that require such advantages.

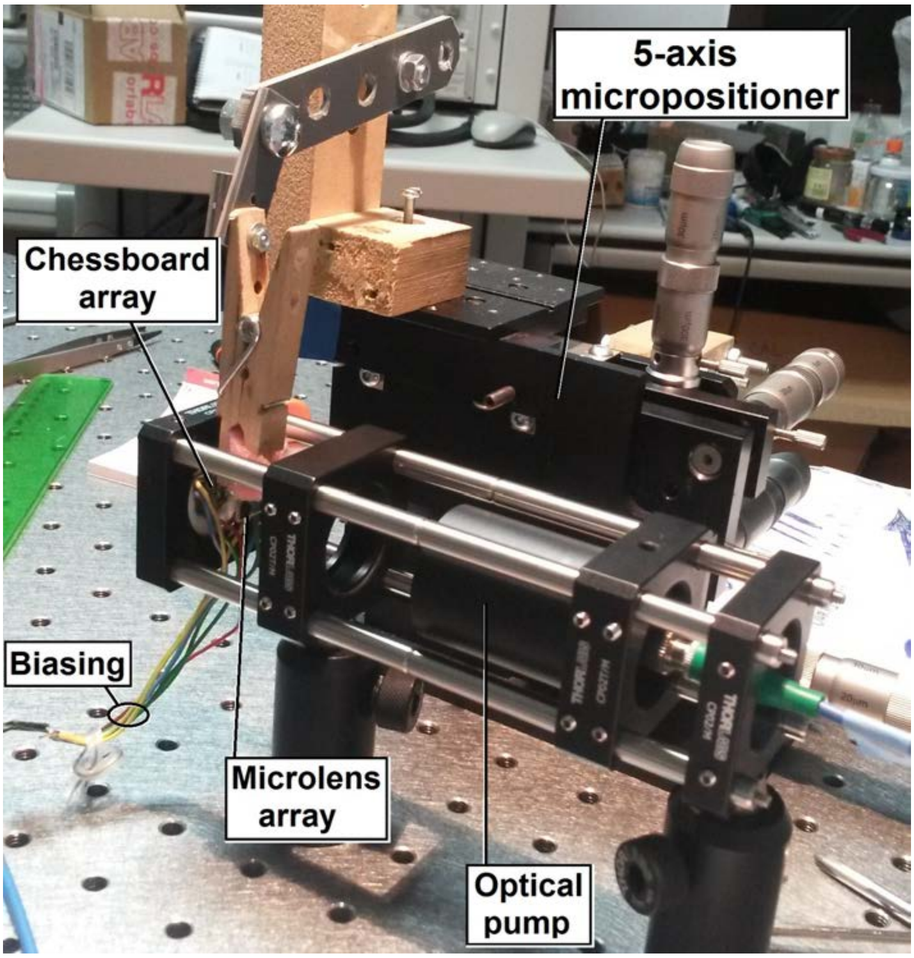

Figure 3.19: The experiment setup for the Chessboard array.

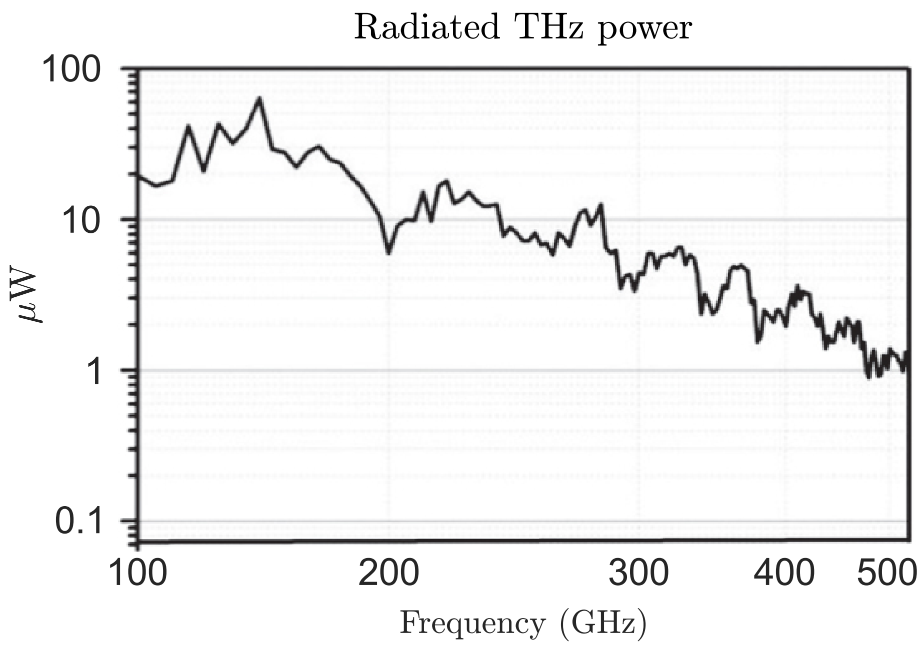

Figure 3.20: The measured THz power radiated from the Chessboard array.

3.5. Effect of metal losses in THz planar antennas

3.5.1. Metalization of the THz planar antennas

As mentioned in this chapter, there are several methods to increase the power for the THz planar antennas with photomixers (AEs). Generally, they can be dived into two main categories, firstly, by increasing the generated power, for example by combining multiple sources. Secondly, keeping the same generated power and increasing the extracted or the radiated power either by increasing the antenna directivity or by avoiding power reduction from the system such as illumination efficiency.

Another source of the power reduction is the metal resistive losses of the antenna itself. Although this issue has rarely been analyzed in the literature, following the collaborated work with Prof. Elliott R. Brown and Dr. Weidong Zhang (Wright State University) that presented in [107], it will be demonstrated in this section how this can be a critical problem and can be a significant source for power loss which avoiding it would enable extracting much high radiated THz power from the AE.

The problem is mainly coming from the assumption of the bulk value for the conducting metal of the antenna material which most the THz antenna designers follow. Or at least, considering the basic updated conductivity value in corresponding to the used metal thickness in case of thin-metal films (on the order of a few or tens of nm) [108]. However, there are several other issues that can affect metal conductivity. Additionally, it is not just related to the actual measured conductivity value for the fabricated metal but also to check the relation between its updated skin depth and the fabricated metal thickness.

This is because, at some frequency ranges, the antenna metal thickness can be close or even lower than the skin depth. In this case, the bulk value of the metal is not valid anymore and the antenna losses would be much higher. This reduces the antenna gain and makes it much lower than its directivity, which in turn would decrease the radiated THz power. The exact reduction in the antenna gain depends on several parameters such as metal deposition, fabrication technique, metal thickness, surface roughness, operating frequency, and antenna topology.

For all of these studies, we will focus on spiral antennas as a common example for THz planar antennas. Spiral antennas provide circular-polarized radiation patterns that are symmetric along UWB frequency range as it was shown in Chapter 2. For this first study, we will consider the case of a square spiral as depicted in Fig. 3.21 which has the benefit of a small footprint that makes it suitable for 2D THz AE array.

The antenna consists of four-arm turns and its dimensions are set to be $W_a \times L_a = 293\,\mu\text{m} \times 322\,\mu\text{m}$ to completely cover the band under interest which is from 100 GHz to 800 GHz as this is the band where the majority of mm-wave and THz system applications presently reside. It is printed on a GaAs substrate with dimensions of $2\,\text{mm} \times 4\,\text{mm}$ and thickness of 0.35 mm. The photomixer is introduced in its center within an area of

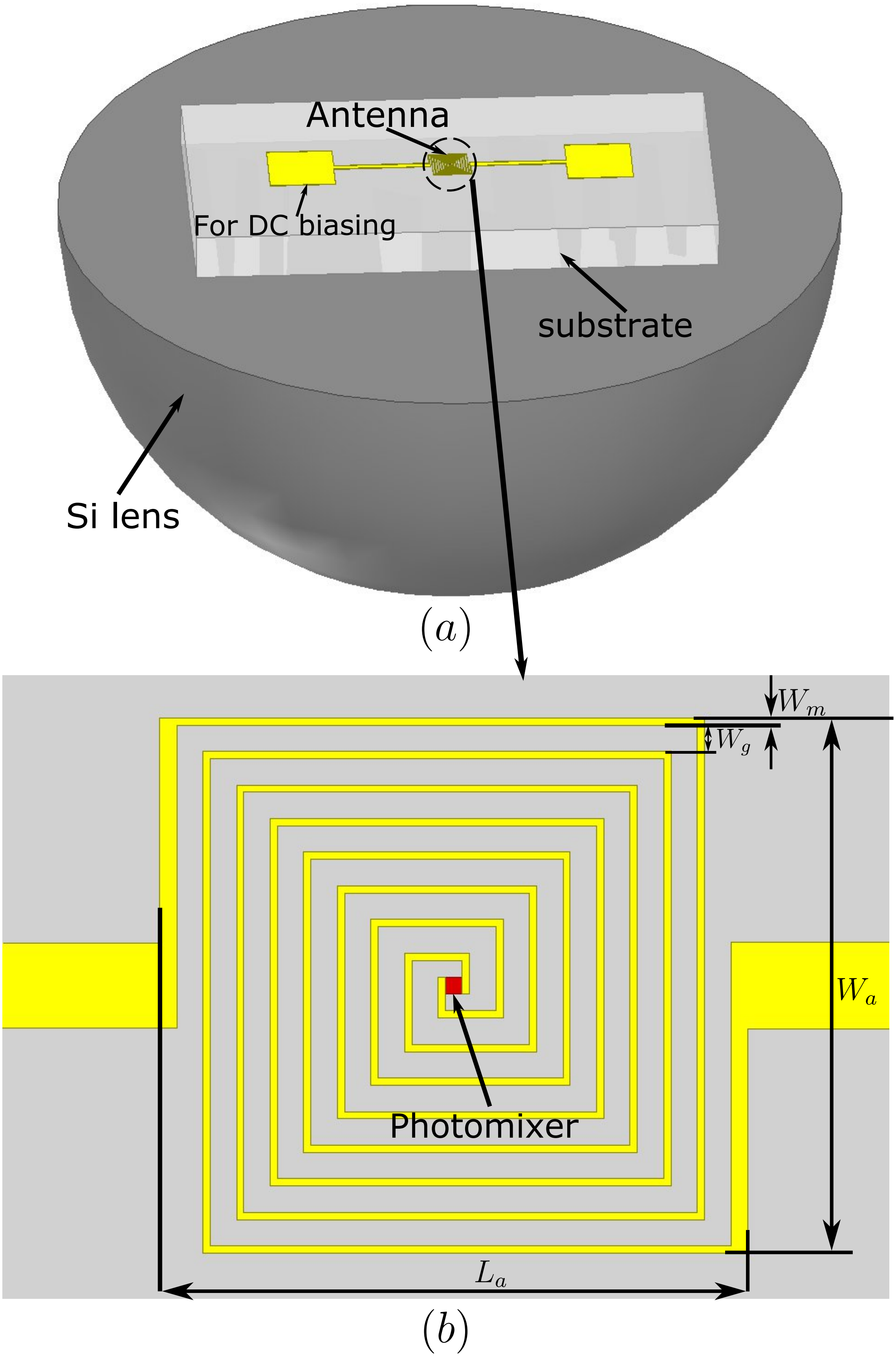

Figure 3.21: The tested square spiral antenna (a) with hemispherical lens and (b) detailed view.

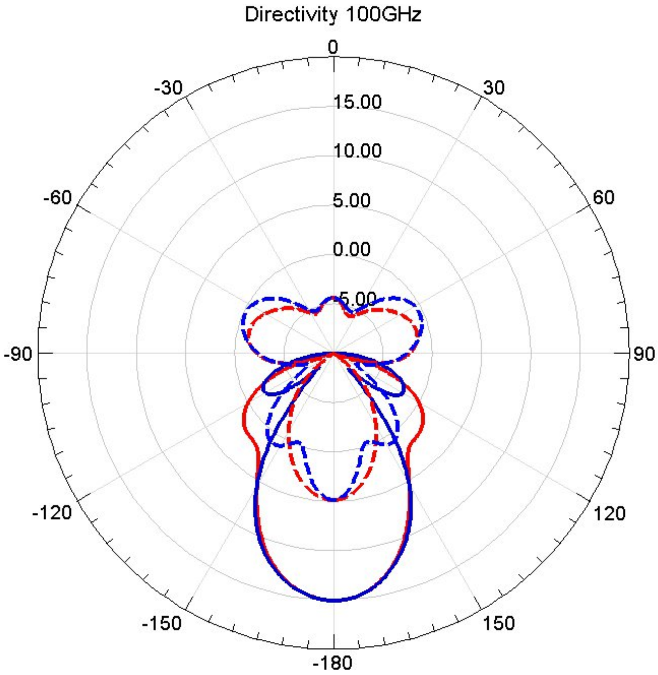

Figure 3.22: The radiation patterns for the square spiral antenna lies on a hemispherical Si lens.

$9\,\mu$m $\times$ $9\,\mu$m. Although the spiral metal width (W_m) should be equal to the gap width (W_g) to be a self-complementary antenna, increasing the gap width will allow the AE to generate higher THz power [109], hence the metal width is set to be $4\,\mu$m while the gap distance is equal to $14\,\mu$m.

The radiation patterns of the tested square spiral plus the hemispherical Si lens with diameter $D = 6$ mm are shown in Fig. 3.22 at 100 GHz. Both circular-polarized co-polar and X-polar directivity (LHCP and RHCP respectively) are presented for both E- and H-planes. Even though the antenna directivity here is about 15dBi, it can be significantly enhanced with the use of an extended-hemispherical lens [110] as was demonstrated in Fig. 3.2. Nevertheless, this is not relevant here because, in these studies, we are only interested to see the effect of the metal resistive losses and the relative reduction in the antenna gain in relation to its directivity so such a simple hemispherical lens would be enough.

As the THz planar antenna is printed on a semiconductor substrate such as GaAs or InP, one of the main requirements of the antenna metalization is to make the metal-semiconductor contact more ohmic as possible, especially near the antenna center (where the photomixer is placed). If not, the metal-semiconductor contacts will show rectifying behavior and act as Schottky barriers that will disturb the flow of the generated THz current into the antenna arms. Because of this, such antennas need a special metalization to ensure the construction of the ohmic contacts between the metal (antenna) and the semiconductor (substrate). This is usually performed by depositing thin metal films followed by a thermal annealing step to improve adhesion and alloying of the metal to the

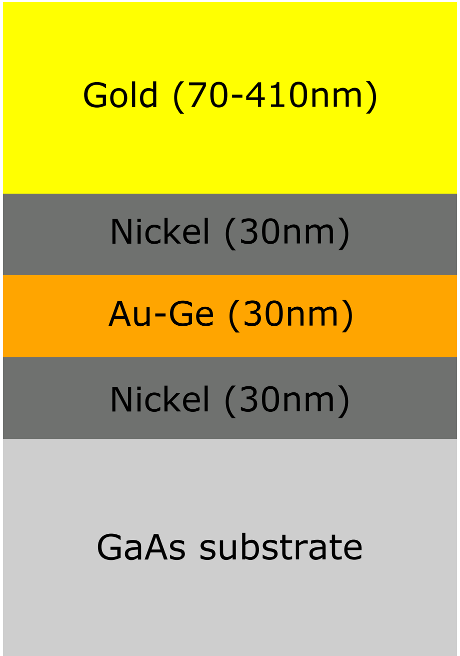

Figure 3.23: Metalization of THz antenna lies on GaAs substrate.

semiconductor with low contact resistance and linear I-V behavior [111].

For manufacturing this spiral antenna, a metal deposition technique consisting of evaporation of four layers of metal films sequentially is used as shown in Fig. 3.23. These four layers are, three metal films which each of them has a thickness of 30 nm, and consists of two Nickel layers with one eutectic alloy made of Gold-Germanium (Au-Ge) in between. The Au-Ge alloy mixture percentages are 88% and 12% of Au and Ge materials respectively and its melting temperature is 356°C. In the end, the last layer is pure gold with larges variable thickness, here we tried two extremes of 70 and 410 nm. This makes the total thickness of the antenna metal equals to 160 nm and 500 nm. With such relatively thick gold thickness, the conductivity reduction phenomenon (or the resistivity increase) caused by thin metallic films is avoided as the minimum thickness is around three times the gold electron mean free path (57 nm). So theoretically, the resistivity increase is expected to be negligible amount less than 10% [108].

The DC electrical resistivity of such metal is measured with the top gold layer having a medium thickness of 330 nm using a standard four-point probe method. To have an accurate estimation of the bulk resistivity, this experiment is repeated five times with different manufactured prototypes then the average of the six samples is considered. Figure 3.24 presents the resistivity of the six samples which all provide comparable results with an average of 2.9×10^{-8} Ω-m. As expected from the relatively-large thickness of the gold layer, the resistivity of the metal films is so close (only 21% higher) to the pure gold resistivity (2.4×10^{-8} Ω-m). This is proof of the high quality of the metal films and means that they are supporting most of the generated current through the entire thickness.

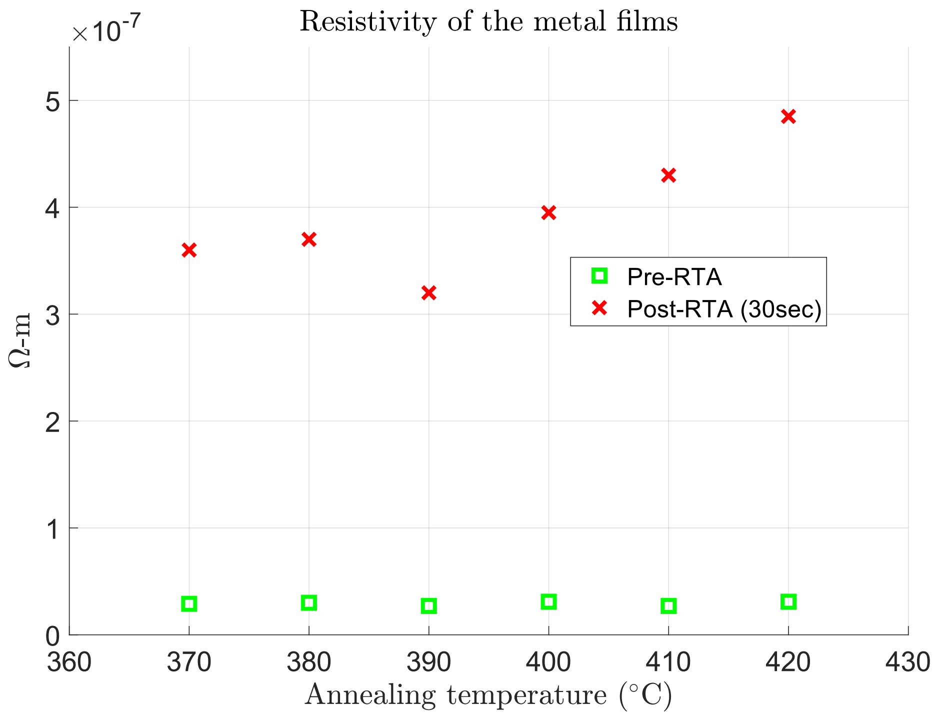

Figure 3.24: Measured resistivity of different metal samples before and after the annealing.

3.5.2. Metal losses based on measured properties of the manufactured metal film

Using Rapid-Thermal Anneal (RTA), the six samples are annealed for a period of 30 sec at different temperatures in the range from 370 to 420°C with a step of 10°C in an inert gas environment. Then, the resistivity measurements are repeated and the updated value for each sample after the annealing is also plotted in Fig. 3.24. All of the six samples show a significant increase in resistivity especially at higher annealing temperatures that are much higher than the melting temperature of the Au-Ge alloy. However, from another perspective, this means that the gold layers are mixed together with the Au-Ge layer below it. And since the GaAs substrate exists at the bottom of the samples, the RTA and alloying processes are successful to make their roles and provide good adhesion of the metal to the substrate.

For these studies, the two extremes metal thicknesses will be considered, lower thickness with 160 nm and higher one with 500 nm. For the resistivity, the worse case of the measured gold alloy would be considered which shows a bulk resistivity of $5{\times}10^{-7}$ Ω-m. Although such high resistivity values are around 20 times greater than the pure gold one, it should be highlighted here that it is not surprising and similar values are measured in literature for gold films on the order of tens or hundreds of nm [112], [113].

The simulated co-polar gain (LHCP) considering the two metals is plotted in Fig. 3.25a and Fig. 3.25b for the thinner and thicker metal respectively. This is for the pure gold (in solid) and the measured actual gold alloy (in dashed with circle markers). For compression purposes, the antenna directivity is plotted too in the dotted-magenta curve.

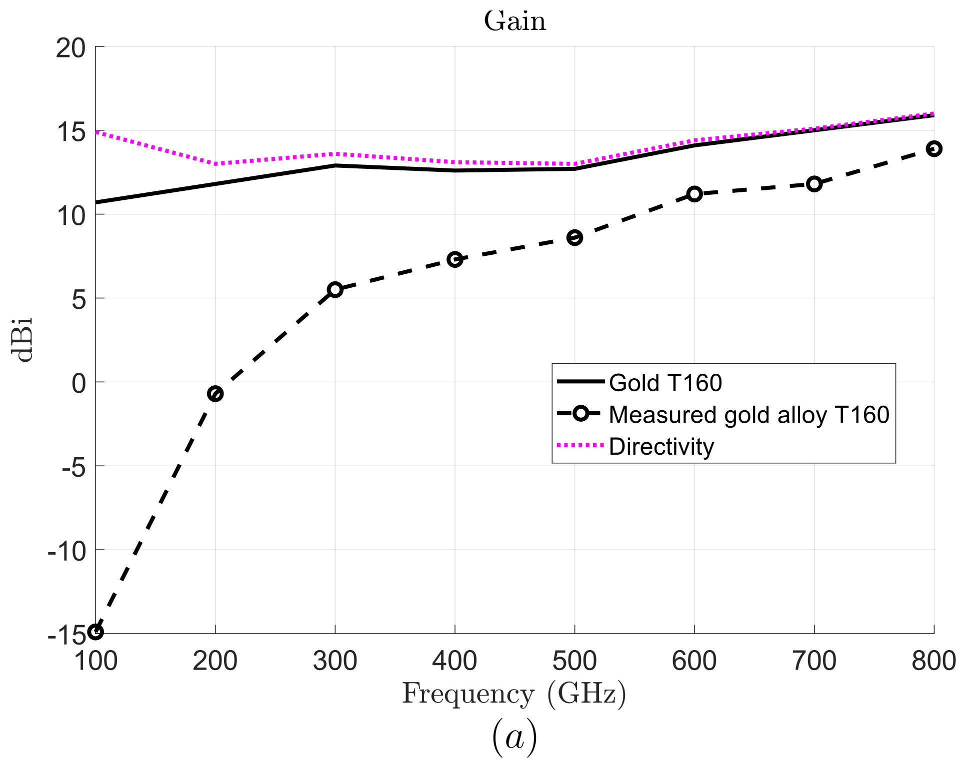

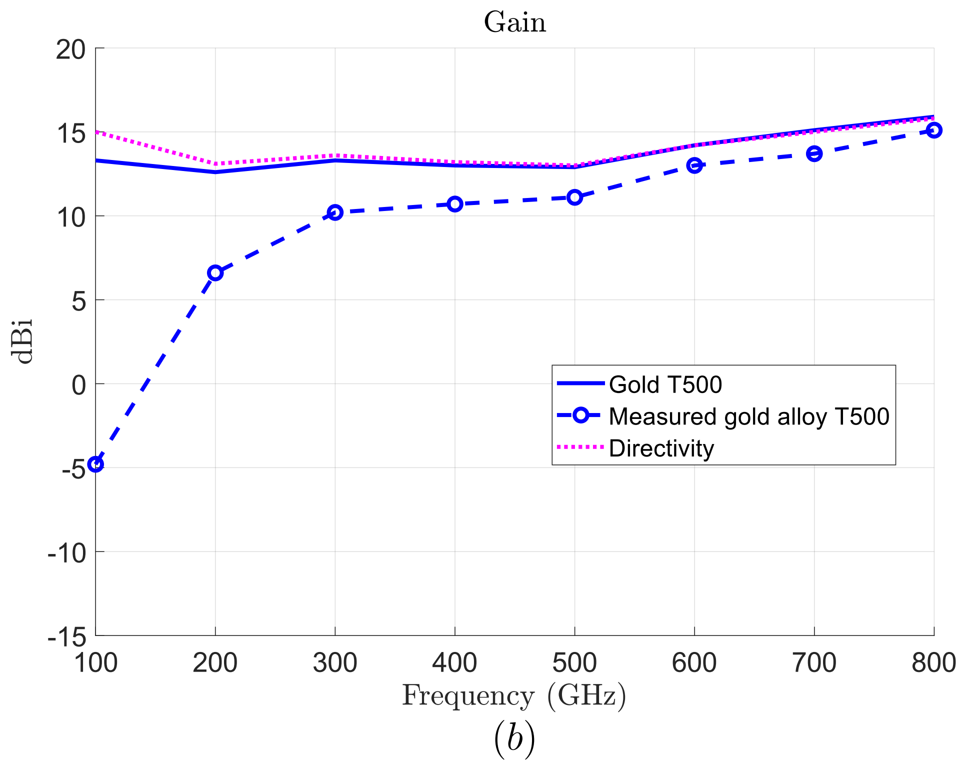

Figure 3.25: Gain of the square spiral with a metal thickness of (a)160 nm and (b)500 nm.

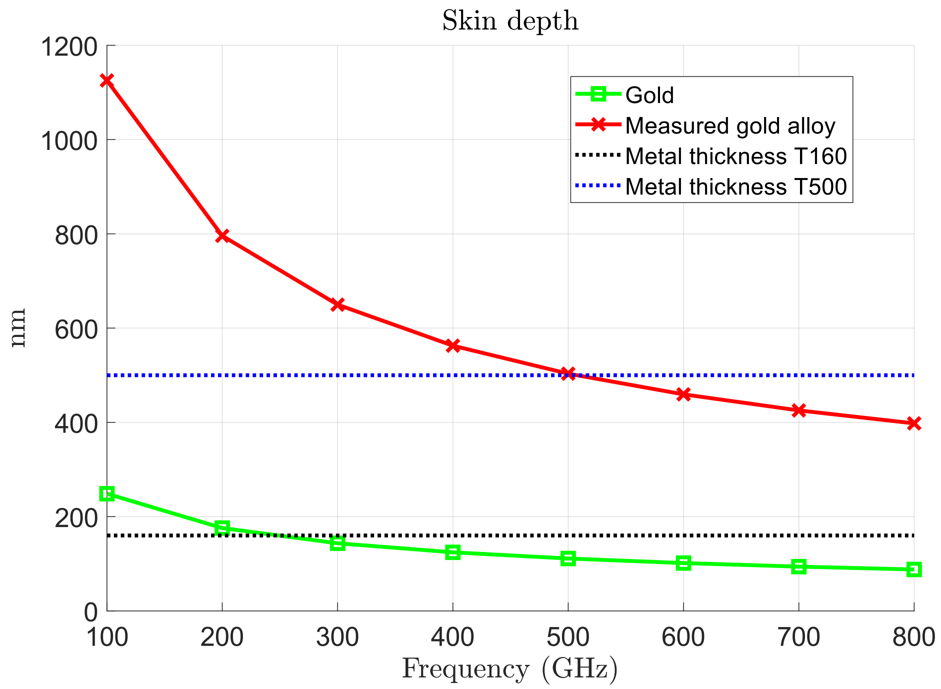

Figure 3.26: Skin depth vs frequency for pure gold and annealed gold alloy.

Regarding the smaller thickness of $T = 160\,\text{nm}$ (black-curves), a significant decrease in antenna gain occurs for the stack film antenna compared to the pure gold antenna. Although the discrepancy between them is only around 3 dB at the high-frequency end, it dramatically increases by more than 25 dB at 100 GHz. Even for the pure gold antenna, it has a drop in gain of about 5 dB at the lower frequencies end compared to its directivity, which is not expected for such self-complementary spiral that it is known to have a flat behavior over the entire band (as in the dotted-curve).

To have a better understanding of such observations, let's see the computed gain for the thicker thickness $T = 500\,\text{nm}$ (blue curves). Here, the antenna provides almost flat performance for the pure gold with metal losses lower than 2 dB and perfect matching at the higher frequency range. Even, for the lossy alloy (dashed), it is increased too and becomes closer to the pure curve (solid) as now, it rolls off much more gradually. The difference between them is increasing with decreasing the frequency up to a peak value of 18 dB at 100 GHz. At higher frequencies above 400 GHz, this difference in gain is decreased to be only in the range from 1 to 2 dB.

The physical meaning behind this behavior can be obtained by estimating the skin depths of both metals and comparing them to the two metal thicknesses as in Fig. 3.26. As it is expected from the high resistivity of the gold alloy which is around 20 times greater pure gold case, its skin depth is around 4.5 ($\sqrt{20}$) higher than its corresponding for the pure gold at all frequencies.

As it is shown in Fig. 3.26, regrading the first metal thickness $T = 160\,\text{nm}$ (dotted-black), even pure gold (solid-green) presents comparable skin depth or slightly lower in the frequency range above 300 GHz. This is the reason why it has acceptable results in this range (solid-black in Fig. 3.25a). However, for the actual measured gold alloy (solid-red), the skin depth is much higher than the thickness. By moving towards the higher frequency, the difference starts to decrease and this is the physical reason that the square spiral provides much worse gain at the lower frequencies and enhances gradually by increasing the frequency (dashed-black in Fig. 3.25a). Although the results are enhanced by increasing the frequency, still the metal losses are so high and the gain-directivity difference is not acceptable in any part of the frequency range.

In contrast, regarding the second thickness $T = 500\,\mathrm{nm}$ (dotted-blue), the pure gold skin depth (solid-green) is already less than three times the thickness (except at 100 GHz which is only about the half), so such thick thickness will enable the metal to act similar to the good conductor and provides high gain over the whole band (solid-blue in Fig. 3.25b). Therefore, the metal losses here are negligible which makes the gain to be so close to the antenna directivity. Also, for the case of the measured lossy gold alloy, the thickness becomes closer to its skin depth (solid-red) and even higher.

Although this thicker thickness is still smaller than the skin depth at the low-frequency range (from 100 GHz to 400 GHz), this increment in the thickness enables a significant reduction in the metal losses as shown in Fig. 3.27. This is in turn would deliver an expected higher radiated THz power that is corresponding to the same amount of the losses reduction. This means that, for the same actual measured metal characteristics, the increment of the metal thickness from $T = 160\,\mathrm{nm}$ to $T = 500\,\mathrm{nm}$ would let the same spiral antenna provide a higher power with a peak enhancement of 10 dB at the lower frequency range.

Furthermore, it is worth noting here that as we demonstrated in [114], such THz metallic antennas are needed to be modeled adequately to have accurate simulation results at the lower frequencies. As at these frequencies, the skin depth can be larger than (or comparable to) the metal thickness either due to the annealing process or any other factors such as surface roughness [115], deposition non-uniformity, and so on. The standard direct EM simulations are not so accurate for these cases as with even this lower conductivity ranges, by default, the simulators are still considering them as good conductors regardless the metal thickness. Hence, the tangential electric field components are approximated to be zero and this can caused a mismatching (for this spiral case can be up to 2 dB).

For avoiding such mismatching, two non-default methods can be used. Firstly, forcing the simulator to mesh inside the antenna 3D metal objects and hence calculates the actual non-zero tangential electric field. Secondly, to model the antenna metal as a 2D layered impedance boundary (in HFSS simulator) which implies the estimation of the tangential electric fields using the surface impedance of the boundary based on the provided material conductivity and the actual antenna metal thickness. Although, the second method has lower time consumption, the first method is used to have a fix modeling-method with acceptable-level of accuracy for all frequencies.

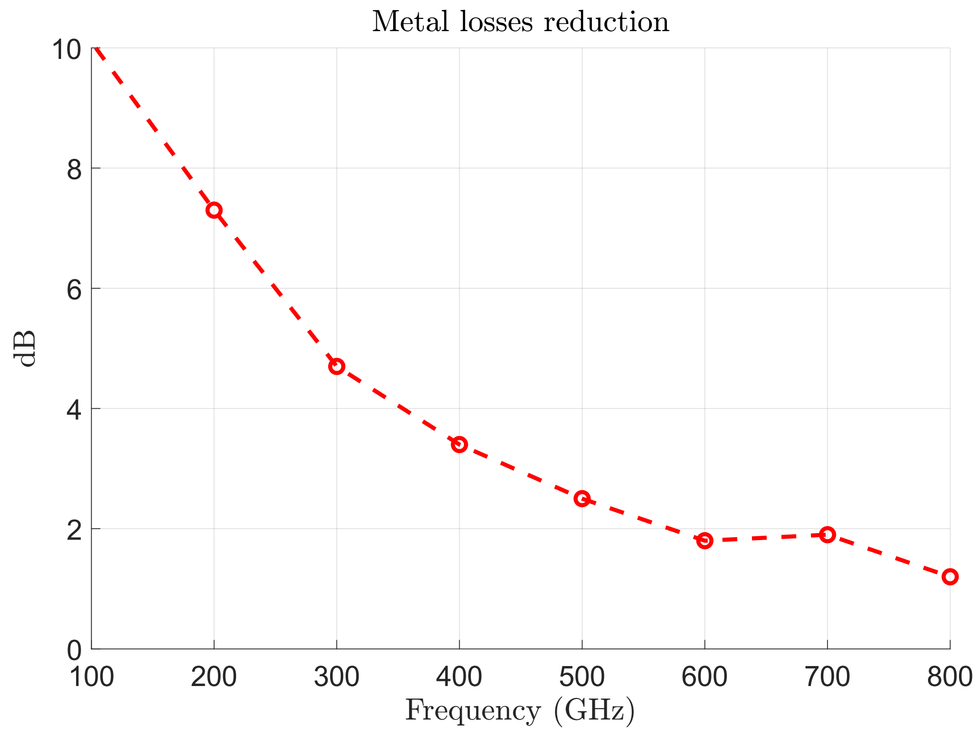

Figure 3.27: Reduction of metal losses of the square spiral antenna by the increment of its metal thickness.

Another important issue is how these metal losses affect different antenna typologies, to answer this question, another common example would be studied which is the log spiral antenna. The antenna lies on GaAs substrate (Fig. 3.28) which is attached to a hemispherical Si lens. For fair comparisons, both the substrate and the si lens have similar dimensions as the one used for the previous square spiral, just the substrate width is slightly increased from 2 mm to 2.5 mm. This is due to the larger antenna size for the log spiral as the length should be comparable to $1\lambda_{min}$ [98] which is around 3 mm to cover the required lowest frequency (100 GHz). Hence, the antenna size needs to be increased from $W_a \times L_a = 293\,\mu\text{m} \times 322\,\mu\text{m}$ (for square spiral) to be $W_a \times L_a = 1527\,\mu\text{m} \times 2585\,\mu\text{m}$. Such size increment demonstrates the benefits for the square spiral for being a compact antenna.

The gain of the log spiral antenna is shown in Fig. 3.29 for both pure gold and gold alloy metals. It is clear how these results outperform that of the square spiral, especially at lower frequencies. Even with this small thickness of $T = 160$ nm, the pure gold antenna (solid-black) provides an almost flat gain of about 14.5±1 dBi with almost no metal losses as this gain is identical to the antenna directivity. Although there is still a discrepancy between the gain of the gold alloy (dashed-black) and its directivity, the metal losses are much better compared to the square spiral of the same thickness (of $T = 160$ nm). Besides, the losses here are at an acceptable level as they are lower than 4 dB for the whole band.

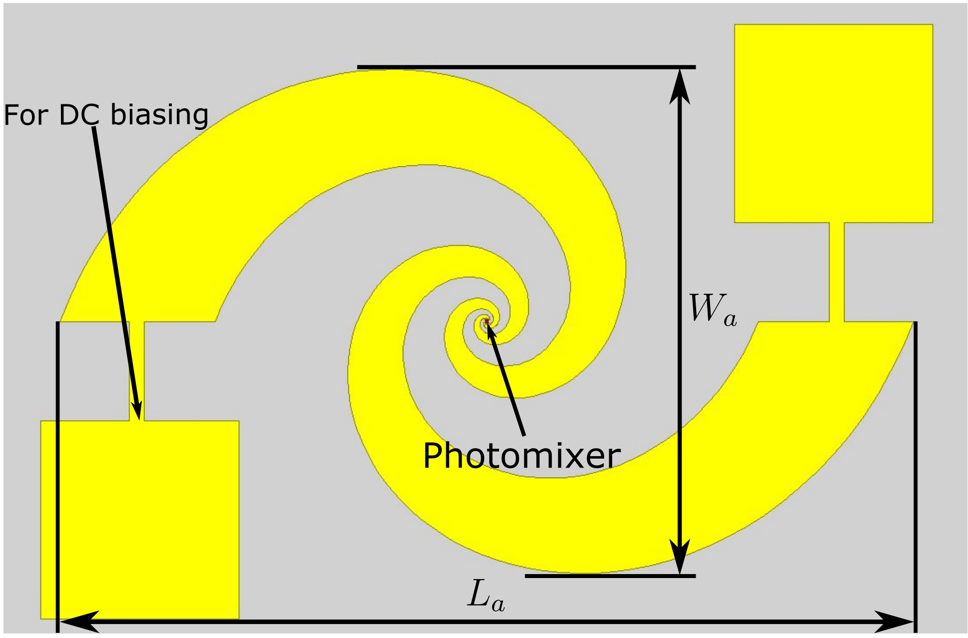

Figure 3.28: The tested log spiral antenna.

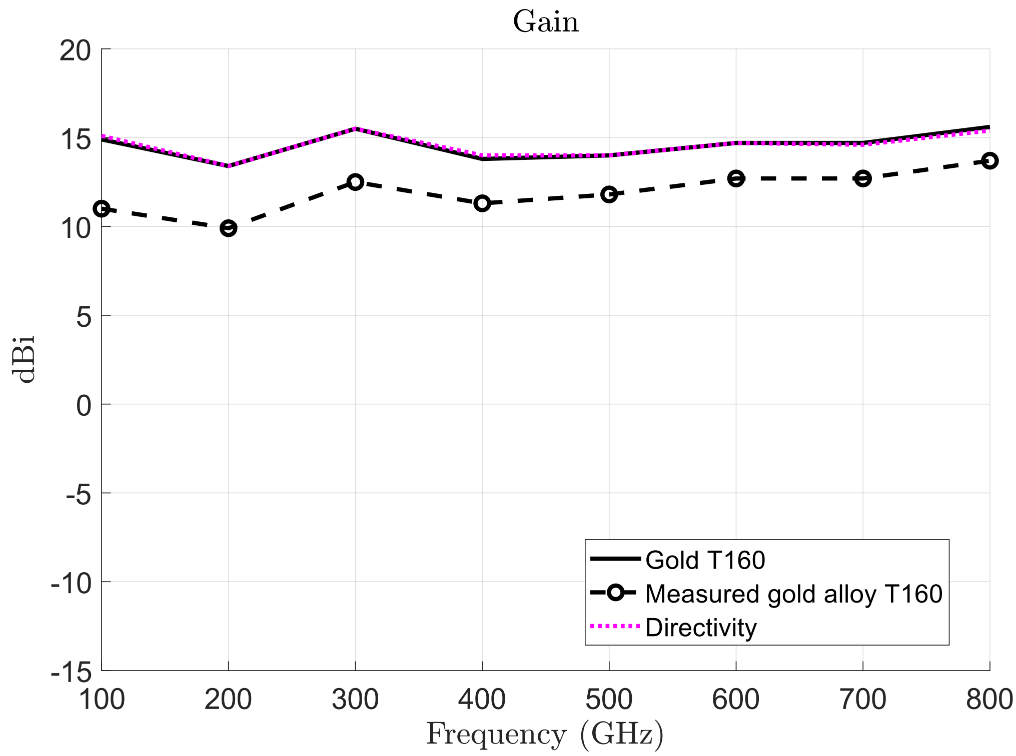

Figure 3.29: Gain of the log spiral with a metal thickness of 160 nm.

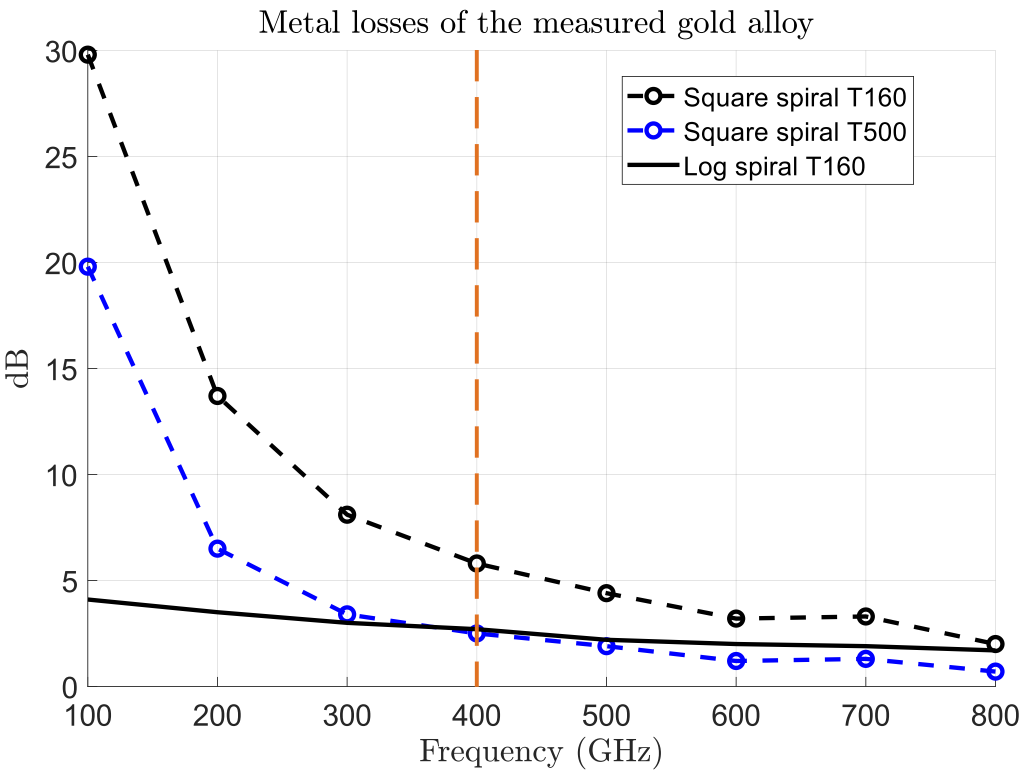

Figure 3.30: Summary of metal losses of square and log spirals.

To summarize and have a general comparison, Fig. 3.30 represents the metal losses for all the tested cases. This includes the square spiral with the low thickness of $T = 160$ nm and the possible two solutions to overcome its huge losses which are either increasing the metal thickness or using another antenna topology. For comparison purposes, the whole band can be divided into two sub-bands. In the first sub-band from 100 GHz to 400 GHz, log spiral significantly outperforms both square spirals (with the two thicknesses) as it provides metal losses in the range from 2.5 to 4 dB while square spiral has losses from 6 to 30 dB and 2.5 to 20 dB for $T = 160$ nm and $T = 500$ nm respectively.

For the other higher sub-band (above 400 GHz), the square spiral with larger thickness is considered the best solution as its losses are from 0.7 to 2.5 dB while the losses from the log spiral and the low thickness square are from 1.5 to 2.5 dB and 2 to 6 dB respectively. These studies provide different alternatives for THz antenna designing, for example, one can select square spiral with a large thickness in case that compact design or better performance are needed at the higher frequencies. On the other way around, log spiral can be selected if a simple thin metal fabrication or stable behavior over the whole band are preferred.

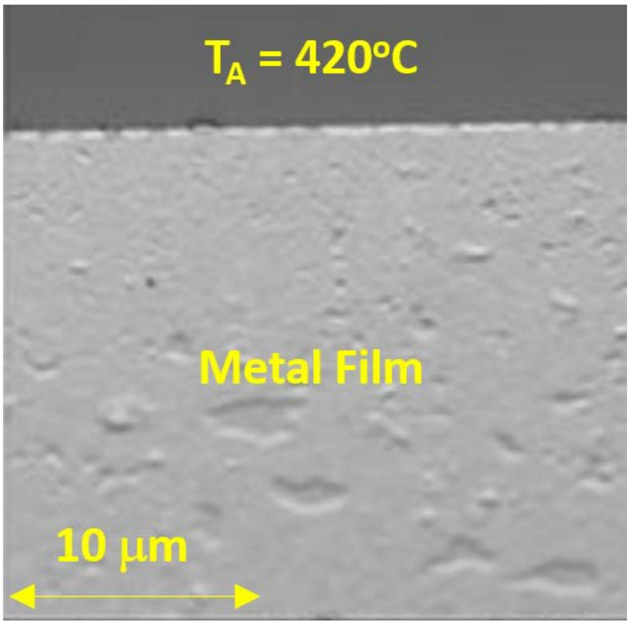

Figure 3.31: Micrograph of the annealed metal surface.

3.5.3. Surface neness effects on metal losses

Another stage in the characterization of the antenna metalization is the microscopic inspection and surface profilometry. Figure 3.31 presents the scanning electron microscope image for the metal surface of the sample that was annealed at 420°. As expected for evaporating metal films with a small thickness (below 1 μm), it is clear how the metal surface is not uniformly smooth and it has a significant roughness. The effect of this measured surface roughness is included in the EM simulations by modifying the metal conductivity.

The updated metal conductivity can be estimated following Groiss model [116] as $\sigma(f) = \sigma_0(f)\{1 + \exp[(-\delta(f)/2h)^{1.6}]\}^{-2}$ where σ_0 is the nominal conductivity, h_s is the measured Root Mean Square (RMS) surface roughness, and the $\delta(f)$ is skin depth. Based on these estimations and the average measured RMS surface roughness which is around 50 nm, Fig. 3.32 presents the resistivity for the pure gold (solid-green) and for the gold alloy (solid-red). To better interpret the estimations, the nominal resistivity for the two metals without the surface roughness is plotted too in the dashed curves.

For the pure gold, it can be seen that the surface roughness has an effect only at the higher frequencies but this influence is not significant compared to the effect to the alloy and annealing themselves which was previously studied in Sec. 3.5.2. On the other hand, for the annealed gold alloy, the resistivity is remaining almost the same even after including the surface roughness. This is because the skin depth is already much higher than the measured surface roughness for the whole frequency range which would decrease the value of the exponential term in the Groiss equation and make the conductivity to be equal to the nominal value.

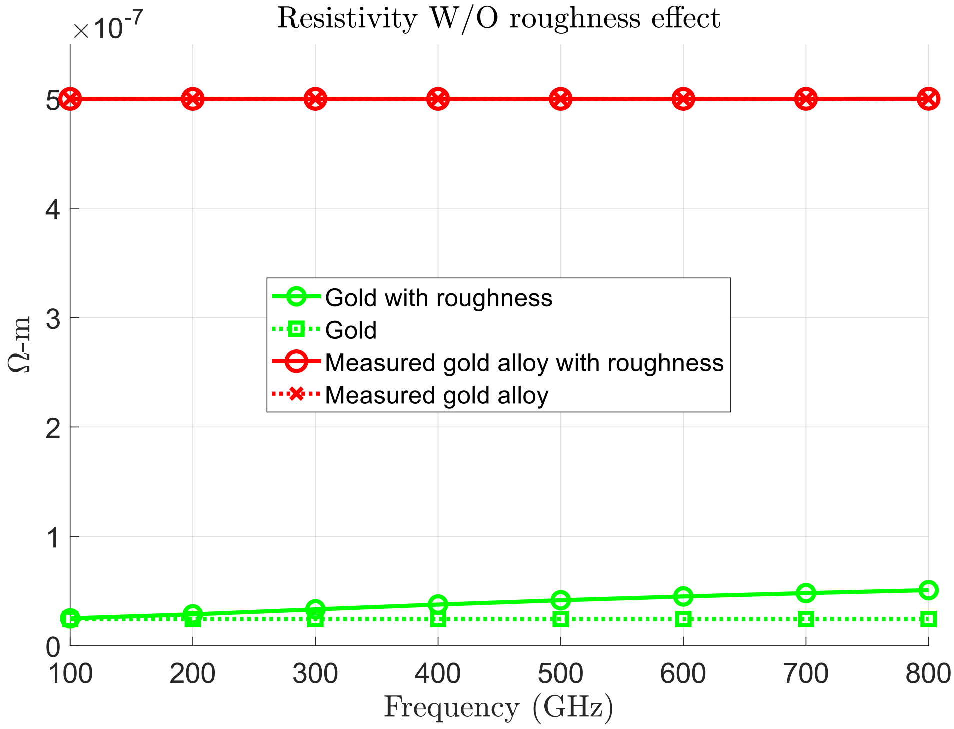

Figure 3.32: Resistivity of pure gold and annealed gold alloy considering the measured surface roughness.

3.6. Conclusions and principal remarks

Three mm-wave and THz planar antenna-based emitter arrays covering UWB frequency ranges from 50 GHz to 0.5 THz, from 100 GHz to 1 THz, and from 200 GHz to 2 THz are presented. They are consist of 3×3 self-complementary bow-tie antennas with a photomixer implemented in each element center (forming the shape of a Chessboard). The arrays elements are electrically-small (around $0.038\lambda_{min} \times 0.038\lambda_{min}$) and in contact with each other which purposefully increases the mutual coupling between them to cause constructive interference. This forms a high-density array with a compact size that does not have the problem of out-of-focus when the AE array is placed over Si lens.

The electrically-large extended-hemispherical lens has the role of increasing the radiated power compared to the extracted power and having a single beam directed downwards below the Si-lens with very high directivity. The effect of different commercially-available Si lenses (with a maximum diameter of 25 mm) is studied depicting, in some cases, a considerable change in the radiation patterns that can be reflected with about 10 dB difference in antenna-directivity even with the use of the same antenna array. These proposed arrays provide stable radiation patterns in their corresponding UWB THz ranges with average directivity of 27, 33, and 35 dBi for the three arrays respectively.

A proof of concept array is fabricated with a PCB for the DC biasing and assigned to a commercially-available Si lens. The experimental setup and assembly processes are discussed. A microlens array that is held by a 5-axis micro-positioner is used to direct the optical beam towards the photomixers. The THz radiated power is measured showing a peak CW power of about $60\,\mu$W at 150 GHz. This outperforms other designs based on the same concepts.

Additionally, the metal losses for THz planar antennas are studied in detail based on the measured metal resistivity for the metal alloy used to manufacture a square spiral antenna. The studies are performed for wide mm-wave and THz bands, from 100 GHz to 800 GHz in which most of the THz applications exist. They demonstrate that the antenna losses can reach 30 dB at 100 GHz compared to less than 5 dB if an ideal gold is considered in the losses estimation. It is also described how such losses are enhanced with increasing the frequency reaching a smaller value of 6 dB at 800 GHz. This behavior is physically explained by comparing the skin depths of both metals (ideal gold and measured metal alloy) with their relations to the metal thickness. This comparison shows that, at the lower frequencies, the metal thickness is lower than the skin depth for the actual manufactured metal. The metal surface roughness effect is studied too, however in such case of larger skin depths (of the lossy metal), it seems that its contribution to the metal losses is negligible over the whole studied band.

Generally, the exact amount of such losses depends on several parameters such as metal deposition, metal thickness, surface roughness, operating frequency, and antenna topology. Hence, with fixing the same fabrication process and frequency range, two alternatives are provided to overcome such significant losses. First, by increasing the metal thickness from 160 nm to 500 nm, which would decrease the losses by around ten times at lower frequencies and to its half at higher frequencies. But on other hand, this would increase the fabrication complexity and its cost too. Alternatively, by changing the antenna topology using log-spiral with the same relatively-small metal thickness. This achieves better performance as it decreases the losses to be an almost flat value less than 4 dB in the whole band. However, this comes with the cost of a significant increase in the antenna size. The proper method can be selected depending on the required specific application.

4. PHOTONIC NONLINEAR UP-CONVERSION RECEIVER BASED ON WGM

4.1. Introduction

As is shown in Chapter 2, cryogenic cooling is needed for the proposed direct receiver especially to have good performance for the LNA. Even though the proposed AE in Chapter 3 can operate efficiently without cooling, still the heterodyne receiver may need cooling for the other receiver components (such as the mixer) to work efficiently at such high frequencies. However, in recent years, there is a strong interest in radio astronomy receivers operating at room temperature which would significantly reduce the costs and simplify the implementation since no cryogenic cooling is required. Following the brief introduction for nonlinear up-conversion receivers based on WGM (Sec. 1.3), in this Chapter, a detailed discussion of up-conversion systems is provided with explaining the main techniques for coupling the microwave radiation into the WGM resonator.

The estimation for the photonic efficiency is summarized with possible mechanisms for enhancing the system performance and increasing its photonic efficiency. Then based on such discussion, novel microwave/mm-wave schemes are proposed. To present different alternatives for the direct coupling of the microwave-radiation into the proposed scheme, different DRA elements and array with high gain, low cost, and low losses will be given. The measured results of the 3D-printed DRA element and array are presented.

The second half of this chapter is dedicated to another practical demonstration of the proposed up-conversion scheme. Here an integrated receiver system is provided for satellite missions for climate change forecasting at the mm-wave range (183 GHz). The effects of the fabrication and assembly tolerances are studied, then a phase-matching tuning mechanism is designed to compensate them and reduce the complexity of the manufacturing process.

4.2. Photonic efficiency estimation

The quality of the up-conversion scheme can be defined using its photonic efficiency (η) which is estimated as the ratio of up-converted photons per incoming input photons as follow:

$$\eta = \frac{P_{\pm}/\omega_{\pm}}{P_m/\omega_m} \tag{4.1}$$

Where $P_{\pm}$ and P_m are the power of the generated sideband (with frequency $\omega_{\pm}$) and input microwave power respectively.

This photonic efficiency can be estimated using the cavity model [117] where the resonator can be considered as a weakly coupled WGM cavity, with only three excited modes: microwave input signal, optical pump, and up-converted one. The system is assumed to work in the small-signal regime with undepleted amplitudes for both microwave and pump modes which means that the microwave power is much less than that of the optical pump. The fields are considered to be polarized mainly in a single direction so scalar electromagnetic equations can be used. The model is obtained by computing the total stored energy of the system and then obtaining the Hamiltonian with the quantized fields [118]. Using some simplifications following [50], the photonic efficiency can be expressed by

$$\eta = \frac{g^2 Q_p^2 Q_m}{\hbar\omega_\pm \omega_p^2 \omega_m} P_p \tag{4.2}$$

where P_p is the pump laser power, $\hbar$ is the reduced Planck's constant, Q_p and Q_m are the resonator quality factors at optical and microwave frequency respectively, and g is the nonlinear coupling rate which is defined as

$$g = 2\chi^{(2)} \frac{\omega_p}{n_p^2} \sqrt{\frac{\hbar\omega_m}{2\epsilon_0 n_m^2 V_m}} E'_m(r_p) \tag{4.3}$$

where $\chi^{(2)}$ is the second order susceptibility of the resonator material, n_p and n_m are the refractive indexes for resonator material at optical and microwave frequency respectively, $E'{}_m(r_p)$ is the normalized microwave electric field ($E'_m = E_m/E_m(max)$) at the radius where the optical signal is excited (r_p), and V_m is the mode volume of the microwave signal. By substituting the nonlinear coupling rate (4.3) into (4.2), the photonic efficiency can be estimated using the following form

$$\eta = \frac{2P_p}{\epsilon_0 \omega_\pm} \frac{{\chi^{(2)}}^2 Q_p^2 Q_m}{n_p^4 n_m^2} \frac{E'^2_m(r_p)}{V_m} \tag{4.4}$$

For fair comparisons, usually, the normalized photonic efficiency term is used which can be calculated by dividing the photonic efficiency (η) by the continuous wave (CW) pump power (P_p).

4.3. Enhancement of the photonic efficiency

As the common optically transparent materials have a relatively low $\chi^{(2)}$ on the order of a few pm/V, the main challenge of designing these kinds of up-conversion receivers is ensuring that they have high photonic efficiency. High-Q WGM resonators enhanced the fields interactions and achieved state-of-the-art normalized efficiencies (η/P_p) at mm-wave on the order of 10^{-7} [43], [119]. Our previous experiments showed a record measured normalized efficiency of 2.48×10^{-5} [120]. However, further enhancements in the photonic efficiency are still needed to make such up-conversion approach an excellent candidate for use in satellites, radio astronomy, and many other applications [121]. For example, in [122, 123, 124], we demonstrated that such up-conversion room-temperature receivers based on WGM would have better sensitivity compared to state-of-the-art room-temperature (or even sometimes cooled) mm-wave/THz LNAs and mixers [125, 126, 127, 128, 129, 130] in case high normalized photonic efficiency on the order of ($\eta/P_p = 10^{-2}$) or higher can be achieved.

As it can be seen from (4.4), the photonic efficiency can be divided into three terms. The first one cannot be significantly enhanced because it is related to the frequency (application) and optical pump power. Increasing this pump power could produce problems such as excessive noisy systems. Moreover, it will be mandatory to have a very strong pump suppression for detecting properly the up-converted signals.

The second term is related to the material choice of the resonator. Several nonlinear materials in disk or ring shapes have been reported for WGM resonators such as GaAs [131], [132], Gallium Phosphide (GaP) [133], Lithium Niobate ($LiNbO_3$),[134], Lithium Tetraborate ($Li_2B_4O_7$) [135], Quartz [136], and Zinc Selenide (ZnSe) [137]. Extensive comparisons between the properties of the most common nonlinear materials used for the WGM resonators can be found in [43], [48]. After analyzing several nonlinear materials and returning to the second term in (4.4), $LiNbO_3$ is seen to be a good choice as it implies a high optical Q-factor of 10^8 and an acceptable value for the susceptibility ($\chi^{(2)}$) of about 150 pm/V with reasonable refractive indexes to facilitate achieving the phase matching.

Finally, the third term represents the overlap between the two signals and mainly depends on the resonator geometry and the coupling scheme. This is the main reason for having low photonic efficiency, as, by default, the wavelength difference between the two signals, microwave or mm-wave signal (some tens or hundreds of GHz) and optical signal (193.55 THz corresponding to a 1550 nm laser) implies a very low interaction between photons. For example, Fig. 4.1 shows the analytical estimation of the optical WGM distribution in a $LiNbO_3$ disk resonator, following the expressions in [138]. This demonstrates that the optical mode only occupies a relatively very small area of a few optical wavelengths.

For comparison purposes, Fig. 4.2 describes both microwave and optical WGMs distribution for the previous experiment using a $LiNbO_3$ disk resonator [120]. Although this experiment presents a record measured normalized efficiency of 2.5×10^{-5} at the mm-wave range, there is still a big room for enhancements as only small parts of microwave photons actually hits the optical ones. So enhancing this third term means decreasing the microwave mode volume (in other words, increase the intensity of the field) and/or trying to push it to the rim of the resonator (where the optical signal is circulating). This physically means allowing more microwave photons to interact with the optical ones.

In [139], we propose the use of a silicon lens as general microwave coupling scheme for increasing the intensity of the field inside the resonator which will in turn decrease

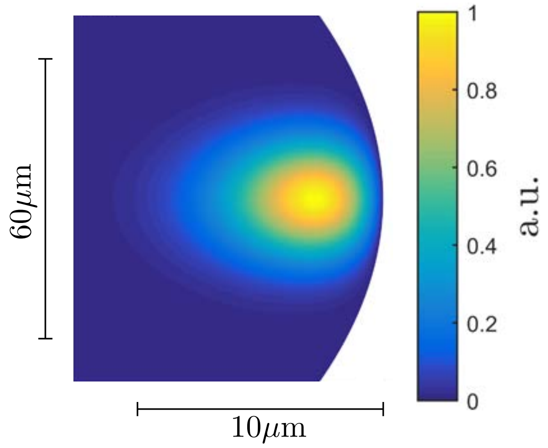

Figure 4.1: The field distribution of an optical WGM inside a disk resonator at 1550 nm.

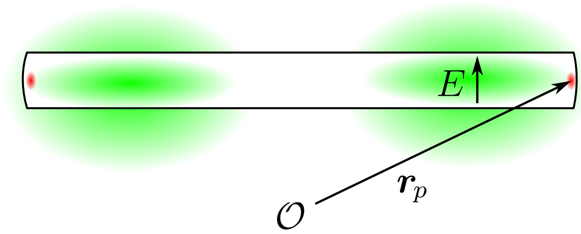

Figure 4.2: Microwave and optical WGMs field distribution in a disk resonator.

its mode volume. Additionally, this scheme will solve the main drawback of the standard coupling scheme using DRW which is the need for bulky interfaces for coupling the free-space radiation into them such as metallic horn antennas and transitions. As here the direct coupling of the free-space radiation is performed decreasing the receiver cost and size and avoid the losses coming from these interfaces. The system is analyzed following the developed analytical framework in [140]. Although the previous scheme shows that the lens increases the intensity of the microwave field around six times [141] compared to the free-space beam coupling scheme without the lens, the photonic efficiency of the receiver still low.

Another possible method for enhancing the mentioned third term is to use a low-thickness resonator and drill a hole in it, making it a thin ring resonator [50] as illustrated in Fig. 4.3. The modification here is only in the resonator while keeping the same standard microwave coupling scheme of DRW. Such solution will partially satisfy these two requirements (decreasing the microwave mode volume and pushing it to the resonator rim), but it is still unable to provide very high photonic efficiency. This is because achieving very high overlapping requires very small resonator thickness. However, very small thicknesses cause the microwave field to start fringing from the edges of the resonator which in turn, negatively affects the overlapping. To reduce such fringing effect and force the field to be confined in a very low-thickness resonator and only in a small area near its

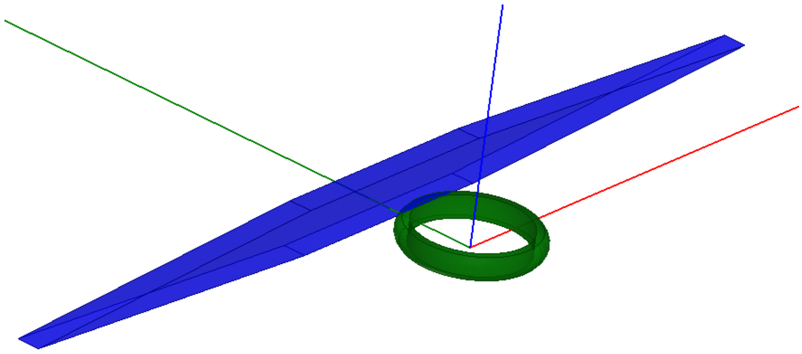

Figure 4.3: Ring WGM resonator with DRW standard coupling scheme.

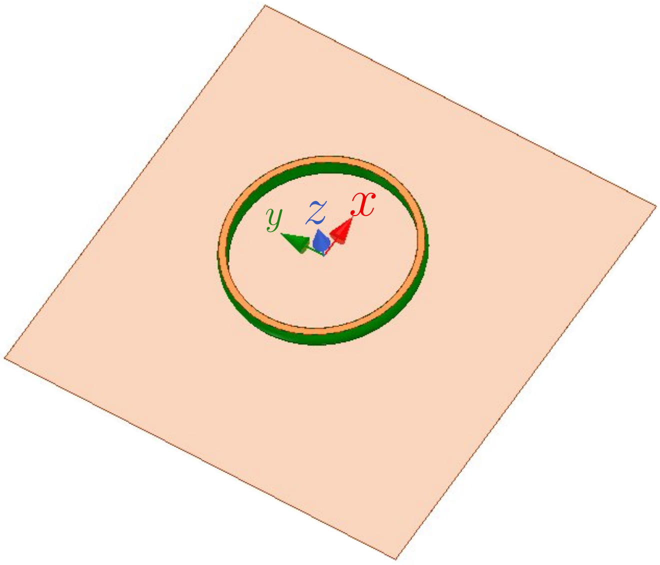

Figure 4.4: Proposed WGM resonator with high photonic efficiency, (a) XY view, (b) YZ cut, and 3D view.

rim, the addition of a metallic strip and ground plane has been proposed as shown in Fig. 4.4 [142].

The analysis of several metal-enclosed resonators from the same material ($LiNbO_3$) has been performed using the eigenmode solver of HFSS software. The resonators have a similar radius and are different in thicknesses and widths. The simulation results show that this modified metal-enclosed resonator will significantly enhance the overlap between the microwave and optical WGMs. This can be visibly seen in Fig. 4.5 which depicts the microwave and optical modes for the disk-resonator shape that provides the previously mentioned record efficiency [120] and the modified metal-enclosed proposed one with the obtained normalized efficiency for each case.

The proposed metal-enclosed WGM resonator has a predicted normalized photonic conversion efficiency on the order of 12% per milliWatt of pump power which is 5000

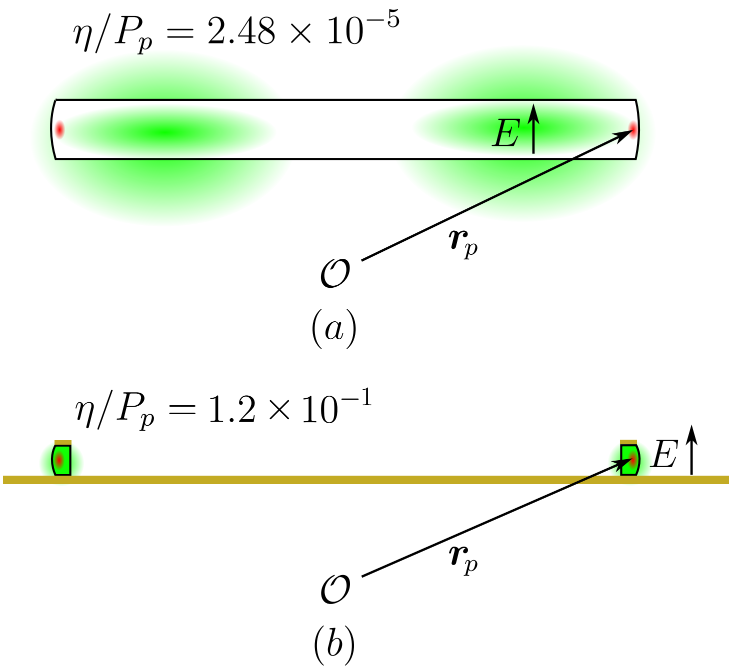

Figure 4.5: Comparison between mm-wave mode for (a) a disk resonator, (b) the proposed metal-enclosed resonator.

better than the one obtained in [120]. Even with considering the mismatching between measured and simulated results, one order of magnitude reduction is expected as it is shown in [50] which means that the expected measured efficiency is still 500 better than the record efficiency.

This overall improvement of 5000 is coming from the increase of the factor $E'^2_m(r_p)$ by more than 13 times and the reduction in the volume (V_m) of about 150 times. Knowing that all other parameters of (4.2) will remain almost the same (as the resonator is made from the same material) except the microwave quality factor Q_m as it will be reduced by quarter after the addition of the metal. Also, as it has been mentioned previously in this chapter for this up-conversion scheme, the proposed system can be scaled easily for providing such very high efficiency for different frequency ranges which would be interesting for several radio astronomy applications. In Sec. 4.4, the proposed scheme would be adjusted to work as a radiometer for 12 GHz CMB spectroscopy. While a similar scheme, after some modifications to have a complete integrated feasible system, would be presented in Sec. 4.6 for 0.2 THz water vapor measurements and climate change forecasting.

4.4. Microwave coupling scheme for the proposed resonator

DRWs are commonly used to efficiently couple radiation to WGM resonators for microwave and mm-wave ranges [143] (as the one in Fig. 4.3). Here, they would be bulky and hard to couple to such electrically tiny metal-enclosed resonator. Different feeding methods have been tested for such updated structure, arriving to the conclusion that the

Table 4.1: The parameters of the microwave coupling scheme.

Parameter	R_r	H_r	r_r	g	W_{wg}	H_{wg}
Value (μm)	3719	100	1225	10	100	100

microstrip line is the best to fit for the radiation coupling. Hence, a microstrip transmission line with silicon substrate is placed near the resonator for evanescent coupling as shown in Fig. 4.6 with its parametric values in Table 4.1. Here, P_2 is connected to the antenna directly (or to a transition then the antenna) and P_1 to a matched load or to the other resonators in case of using an array of WGM resonators for having wider up-conversion BW.

To have an efficient microwave coupling, three goals have to be met. Firstly, the system resonates at the designed frequency with the proper WGM mode to fulfill the phase-matching and energy conservation conditions so the microwave angular velocity would be equal to the optical one. By default, this is tricky to be achieved as the refractive indices of the two signal are far away [144]. Secondly, at this resonance frequency, all the input microwave signal is coupled to the resonator which can be achieved by having a very low transmission coefficient between the input and output (S_{12}). Thirdly, no power is reflected back (small reflection coefficient S_{11}) which means that the WGM inside the resonator is pure traveling mode.

To consider such mismatching caused by the coupling mechanism, the photonic efficiency can be updated by including the microwave power reduction factor as following:

$$\eta = \frac{2P_p}{\epsilon_0\omega_\pm}\frac{\chi^{(2)^2}Q_p^2Q_m}{n_p^4n_m^2}\frac{E'^2_m(r_p)}{V_m}(1-|S_{12}|^2-|S_{11}|^2) \tag{4.5}$$

The S-parameters for the microwave coupling scheme are shown in Fig. 4.7 which clearly demonstrates that this microwave scheme achieves the mentioned three goals. Figure 4.8 presents the microwave field distribution which confirms the exciting of a $M = 4$ WGM at 12 GHz. Also, as expected from the low S_{12} in Fig. 4.7, almost all microwave power is coupled into the resonator leaving a negligible power level at the output port.

With this proposed microwave coupling scheme, DRA fed by an aperture-coupled microstrip line can be easily used to collect the microwave radiation and deliver it to the scheme to be coupled later to the proposed metal-enclosed WGM resonator as shown in Fig. 4.9. In comparison to the standard DRW with transitions, DRA with microstrip provides three major advantages. Firstly, the relatively easier fabrication with low cost and compact size. Secondly, the ability of the direct coupling of the radiation into the resonator without the use of bulky interfaces such as transitions or horn metallic antennas which will significantly enhance the performance by avoiding the extra losses from these elements. Thirdly, a reasonable gain comparable to DRW antennas or horn antennas with the availability to extend to an array version without the increase in system complexity or losses as will be explained in Sec. 4.5.2.

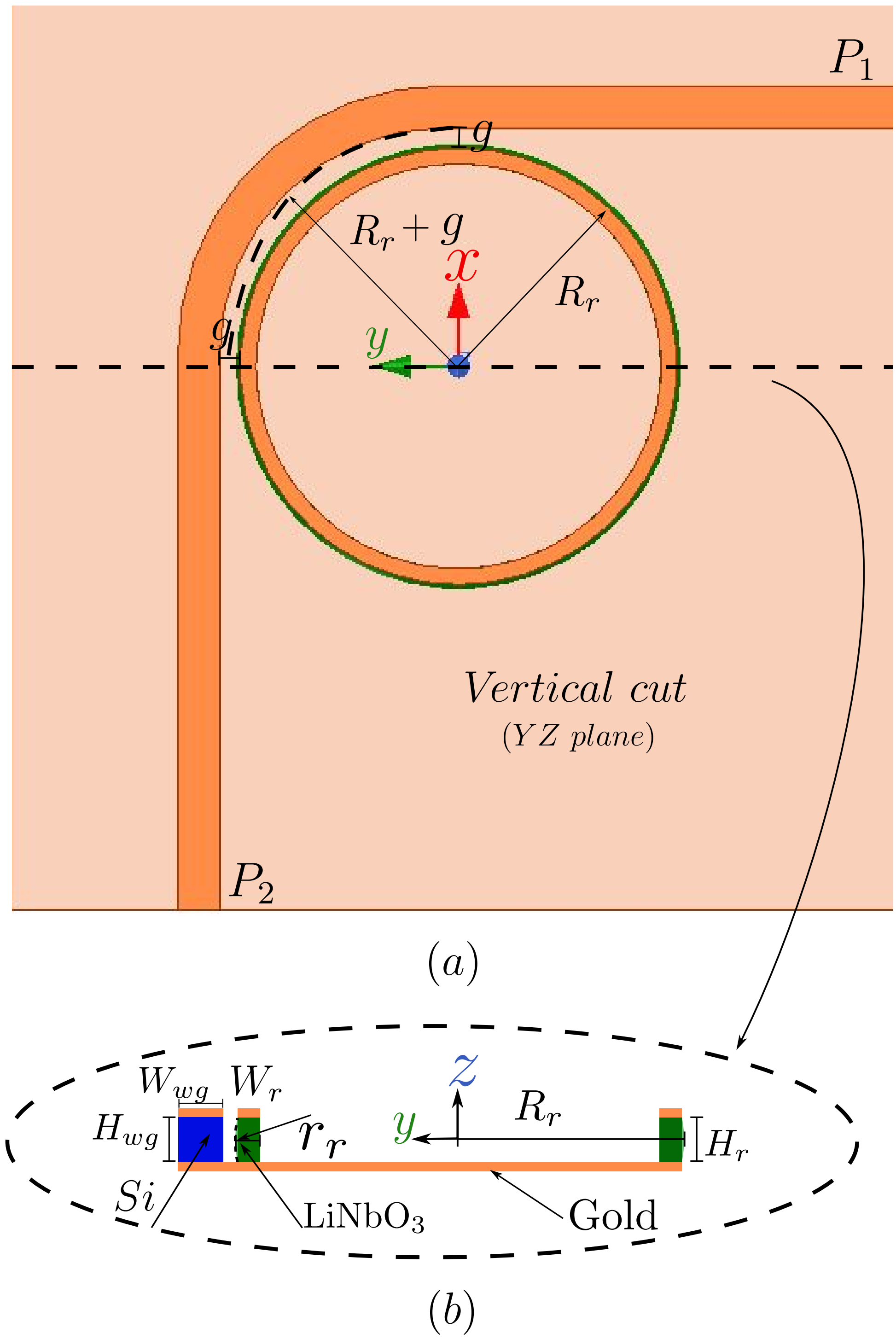

Figure 4.6: Microwave coupling scheme for the proposed metal resonator, (a) top view, (b) vertical cut.

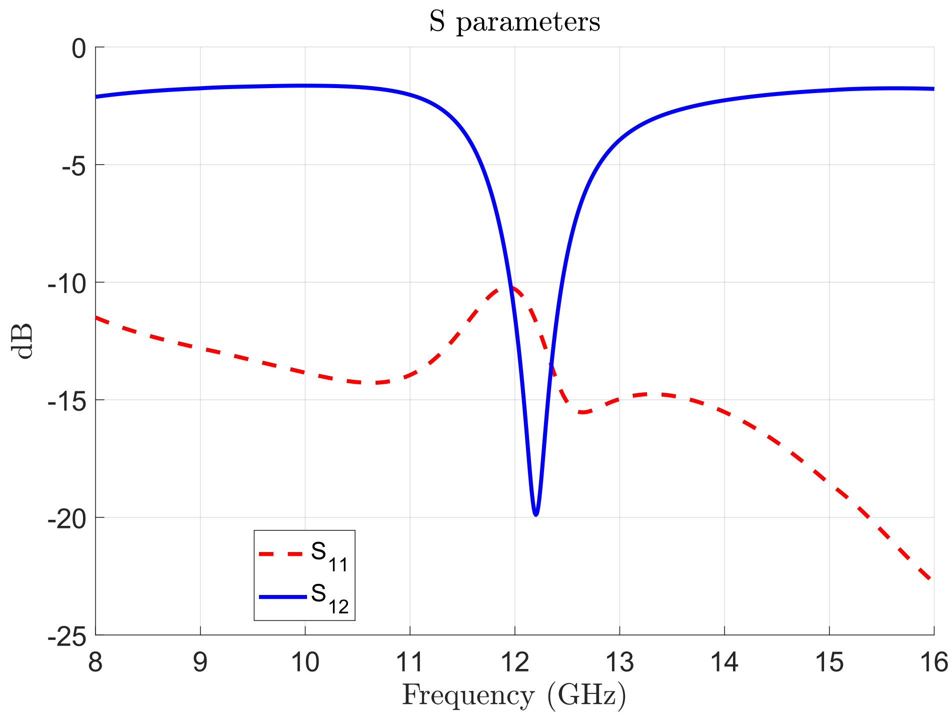

Figure 4.7: S-parameters for the microwave coupling scheme.

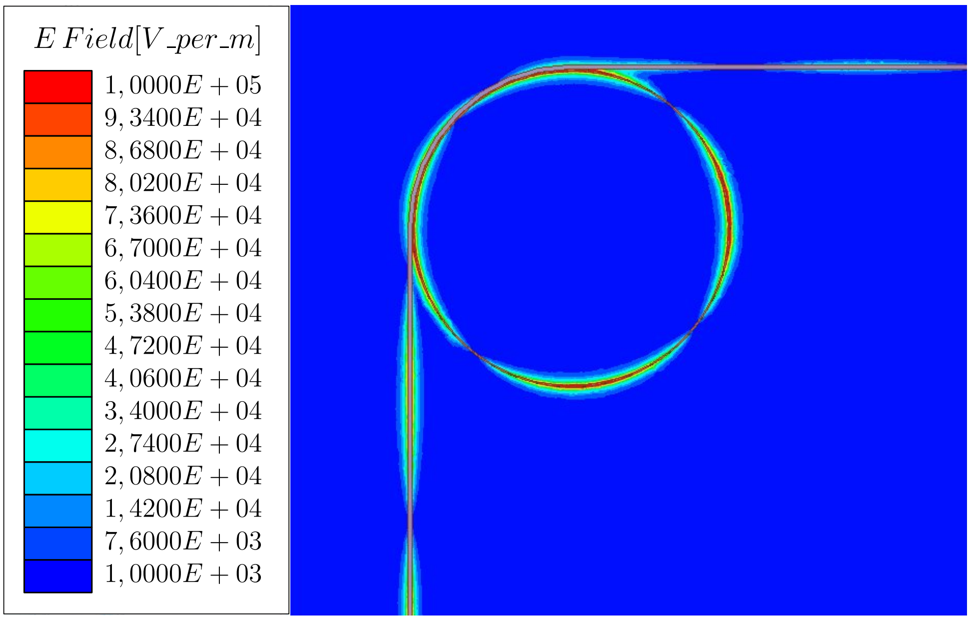

Figure 4.8: The total electric field distribution along the microwave scheme at 12 GHz.

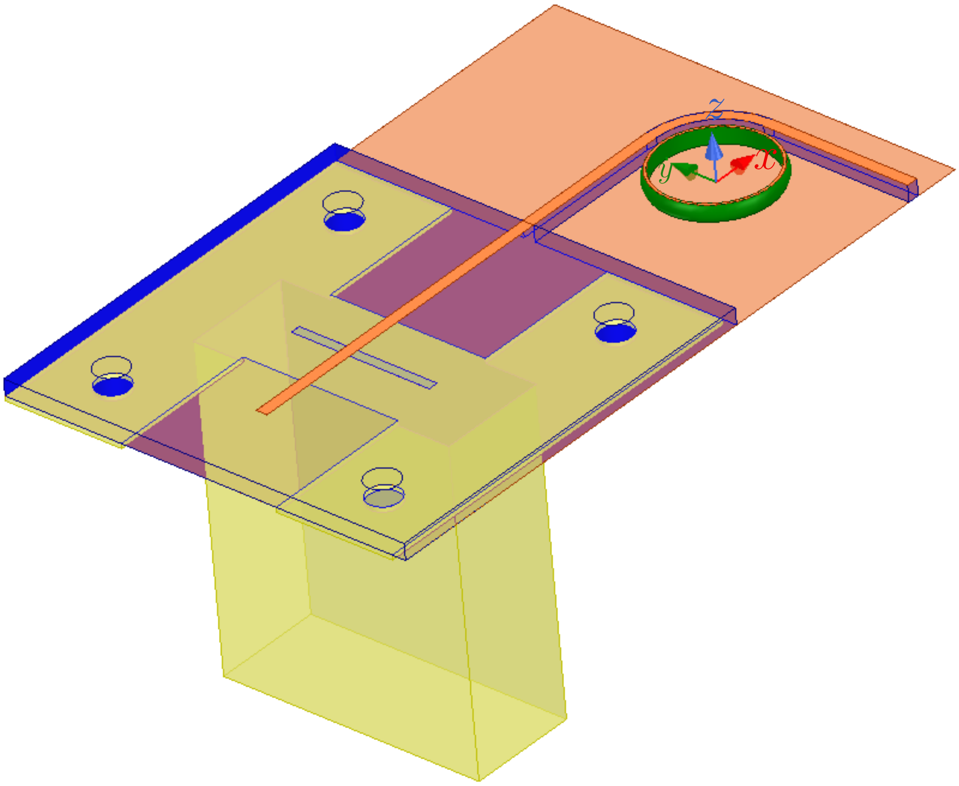

Figure 4.9: DRA connected to the proposed microwave coupling scheme.

Table 4.2: Single-element DRA parameters.

Parameter	W_a	L_a	H_a	W_g	L_g	W_s	L_s	W_m	L_m	L
Value (mm)	17.5	6.25	19.13	25	25	0.9	5.5	1.13	20.77	12.5

It is worth noting here that even for the standard case of the dielectric resonators (as in Fig. 4.3), DRA fed by DRW without transitions can be used too for obtaining the aforementioned advantages as we proposed in [145].

The design parameters of the DRA fed by an aperture-coupled microstrip line are depicted in Fig. 4.10 with their numerical values in Table 4.2. The antenna has been 3D-manufactured using a BCN3D Sigma printer which simplifies the fabrication and decreases its cost. Such technique provides an acceptable accuracy of $\pm 20\,\mu$m which agrees well with the design tolerances. The dielectric element is made of Polylactic Acid (PLA) and is connected to the substrate at the end of the process via two dielectric arms and four nylon screws. Also to facilitate this proof of concept, the Si substrate is replaced by a thicker Arlon one.

Figure 4.11 shows the reflection coefficient of the manufactured single-element DRA in comparison to its simulation result in dashed-black and solid-red respectively. It demonstrates that the antenna is working at the required frequency with a small mismatching between both results which can be due to the assembly tolerances.

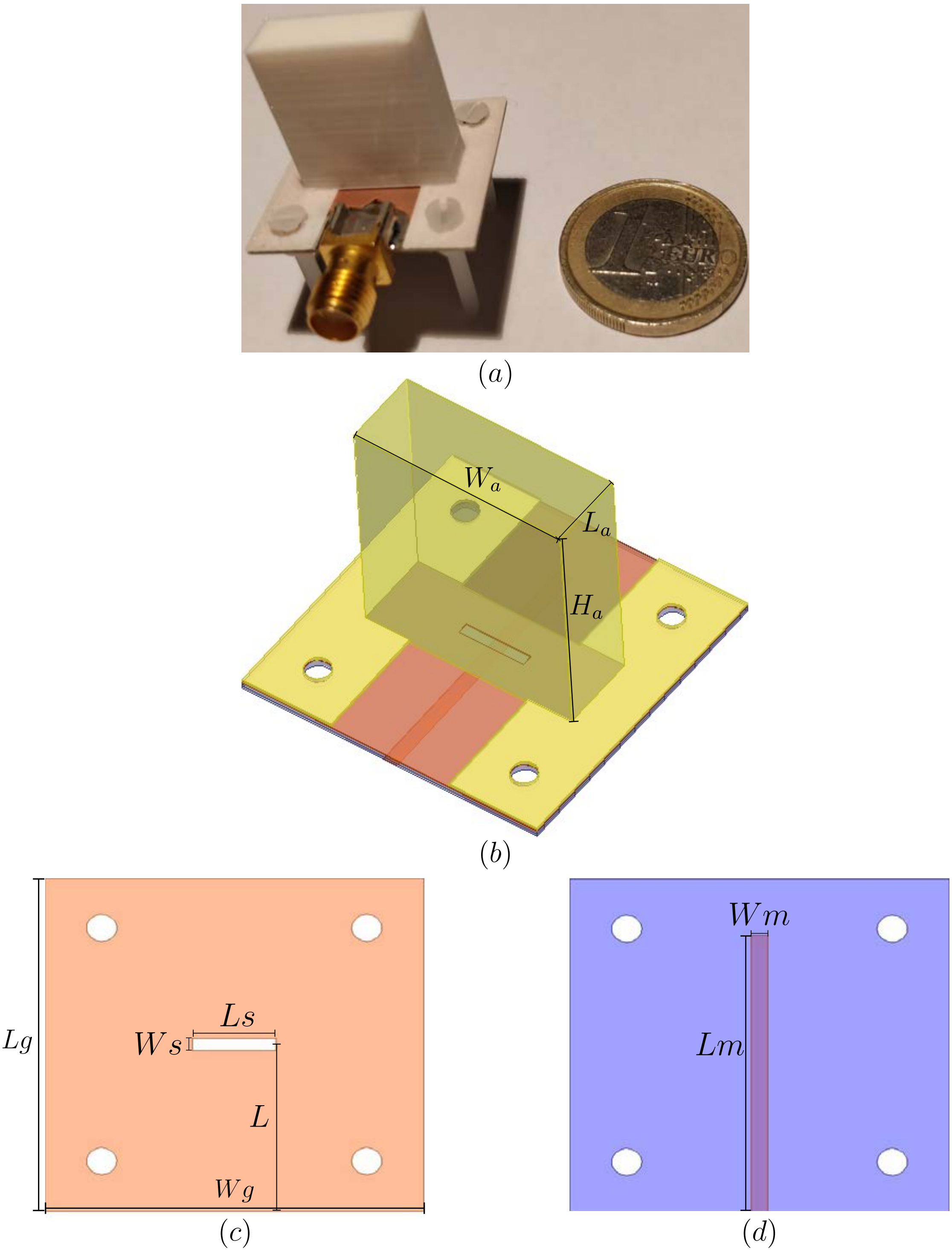

Figure 4.10: Single-element DRA structure (a) fabricated prototype, (b) 3D view, (c) upper, and (d) bottom layers of the aperture-coupled feed.

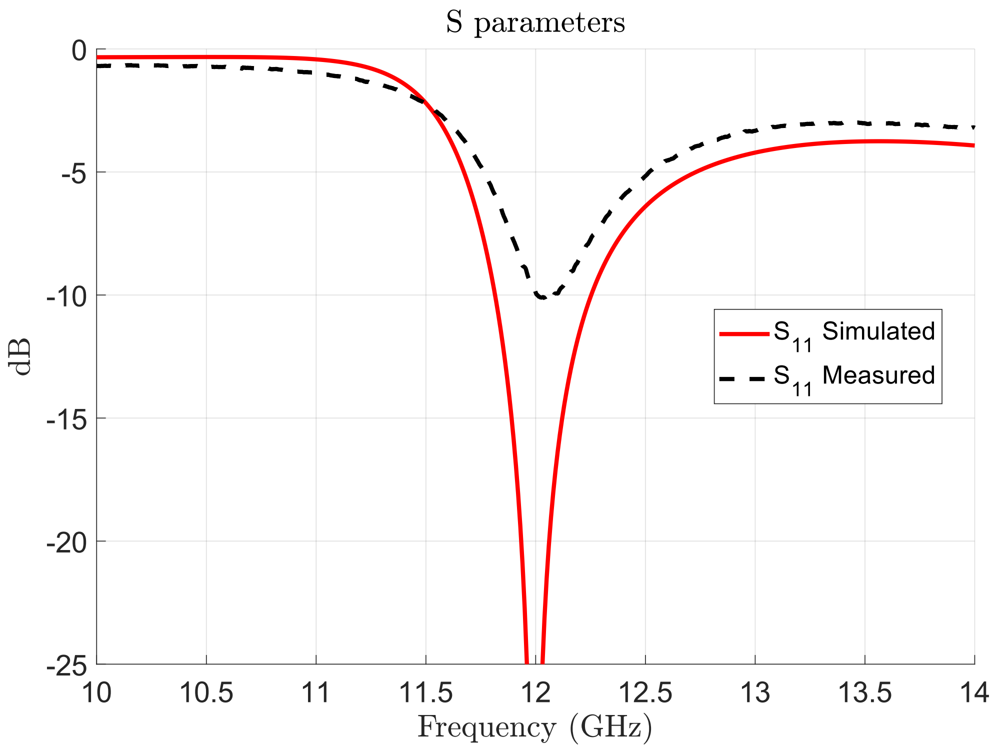

Figure 4.11: Measured and simulated S_{11} of single-element DRA.

The radiation patterns are presented in Fig. 4.12 for E-plane and H-plane for simulated and measured patterns in red and black color respectively with showing the measured cross-polar patterns in blue. The radiation patterns have a high level of matching between the simulated and measured results with a Co/Xp-ratio at broadside greater than 25 dB.

4.5. DRA for better microwave coupling

Although DRAs provide interesting results when they are used for WGM microwave coupling, some applications still need higher gain, especially for the very weak CMB signals. Typically, DRA element has a medium gain of about 5 to 6 dBi [146] which unfavorably affects the other DRA advantages. Three main techniques can be used singly or together to enhance its gain, firstly, forcing it to work at higher-order modes, secondly, modifying the standard dielectric shape, and thirdly, assembling different DRA elements to form an array that is capable of achieving relatively higher gains.

4.5.1. High gain DRA single-element

Regarding the first technique, the rectangular DRA which lies over a metal ground plane as in Fig. 4.10 can be analyzed as a short magnetic dipole. By increasing the element height, more field lobes are excited which can be approximated by an array of short dipoles [147]. So, using simple array theory, the higher-order modes as TE_{113} or TE_{115}

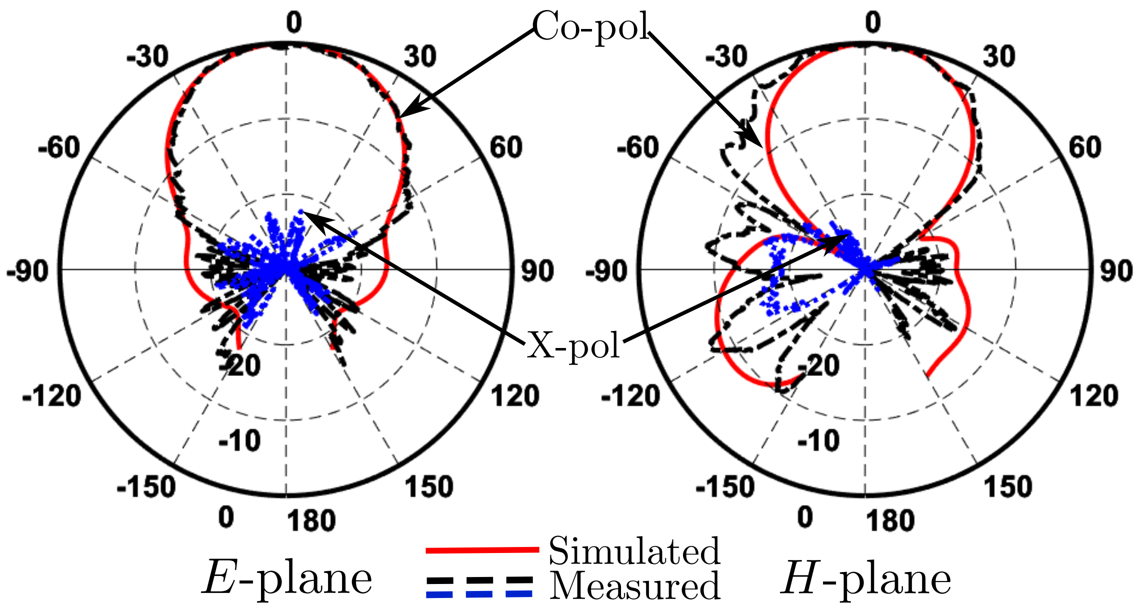

Figure 4.12: Measured and simulated radiation patterns of single-element DRA.

would act as an array of two and three dipoles above the ground plane respectively (or as three and five dipoles respectively after removing the ground plane and applying the image theory). This would produce a higher gain around 2 to 4 dB compared to the same antenna working at the fundamental TE_{111} mode depending on the spacing between the field lobes and the aspect ratio of the dielectric element.

Because of this, in the previous section (Sec. 4.4), the proposed rectangular DRA height was adjusted to operate in the higher-order modes. This can be demonstrated by seeing Fig. 4.13 which presents the magnetic field distribution inside the DRA in the H-plane (X-Z plane). This field distribution demonstrates that the antenna at 12 GHz is working on TE_{113} mode as there are one and half lobes which appear above the ground and the same is expected to be below the ground too (if the image theory is used to remove the ground plane). The antenna produces a peaked gain of about 9 dBi in the broadside direction ($\theta = 0°$) as shown in Fig. 4.14. Such high gain outperforms DRA elements which operate at TE_{113} [147], [148].

For the second technique, the dielectric element can be adjusted in different shapes to achieve higher gain. For example, the same previous DRA can provide a higher gain of about 11 dBi if the rectangle dielectric is replaced by a pyramidal horn shape as shown in Fig. 4.15. This implies keeping all the DRA parameters except the dielectric length which is tapering from the previous length (L_a = 6.25 mm) to a larger one (L_{a2} = 25 mm). So here, the overall antenna dimensions (W_g, L_g, H_a) and the substrate (with its feeding structure) are all identical. It can be seen from Fig. 4.16 that the antenna still resonates at the same frequency but with a higher gain of about 2 dB.

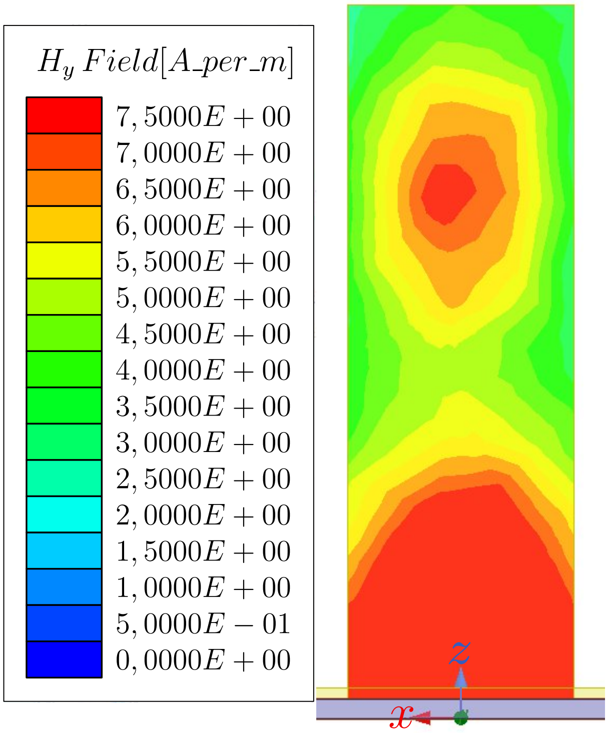

Figure 4.13: Normal magnetic field component inside the DRA.

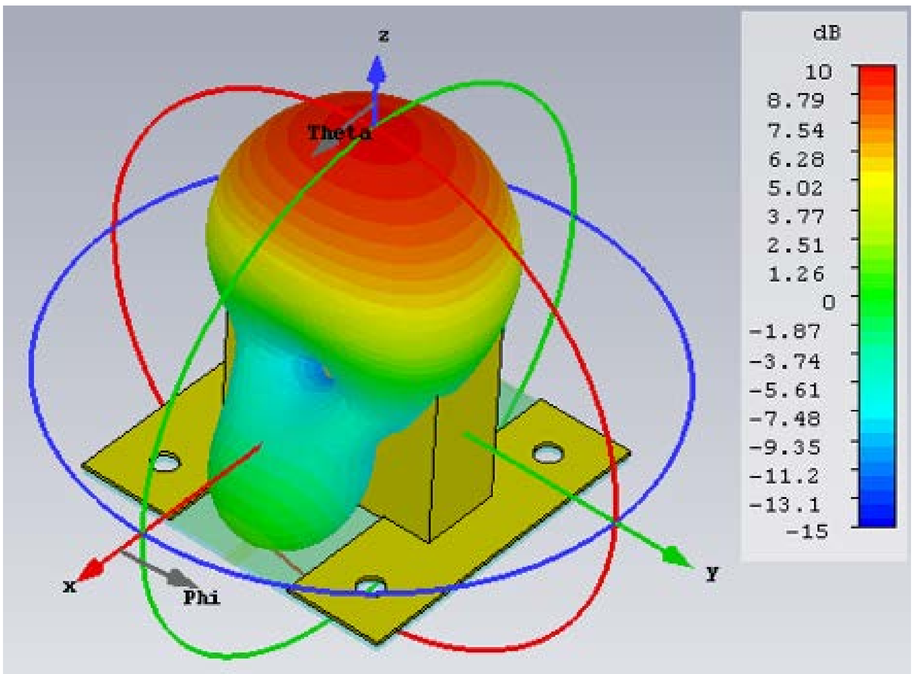

Figure 4.14: Realized gain of the DRA.

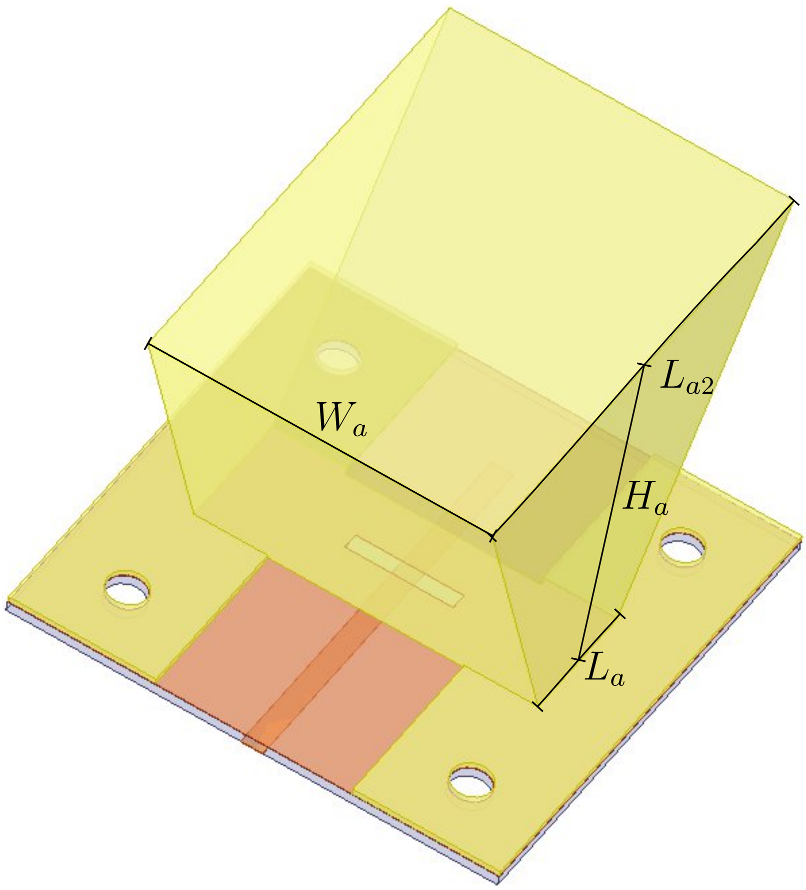

Figure 4.15: Pyramidal horn DRA shape.

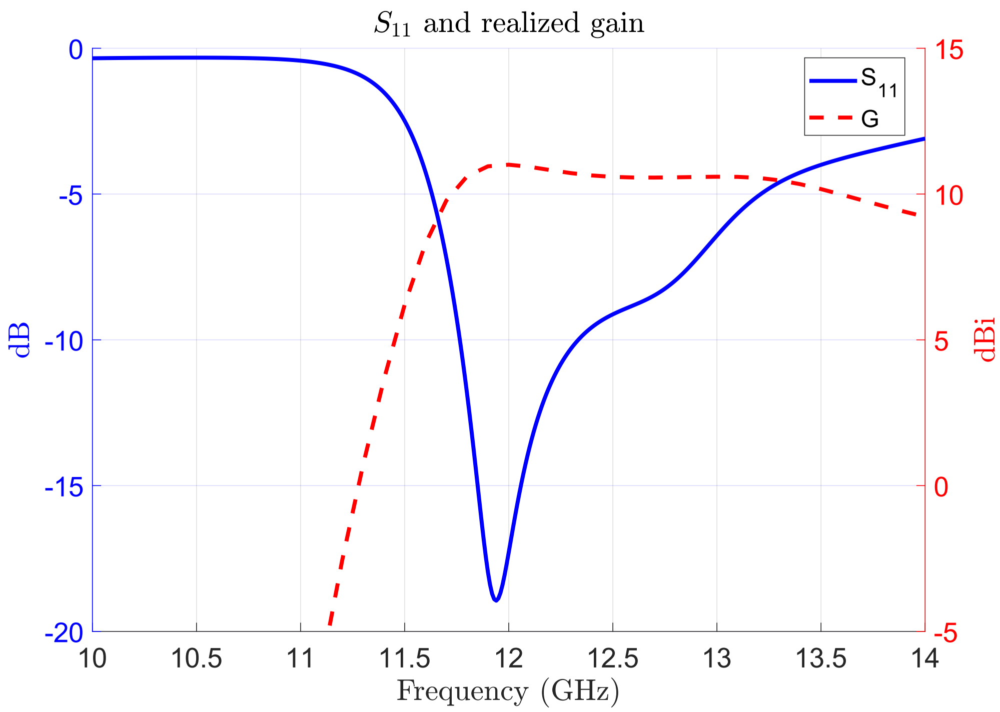

Figure 4.16: S_{11} and realized gain of the pyramidal horn DRA.

4.5.2. High gain DRA array

The third technique for providing high gain is to use an array of DRA elements. Despite the fact that corporate-feeding networks have been used for years as a standard feeding method for DRA arrays, they require several quarter-wavelength transformers and power dividers. Such microstrip discontinuities cause spurious radiation, resulting in high losses especially at high frequencies [149], [149]. Hence, two other state-of-the-art feeding methods, Dielectric Image Guide (DIG) [150] and Substrate Integrated Waveguide (SIW) [151] have been widely used to feed DRA arrays in replacement of the corporate-feeding networks.

However, for this WGM nonlinear up-conversion receiver, both have main limitations. For example, for DIG, considerable back radiation is a major issue [150] in addition to the need of tapered rectangular waveguides for launching the DIG itself which, in turn, make the structure bulky and increase the fabrication cost and losses [152]. Similar issues in SIW as the antenna suffers from significant leakage losses through the metallic vias [153] besides its complex manufacturing. All the previous critical points affect the main advantage of the DRA for being a high radiation efficiency antenna with low cost, simple manufacturing process, and easy to be integrated into the microwave coupling scheme.

Following the previous conclusions, a novel feeding method for DRA arrays based on the concept of standing-wave is developed [154] in collaboration with Southern Methodist University, USA. The standing waves are formed in dielectric bridges covered by metal between the elements. This feeding method effectively excites the entire DRA array structure uniformly with a single feed without the need of any power dividers, transitions, or launchers as shown in Fig. 4.17. Compared to other antenna arrays such as DRW antenna arrays [101] or even DRA arrays fed with standard feeding methods, this proposed feeding technique avoids the losses, extra cost, extra complexity coming from such components, as well as facilitating the alignment process.

As a proof of concept, a DRA array prototype based on the proposed feeding method is manufactured to be working at 5.6 GHz. The impedance of the whole array can be easily matched in the same way as the single DRA by optimizing the aperture slot size along with the stub length (which is defined as the length from the slot center to the end of the microstrip feed line). Figure 4.18 presents the simulated and measured reflection coefficient of the array, it shows that the measured impedance is 35% which is close to the bandwidth of the array element. Further wider bandwidths can be achieved by changing the array element itself, for example, by using a stack of different materials [155] or same material but with different sizes [156].

As expected from removing the power dividers, transitions, and launchers, this feeding technique significantly enhances the array radiation efficiency. This is confirmed by seeing the radiation efficiency in Fig. 4.19 which presents a high value of about 88% with almost flat behavior over the operating band. This is around 20% higher than DRA arrays of comparable number of elements [150]. Also, this feeding technique simplifies

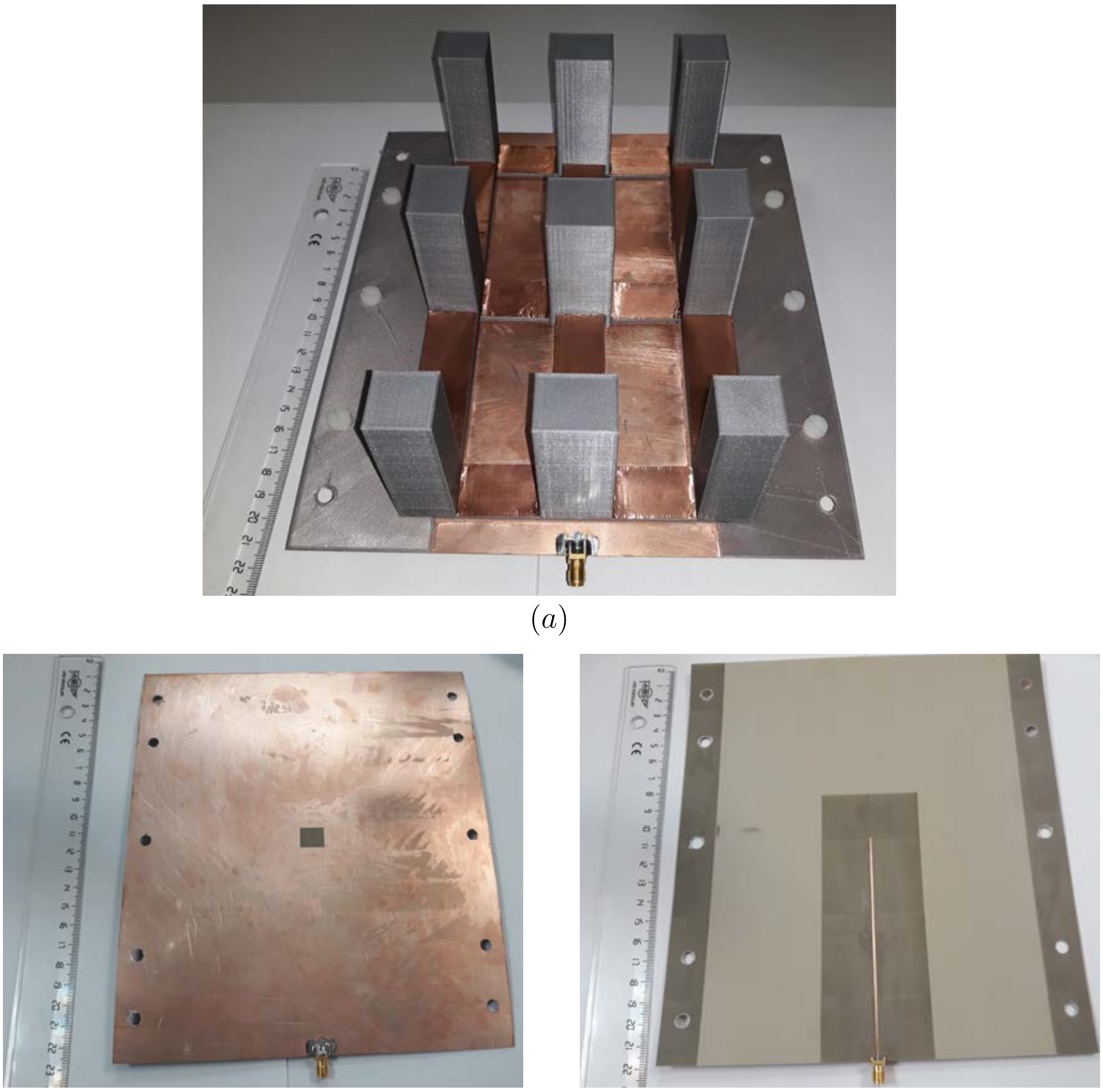

(a)

(b) (c)

Figure 4.17: DRA array structure based on standing-wave (a) fabricated prototype, (b) upper, and (c) bottom layers of the aperture-coupled feed.

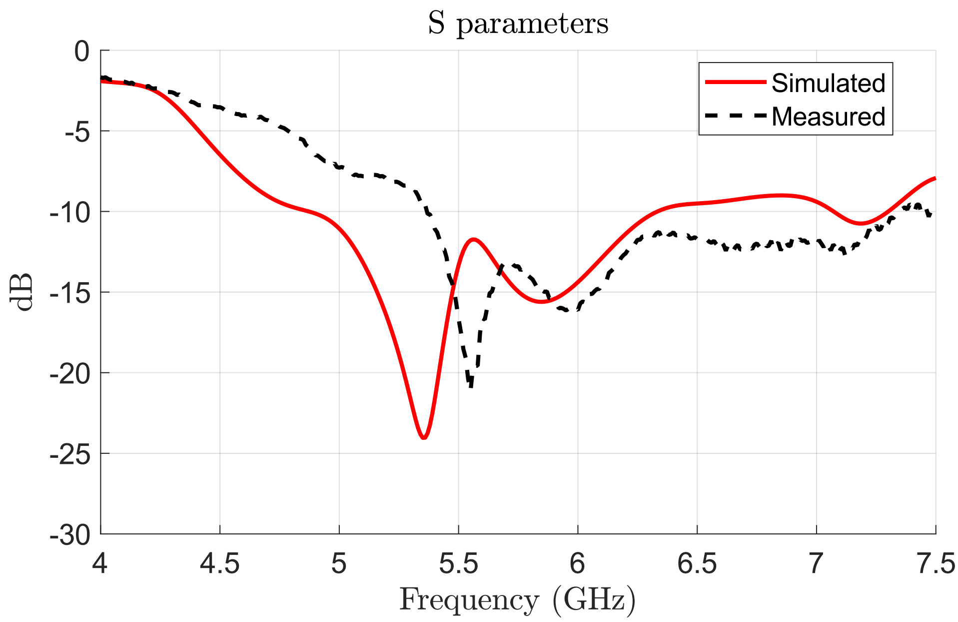

Figure 4.18: Measured and simulated S_{11} of DRA array.

the fabrication and alignment processes and decreases their costs as the whole array is 3D-printed as a single piece.

The previous remarks enable the array to provide high gain as demonstrated in Fig. 4.20 which depicts a high level of matching between the simulated and measured gain. The nine-element array presents a measured gain at the center frequency of 15 dBi which is around 7 dB higher compared to the gain of the array element. Such high gain outperforms DRA arrays based on other feeding techniques. For example, with comparable number of DRA array elements, DIG and SIW have less gain of 7.61 dBi [150] and 11.5 dBi [151] for seven- and eight-element arrays respectively.

All the mentioned advantages are coming with the simple system integration in the same way as the single DRA element which makes it so useful for several wireless applications. Besides, this novel feeding technique is applicable to an array with a large number of elements with similar performance and the same simple design/manufacturing procedures.

4.6. Integrated mm-wave satellite radiometer with high photonic efficiency

In this Section, a practical example for an up-conversion receiver would be presented which is used for CubeSat earth observation at 183 GHz for water vapor profile measurements [54]. As it is discussed in Sec. 1.3, up-converting this 183 GHz mm-wave radiation into the optical domain makes them less affected by the relatively weak thermal noise even without the cooling conditions. The system needs to be fully integrated for proper implementation in the satellite environment.

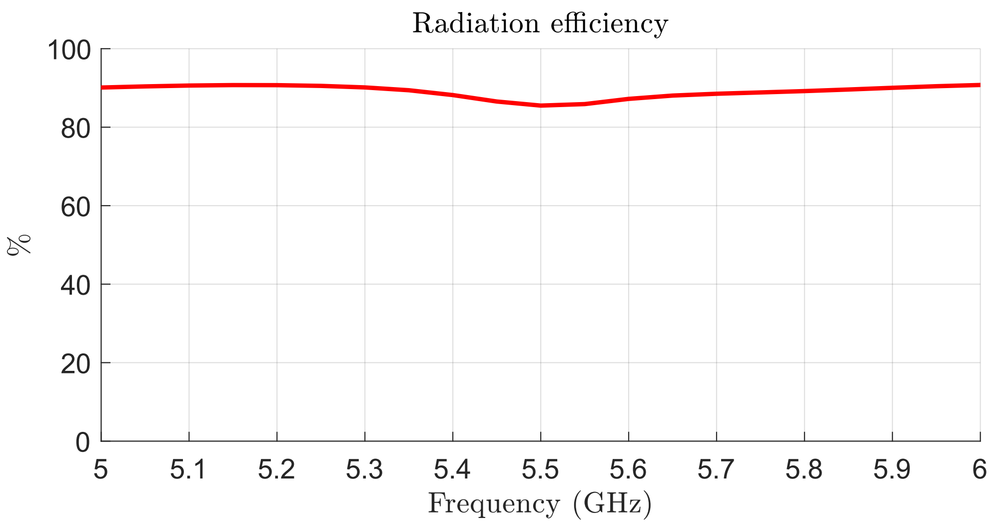

Figure 4.19: Radiation efficiency of DRA array.

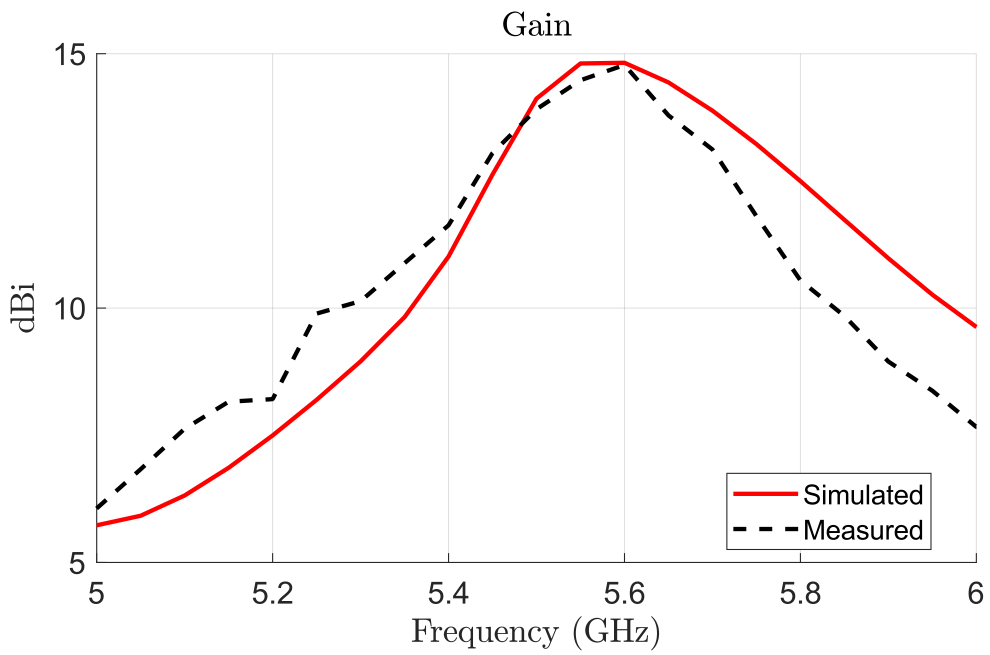

Figure 4.20: Measured and simulated Gain of DRA array.

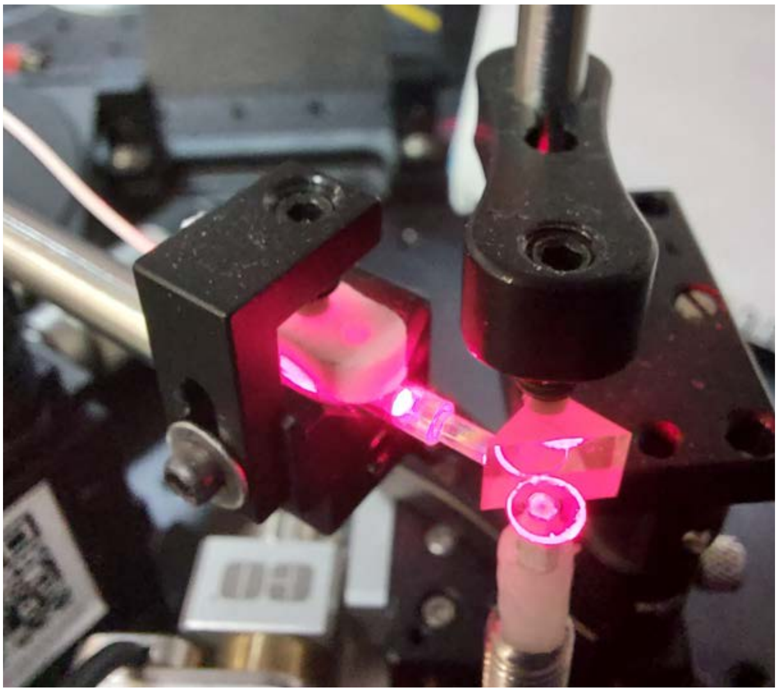

Figure 4.21: Coupling of the optical WGM into the resonator using prism.

Following Sec. 4.3, for increasing the photonic efficiency of this up-conversion scheme, the resonator is placed between two metals forming a microstrip-like resonator to force confining the mm-wave signal to sub-wavelength region and working at quasi Transverse Electromagnetic (TEM) mode configuration. This enables the resonator to have a much lower thickness (tens μm instead of hundreds or thousands μm) which would be close to the optical mode thickness.

Furthermore, the upper metal has a ring-form that forces the mm-wave signal to be pushed towards the resonator rim which will maximize the $E'_m(r_p)$ factor and increase the interaction between the signal photons. Ultimately, because the mm-wave is already well-confined near the resonator rim, no need to drill a hole in the resonator and the ring resonator can be replaced by a standard disk resonator which will significantly relax the fabricating and keeping the same performance.

4.6.1. Proposed up-conversion scheme

The resonator is made of $LiNbO_3$ and has a radius (R_{res}) of 488 μm with a thickness (H_{res}) of 60 μm. This ensures the phase matching at the frequency of interest at 183 GHz in case the proper mm-wave WGM mode is excited, which is here $M = 4$. Hence, four wavelengths of the mm-wave are circulating inside the resonator at the intended frequency.

The coupling of the optical signal which is coming from the laser is performed using standard prism coupling. Figure 4.21 shows a general example of exciting an optical visible WGM in a $LiNbO_3$ disk resonator using a prism. Two points are considered for

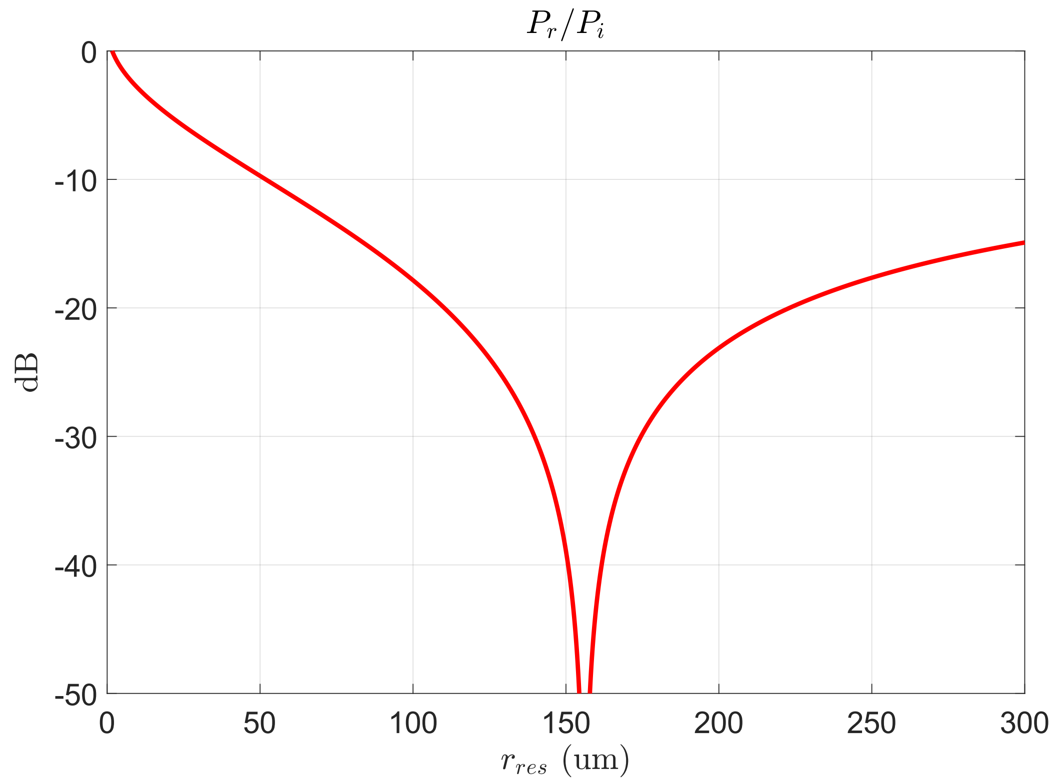

Figure 4.22: Ratio between reflected optical power to the incident one vs resonator curvature radius.

better coupling of the optical signal (to couple most of the laser power) and maximize the intra-cavity power to be orders of magnitude larger than the incoming pump laser. Firstly, the prism angle is set to be equal to the angle of incidence for a normal optical signal incidence with an angle of 64°. This exceeds the critical angle between prism material and air, hence the expected evanescent field needed to couple the signal into the resonator is created in the air gap region. Secondly, instead of a sharp outer edge of resonator, it has a curvature (r_{res}) of 150 μm which is optimized following [157] as is shown in Fig. 4.22 to have a negligible reflected optical power.

Figure 4.23 sketches the proposed mm-wave and optical coupling with a transition to the standard metallic rectangle waveguide working at such frequency range (WR5). The resonator is placed between a ground (at the bottom) and a metal ring (at the top) with a microstrip line for mm-wave coupling. The light-orange parts represent hollow metal boxes filled with air. For the two WR5 metallic waveguides, only the hollow rectangle cross-sections are drawn as the background is assigned as Perfect Electric Conductor (PEC) by default.

Figure 4.24 demonstrates that the microstrip efficiently couples the mm-wave signal at the designed frequency which ensures fulfilling the phase-matching condition. Similar to what is shown for the microwave up-conversion system in Sec. 4.4, the extremely low value for S_{12} means that most of the mm-wave power is coupled to the resonator without

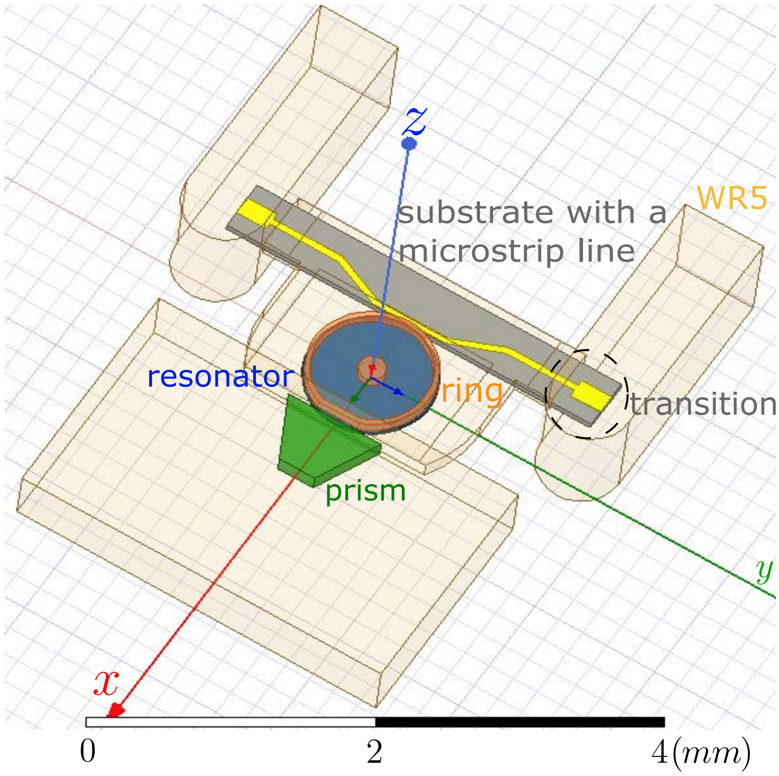

Figure 4.23: The up-conversion scheme with microstrip and prism for mm-wave and optical coupling respectively.

losing power in transition to the output port. Additionally, low S_{11} means that the mode is pure traveling and there is almost no reflection back to the input port.

The prism shape and dimensions are carefully designed to have negligible effects on the mm-wave coupling in the resonator which is confirmed by seeing the relatively weak fields excited in it in Fig. 4.25 which shows the electric field distribution over the system components. Figure 4.25 demonstrates the excitation of the proper mode ($M = 4$) to achieve the phase-matching condition. The normal electric field component E_z (normal to the resonator surface) is the dominant component inside the resonator as it appears in Fig. 4.25(b) while it is negligible inside the metallic waveguide as it works at the fundamental TE_{10}.

Figure 4.25 proves also that the field is well confined at the resonator rim which increases the overlapping between the two signals and hence giving a higher photonic efficiency. Following (4.4), the estimated normalized efficiency is 10^{-2} which is around five orders of magnitude higher than state-of-the-art up-conversion systems using WGM resonators at mm-waves [119] and three orders of magnitude more compared to the recent experiment using a $LiNbO_3$ disk resonator coupled by DRW with a record efficiency [120].

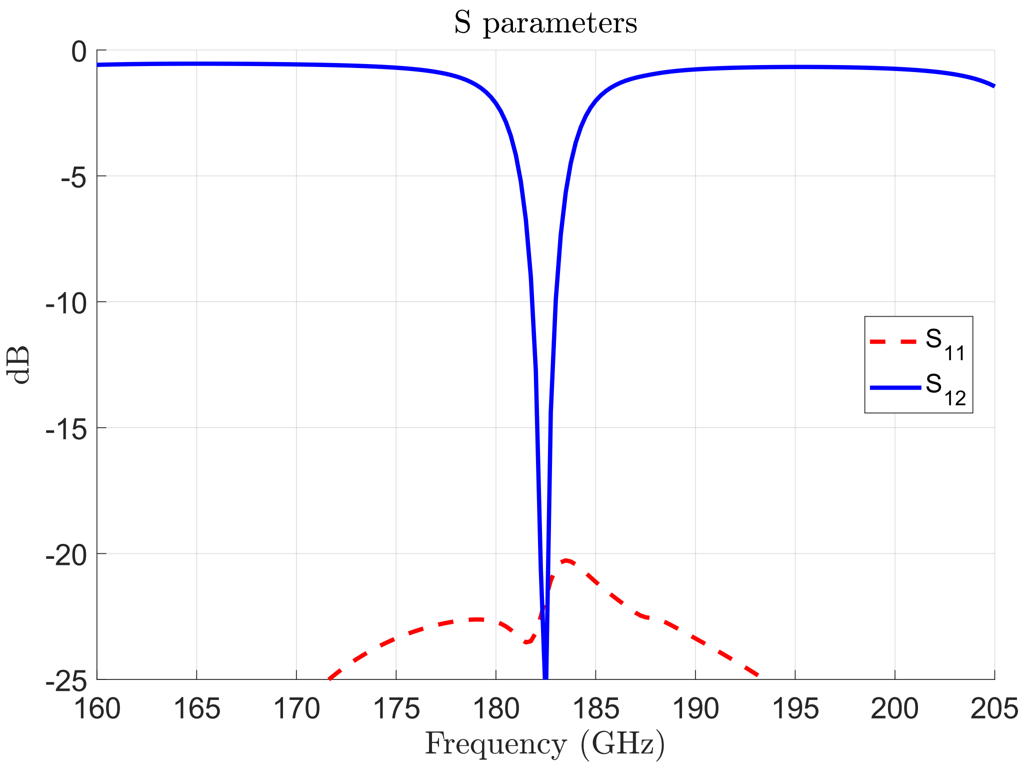

Figure 4.24: Mm-wave coupling for the up-conversion scheme.

4.6.2. Fabrication tolerances

As the system works at such high-frequency range, the fabrication tolerances are one of the main challenges. For example, the proposed resonator has fabrication tolerances of $\pm 10\,\mu$m and $\pm 2\,\mu$m for radius and thickness respectively. To see how this will affect the mm-wave coupling, such tolerances have been simulated as shown in Fig. 4.26 and Fig. 4.27 for radius and thickness tolerances respectively. They demonstrate that such fabrication tolerances of radius would result in a frequency shift of ± 4 GHz while thickness tolerances produce a shift of ± 2 GHz.

Although this frequency shift is relatively small compared to the resonance frequency (around 2%), it is still critical not only for shifting the frequency of satellite application but also for the up-conversion process. With this shift, the phase-matching condition between the mm-wave and optical signals will not be fulfilled.

From this perspective, the proposed scheme has an attractive characteristic of the possibility of refined electric-tuning of the operating frequency over a wide range of frequencies to replace the iteratively fabrication tuning mechanism [50] used in standard up-conversion schemes. The proposed tuning can efficiently scan from 160 GHz to 205 GHz as presented in Fig. 4.28 (for the same $M = 6$ WGM mode). This tuning is performed by moving the metallic ring which is above the resonator as will be shown in Sec. 4.6.3 where moving it towards or away from the resonator would decrease or increase the res-

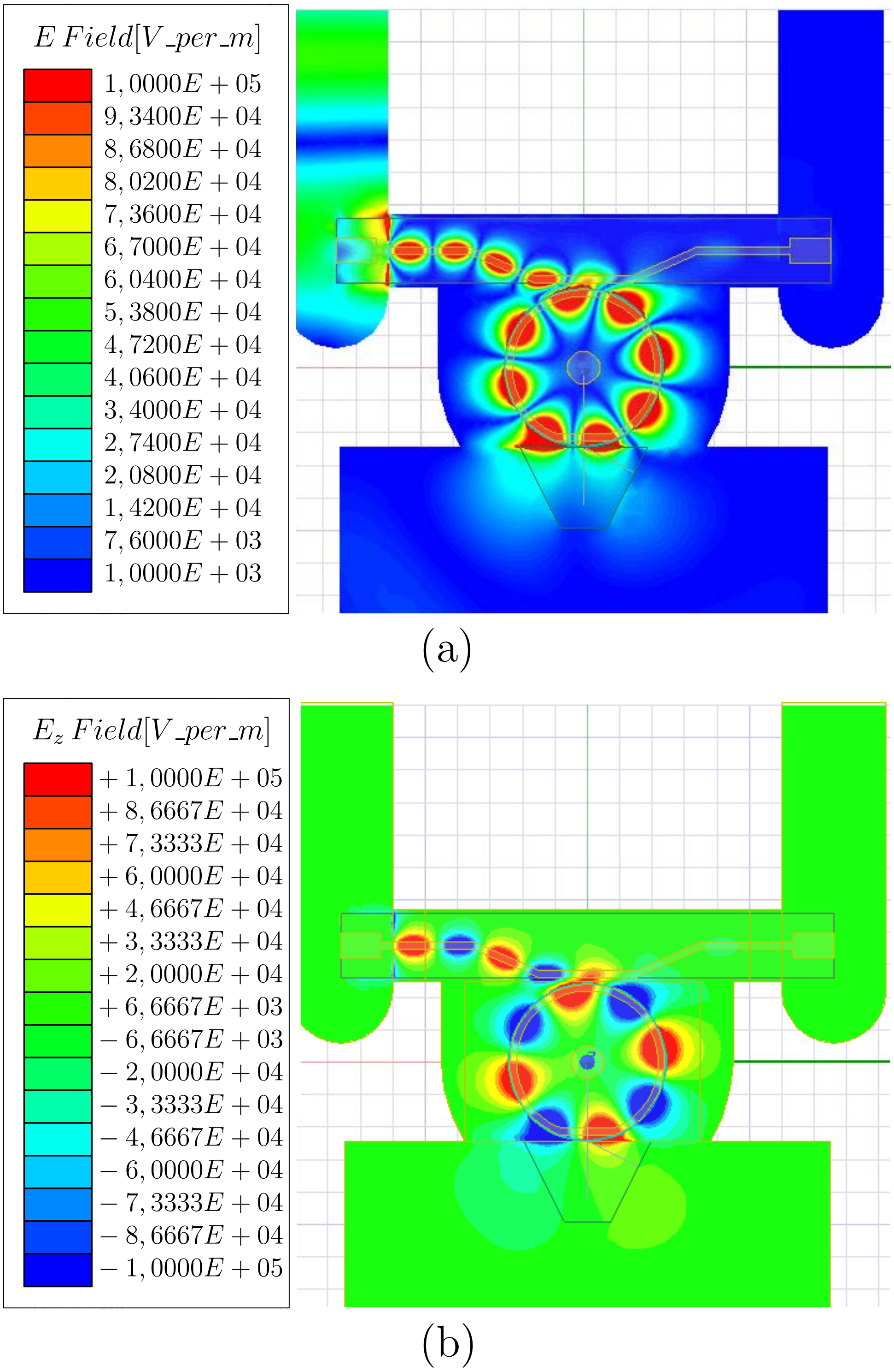

Figure 4.25: The electric field distribution along the main scheme components (a) total magnitude, (b) the normal field component to the resonator surface.

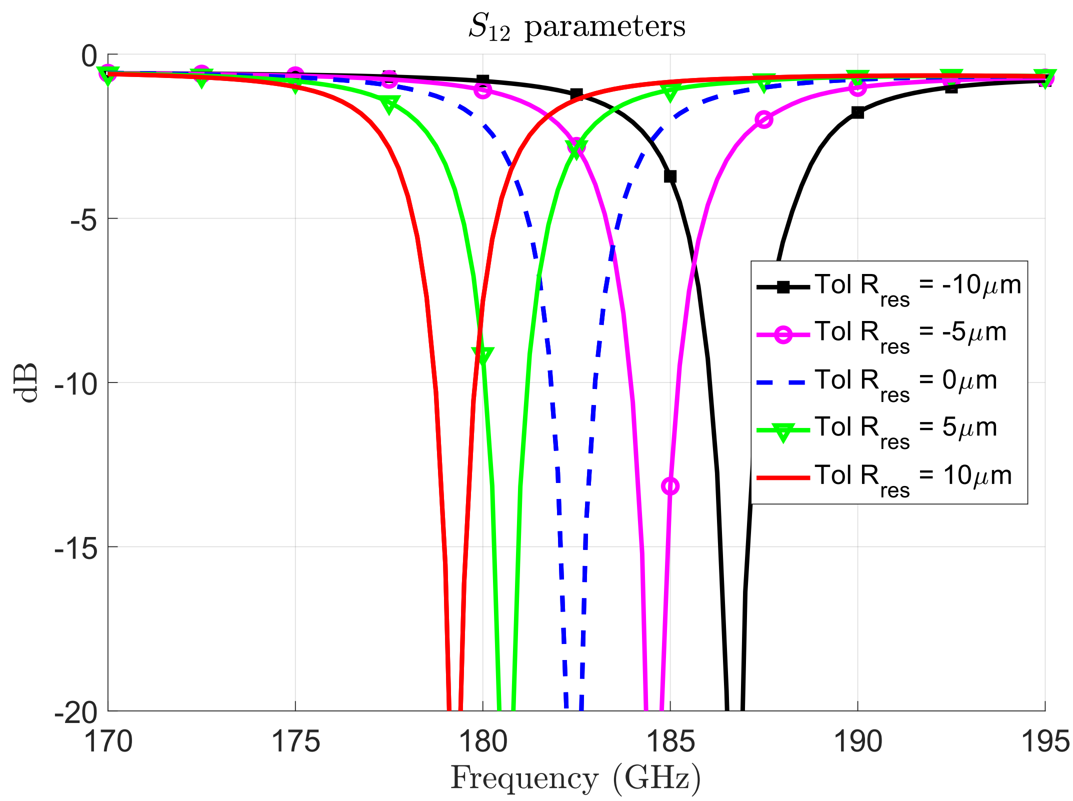

Figure 4.26: Fabrication tolerances of resonator radius.

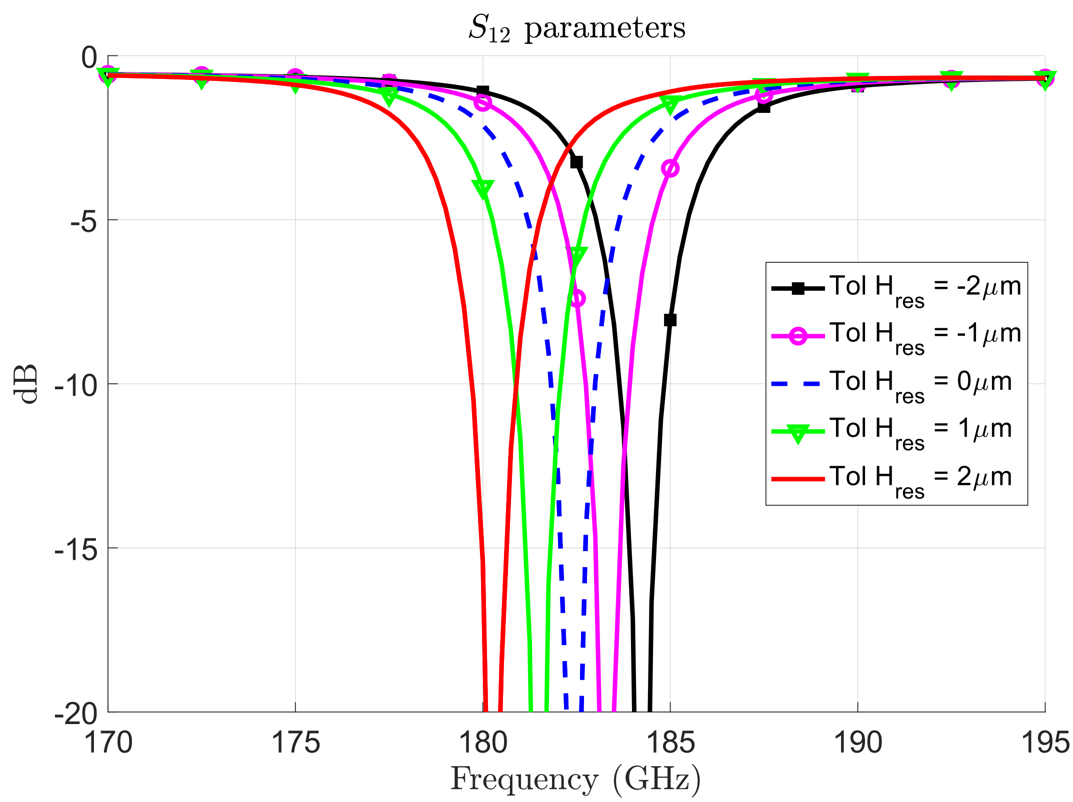

Figure 4.27: Fabrication tolerances of resonator thickness.

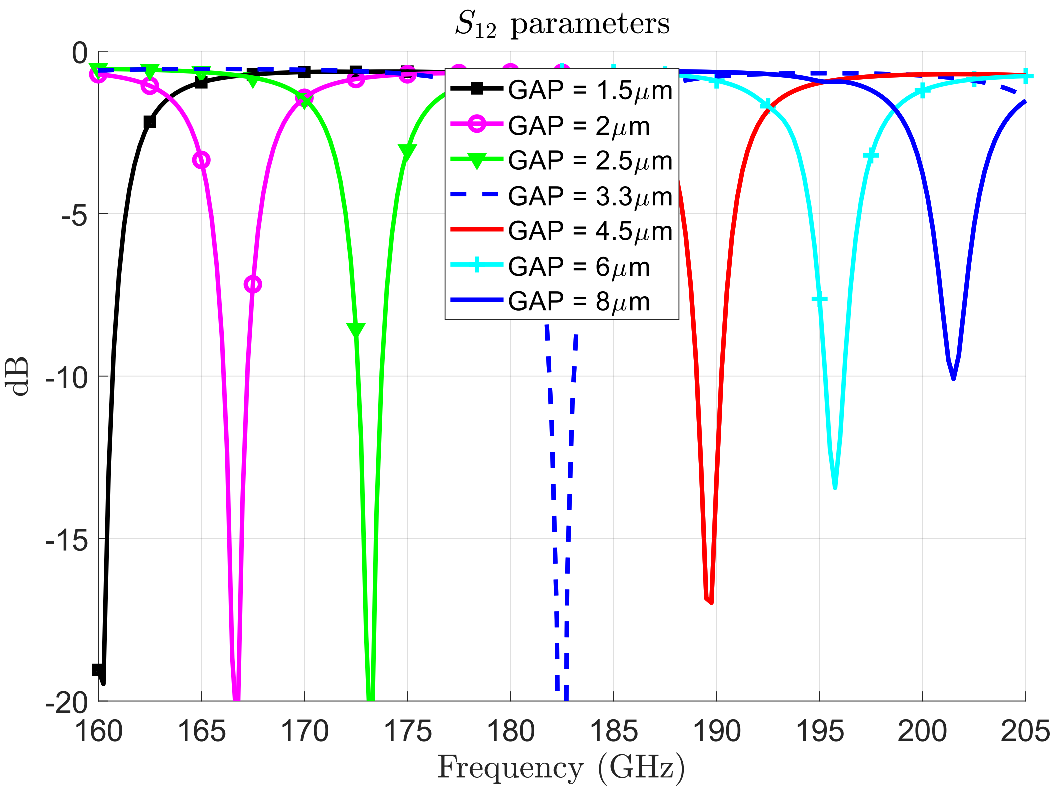

Figure 4.28: Tuning the mm-wave coupling.

onance frequency respectively. This will overcome the manufacturing tolerances for such electrically small and physically small (at the mm-wave range) resonator.

4.6.3. The designing and manufacturing of the integrated up-conversion scheme

Another attractive feature for the proposed scheme is that it can be easily integrated as a single block as presented in Fig. 4.29. This is extremely suitable for CubeSat and spacecraft applications. The structure consists of seven main blocks as follows (from down to up): bottom metal cover, optical housing, bottom cavity, Si substrate with a microstrip, upper cavity, rod extension, and upper metal cover. The brown parts are the top and bottom metallic components machined by Computer Numerical Control (CNC) and they act as a cover for the scheme. They are housing the WR5 metallic waveguide as well to be easily connected later to the antenna as illustrated in the side view of Fig. 4.29.

The metallic ring is connected to a rod extension made of metal too (all in orange) which is controlled by piezo provided by SmartAct [158] and placed above the upper metal block. To achieve the required precise tuning, the piezo is used to move the ring up or down with a precision of 4 nm which corresponds to a frequency shift on the order of tens of MHz.

Regarding the optical coupling, the optical signal is coming from a laser and is focused using a GRIN lens to a Chemical Vapor Deposition (CVD) diamond prism (in

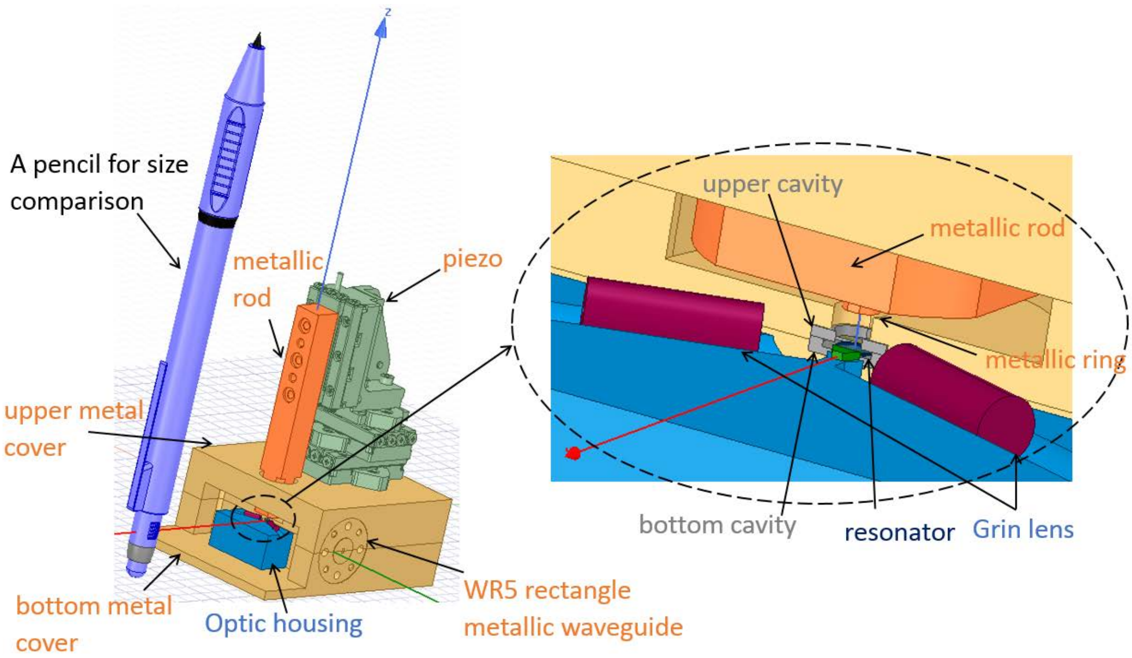

Figure 4.29: Overview of the integrated system.

green), then the side-band optical signal is coupled out using another GRIN lens. Both the prism and the two GRIN lenses are glued in the same optical housing which is made of Aluminum. The whole optical housing is controlled by another piezo to ensure good optical coupling, the piezo is omitted in the pictures for simplicity. While the GRIN lenses are standard GRIN2915 that are commercially available in Thorlabs [104], the prism is designed specifically for this system to have a better optical coupling and also because the standard prisms would be bulky for this small resonator and would affect the mm-wave coupling.

Then the parts in gray are Si micro-machined and gold-plated (except the substrate). They act as the cavity (holder) for the resonator and house the microstrip and WR5 transitions too as presented in Fig. 4.30. The hole in the upper cavity is for letting the moving metallic ring pass up or down to arrive to the resonator. Moreover, it is bigger than the ring which allows horizontal movements for the ring using the 3-axis piezo to ensure a good alignment between the ring and the dielectric resonator which compensates misalignment in the placement of the resonator in the micro-machined holder.

The disk resonator is manufactured mechanically with high-precision single-point diamond turning from single $LiNbO_3$ crystalline in Resonant Optics group at University of Otago [159]. Then it is glued with wax onto a brass rod as in Fig. 4.31(a) to be polished carefully for smoothing the optical surface and have high optical Q-factor in order of 10^8. Such brass rod can be easily heated up to $100°C$ for melting the wax and preparing resonator for the pick-and-place in the micro-machined cavity.

Five prism prototypes (Fig. 4.31(b)) made of CVD diamond are manufactured with

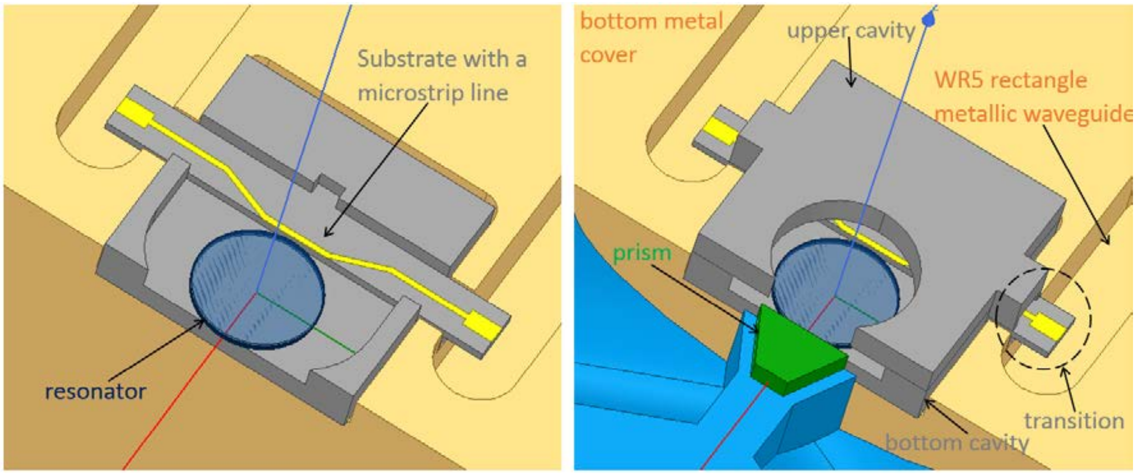

Figure 4.30: Signals coupling of the up-conversion scheme, left is mm-wave coupling only, right is both mm-wave and optical.

a shape of isosceles trapezoid by the Applied Diamond Inc. [160]. They have a thin thickness of about 200 μm which is small enough to not affect the microwave coupling for this tiny metal-enclosed resonator but at the same time large enough to have all power from the optical signal contained inside it. It has also a relatively small long-side of about 800 μm and angle of 64° which are designed for the optical coupling between the two GRIN lenses in the integrated scheme.

The metallic ring which has a radius close to the resonator one is manufactured using CNC-machining as shown in Fig. 4.31(c). The extra part of the ring is the rod extension which is used to enhance the mechanical stability and enable the ring to be connected to the 3-axis piezo.

Micrographs of the manufactured bottom micro-machined cavity attached to the bottom CNC-machined metal cover are shown in Fig. 4.32(a) for two cases, without and with the upper cavity. It illustrates also how the microstrip substrate (where the microstrip line and the two WR5 transitions are printed) lies on this bottom cavity. All blocks and metallic ring are manufactured in Nano-Rennes (Rennes University) [161].

The upper micro-machined cavity attached to the upper metal cover is presented in Fig. 4.32(b), before and after the addition of the metallic ring. It depicts the rule of the hole in the upper cavity which the metallic ring would pass through it towards and outwards the resonator for tuning purposes. Finally, Fig. 4.32(c) shows the overall integrated system after including the upper/lower metallic covers to the upper/lower Si-cavities and the microstrip substrate.

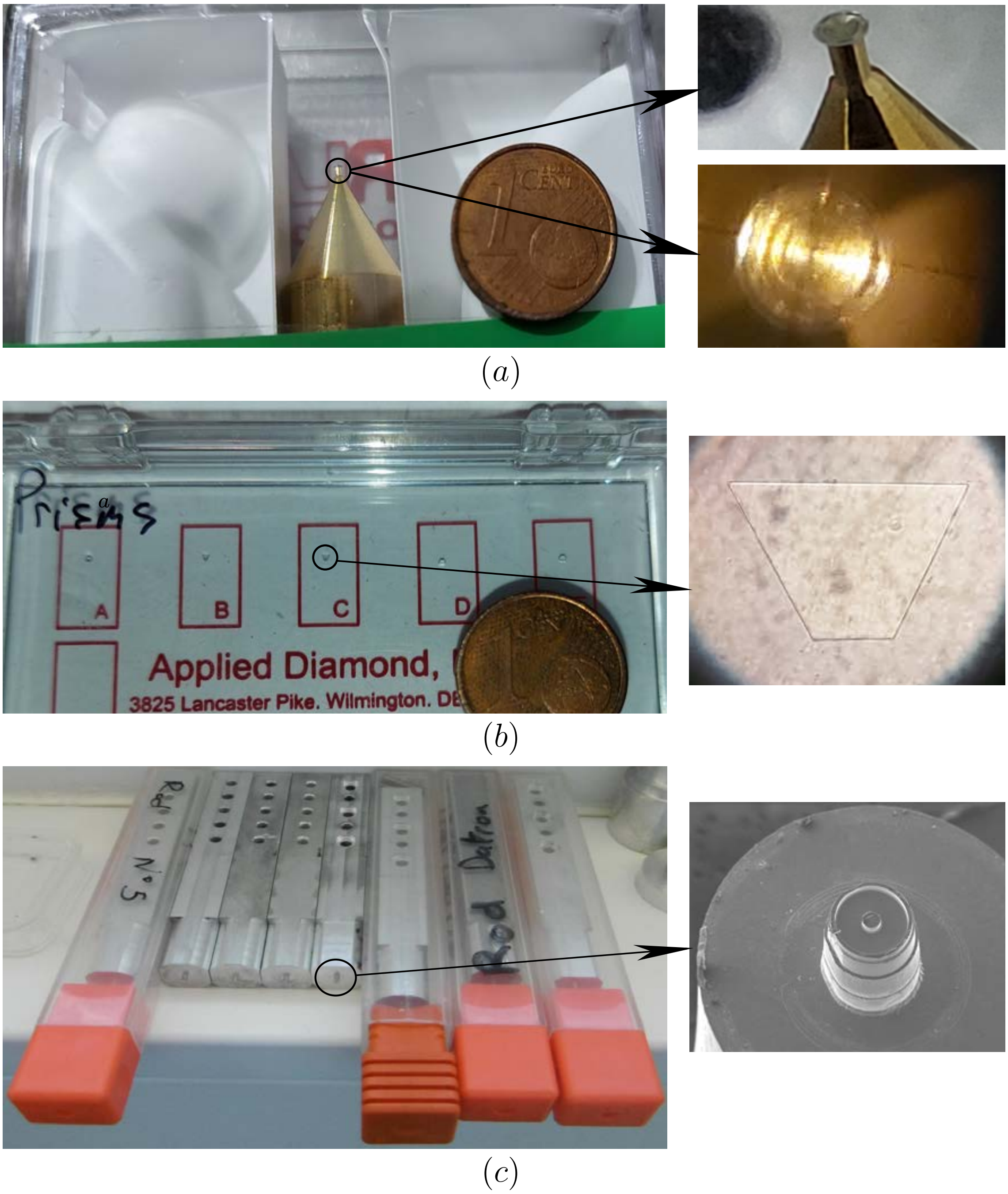

Figure 4.31: Photo and micrograph of the manufactured (a) $LiNbO_3$ disk resonator, (b) CVD diamond prism, and (c) metallic ring with its rod extension.

(a)

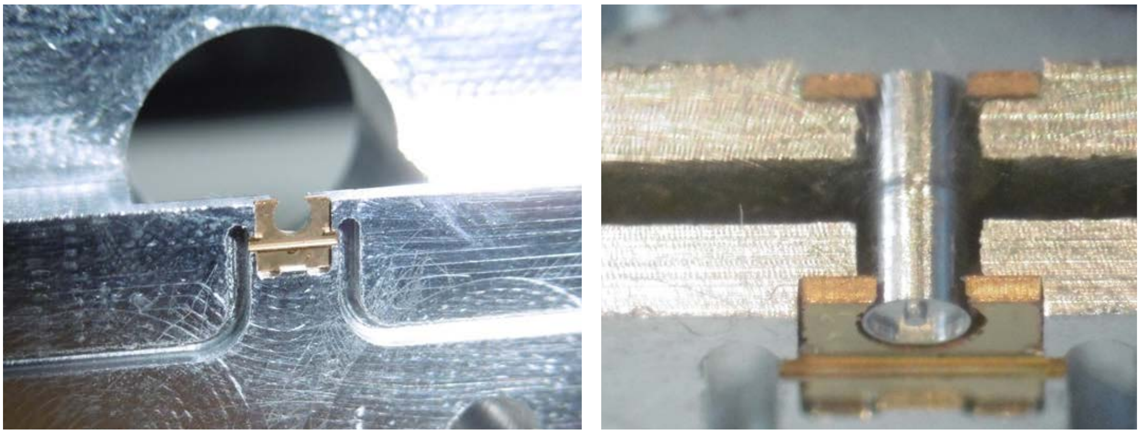

(b)

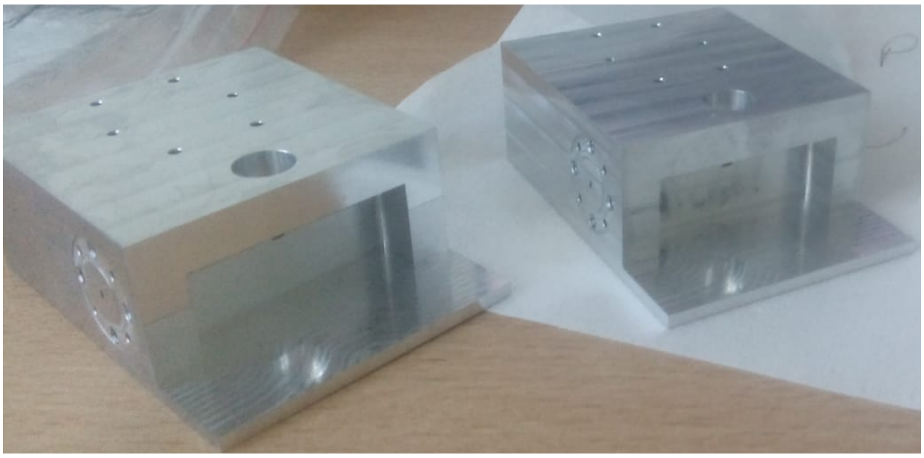

(c)

Figure 4.32: Micrograph of the manufactured integrated system (a) bottom part, (b) upper part, and (c) whole system.

4.7. Conclusions and principal remarks

A nonlinear up-conversion radio astronomy receiver is introduced, it is based on up-converting the microwave (or mm-wave or even THz) radiation into the optical domain where standard devices are widely available. This is performed by exciting WGMs for both microwave and optical input signals inside a nonlinear material. This receiver can work efficiently at room temperature without the need for bulky and high-cost cryogenic cooling and it can be easily scaled to cover any desired frequency from microwave up to THz.

A study of the photonic efficiency estimation for the system has been briefly discussed which is a key parameter for such receivers. This is followed by possible techniques for maximizing it which is mainly achieved by enhancing the modes overlapping while satisfying the phase-matching condition between the two input signals. A metal-covered WGM resonator has been proposed with an enhancement of the photonic efficiency around 5000 times compared to the corresponding standard dielectric ones. The proper design for the microwave coupling scheme for such proposed resonator is discussed.

Several DRA designs are given for the direct radiation coupling to the resonator without using any extra interfaces which enhances the performance of the system and reduces both cost and size. Higher gain DRAs are achieved by either a single antenna working at higher-order modes or by changing dielectric shape or by configuring a DRA array fed by a novel feeding technique based on standing-wave excitation. This novel feeding technique eliminates the use of power dividers or quarter-wave transformers to keep the low losses feature of the DRA and have a high radiation efficiency. All three antenna alternatives provide high gain of about 9 dBi, 11 dBi, and 15 dBi for the single rectangle, single-pyramidal horn, and a 3×3 rectangle array respectively. The rectangle element and array antennas are 3D manufactured and the measured results show a good matching compared to the simulated ones with a measured peak gain of about 15 dBi for the array.

Additionally, in this chapter, an integrated 183 GHz radiometer working at room temperature for earth observation applications on CubeSat satellites is presented. Eliminating the need of using a cryostat makes a payload compact, low weight, and extends satellite mission lifetime. By engineering a micro-machined mm-wave cavity that maximizes the modal overlap and fulfilling the phase-matching and energy conservation conditions, the system has a predicted high photonic efficiency $\eta \approx 10^{-2}$. This is surpassing the state-of-the-art by around three orders of magnitude in this frequency range. The microwave coupling is performed using a microstrip line printed in a Si substrate which has two transitions to standard WR5 metallic waveguides which makes the whole system ready to integrate to any mm-wave antennas with a metallic waveguide end. A CVD diamond prism and two GRIN lenses are used for the optical coupling.

The tolerance study for each of the dominant system parameters is done which shows that the microwave frequency resonance is shifted around 2 GHz in case a tolerance of about 5 μm or 2 μm occurs for the resonator radius or thickness respectively. A metallic rod with a ring-ended connected to a piezo is designed to shift up or down the resonance by moving it upwards or downwards to the resonator respectively. this enables the system to be tuned over a very wide band (183 GHz ± 22 GHz) with fine-tuning on the order of tens of MHz. With this mechanism, the complexity of the manufacturing process is reduced and both fabrication and alignment tolerances are completely compensated. The resonator, diamond prism, micro-machined Si cavities, microstrip substrate with transitions, and CNC-machined metallic covers are manufactured and under assembling process to be ready for the measurements.

5. FINAL CONCLUSIONS AND FUTURE LINES

5.1. Conclusions

The contributions in this thesis are:

- UWB circularly-polarized feed systems (antennas+baluns) for VLBI and Earth observation direct radio astronomy receivers.
- High-directivity UWB THz antenna arrays with high radiated power for down-converter heterodyne receiver and studies of the metal losses for THz planar antennas.
- Up-converter WGM-based receiver working at room temperature with high photonic efficiency, high-gain DRAs for its microwave coupling, and integrated mm-wave scheme for CubeSat applications.

In the first part, associated with the Chapter 2, two UWB circularly-polarized antenna feed solutions for covering the VLBI requirements are proposed to cover the frequency range from 2 GHz to 14 GHz. Firstly the conical log spiral antenna for single CP. Secondly, an array of four spirals that is based on a four-elements array for dual CP operations which is called DYQSA. The proper designs for the balun and four-baluns system are provided to excite the two proposed antennas respectively. A summary of the designing steps is discussed with the possible procedures to overcome the fabrication challenge, especially at such relatively high frequencies. The antennas are 3D manufactured and the measurements show a high level of similarity to the simulated ones. These feeds provide three new attractive characteristics compared to the state-of-the-art feeds: a direct single/dual circular polarization in contrast to single/dual linear polarization which avoids the use of additional analog hardware or digital software for linear-to-circular polarization converting. Secondly, stable radiation patterns and beamwidths over a UWB with the easy adaptation to different radio telescopes. Thirdly, the constant with an almost real input impedance of the antenna due to its self-complementary geometry (which is beneficial for the other receiver components such as LNA and/or balun). All the previous conclusions make the proposed antennas beneficial not only as radio astronomy feeds but for many other UWB applications that require such tricky performance. Additionally, the single CP single-element antenna is redesigned for the CryoRad low-frequency future Earth observation radiometer. The simulation results demonstrate its ability for efficiently-covering all system requirements in the required band from 400 MHz to 2 GHz with low weight and compact solution compared to other standards feeds.

With respect to the second part (Chapter 3), three UWB planar antenna arrays based an bow-ties and photomixers are presented, each of them is laying on a dielectric lens forming an AE THz source. These AEs cover different frequency ranges from 50 GHz to 0.5 THz, from 100 GHz to 1 THz, and from 200 GHz to 2 THz. Several commercial extended-hemispherical Si lenses are tested which demonstrate the significant influences of the lens dimensions on the antenna performance. These compact arrays have electrically small element-spacing to ensure constructive interference between them which avoid the out-of-focus problem. They are called Chessboard arrays following the resulting shape of this high-density element-distribution. A proof-of-concept array is manufactured showing the details of the complete assembly of the AE and measurements setup. The measured THz radiated power outperforms other integrated THz sources working at the same range which are based on the same concept of combining photomixers and self-complementary antennas. The proposed antenna sources have several advantages such as high directivity, compact, ease of integration, relatively high radiated power, tunable, and low cost, in addition to operating at room temperature. This makes it a good candidate as a local oscillator in radio astronomy heterodyne receivers as well as a directed CW source for several THz applications transmitters that require these advantages.

Additionally, in the same second part, studies for the metal losses of planar THz antennas based on the common assumption of the gold characteristics and the actual measured gold alloy characteristic are performed. These studies demonstrate that, unlike the conclusion that can be derived from the gold characteristic assumption, the metal losses have dominant and very strong effects on the antenna gain (which in turn would affect its radiated power). This especially occurs at lower frequencies where the skin depth of the manufactured metal alloy goes greater than its thickness. These high loss levels can be enhanced either by using thicker metal (larger than the metal skin depth for whole frequency band) or by changing the antenna topology, the trade-off between these two solutions are investigated. Such studies are interesting for avoiding the huge losses from the metal which if it is correctly considered, can significantly enhance the radiated THz of the antennas.

In the third part and in contrast to the cooled radio astronomy receivers presented in Chapter 2, Chapter 4 presents a non-standard radio astronomy receiver based on the non-linear up-conversion of the microwave radiation into optical domain using WGM. The receiver can be easily scaled to be used in different frequency bands (microwave, mm-wave or THz). A novel metal-enclosed WGM resonator and microwave coupling scheme are proposed which enable the receiver to have a photonic efficiency that significantly outperforms other up-conversion WGM systems. This is achieved by dramatically decreasing the mode volume of the microwave and pushing it towards the rim of the resonator to enhance the overlap between the microwave and optical signals. Three high-gain DRAs in single-element and array configurations are proposed for the direct coupling of the microwave radiation to the metal-enclosed resonator. Two of them are 3D manufactured showing excellent measured results close to the simulated ones.

Also, in this third part, a practical application for the proposed high photonic efficiency receiver is discussed. A complete integrated opto-electronic up-conversion system for CubeSat satellite radiometer has been proposed for 183 GHz water vapor profile measurements and weather forecasting. The proposed receiver has four main attractive features, firstly, it operates without cryogenic cooling which decreases the satellite cost, weight, and volume with a significant increase in the satellite mission lifetime. Secondly, it has a very high photonic efficiency that outperforms other mm-wave up-conversion schemes. Thirdly, it is fully integrated which makes it convenient for the satellite environment. Fourthly, it has the ability to have a refined tuning over a wide frequency range which completely compensates both fabrication and alignment tolerances.

Finally, it is worth noting here that the development of this Ph.D. dissertation work has directly or indirectly led to the publication of 11 JCR journal papers (7 in Q1 and 3 in Q2), 2 invited papers, and 33 conference papers. The list of contributions is detailed in "published and submitted content" and "other publications" sections at the beginning of this thesis.

5.2. Future lines

From the first part and related to VGOS radio telescope feed, the reduction of the averaged DYQSA array efficient from 65% in simulations to 50% in the measurements needs further investigation to elucidate the reasons behind this degradation. Following the excellent measured results of the proposed conical log-spiral element which presents a high total aperture efficiency of about 70%, the degradation for DYQSA may be due to misalignment issues. Especially that the misalignment between the elements will cause a phase mismatch between one turn of the spiral and its corresponding turn in the other antenna for the same polarization and this will affect the symmetry of the patterns. Also, the antenna can be over-designed at the lower band (increase the largest diameter) to enhance the behavior of the feed at the lower frequencies. This will only increase the feed size without affecting its manufacturing/alignment complexity. Finally, related to CryoRad radio telescope feed, the extensive studies which performed for VGOS, should done here including the analysis of the whole receiver system once the feed are integrated with the radio telescope. Then the same should be repeated but by using multiple feeds to achieve the requested complete ground swath width with the required resolution and efficiency. Although that the multiple feeds configuration achieve the application requirements, primarily studies show that there is a limit with the inter-element spacing as at higher frequencies as the array radiating elements (which are the small arms close to the top small diameter) have large separation above 1λ due to the much bigger size of the large diameter. This in its turns would result in sidelobes at the higher frequencies. This can be avoided by dividing the full band to two smaller bands from 400 MHz to 900 MHz and from 900 MHz to 2 GHz and use an array of multiple feed for covering each sub-band. Finally, the manufacturing and measurements of the antenna should be performed.

Regarding the second part, although the proposed THz Chessboard array provides very high directivity of about 30 dBi which enables it to have a high measured radiated

THz power of $60\,\mu$W at 150 GHz, it is remarked that there is a big room for enhancement from five main factors, in case higher THz power is needed by doing one or a combination of these options:

- Extending the array to larger number of elements which is an easy and straightforward solution as the design procedure and manufacturing/alignment setup would kept the same.
- Using better micro-positioners or high-accuracy piezoelectric to reach higher alignment accuracy and increase the illumination efficiency of the photomixers array.
- Relaxing the lens size restriction and allowing the testing/use of lenses with larger diameters.
- Fabricating a non-standard microlens array that is corresponding to the exact designed pitch size (for example, $227\,\mu$m instead of this modified pitch of $300\,\mu$m).
- Over-designing the array at the higher frequency end to have stable properties at the high-frequency end.

Additionally, for the metal losses study and following what is done for square spiral and log-spiral antennas, further investigations should be done to extend the study to different standard planar THz antenna typologies such as bow-tie and log-periodic antennas. Also, to have a fair comparison between the four antennas, the aperture efficiency should be estimated for each case in which both the antenna gain (in turn, the losses) and the physical size are considered.

For the third part, as discussed before, both pyramidal horn DRA single-element and the rectangle array based on standing-wave feeding could enhance the antenna gain. Possible main extensions for the work are to design an array based on the same feeding method but using the pyramidal horn DRA element instead of the standard rectangle one, extend the array to larger number of elements, and scale the design to mm-wave range. Actually, due to the mentioned advantages of such proposed DRAs and their low losses, compact size, and low cost, an array based on an adjusted version of the proposed pyramidal horn is recently implemented within a project funded by Huawei to be used for 5G base station antennas (it is omitted in the thesis as the focus here in the radio astronomy applications) Regarding the up-conversion satellite receiver, although the proposed receiver provides an integrated scheme with a metallic waveguide front-end to be able to use any standard mm-wave antennas, DRA array working at mm-wave range with high gain would be a better solution. This is because such a solution avoids the use of the metallic waveguide to microstrip transitions and achieves a direct coupling for the radiation to the system. Also, the BW of the up-conversion scheme can be increased by applying selective optical coupling techniques or by using an array of resonators working at different resonances. Additionally, the whole system can be easily adapted from the mm-wave to work at THz range (above 1 THz) in which it would outperform the state-of-the-art LNAs and mixers working at cryogenic cooling (below 120 K) even when the system is working at room temperature.

BIBLIOGRAPHY

[1] H. Schuh and D. Behrend, "VLBI: A fascinating technique for geodesy and astrometry," *Journal of Geodynamics*, vol. 61, pp. 68–80, Oct. 2012.

[2] The Event Horizon Telescope Collaboration et al, "First M87 Event Horizon Telescope Results. I. The Shadow of the Supermassive Black Hole," *Astrophysical Journal Letters*, vol. 875, 2019.

[3] ——, "First M87 Event Horizon Telescope Results. IV. Imaging the Central Supermassive Black Hole," *Astrophysical Journal Letters*, vol. 875, 2019.

[4] C. Ma *et al.*, "The International Celestial Reference Frame as Realized by Very Long Baseline Interferometry," *The Astronomical Journal*, vol. 116, no. 1, pp. 516–546, Jul. 1998.

[5] W. T. Petrachenko, A. E. Niell, B. E. Corey, D. Behrend, H. Schuh, and J. Wresnik, "VLBI2010: Next Generation VLBI System for Geodesy and Astrometry," in *International Association of Geodesy Symposia*, 2012, vol. 136, pp. 999–1005.

[6] H. Hase, D. Behrend, C. Ma, B. Petrachenko, H. Schuh, and A. Whitney, "The Emerging VGOS Network of the IVS," in *IVS 2012 General Meeting Proceedings*, no. September 2003, 2012, pp. 8–12.

[7] B. Petrachenko, "Review of VLBI2010 Concept and General Specifications," in *IVS TecSpec Workshop*, Bad Kötzting, Germany, 2012.

[8] "DIFRAGEOS," [Online]. Available: https://grema.webs.tsc.uc3m.es/difrageos-main/.

[9] A. Akgiray, S. Weinreb, W. A. Imbriale, and C. Beaudoin, "Circular Quadruple-Ridged Flared Horn Achieving Near-Constant Beamwidth Over Multioctave Bandwidth: Design and Measurements," *IEEE Transactions on Antennas and Propagation*, vol. 61, no. 3, pp. 1099–1108, Mar. 2013.

[10] J. Yang, M. Pantaleev, P.-S. Kildal, and L. Helldner, "Design of Compact Dual-Polarized 1.2–10 GHz Eleven Feed for Decade Bandwidth Radio Telescopes," *IEEE Transactions on Antennas and Propagation*, vol. 60, no. 5, pp. 2210–2218, May 2012.

[11] J. Yang *et al.*, "Cryogenic 2–13 GHz Eleven Feed for Reflector Antennas in Future Wideband Radio Telescopes," *IEEE Transactions on Antennas and Propagation*, vol. 59, no. 6, pp. 1918–1934, Jun. 2011.

[12] B. Petrachenko, "VLBI2010 Feed Comparison," in *International VLBI Service for Geodesy and Astrometry 2012 Annual Report, NASA/TP-2013-217511*. NASA, 2013, pp. 48–51.

[13] C. J. Beaudoin *et al.*, "A Cost and Complexity Survey on Emerging Technologies for the VGOS," in *International VLBI Service for Geodesy and Astrometry 2014 General Meeting Proceedings: "VGOS: The New VLBI Network"*, K. L. A. Dirk Behrend, Karen D. Baver, Ed. Beijing, China: Science Press, 2014, pp. 53–59.

[14] X. Du, T. Johnson, T. Landecker, and B. Veidt, "An ultra-wideband nested coaxial waveguide feed antenna for radio astronomy," *IEEE Transactions on Antennas and Propagation*, pp. 1–1, 2021.

[15] G. Macelloni *et al.*, "Cryorad: A low frequency wideband radiometer mission for the study of the cryosphere," in *IGARSS 2018 - 2018 IEEE International Geoscience and Remote Sensing Symposium*, 2018, pp. 1998–2000.

[16] A. V. Bosisio, M. Brogioni, and G. Macelloni, "Atmospheric emission at low microwave frequencies: A site-based analysis," in *2021 IEEE International Geoscience and Remote Sensing Symposium IGARSS*, 2021, pp. 7999–8002.

[17] A. Jaradat, F. Jaron, J. Gruber, and A. Nothnagel, "Considerations of VLBI transmitters on galileo satellites," *Advances in Space Research*, vol. 68, no. 3, pp. 1281–1300, 2021.

[18] J. Flygare, M. Pantaleev, B. Billade, M. Dahlgren, L. Helldner, and R. Haas, "Sensitivity and Antenna Noise Temperature Analysis of the Feed System for the Onsala Twin Telescopes," *23rd European Very Long Baseline Interferometry Group for Geodesy and Astrometry (EVGA)*, pp. 10–14, 2017.

[19] P.-S. Kildal, "Factorization of the feed efficiency of paraboloids and Cassegrain antennas," *IEEE Transactions on Antennas and Propagation*, vol. 33, no. 8, pp. 903–908, Aug. 1985.

[20] T. Y. Otoshi, *Noise temperature theory and applications for deep space communications antenna systems*. Artech House, 2008.

[21] "Ticra engineering consultants, GRASP," [Online]. Available: https://www.ticra.com/.

[22] G. Cortes-Medellin, "MEMO 95 antenna noise temperature calculation," National Astronomy and Atmospheric Center, Cornell University, Tech. Rep., 2007.

[23] Y. Lee, *Principles of Terahertz Science and Technology*, ser. Lecture Notes in Physics. Springer US, 2009.

[24] P. Siegel, "Terahertz technology," *IEEE Transactions on Microwave Theory and Techniques*, vol. 50, no. 3, pp. 910–928, 2002.

[25] I. F. Akyildiz, J. M. Jornet, and C. Han, "Terahertz band: Next frontier for wireless communications," *Physical Communication*, vol. 12, pp. 16–32, 2014.

[26] J. Wei, D. Olaya, B. S. Karasik, S. V. Pereverzev, A. V. Sergeev, and M. E. Gershenson, "Ultrasensitive hot-electron nanobolometers for terahertz astrophysics," *Nature nanotechnology*, vol. 3, no. 8, pp. 496–500, 2008.

[27] P. Yang, Y. Xiao, M. Xiao, and S. Li, "6G wireless communications: Vision and potential techniques," *IEEE Network*, vol. 33, no. 4, pp. 70–75, 2019.

[28] M. Fujishima and S. Amakawa, "Integrated-circuit approaches to THz communications: Challenges, advances, and future prospects," *IEICE Transactions on Fundamentals of Electronics, Communications and Computer Sciences*, vol. E100.A, no. 2, pp. 516–523, 2017.

[29] S. Koenig *et al.*, "Wireless sub-THz communication system with high data rate," *Nature photonics*, vol. 7, no. 12, pp. 977–981, 2013.

[30] A. Rahman, A. K. Rahman, and B. Rao, "Early detection of skin cancer via terahertz spectral profiling and 3D imaging," *Biosensors and Bioelectronics*, vol. 82, pp. 64–70, 2016.

[31] Z. D. Taylor *et al.*, "THz medical imaging: in vivo hydration sensing," *IEEE Transactions on Terahertz Science and Technology*, vol. 1, no. 1, pp. 201–219, 2011.

[32] J. F. Federici *et al.*, "THz imaging and sensing for security applications—explosives, weapons and drugs," *Semiconductor Science and Technology*, vol. 20, no. 7, pp. S266–S280, jun 2005.

[33] G. P. Williams, "Filling the THz gap—high power sources and applications," *Reports on Progress in Physics*, vol. 69, no. 2, pp. 301–326, dec 2005.

[34] A. MacDonald, *Terahertz Technology: Fundamentals and Applications*. White Press Academics, 2018.

[35] C. M. Armstrong, "The truth about terahertz," *IEEE Spectrum*, vol. 49, no. 9, pp. 36–41, 2012.

[36] A. Y. Pawar, D. D. Sonawane, K. B. Erande, and D. V. Derle, "Terahertz technology and its applications," *Drug Invention Today*, vol. 5, no. 2, pp. 157–163, 2013.

[37] S. Preu, G. H. Döhler, S. Malzer, L. J. Wang, and A. C. Gossard, "Tunable, continuous-wave terahertz photomixer sources and applications," *Journal of Applied Physics*, vol. 109, no. 6, p. 061301, 2011.

[38] M. A. Belkin *et al.*, "Room temperature terahertz quantum cascade laser source based on intracavity difference-frequency generation," *Applied Physics Letters*, vol. 92, no. 20, p. 201101, 2008.

[39] I. C. Mayorga, A. Schmitz, T. Klein, C. Leinz, and R. Gusten, “First in-field application of a full photonic local oscillator to terahertz astronomy,” *IEEE Transactions on Terahertz Science and Technology*, vol. 2, no. 4, pp. 393–399, 2012.

[40] S. Verghese, K. McIntosh, and E. Brown, “Highly tunable fiber-coupled photomixers with coherent terahertz output power,” *IEEE Transactions on Microwave Theory and Techniques*, vol. 45, no. 8, pp. 1301–1309, 1997.

[41] B. S. Karasik, W. R. McGrath, H. G. LeDuc, and M. E. Gershenson, “A hot-electron direct detector for radioastronomy,” *Superconductor Science and Technology*, vol. 12, no. 11, pp. 745–747, Nov. 1999.

[42] A. Sergeev, V. Mitin, and B. Karasik, “Ultrasensitive hot-electron kinetic-inductance detectors operating well below the superconducting transition,” *Applied physics letters*, vol. 80, no. 5, pp. 817–819, 2002.

[43] D. V. Strekalov, C. Marquardt, A. B. Matsko, H. G. L. Schwefel, and G. Leuchs, “Nonlinear and quantum optics with whispering gallery resonators,” *Journal of Optics*, vol. 18, no. 12, p. 123002, Nov. 2016.

[44] A. N. Oraevsky, “Whispering-gallery waves,” *Quantum Electronics*, vol. 32, no. 5, pp. 377–400, May 2002.

[45] M. R. Foreman, J. D. Swaim, and F. Vollmer, “Whispering gallery mode sensors,” *Adv. Opt. Photon.*, vol. 7, no. 2, pp. 168–240, Jun. 2015.

[46] J. W. S. Rayleigh, *The theory of sound*. Macmillan, 1896, vol. 2.

[47] L. Rayleigh, “Cxii. the problem of the whispering gallery,” *The London, Edinburgh, and Dublin Philosophical Magazine and Journal of Science*, vol. 20, no. 120, pp. 1001–1004, 1910.

[48] I. Breunig, “Three-wave mixing in whispering gallery resonators,” *Laser & Photonics Reviews*, vol. 10, no. 4, pp. 569–587, 2016.

[49] A. B. Matsko, D. V. Strekalov, and N. Yu, “Sensitivity of terahertz photonic receivers,” *Phys. Rev. A*, vol. 77, p. 043812, Apr. 2008.

[50] F. Sedlmeir, “Crystalline whispering gallery mode resonators,” doctoral thesis, Friedrich-Alexander-Universität Erlangen-Nürnberg (FAU), 2016.

[51] R. W. Boyd, *Nonlinear optics*. Academic press, 2020.

[52] D. V. Strekalov, H. G. L. Schwefel, A. A. Savchenkov, A. B. Matsko, L. J. Wang, and N. Yu, “Microwave whispering-gallery resonator for efficient optical up-conversion,” *Phys. Rev. A*, vol. 80, p. 033810, Sep. 2009.

[53] D. W. Vogt and R. Leonhardt, "Terahertz whispering gallery mode bubble resonator," *Optica*, vol. 4, no. 7, pp. 809–812, Jul. 2017.

[54] F. Aires *et al.*, "Microwave hyperspectral measurements for temperature and humidity atmospheric profiling from satellite: The clear-sky case," *Journal of Geophysical Research: Atmospheres*, vol. 120, no. 21, pp. 11–334, 2015.

[55] M. Linder, N. Rando, A. Peacock, and B. Collaudin, "Cryogenics in space - a review of the missions and technologies," *ESA Bulletin*, vol. 107, pp. 92–105, Aug. 2001.

[56] K. A. Abdalmalak *et al.*, "Ultrawideband conical log-spiral circularly polarized feed for radio astronomy," *IEEE Transactions on Antennas and Propagation*, vol. 68, no. 3, pp. 1995–2007, 2020.

[57] M. Wasiak *et al.*, "Compact millimeter and submillimeter-wave photonic radiometer for cubesats," in *2020 14th European Conference on Antennas and Propagation (EuCAP)*, 2020, pp. 1–5.

[58] "MARTINLARA," [Online]. Available: https://martinlara3.webnode.es/.

[59] T. Latha, G. Ram, G. A. Kumar, and M. Chakravarthy, "Review on ultra-wideband phased array antennas," *IEEE Access*, vol. 9, pp. 129 742–129 755, 2021.

[60] C. A. Balanis, *Modern antenna handbook*. John Wiley & Sons, 2011.

[61] E. García-Muñoz *et al.*, "Photonic-based integrated sources and antenna arrays for broadband wireless links in terahertz communications," *Semiconductor Science and Technology*, vol. 34, no. 5, p. 054001, Apr. 2019.

[62] R. Gawande and R. Bradley, "Towards an Ultra Wideband Low Noise Active Sinuous Feed for Next Generation Radio Telescopes," *IEEE Transactions on Antennas and Propagation*, vol. 59, no. 6, pp. 1945–1953, Jun. 2011.

[63] R. S. Gawande and R. F. Bradley, "Characterization of the Active, Inverted, Conical Sinuous Antenna," in *XXIX General Assembly of URSI*, Chicago, IL, 2008.

[64] R. S. Gawande, "Ambient and cryogenic, decade bandwidth, low noise receiving system for radio astronomy using sinuous antenna," Ph.D. dissertation, University of Virginia, Doctoral dissertation, 2011.

[65] J. Dyson, "The unidirectional equiangular spiral antenna," *IRE Transactions on Antennas and Propagation*, vol. 7, no. 4, pp. 329–334, Oct. 1959.

[66] J. Dyson, "The characteristics and design of the conical log-spiral antenna," *IEEE Transactions on Antennas and Propagation*, vol. 13, no. 4, pp. 488–499, Jul. 1965.

[67] "ANSYS Simulation driven product development, HFSS," [Online]. Available: https://www.ansys.com/.

[68] "Computer Simulation Technology, CST," [Online]. Available: https://www.cst.com/.

[69] J.-p. Shang, De-min Fu, Ying-bo Deng, and Shuai Jiang, "Measurement of phase center for antenna with the method of moving reference point," in *2008 8th International Symposium on Antennas, Propagation and EM Theory*. IEEE, Nov. 2008, pp. 114–117.

[70] P.-S. Kildal, "Combined E-and H-plane phase centers of antenna feeds," *IEEE Transactions on Antennas and Propagation*, vol. 31, no. 1, pp. 199–202, Jan. 1983.

[71] N. Wadefalk, P. Kildal, and H. Zirath, "A low noise integrated 0.3-16 GHz differential amplifier for balanced ultra wideband antennas," in *2010 IEEE Compound Semiconductor Integrated Circuit Symposium (CSICS)*, 2010, pp. 1–4.

[72] K. Vinayagamoorthy, J. Coetzee, and D. Jayalath, "Microstrip to parallel strip balun as spiral antenna feed," in *2012 IEEE 75th Vehicular Technology Conference (VTC Spring)*, 2012, pp. 1–5.

[73] K. A. Abdalmalak *et al.*, "Radio astronomy ultra wideband receiver covering the 2–14 GHz frequency band for VGOS applications," in *2016 10th European Conference on Antennas and Propagation (EuCAP)*. IEEE, Apr. 2016, pp. 1–5.

[74] B. Petrachenko *et al.*, "Design aspects of the VLBI2010 system-progress report of the IVS VLBI2010 committee," NASA, Tech. Rep., 2009.

[75] A. H. Akgiray, "New technologies driving decade-bandwidth radio astronomy : quad-ridged flared horn and compound-semiconductor LNAs," Doctoral dissertation, California Institute of Technology, Doctoral dissertation, 2013.

[76] D. Warmowska, K. A. Abdalmalak, L. E. G. Muñoz, and Z. Raida, "A compact circularly polarized high-gain antenna array for Ka-band cubesats applications," in *2019 IEEE-APS Topical Conference on Antennas and Propagation in Wireless Communications (APWC)*, 2019, pp. 178–180.

[77] I. Martí-Vidal, A. Roy, J. Conway, and A. J. Zensus, "Calibration of mixed-polarization interferometric observations - Tools for the reduction of interferometric data from elements with linear and circular polarization receivers," *Astronomy & Astrophysics*, vol. 587, p. A143, 2016.

[78] K. Das, "Conversion from linear to circular polarization in FPGA in real time," Ph.D. dissertation, Universität zu Köln, Doctoral dissertation, Jun. 2013.

[79] M. Pantaleev *et al.*, “Broadband feeds for VGOS,” in *International VLBI Service for Geodesy and Astrometry 2014 General Meeting Proceedings: "VGOS: The New VLBI Network"*, D. Behrend, K. D. Baver, and K. L. Armstrong, Eds. Beijing, China: Science Press, 2014, pp. 60–49.

[80] A. Dunning, M. Bowen, M. Bourne, D. Hayman, and S. L. Smith, “An ultra-wideband dielectrically loaded quad-ridged feed horn for radio astronomy,” in *2015 IEEE-APS Topical Conference on Antennas and Propagation in Wireless Communications (APWC)*. IEEE, Sep. 2015, pp. 787–790.

[81] “3D Systems Manufacturing,” [Online]. Available: https://www.3dsystems.com/.

[82] K. A. Abdalmalak, G. Santamaría Botello, S. L. Romano, L. E. García Muñoz, and D. S. Vargas, “An updated version of the dyson conical quad-spiral array (DYQSA) feed system for VGOS applications,” in *2017 IEEE International Symposium on Antennas and Propagation & USNC/URSI National Radio Science Meeting*, 2017, pp. 1539–1540.

[83] K. A. Abdalmalak, S. L. Romano, L. E. García Muñoz, and D. S. Vargas, “Dual polarized ultra wideband feed system for VLBI global observation system applications,” in *2016 Global Symposium on Millimeter Waves (GSMM) & ESA Workshop on Millimetre-Wave Technology and Applications*, 2016, pp. 1–4.

[84] J. D. Gallego, I. López-Fernández, C. Diez, and A. Barcia, “Experimental results of gain fluctuations and noise in microwave low-noise cryogenic amplifiers,” in *Noise in Devices and Circuits II*, vol. 5470. International Society for Optics and Photonics, 2004, pp. 402–413.

[85] J. A. López-Fernández *et al.*, “IGN Yebes technology development center,” in *International VLBI Service for Geodesy and Astrometry 2014 Annual Report, NASA/TP-2015-217532*, K. D. Baver, D. Behrend, and K. L. Armstrong, Eds., 2015.

[86] J. Yang, S. Pivnenko, and P. Kildal, “Comparison of two decade-bandwidth feeds for reflector antennas: The Eleven Antenna and quadridge horn,” in *Proceedings of the Fourth European Conference on Antennas and Propagation*, 2010, pp. 1–5.

[87] S. Parekh, “Simple formulae for circular-polarization axial-ratio calculations,” *IEEE Antennas and Propagation Magazine*, vol. 33, no. 1, pp. 30–32, 1991.

[88] A. Rivera-Lavado *et al.*, “High-power terahertz emitter for a communication link: The chessboard array,” in *2017 11th European Conference on Antennas and Propagation (EUCAP)*, 2017, pp. 1377–1380.

[89] C. A. Balanis, *Antenna theory: analysis and design*. John wiley & sons, 2015.

[90] E. R. Brown, K. A. McIntosh, K. B. Nichols, and C. L. Dennis, "Photomixing up to 3.8 THz in low-temperature-grown GaAs," *Applied Physics Letters*, vol. 66, no. 3, pp. 285–287, 1995.

[91] K. A. McIntosh, E. R. Brown, K. B. Nichols, O. B. McMahon, W. F. DiNatale, and T. M. Lyszczarz, "Terahertz photomixing with diode lasers in low-temperature-grown GaAs," *Applied Physics Letters*, vol. 67, no. 26, pp. 3844–3846, 1995.

[92] E. R. Brown, F. W. Smith, and K. A. McIntosh, "Coherent millimeter-wave generation by heterodyne conversion in low-temperature-grown GaAs photoconductors," *Journal of Applied Physics*, vol. 73, no. 3, pp. 1480–1484, 1993.

[93] M. Tani, O. Morikawa, S. Matsuura, and M. Hangyo, "Generation of terahertz radiation by photomixing with dual- and multiple-mode lasers," *Semiconductor Science and Technology*, vol. 20, no. 7, pp. S151–S163, jun 2005.

[94] E. R. Brown, B. Globisch, G. C. del Barrio, A. Rivera, D. Segovia-Vargas, and A. Steiger, *Photoconductive THz Sources Driven at 1550 nm.* John Wiley & Sons, Ltd, 2021, ch. 3, pp. 43–136.

[95] G. Carpintero, E. García-Muñoz, H. Hartnagel, S. Preu, and A. Raisanen, *Semiconductor TeraHertz Technology: Devices and Systems at Room Temperature Operation*, ser. Wiley - IEEE. Wiley, 2015.

[96] A. Rivera-Lavado *et al.*, "High-power terahertz emitter arrays," in *2017 International Workshop on Antenna Technology: Small Antennas, Innovative Structures, and Applications (iWAT)*, 2017, pp. 142–145.

[97] J. Volakis, *Antenna Engineering Handbook.* McGraw-Hill Education, 2018.

[98] A. R. Lavado, "Covering THz gap using photomixers techonologies: arrays and new antenna topologies," Ph.D. dissertation, Universidad Carlos III de Madrid, 2016.

[99] T. Ishibashi and H. Ito, "Uni-traveling-carrier photodiodes," *Journal of Applied Physics*, vol. 127, no. 3, p. 031101, 2020.

[100] S. Preu, S. Malzer, G. H. Döhler, J. Zhang, Z. H. Lu, and L. J. Wang, "Highly collimated and directional continous-wave terahertz emission by photomixing in semiconductor device arrays," in *Millimeter-Wave and Terahertz Photonics*, D. Jäger and A. Stöhr, Eds., vol. 6194, International Society for Optics and Photonics. SPIE, 2006, pp. 111 – 119.

[101] A. Rivera-Lavado *et al.*, "Design of a dielectric rod waveguide antenna array for millimeter waves," *Journal of Infrared, Millimeter, and Terahertz Waves*, vol. 38, no. 1, pp. 33–46, 2017.

[102] S. Preu *et al.*, “Interference between two coherently driven monochromatic terahertz sources,” *Applied Physics Letters*, vol. 92, no. 22, p. 221107, 2008.

[103] J. M. de Paz, “Improving the capabilities from the antenna point of view at THz and sub-THz frequencies,” Ph.D. dissertation, Universidad Carlos III de Madrid, 2014.

[104] “Thorlabs,” [Online]. Available: https://www.thorlabs.com/.

[105] J. Montero-de Paz, E. Ugarte-Muñoz, L. E. García-Muñoz, I. C. Mayorga, and D. Segovia-Vargas, “Meander dipole antenna to increase CW THz photomixing emitted power,” *IEEE Transactions on Antennas and Propagation*, vol. 62, no. 9, pp. 4868–4872, 2014.

[106] J. R. Demers, R. T. Logan, and E. R. Brown, “An optically integrated coherent frequency-domain THz spectrometer with signal-to-noise ratio up to 80 dB,” in *Microwave Photonics, 2007 Interntional Topical Meeting on*, 2007, pp. 92–95.

[107] E. R. Brown, K. A. Abdalmalak, and W. Zhang, “Effect of metal resistive losses on the gain of a THz planar spiral antenna,” in *2020 14th European Conference on Antennas and Propagation (EuCAP)*, 2020, pp. 1–4.

[108] R. Hansen and W. Pawlewicz, “Effective conductivity and microwave reflectivity of thin metallic films,” *IEEE Transactions on Microwave Theory and Techniques*, vol. 30, no. 11, pp. 2064–2066, 1982.

[109] A. Mingardi, W.-D. Zhang, E. R. Brown, A. D. Feldman, T. E. Harvey, and R. P. Mirin, “High power generation of THz from 1550-nm photoconductive emitters,” *Opt. Express*, vol. 26, no. 11, pp. 14 472–14 478, May 2018.

[110] E. R. Brown, A. W. M. Lee, B. S. Navi, and J. E. Bjarnason, “Characterization of a planar self-complementary square-spiral antenna in the THz region,” *Microwave and Optical Technology Letters*, vol. 48, no. 3, pp. 524–529, 2006.

[111] C. Lin and C. P. Lee, “Comparison of Au/Ni/Ge, Au/Pd/Ge, and Au/Pt/Ge ohmic contacts to n-type GaAs,” *Journal of Applied Physics*, vol. 67, no. 1, pp. 260–263, 1990.

[112] F. Aviles, O. Ceh, and A. I. Oliva, “physical properties of Au and Al thin films measured by resistive heating,” *Surface Review and Letters*, vol. 12, no. 01, pp. 101–106, 2005.

[113] Y. Poo, R.-x. Wu, X. Fan, J. Q. Xiao, and B.-b. Jin, “An experiment study of gold nano-film’s conductivity at microwave and terahertz frequencies,” in *2010 Asia-Pacific Microwave Conference*, 2010, pp. 1452–1454.

[114] D. Warmowska, K. A. Abdalmalak, L. E. G. Muñoz, and Z. Raida, "High-gain, circularly-polarized THz antenna with proper modeling of structures with thin metallic walls," *IEEE Access*, vol. 8, pp. 125 223–125 233, 2020.

[115] D. Warmowska, "Terahertz antenna arrays for communications," Ph.D. dissertation, Brno University of Technology, 2020.

[116] S. Groiss, I. Bardi, O. Biro, K. Preis, and K. Richter, "Parameters of lossy cavity resonators calculated by the finite element method," *IEEE Transactions on Magnetics*, vol. 32, no. 3, pp. 894–897, 1996.

[117] V. S. Ilchenko, A. A. Savchenkov, A. B. Matsko, and L. Maleki, "Whispering-gallery-mode electro-optic modulator and photonic microwave receiver," *J. Opt. Soc. Am. B*, vol. 20, no. 2, pp. 333–342, Feb. 2003.

[118] A. Rueda *et al.*, "Efficient microwave to optical photon conversion: an electro-optical realization," *Optica*, vol. 3, no. 6, pp. 597–604, Jun. 2016.

[119] D. V. Strekalov, A. A. Savchenkov, A. B. Matsko, and N. Yu, "Efficient upconversion of subterahertz radiation in a high-Q whispering gallery resonator," *Opt. Lett.*, vol. 34, no. 6, pp. 713–715, Mar. 2009.

[120] G. S. Botello *et al.*, "Sensitivity limits of millimeter-wave photonic radiometers based on efficient electro-optic upconverters," *Optica*, vol. 5, no. 10, pp. 1210–1219, Oct. 2018.

[121] L. E. G. Muñoz, G. S. Botello, K. Abdalmalak, and M. Wasiak, "Room temperature radiometer based on an up conversion process for CubeSats applications," in *Terahertz Photonics*, vol. 11348, International Society for Optics and Photonics. SPIE, 2020, pp. 27 – 34.

[122] G. Santamaría-Botello, Z. Popovic, K. A. Abdalmalak, D. Segovia-Vargas, E. R. Brown, and L. E. G. Muñoz, "Sensitivity and noise in THz electro-optic upconversion radiometers," *Scientific Reports*, vol. 10, no. 1, pp. 1–13, 2020.

[123] G. S. Botello, K. A. Abdalmalak, D. Segovia-Vargas, and L. E. G. Muñoz, "Photonic upconversion for thz radiometry," in *2019 44th International Conference on Infrared, Millimeter, and Terahertz Waves (IRMMW-THz)*, 2019, pp. 1–2.

[124] G. S. Botello, K. A. Abdalmalak, D. Segovia-Vargas, A. Murk, and L. E. G. Muñoz, "On the comparison between low noise amplifiers and photonic upconverters for millimeter and terahertz radiometry," in *2019 30th International Symposium on Space Terahertz Technology (ISSTT)*, 2019.

[125] J. Treuttel *et al.*, "A 520–620-GHz schottky receiver front-end for planetary science and remote sensing with 1070 K–1500 K DSB noise temperature at room temperature," *IEEE Transactions on Terahertz Science and Technology*, vol. 6, no. 1, pp. 148–155, 2016.

[126] K. M. K. H. Leong *et al.*, “A 0.85 THz low noise amplifier using InP HEMT transistors,” *IEEE Microwave and Wireless Components Letters*, vol. 25, no. 6, pp. 397–399, 2015.

[127] A. Tessmann *et al.*, “243 GHz low-noise amplifier mmics and modules based on metamorphic HEMT technology,” *International Journal of Microwave and Wireless Technologies*, vol. 6, no. 3-4, p. 215–223, 2014.

[128] E. Schlecht *et al.*, “Schottky diode based 1.2 THz receivers operating at room-temperature and below for planetary atmospheric sounding,” *IEEE Transactions on Terahertz Science and Technology*, vol. 4, no. 6, pp. 661–669, 2014.

[129] W. Deal *et al.*, “A 670 GHz low noise amplifier with <10 dB packaged noise figure,” *IEEE Microwave and Wireless Components Letters*, vol. 26, no. 10, pp. 837–839, 2016.

[130] D. Hayton *et al.*, “A compact schottky heterodyne receiver for 2.06 THz neutral oxygen [OI],” in *2018 43rd International Conference on Infrared, Millimeter, and Terahertz Waves (IRMMW-THz)*, 2018, pp. 1–2.

[131] B. Guha *et al.*, “Surface-enhanced gallium arsenide photonic resonator with quality factor of 6×10^6,” *Optica*, vol. 4, no. 2, pp. 218–221, Feb. 2017.

[132] P. S. Kuo, J. Bravo-Abad, and G. S. Solomon, “Second-harmonic generation using-quasi-phasematching in a GaAs whispering-gallery-mode microcavity,” *Nature communications*, vol. 5, no. 1, pp. 1–7, 2014.

[133] D. P. Lake, M. Mitchell, H. Jayakumar, L. F. dos Santos, D. Curic, and P. E. Barclay, “Efficient telecom to visible wavelength conversion in doubly resonant gallium phosphide microdisks,” *Applied Physics Letters*, vol. 108, no. 3, p. 031109, 2016.

[134] C. S. Werner, W. Yoshiki, S. J. Herr, I. Breunig, and K. Buse, “Geometric tuning: spectroscopy using whispering-gallery resonator frequency-synthesizers,” *Optica*, vol. 4, no. 10, pp. 1205–1208, 2017.

[135] J. U. Fürst, K. Buse, I. Breunig, P. Becker, J. Liebertz, and L. Bohatý, “Second-harmonic generation of light at 245 nm in a lithium tetraborate whispering gallery resonator,” *Opt. Lett.*, vol. 40, no. 9, pp. 1932–1935, May 2015.

[136] V. S. Ilchenko *et al.*, “Crystal quartz optical whispering-gallery resonators,” *Opt. Lett.*, vol. 33, no. 14, pp. 1569–1571, Jul. 2008.

[137] N. Vukovic, N. Healy, J. Sparks, J. Badding, P. Horak, and A. Peacock, “Tunable continuous wave emission via phase-matched second harmonic generation in a ZnSe microcylindrical resonator,” *Scientific reports*, vol. 5, no. 1, pp. 1–9, 2015.

[138] A. Yariv, “Universal relations for coupling of optical power between microresonators and dielectric waveguides,” *Electronics Letters*, vol. 36, pp. 321–322, Feb. 2000.

[139] G. Santamaría-Botello *et al.*, “Study of free-space coupling into mm-wave whispering-gallery mode resonators for a radioastronomy receiver,” in *2017 IEEE International Symposium on Antennas and Propagation USNC/URSI National Radio Science Meeting*, 2017, pp. 1277–1278.

[140] G. S. Botello, K. A. Abdalmalak, D. Segovia-Vargas, and L.-E. García-Muñoz, “Study of near-field coupling in whispering gallery mode resonators,” in *2017 IEEE MTT-S International Conference on Numerical Electromagnetic and Multiphysics Modeling and Optimization for RF, Microwave, and Terahertz Applications (NEMO)*, 2017, pp. 155–157.

[141] G. S. Botello *et al.*, “Analytical study of free-space coupling of THz radiation for a new radioastronomy receiver concept,” in *2017 11th European Conference on Antennas and Propagation (EUCAP)*, 2017, pp. 836–840.

[142] K. A. Abdalmalak *et al.*, “Microwave radiation coupling into a WGM resonator for a high-photonic-efficiency nonlinear receiver,” in *2018 48th European Microwave Conference (EuMC)*, 2018, pp. 781–784.

[143] A. Rivera-Lavado *et al.*, “Planar lens–based ultra-wideband dielectric rod waveguide antenna for tunable THz and sub-THz photomixer sources,” *Journal of Infrared, Millimeter, and Terahertz Waves*, vol. 40, no. 8, pp. 838–855, 2019.

[144] G. A. Santamaría Botello, “Low noise THz detection via optical parametric upconversion,” Ph.D. dissertation, Universidad Carlos III de Madrid, 2020.

[145] K. Alsirhani, K. A. Abdalmalak, C. S. Lee, G. Santamaría-Botello, D. Segovia-Vargas, and L. E. García-Muñoz, “Dielectric resonator antenna fed by tapered dielectric rod waveguide for 5G mm-wave applications,” in *2020 IEEE International Symposium on Antennas and Propagation and North American Radio Science Meeting*, 2020, pp. 149–150.

[146] K. Luk and K. Leung, *Dielectric Resonator Antennas*, ser. Antennas S. Research Studies Press, 2003.

[147] A. Petosa and S. Thirakoune, “Rectangular dielectric resonator antennas with enhanced gain,” *IEEE Transactions on Antennas and Propagation*, vol. 59, no. 4, pp. 1385–1389, 2011.

[148] X. S. Fang, C. K. Chow, K. W. Leung, and E. H. Lim, “New single-/dual-mode design formulas of the rectangular dielectric resonator antenna using covariance matrix adaptation evolutionary strategy,” *IEEE Antennas and Wireless Propagation Letters*, vol. 10, pp. 734–737, 2011.

[149] P. Bhartia, K. Rao, and R. Tomar, *Millimeter-wave Microstrip and Printed Circuit Antennas*, ser. Antennas and Propagation Library. Artech House, 1991.

[150] A. S. Al-Zoubi, A. A. Kishk, and A. W. Glisson, "A linear rectangular dielectric resonator antenna array fed by dielectric image guide with low cross polarization," *IEEE Transactions on Antennas and Propagation*, vol. 58, no. 3, pp. 697–705, Mar. 2010.

[151] M. S. Abdallah, Y. Wang, W. M. Abdel-Wahab, and S. Safavi-Naeini, "Design and optimization of SIW center-fed series rectangular dielectric resonator antenna array with 45 linear polarization," *IEEE Transactions on Antennas and Propagation*, vol. 66, no. 1, pp. 23–31, Jan. 2018.

[152] P. Bhartia and I. Bahl, *Millimeter wave engineering and applications*, ser. A Wiley-Interscience publication. Wiley, 1984.

[153] F. Xu and K. Wu, "Guided-wave and leakage characteristics of substrate integrated waveguide," *IEEE Transactions on Microwave Theory and Techniques*, vol. 53, no. 1, pp. 66–73, Jan. 2005.

[154] A. A. Althuwayb *et al.*, "3-D-printed dielectric resonator antenna arrays based on standing-wave feeding approach," *IEEE Antennas and Wireless Propagation Letters*, vol. 18, no. 10, pp. 2180–2183, Oct. 2019.

[155] W. Huang and A. Kishk, "Compact wideband multi-layer cylindrical dielectric resonator antennas," *IET microwaves, antennas & propagation*, vol. 1, no. 5, pp. 998–1005, 2007.

[156] R. Chair, A. Kishk, K. Lee, and C. Smith, "Wideband flipped staired pyramid dielectric resonator antennas," *Electronics Letters*, vol. 40, no. 10, pp. 581–582, 2004.

[157] G. A. Santamaría-Botello *et al.*, "Maximization of the optical intra-cavity power of whispering-gallery mode resonators via coupling prism," *Opt. Express*, vol. 24, no. 23, pp. 26 503–26 514, Nov. 2016.

[158] "Smartact," [Online]. Available: https://www.smaract.com.

[159] "The Resonant Optics group," [Online]. Available: https://www.physics.otago.ac.nz/research/resonantoptics.

[160] "The Applied Diamond Inc." [Online]. Available: http://usapplieddiamond.com.

[161] "NanoRennes," [Online]. Available: https://www.ietr.fr/en/nr-nanorennes-platform.

About the Author

Kerlos Atia Abdalmalak is a Research Associate in the GREMA Group (Radiofrequency, Electromagnetism, Microwaves and Antennas Group) at Carlos III University of Madrid, Spain. He was born in Luxor, Egypt, in 1990. He received the B.Sc. degree (Hons.) (ranked 2nd among the colleagues) in communication engineering from Aswan University, Egypt in 2011 then he joined the department of electrical engineering, Aswan University as a teaching assistant. He received the M.Sc. degree (excellent grade) in multimedia and communication from Carlos III University of Madrid in 2015.

He has authored/co-authored 11 Journal Citation Ranking "JCR" journals (7 in the first quartile Q1 and 3 in the second quartile Q2 following Thomson Reuters), 2 invited papers, and 33 international conference papers. He has participated in 12 research projects financed by Madrid Regional Ministry of Education, Ministry of Economy and Business, Huawei, European Space Agency (ESA), SENER, and other private companies with total fund exceeds 2.5 million Euros. His technical interests include antennas and propagation, ultra-wideband/multiband antennas, reflector/feed systems, radio astronomy receivers, base stations, 5G communications, antenna arrays, THz technologies, whispering gallery mode resonators, and millimeter/submillimeter waves.

Mr. Abdalmalak served as a Peer-Reviewer/TPC Member for several JCR journals and international conferences, such as Optics Express (Q1), IEEE ACCESS (Q1), Progress in Electromagnetics Research (PIER) (Q2), International Journal of Infrared and Millimeter Waves (IJIM) (Q3), the European Conference on Antennas and Propagation (EuCAP), the International Conference on Innovative Trends in Computer Engineering (ITCE), the Asia Simulation Conference (AsiaSim), Communication Theory, Information Theory, Antennas and Propagation (CIAP), and the International Conference on Electrical, Electronic, Communication and Control Engineering (ICEECC). He received the Erasmus Mundus GreenIT grant in 2014, the Young Scientists Award (2nd prize) by URSI/Spain in 2017, was selected as IEEE Ambassador for the IEEEXtreme 14.0 competition at Region 8 (Europe, Middle East and Africa) in 2020, and was selected as the IEEE section lead for Spain for the IEEEXtreme 15.0 Competition in 2021.

Google Scholar: https://scholar.google.com/citations?user=MgVFmyEAAAAJ&hl=en
ResearchGate: https://www.researchgate.net/profile/Kerlos_Atia_Abdalmalak
ORCID Code: https://orcid.org/0000-0002-9544-2412